Near-field-scattering-based optical control & Brillouin optomechanics in optical microresonators

Andreas Øverlie Svela
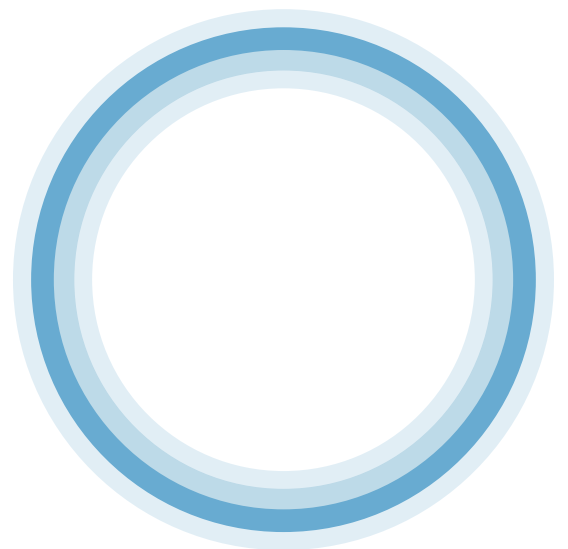
Department of Physics
Imperial College London

Submitted for the degree of Doctor of Philosophy
April 2022

STATEMENT OF ORIGINALITY The content presented in this thesis is the author's own
work unless otherwise noted and referenced. Collaborators and research colleagues have
made crucial contributions, and are acknowledged in the text where appropriate. To the
best of the author's knowledge, relevant related work has been referenced throughout as
appropriate.

Typeset using LATEX with Minion Pro 11/10 pt.

Version 2.0 | 16th June 2022

Abstract

Resonance is a powerful effect that occurs throughout nature. For example, the effect is key to the excitement of playground swings and it underpins technologies ranging from musical instruments to atomic clocks. In optics, microresonators are extensively used to provide such enhancement and are employed in a number of areas including sensing, metrology, optomechanics, and quantum optics to name a few prominent examples.

This thesis comprises two main parts. One part expands the optical microresonator control toolbox by demonstrating suppression of backscattering. The other part uses a whispering-gallery-mode microresonator for resonant enhancement of a Brillouin optomechanical interaction to prepare and characterise non-Gaussian mechanical states.

   The first part explores a technique for coherently controlling backscattering in microresonators by introducing a sub-wavelength-size scatterer within the near field of the resonator. The scatterer's position determines the phase and amplitude of the induced backscattering, and by tuning its position, destructive interference between the induced and intrinsic backscattering can reduce unwanted optical back reflections. The presented experiment demonstrates a suppression exceeding 34 dB of the intrinsic backscattering level, limited by photodetector noise. The technique can be applied to experiments where backscattering is currently limiting performance, such as optical gyroscopes.

   The second part of this thesis presents an experiment preparing non-Gaussian states of mechanical motion via heralded single- and double-phonon subtraction from a laser-cooled thermal mechanical state. The experiment utilises a combination of single-photon detection for heralded state-preparation, and heterodyne detection for verification and characterisation of the prepared states. The work advances the state of the art for optics-based tomography of mechanical states by showing more than one order of magnitude improvement in the s-parameter, which captures the effects of measurement inefficiencies and added noise in tomography and state reconstruction experiments. Further improving the measurement efficiency provides a path towards tomography of non-classical mechanical states via optomechanics.

Acknowledgements

These three years have truly been a journey in both the most literal and figurative sense. I have met wondrous people along the way, many of which I am indebted to for their scientific contributions and insight, and many more for their help and support, friendships and patience. Crucially, all of these things have been necessary for making it possible to do this work. I want to thank you all.

A doctorate seldom goes according to plan. When we first discussed the research plan in 2018 we did not anticipate a novel coronavirus to appear, nor that Pascal's lab would move from the UK to Germany, nor the multiple delays to Michael's planned lab move from Oxford to London. As a result, this thesis is the culmination of the work I have been doing across four different research institutions as a student in the Quantum Systems Engineering Skills Hub at Imperial College London. I have been lucky to have had the opportunity to work within two research groups, focussing on different types of physics, and to spend time at four distinctive institutions.

Firstly, a big thank you to my two supervisors *Dr Michael Vanner* and *Dr Pascal Del'Haye* for taking me on as a student and for warmly welcoming me to your respective groups. I am grateful for what that you have taught me, and the considerable administrative efforts you have both put down to make this project happen. Thank you also for the flexibility and trust, for letting me explore, both in the lab and the world outside it.

The first year of the PhD was spent at the National Physical Laboratory, generously providing laboratory space within the Time and Frequency group on the Teddington site. The time in Pascal's Microcombs team during my master's year was such an enjoyable and inspiring experience that I decided to pursue the PhD, which says a lot about that group. *Dr Jonathan Silver*, *now-Dr Leonardo Del Bino* and *Dr Shuangyou Zhang* taught me from scratch how to build and operate optics experiments and all the other things related to doing lab work – that required a lot of time, and patience. Together with *George Ghalanos* and *Niall Moroney* who started their doctorates at the same time as myself and *now-Dr Michael Woodley*, this was a warm and open team, with important contributions from spiritual-associate group member *Dr Alissa Silva*.

When joining Michael's team, then at the University of Oxford, I got to work with more brilliant colleagues and also new (to me) physics. The talented *now-Dr Georg Enzian* laid much of the experimental ground work, building an impressive machine for Brillouin optomechanics and starting experiments we are still working on today. Together with *just-turned-Dr John Price* and *Lars Freisem* we were a small experimental team, but managed to overcome lots of challenges in and beyond the lab to get the results presented here.

The lab move from Oxford to the basement of the Blackett Laboratory at Imperial College was carried out in the summer of 2020, with its last delay as a result of the Covid pandemic. It still seems incredible John and I managed to pack it up in one week only.

At Imperial, I got to know and work with the theory wizards *Lydia Kanari-Naish* and *Jack Clarke*. Thanks for the patience when explaining what we are actually doing, and I appreciate the helpful Slack-exchanges with Jack no matter the time of the day. Since then, new members have joined the team, *Evan Cryer-Jenkins* and *Dr Kyle Major* – it has been a pleasure to work with you and good to see that the experiments are in good hands going forward. Thanks to Kyle and Lars for the helpful discussions in the office whilst writing up this thesis and to John for his helpful messages.

Contents

I   Backscattering control in microresonators

List of publications

PEER-REVIEWED JOURNAL PUBLICATIONS

Coherent suppression of backscattering in optical microresonators by A. Svela, J. Silver, L. Del Bino, S. Zhang, M. Woodley, M. Vanner, P. Del'Haye in Light: Science & Applications 9, 202 (2020).

Non-Gaussian mechanical motion via single and multiphonon subtraction from a thermal state by G. Enzian,[†] L. Freisem,[†] J. Price,[†] A. Svela,[†] J. Clarke, B. Shajilal, J. Janousek, B. Buchler, P. K. Lam, and M. Vanner in Physical Review Letters 127, 243601 (2021).

Coauthor publications

- *Sub-milliwatt-level microresonator solitons with extended access range using an auxiliary laser* by S. Zhang, JMS, LDB, FC, MTMW, GG, A. Svela, NM, P. Del'Haye in Optica 6, 206–212 (2019).
- *Logic gates based on interaction of counterpropagating light in microresonators* by N. Moroney, LDB, MTMW, GG, JMS, A. Svela, SZ, P. Del'Haye in Journal of Lightwave Technology 38, 1414–1419 (2020).
- *Kerr-nonlinearity-induced mode-splitting in optical microresonators* by G. Ghalanos, JMS, LDB, NM, SZ, MTMW, A. Svela, P. Del'Haye in Physical Review Letters 124, 223901 (2020).
- *Nonlinear enhanced microresonator gyroscope* by J. Silver, LDB, MTMW, GG, A.Svela, NM, SZ, KTVG, P. Del'Haye in Optica 8, 1219–1226 (2021).

PUBLISHED CONFERENCE PROCEEDINGS

Listing only those for which the author of this thesis presented the talk.

- Conference on Lasers and Electro-Optics (CLEO) 2019, San Jose, USA:
  Spontaneous symmetry breaking based near-field sensing with a microresonator, paper JM3B.3, by A. Svela, JMS, LDB, SZ, MTMW, MV, P. Del'Haye
- CLEO Pacific Rim 2020, Online (Sydney, Australia):
  Suppressing intrinsic backscattering in ultra-high-Q optical microresonators, paper C5B-4, by A. Svela, JMS, LDB, SZ, MTMW, MV, P. Del'Haye.
- CLEO 2021, Online (San Jose, USA):
  >30 dB suppression of intrinsic backscattering in whispering-gallery-mode microresonators, paper STu1F.2, by A. Svela, JMS, LDB, SZ, MTMW, MV, P. Del'Haye.
- CLEO Europe-EQEC 2021, Online (Munich, Germany):
  More than 34 dB backscattering suppression in microresonators paper ED-4.3, by A. Svela, JMS, LDB, SZ, MTMW, MV, P. Del'Haye.
- Frontiers in Optics 2021, Online (Washington DC, USA):
  Single- and multi-phonon subtraction to a mechanical thermal state via optomechanics, paper LM6E.1, by G. Enzian,[†] L. Freisem,[†] J. Price,[†] A. Svela,[†] JC, BS, JJ, BB, PKL, M. Vanner.
- CLEO Pacific Rim 2022, Sapporo, Japan:
  Single- and multi-phonon subtraction to a mechanical thermal state via optomechanics, accepted, by A. Svela,[†] G. Enzian,[†] L. Freisem,[†] J. Price,[†] JC, BS, JJ, BB, PKL, M. Vanner.

[†] These authors contributed equally and are listed alphabetically

MANUSCRIPTS IN PREPARATION

- *Second-order coherence across the Brillouin lasing threshold* by E. Cryer-Jenkins, GE, LF, NM, JP, A. Svela, KM, M. Vanner.
- *Phase-sensitive measurement-based mechanical time-bin state preparation using Franson-type interferometry* by J. Price, LKN, A. Svela, LF, JJ, GE, M. Vanner.

AWARDS

- Best contributed talk at AMOLF *Summer School on Nanophotonics*, Amsterdam, The Netherlands, 2019
- Best student talk at *Conference on Optics, Atoms and Laser Applications (KOALA)*, Dunedin, New Zealand, 2019
- Runner-up student talk at *Faculty of Natural Sciences Research Showcase*, Imperial College London, 2020
- Best talk at *Department of Physics Postgraduate Research Symposium*, Imperial College London, 2021

List of figures

APPENDIX A

APPENDIX B

List of tables

List of acronyms & abbreviations

AC	alternating current
APC	angled physical contact (fibre connector standard)
API	application programming interface
AS	anti-Stokes
BNC	Bayonet Neill–Concelman (electrical cable connector)
BW	bandwidth
CCW	counter-clockwise
CW	clockwise
DC	direct current
ECDL	external-cavity diode laser
EDFA	erbium doped fibre amplifier
EIT	electromagnetically induced transparency
EOM	electro-optic modulator
ESA	electronic spectrum analyser
FP	Fabry–Pérot (cavity)
FSR	free spectral range
FWHM	full width at half maximum
HEPA	high-efficiency particulate air [filter]
IPA	isopropanol
IR	infrared
LO	local oscillator
MEMS	micro-electromechanical
OMIT	optomechanically induced transparency
PC	polarisation controller
PDH	Pound–Dreyer–Hall (locking method)
PD	photodiode
PID	proportional–integral–derivative [controller]
PLA	polylactic acid (polymer)
Q	(optical or mechanical) quality [factor]
RF	radio frequency
SEM	scanning electron microscope
SMF-28	standard telecoms single-mode optical fibre
SNOM	scanning near-field microscopy
SNSPD	superconducting-nanowire single-photon detector
SPAD	single photon avalanche diode
SPM	self-phase modulation
TECC	thermoelectric-cooler controller
TEC	thermoelectric-cooler
TE	transverse electric
TM	transverse magnetic
UV	ultraviolet
VOA	variable optical attenuator
WGM	whispering-gallery mode
XPM	cross-phase modulation

CHAPTER 1

Introduction and thesis overview

Since optical whispering-gallery-mode (WGM) microresonators were experimentally introduced in 1989 by Braginsky *et al.* [1], an extensive research field has emerged, as covered in reviews [2–7], textbooks [8–11], and a number of dissertations. The micrometre-size geometric features of the resonators confine the light to small volumes, which, combined with low optical losses, means high optical intensities build up inside the resonators for comparatively low input powers. The high optical intensity gives access to nonlinear optical effects at relatively low optical input powers. And like so many things in life and physics, when something is nonlinear, it is usually more interesting.

[..] whispering-gallery microresonators can open the way to realize Feynman's quantum-mechanical computer.
— Braginsky *et al.* [1]

Nonlinear optics refers to phenomena occurring when a dielectric material's response to an optical field depends on the applied electromagnetic field in a nonlinear manner [12, 13]. In a classical picture, this means that the dipole moment per volume, called the polarisation density, depends nonlinearly on the applied field. The nonlinearly induced dipole moment from the field can act as a classical source for the field, for instance generating light at twice the frequency of the applied field, or affect the optical properties of the material such as modifying the index of refraction. In a quantum picture, where the fields are quantised, the notion of photons is helpful for understanding nonlinear effects as photons of different frequencies being created and destroyed, with the total momentum and energy being conserved. A quantum representation is necessary for describing spontaneous processes – those where spontaneous emission occurs due to vacuum fluctuations [14].

The quantum picture is also useful for describing nonlinear phenomena where photons interact with quantised vibrations in a medium, called phonons [15]. To observe and study this form of exchange of momentum and energy between optical fields and mechanical waves, high optical powers are typically needed to drive the interaction due to the relatively low coupling between the light and mechanical vibrations. Microresonators can provide these high optical powers combined with appreciable coupling and low damping of the mechanical vibrations, meaning microresonators can be a compact experimental platform for these types of studies.

Over the last three decades, a range of nonlinear optical effects have been observed in microresonators such as spontaneous symmetry breaking [16, 17], parametric oscillations [18], Raman lasing [19], four-wave mixing [20], and frequency doubling [21] and tripling [22]. Also optomechanical phenomena have been studied in microresonators, including radiation-pressure-based [23–26] and Brillouin-scattering-based systems [27–31], with the latter type first reported for WGM resonators in 2009 by Grudinin *et al.* [32] and Tomes and Carmon [33].

With the broad range of effects observed in microresonators, these devices have become a platform for studying optical phenomena, and have found numerous applications within sensing [2, 7, 8, 34–39], ranging from detection of a single virus [40] to displacements of attometres [41], metrology [42–44], quantum optics [45, 46], and classical and quantum information processing [47–50], to name a few.

The work presented in this thesis aims to expand the body of research on WGM resonators, in particular demonstrating a technique for reducing unwanted optical backscattering and investigating applications of the platform for sensing and quantum state preparation of acoustic modes. The work is split into two parts: one part focussing on backscattering suppression and near-field sensing using the Kerr nonlinearity, and the second part on Brillouin quantum optomechanics.

The investigation is not so complete as I should wish it to be; but it has been carried forward as far as my limited time and means would allow.
— Kerr [51]

1.1   WGM RESONATOR BACKSCATTERING CONTROL

As microresonators are becoming an optical component increasingly used for various applications, including commercial applications in out-of-lab environments, research seeking to improve the performance, stability, and other key parameters is flourishing. One avenue for improvement is to exploit new ideas and effects to introduce novel protocols, another is to better control properties currently limiting an application. One such limiting property is the phase and magnitude of backreflection inside the microresonator, which is crucial to control for some applications.

A range of different microresonator geometries exist, and they can be made from a variety of dielectric materials, both crystalline and amorphous. For chip-based resonators, fabrication usually involves complex cleanroom processes [52, 53], whereas for other geometries, time-consuming manual polishing [21, 54] is often needed. In 2013, Del'Haye *et al.* [55] introduced laser-machined fused silica rods, permitting fabrication time of the order of minutes, using relatively inexpensive equipment, with high reproducibility and low optical losses.

However, for all fabrication methods and materials, imperfections in the resonator surface or bulk material can cause scattering of some portion of the light circulating in the resonator into the counter-propagating whispering-gallery mode through Rayleigh scattering [56]. The backscattered light can reduce the performance of the device for some applications and experiments, and thus methods for suppressing these backreflections are sought in the community. Recently, Kim *et al.* [57] demonstrated a Brillouin-optomechanical method to reduce backscattering, showing ≃13 dB suppression. The method is elegant but sets some experimental requirements that can be challenging to fulfil, and the backscattering suppression scales in an unfavourable fashion with optomechanical coupling if high suppression is desired.

THIS THESIS. Here, a method for suppressing backscattering in microresonators using a near-field probe is presented, along with results from an experimental demonstration showing a record >34 dB reduction in the backscattered optical power. The method works by the near-field probe coherently inducing backscattering with a controllable phase and amplitude, which can be made to interfere destructively with the intrinsic backscattering, eliminating the total backscattered power. This work is the first experimental investigation of backscattering suppression with this method, and the technique and experimental results are published in Svela *et al.* [58].

The presented method can be applied not only to the microrod WGM resonator used here but also to on-chip optical resonators. The control scatterer can be permanently integrated on-chip for better stability and for example microelectromechanical actuators can provide tuning.

For this work, silica rod microresonators with exceptionally high optical quality factors ($\geq 10^9$) were fabricated using a – to the best of the author's knowledge – novel modification to the laser-lathe fabrication technique of Del'Haye *et al.* [55]. The resonators were fabricated in a nitrogen atmosphere to avoid the possible formation of absorbing hydroxyl groups, with data suggesting an improvement in the achieved quality factor by approximately a factor of three. Furthermore, a rig for fabrication of tungsten tip near-field probes was built. By computer-controlling the voltage cutoff time for the electrochemical etching process, sub-100-nm tips were successfully fabricated. The tip size versus delay in the voltage cutoff was explored and was used to control the tip size.

1.2   CAVITY QUANTUM OPTOMECHANICS WITH BRILLOUIN SCATTERING

It has been known for a century that particles of light carry momentum, which can be transferred to matter, and vice versa. This insight led Ashkin [59] to utilise radiation pressure for optical trapping of dielectric particles, and later live bacteria [60], an important technique used in many labs for research and applications around the world, and awarded a Nobel Prize for its significant contribution to science. Another recent Nobel Prize, awarded for the detection of gravitational waves using optomechanical displacement sensing [61], further highlights the impact of research in the area of momentum transfer between light and mechanical degrees of freedom.

What is now commonly called *optomechanics* – the momentum exchange between light and matter – has become an increasingly studied subject, with the realisation that performing optomechanical experiments in optical cavities significantly increases the interaction. Microresonators have greatly improved the accessibility of optomechanical experiments because they provide low optical and mechanical losses with appreciable optomechanical coupling in compact systems. Together with advances in microfabrication techniques and cryogenic systems being more widely available, the research field has developed quickly over the last decades.

OPTOMECHANICS WITH WGM RESONATORS. The term 'whispering-gallery mode' used to describe a type of optical microresonators actually originates from a phenomenon in the acoustic domain: whispering galleries are found in many round buildings across the globe, where a whisper close to the gallery circumference can be clearly heard along the arc, even at long distances from the whisperer. It was this discovery that prompted the theoretical work on the extension of WGMs to the electromagnetic domain [62, 63].

Unsurprisingly then, optical WGM resonators can also support acoustic whispering-gallery modes. Over the last decade, optomechanics using the Brillouin-scattering interaction has emerged, where optical and high-frequency acoustic modes interact through electrostriction and photoelasticity. The GHz-frequency acoustic modes can be excited by the thermal surrounding environment or by optical stimulation. Recently, strong optomechanical coupling mediated via Brillouin scattering between an optical and a GHz-mechanical mode of a WGM resonator was demonstrated [64]. The combination of strong optomechanical coupling, high-frequency phonons, and long phonon lifetimes is a promising platform for further optomechanical experiments with quantum control of the mechanical motion in mind.

HYBRID SYSTEMS FOR QUANTUM TECHNOLOGIES. The coupling of coherent light fields and mechanical degrees of freedom allows one to probe the quantum nature of the mechanics, mapping the mechanical motion onto the light field; or conversely, provide coherent control over the mechanical motion. In the optomechanics literature, a main focus is on controlling and exploring the quantum states of massive objects, where generation of macroscopic non-classical states is a main goal.

Coherent coupling between photons and phonons has proven useful in the context of the current rapid advance in quantum technologies for sensing, metrology, and information transfer and processing, with a recent review by Barzanjeh *et al.* [65] devoted to this topic. One use-case, where promising results have already been demonstrated in optomechanical experiments, is the transduction of quantum information from optical frequencies to microwave frequencies compatible with electronics [66], as well as between different optical frequencies, mediated by optomechanics [67]. This type of frequency conversion for quantum information might prove essential for future quantum networks [68], as photons, for their many favourable properties as information carriers, will most likely be the choice of transmitted carrier, but locally, computing steps might involve microwave qubits in for instance superconducting qubit systems [69]. Phononic circuits with optomechanical interfaces have also been demonstrated [70–73]. The fidelity, i.e., the likeness of the input state to the output state, of such conversion must be high for a quantum network to work efficiently and reliably, and there is still a long way to go to boost the fidelity and operation rates. An important step towards better quantum control and measurement of mechanical states within optomechanics is to generate and characterise non-classical mechanical states.

THIS THESIS. This work contributes toward the goal of non-classical mechanical state generation and characterisation by experimentally demonstrating a photon-counting method for multi-phonon subtraction and advancing the state-of-the-art overall measurement efficiency of the mechanical state. Building on techniques from quantum optics and recent work demonstrating single-phonon subtraction from a thermal mechanical state [74], the phase-space distributions of non-Gaussian phonon-subtracted mechanical thermal states are measured using photon counting for state preparation and simultaneous optical heterodyne detection for characterisation. The measurements show that the initial thermal state is transformed by the phonon subtraction events from an initial Gaussian in phase space into a ring shape with a diameter that increases with the number of phonons subtracted. The experiment is the first observation of the effect that the mean phonon occupation triples when a two-phonon subtraction is performed to the thermal mechanical state. The work has recently been published, Enzian, Freisem, Price, Svela *et al.* [75], where the four first authors contributed equally and are listed alphabetically.

The work presented expands the toolkit for optical control and readout of mechanical states, and can be applied to future room-temperature or cryogenic experiments to exploit and characterise the non-Gaussian and non-classical properties these operations generate. The experiment represents an advance in the state of the art for optics-based tomography of mechanical states and will be useful not only for Brillouin-based cavity optomechanics, but for a broad range of both applied and fundamental studies of mechanical quantum-state engineering and tomography. Pursuing this line of research will facilitate the development of mechanical-oscillator-based quantum technology such as quantum memories exploiting the long coherence times available.

1.3 OUTLINE OF THE THESIS

This thesis is comprised of two main parts as outlined above. Additionally, there is an introductory part with material serving as a background for all following chapters.

BACKGROUND: *Fundamentals & experimental techniques*

Chapter 2   covers the fundamentals of whispering-gallery-mode resonators, explaining key concepts and deriving results used elsewhere in the thesis. For those working with WGM resonators this will largely be familiar material.

Chapter 3   describes fabrication methods for the custom-made components used in the work presented in this thesis, as well as some experimental methods used. This includes the two types of rod optical resonators, tapered optical fibres for coupling to resonators and sub-optical-wavelength-size tungsten tips to be used as near-field probes.

PART I: *Backscattering control in microresonators*

Chapter 4   presents a method, theoretical model and experimental results for suppression of backscattering in WGM resonators. The chapter is based on a publication by Svela *et al.* [58].

PART II: *Towards quantum applications with Brillouin cavity optomechanics*

Chapter 5 serves as an introduction to optomechanics, focussing on electrostriction-mediated Brillouin optomechanics. The chapter motivates the direction of research, defines important figures of merit for an optomechanical system, and then describes Brillouin optomechanics in whispering-gallery-mode resonators.

Chapter 6 describes an optomechanical experiment in which non-Gaussian states of motion are generated by subtraction of phonons from a thermal state. The subtracted states are characterised via heterodyne tomography. The chapter is based on a publication by Enzian, Freisem, Price, Svela *et al.* [75].

CHAPTER 2

Fundamentals of whispering-gallery-mode microresonators

A whispering-gallery mode might sound like it has little to do with optics. The name comes from a phenomenon in the acoustic domain known as whispering galleries, which can be found in many buildings with circular structures, often in temples or cathedral domes. In these galleries, if one whispers close to the wall, the whisper can be clearly heard along the gallery arc, even far from the whisperer.

Although the phenomenon of whispering galleries has been well-known for centuries, up until the late nineteenth century the "acoustical authorities [were] not entirely agreed," as Lord Rayleigh [76] wrote in 1878, about these galleries' "precise mode of action." Some believed the sound was reflected in the domes above them. Rayleigh[i] wanted to settle the question, spent some time in St. Paul's cathedral in London to study the phenomenon, and wrote:

> Judging from some observations I have made in St. Paul's whispering gallery, I am disposed to think that the phenomenon is to be explained somewhat differently. [..] *The whisper seems to creep round the gallery horizontally.*
> [76, p. 127, emphasis added]

His theory was indeed correct; the longitudinal pressure waves we know as sound are guided along the gallery wall, decaying slower than the typical inverse square distance. This kind of pressure waves will be important later in this thesis, but in this chapter, it is the optical equivalent of the whispering gallery that is described.

Rayleigh extended his theory from the acoustic to the electromagnetic domain in the 1910s [62, 78], and Raman and Sutherland [79, 80] provided corrections revealing more complex radial modal structures, now known as whispering-gallery modes (WGM).[ii] A couple of decades later, in 1939, Richtmyer [63] proposed dielectric WGM resonators for electromagnetic fields. However, it was first a few years after the advent of the laser by Maiman [84] in 1960 that the first experimental observation of optical WGMs was reported: Garrett *et al.* [85] observed stimulated emission from WGMs in millimetre-sized, doped calcium fluoride spheres. Optical WGMs were encountered in optical experiments over the years, but it was first in 1989 that Braginsky *et al.* [1] introduced the first optical whispering-gallery-mode resonators with high-efficiency coupling to external light fields.

Since the first WGM microresonator experiments three decades ago, optical WGM resonators have enabled optical research in many directions, probing interesting physics and finding

[i] Coincidentally, Rayleigh was the chair of the committee that in 1897 recommended the establishment of the National Physical Laboratory in Teddington where most of the work described in Chapter 4 of this thesis was carried out. From NPL's establishment in 1899 until 1919, Rayleigh was the chair of its executive committee [77].
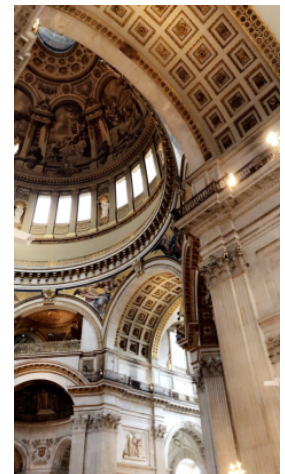
Figure 2.1. Rayleigh's laboratory: St. Paul's whispering gallery.

[ii] On a very different scale than the one this thesis is exploring, other examples of electromagnetic and acoustic WGMs include the ionosphere that can act as waveguide supporting low frequency radio wave WGMs [81], or the earth itself supporting seismic WGM modes [82], where waves lasting for more than 100 hours with a one-hour roundtrip time have been observed [83].

a range of research and commercial applications, with some examples listed in the opening chapter of this thesis. As whispering-gallery-mode resonators are central to all aspects of the work described in this thesis, this chapter gives an introduction to the physics of WGM resonators, serving as a base for the other parts of this thesis.

CHAPTER CONTENTS

2.1   THE CAVITY RESONANCE CRITERIUM, LOSSES, AND FIGURES OF MERIT

Optical microresonators are optical cavities where light is confined to micrometre-scale volumes and can sustain propagation over multiple roundtrips. The optical modes of the resonator are defined by the frequencies that interfere constructively over a cavity roundtrip, and with the appropriate polarisation. The constructively interfering frequencies are those with an integer number of wavelengths λ for a roundtrip, thus for a cavity of effective roundtrip length L', the modes are given by the resonance criterium

$$m\lambda_m = L' = nL \,, \tag{2.1}$$

where the *mode number m* is an integer corresponding to the number wavelengths over a roundtrip. The wavelength λ_m is given as a vacuum wavelength, which gives the effective roundtrip length $L' = nL$ for a resonator of geometric roundtrip length L and with refractive index n. Note that throughout this thesis, optical wavelengths are always given as vacuum wavelengths. The corresponding resonance frequencies are given by

$$\upsilon_m = m \, \frac{c}{nL} \,, \tag{2.2}$$

mode number m

where c is the vacuum speed of light, and $c/n = v_\mathrm{ph}$ the *phase velocity* of the optical field in the resonator material. The spectral separation between resonances,

phase velocity v_{ph}

$$\upsilon_{m+1} - \upsilon_m \ = \frac{c}{nL} \equiv \upsilon_\mathrm{FSR} \,, \tag{2.3}$$

is called the *free spectral range* (FSR) of the cavity. Note that nL/c is the time it takes for the light to make a roundtrip of the cavity, and thus the FSR is the inverse of the cavity roundtrip time, $T_\mathrm{rt} = \upsilon_\mathrm{FSR}^{-1}$.

free spectral range v_{FSR}

roundtrip time T_{rt}

2.1.1   *Cavity lifetime, linewidth, and losses*

The light circulating in the cavity has a finite lifetime due to energy dissipation. The losses are usually categorised as intrinsic or extrinsic losses: Intrinsic loss sources are for instance material absorption or scattering (see Section 2.4), whereas the extrinsic losses are related to the deliberate coupling of the resonator to the environment to interact with it (see Section 2.3). The *cavity lifetime* τ is defined as the time it takes for the energy of the field to be reduced by Euler's number, e, and is given by the ratio of the energy stored in the cavity and the dissipated power,

cavity lifetime τ

$$\tau = \frac{\mathcal{E}_\mathrm{cav}}{-\dot{\mathcal{E}}_\mathrm{cav}} = \frac{\mathcal{E}_\mathrm{cav}}{\mathcal{P}_\mathrm{dis}} \,, \tag{2.4}$$

where the dot represents the time-derivative of the quantity.

To show that this definition of the lifetime corresponds to the time of reduction of the field by a factor of e, consider an intra-cavity energy attenuation parameter α_att for the

electric field E so that after N cavity roundtrips, the cavity energy $\mathcal{E}_{\text{cav}}$ is proportional to

$$|E_N|^2 = \exp(-\alpha_{\text{att}}L)\,|E_{N-1}|^2 = \exp(-\alpha_{\text{att}}NL)\,|E_0|^2 \,, \tag{2.5}$$

where $|E_0|^2$ is the initial field energy up to the same proportionality factor as $|E_N|^2$. The energy is reduced by a factor of e after N_e roundtrips, and can be calculated from $\exp(-\alpha_{\text{att}}N_e L) = \exp(-1)$, which yields

$$N_e = (\alpha_{\text{att}}L)^{-1} \,. \tag{2.6}$$

To find the dissipated power loss $\mathcal{P}_{\text{dis}}$, the time derivative of $|E_N|^2$ can be calculated

$$\frac{\mathrm{d}|E_N|^2}{\mathrm{d}t} = \frac{\mathrm{d}|E_N|^2}{\mathrm{d}N}\frac{\mathrm{d}N}{\mathrm{d}t} = -\alpha_{\text{att}}L\,|E_N|^2\frac{1}{T_{\text{rt}}} \,, \tag{2.7}$$

where T_{rt} is the roundtrip time, and the derivative $\mathrm{d}\,|E_N|^2/\mathrm{d}N$ is calculated from Eq. (2.5) considering N to be a continuous variable as it is expected to be large – an assumption valid for low-loss resonators. Then, following the definition of the lifetime Eq. (2.4) as the ratio of the of the energy after N roundtrips and the power dissipation at that time and plugging in the two above equations,

$$\tau = \frac{|E_N|^2}{-\mathrm{d}\,|E_N|^2/\mathrm{d}t} = \frac{T_{\text{rt}}}{\alpha_{\text{att}}L} = N_e\,T_{\text{rt}} \,, \tag{2.8}$$

showing that τ is the time after the number of roundtrips reducing the field energy by a factor of e.

The finite lifetime of the cavity light corresponds to a finite linewidth of the resonance in frequency space. The linewidth is often given as the 3-dB bandwidth of the resonance, i.e., the *full-width-at-half-maximum* (FWHM) linewidth, Δv. The FWHM linewidth is proportional to the inverse of the lifetime, $2\pi\Delta v = \tau^{-1}$.

FWHM *linewidth* Δv

The optical losses are often given as a decay rate, typically the *amplitude decay rate* κ (see Eq. (2.44) for why it is the *amplitude* decay rate), which is related to the linewidth and lifetime by

amplitude decay rate κ

$$2\kappa = 2\pi\Delta v = \tau^{-1} \,. \tag{2.9}$$

The decay rate κ is often split into two contributing factors, the intrinsic and extrinsic contributions: the intrinsic losses are related to damping mechanisms in the resonator, and the extrinsic losses comes from the deliberate coupling of the resonator to the environment to interact with the resonator. The two independent contributions can simply be added together:

$$\kappa = \kappa_0 + \kappa_{\text{ex}} \,. \tag{2.10}$$

Coupling methods and coupling operating regimes, given by the ratio between the intrinsic and extrinsic losses, are described in Section 2.3, whereas intrinsic loss mechanism are discussed in Section 2.4.

2.1.2 *The quality factor and finesse of a cavity*

Low optical losses are generally desired in resonator applications, and especially two ratios are often used to quantify the relative losses of an optical cavity: The quality factor and the finesse.

The *quality factor Q* is defined as the amount of energy in the cavity compared to the dissipated energy over one optical cycle [e.g. 10]. This is a useful quantity for instance *quality factor Q* when working with nonlinear effects as it effectively gives the number of cycles over which the cavity interaction takes place before the field is depleted. For many applications of microresonators, the performance scales linearly or even quadratically with the Q factor, see e.g., examples in Gao *et al.* [86].

For a cavity resonance frequency v_{cav}, the quality factor is defined as

$$Q \;\equiv\; 2\pi \frac{\mathcal{E}_{\mathrm{cav}}}{\mathcal{P}_{\mathrm{dis}}/v_{\mathrm{cav}}} \;=\; 2\pi v_{\mathrm{cav}} \tau \;=\; \omega_{\mathrm{cav}} \tau \,, \tag{2.11}$$

where $\omega_{\mathrm{cav}} = 2\pi v_{\mathrm{cav}}$ is the angular frequency of the cavity, showing that Q factor is proportional to the product of the cavity lifetime and the field's oscillation frequency, i.e., giving the number of cycles over which it propagates in the resonator.

The Q factor can also be defined as the sharpness of the resonance relative to its central frequency,

$$Q = \frac{v_{\mathrm{cav}}}{\Delta v} = \frac{\omega_{\mathrm{cav}}}{2\kappa} \,. \tag{2.12}$$

Plugging in the lifetime–decay-rate-relation, Eq. (2.9), this quality factor definition is consistent with Eq. (2.11).

The other important figure of merit for a resonator is the cavity *finesse*. It describes the number of cavity roundtrips before the field is depleted, in contrast to the Q factor, which *finesse F* is proportional to the number of optical cycles before the field is depleted. The finesse is typically defined as the ratio of the free spectral range to the spectral linewidth of the cavity [e.g. 10],

$$F \equiv \frac{v_{\mathrm{FSR}}}{\Delta v} = \frac{\omega_{\mathrm{FSR}}}{2\kappa} \,, \tag{2.13}$$

which, by inserting Eqs. (2.3) and (2.8), can be written

$$F = 2\pi \frac{c}{nL} N_{\mathrm{e}} T_{\mathrm{rt}} = 2\pi N_{\mathrm{e}} \,, \tag{2.14}$$

showing that the finesse is the number of roundtrips before the field is reduced by a factor of e. Comparing Eqs. (2.12) and (2.13), the Q factor and finesse can shown to be related by the mode number,

$$Q = \frac{nLF}{\lambda} = mF \,. \tag{2.15}$$

Both the Q factor and finesse can be separated into their intrinsic and extrinsic parts, which add reciprocally:

$$Q^{-1} = Q_0^{-1} + Q_{\mathrm{ex}}^{-1} = \frac{2\kappa_0}{\omega_{\mathrm{cav}}} + \frac{2\kappa_{\mathrm{ex}}}{\omega_{\mathrm{cav}}} \,, \tag{2.16}$$
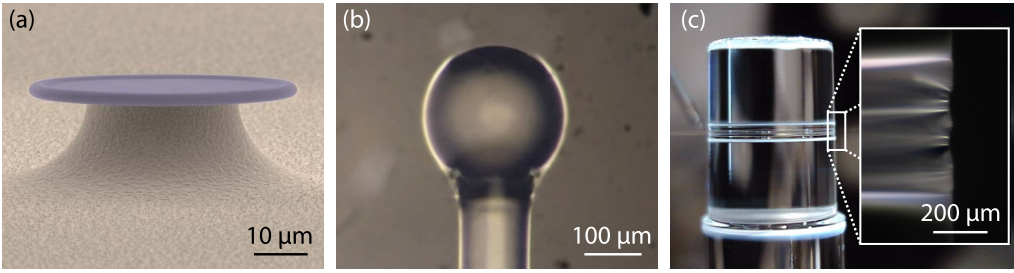
Figure 2.2. Examples of whispering-gallery-mode optical resonators. (a) Silica on silicon microtoroid by Del'Haye *et al.* [44]. Copyright Nature Publishing Group, reprinted with permission from Springer Nature. The light field propagates in the toroidal structure. (b) Silica sphere at the end of an optical fibre. The light field is confined in a band along the equator. (c) Silica rod resonator with inset showing the 'bulge' confining the field.

as is consistent with Eq. (2.10). The total Q factor is sometimes referred to as the *loaded* Q factor, whereas Q_0 is referred to as the *unloaded* Q factor.

The achievable finesse and quality factors vary for different microresonator platforms, with whispering-gallery-mode resonators showing quality factors of up to several billion, see e.g. Refs. 58, 87–89.

2.2   OPTICAL WHISPERING-GALLERY MODES

A range of different types and sizes of optical microresonators made from different dielectric materials exist. A few examples of geometries used are disks [53], spheres [1, 90], toroids [52], rods [54, 55], Bragg grated micropillars [91], and rings [92] – some of which are shown in Fig. 2.2. For disk, toroid, ring, and pillar resonators, fabrication techniques often involve lithography and cleanroom processes. For rod resonators either mechanical lathe machining and polishing [21, 54] or laser lathes are used [55]. Fabrication of spheres can be easily done using an electric arc to melt a fibre tip. The fabrication processes for the resonators used in this work are presented in Chapter 3.

With the exception of micropillars[iii] and ring resonators, the resonator types listed above are *whispering-gallery-mode* (WGM) resonators. In WGM resonators, the electromagnetic field propagates close to the surface of a circular structure due to total internal reflection at the interface between the resonator material and the surrounding medium [1]. The guiding mechanism is similar to other waveguides where the difference between the refractive indices of the waveguide n and surroundings n_s causes total internal reflection: In the optical ray picture, if the angle of incidence of a ray to the boundary between the waveguide and the surrounding medium is at the critical angle or greater, $\vartheta \geq \vartheta_{crit}$, the ray will be fully reflected inside the waveguide surface. The critical angle is given by

$$\vartheta_{crit} = \arcsin \frac{n_s}{n} , \qquad (2.17)$$

which gives $\vartheta_{crit} = 43.8°$ for silica in air at a wavelength of 1550 nm ($n_{SiO_2} = 1.4440$ [94], $n_s \simeq 1$). If a ray is tangential to the media interface in a circular geometry the reflection process is close to continuous, trapping the light close to the surface inside the structure.

[iii] Micropillars have also been used as WGM resonators along the curved surface [93].

Shifting back to the wave description of the optical field, if the light making a roundtrip interferes constructively with itself, the WGM is resonant. For a resonator of radius r, the cavity roundtrip length is $L = 2\pi r$, resulting in the resonance criterium

$$\omega_m = m\, \frac{c}{nr} \tag{2.18}$$

for the mode with m number of maxima in the field along the resonance path [cf. Eq. (2.2)]. Resonators typically have a wide spectral range of resonance frequencies, and can be made to cover the full transparency window of the dielectric chosen as the resonator material [45]. The free spectral range of a resonator can be engineered by choosing its radius:

$$\omega_{\text{FSR}} = \frac{c}{nr}\ . \tag{2.19}$$

For example, for a silica resonator with $r = 1000\,\mu$m, $\nu_{\text{FSR}} \simeq 33\,$GHz when the vacuum wavelength $\lambda = 1.55\,\mu$m.

However, the expressions for the resonance frequency and other derived parameters assume a dispersion-less medium and knowledge of the radius of the whispering-gallery *mode* itself. The next two sections briefly explains how the material and waveguide dispersion affects the WGMs, imposing a frequency dependence to the refractive index and to the WGM radius.

2.2.1 *Material and waveguide dispersion*

In general, the refractive index of a dielectric medium is frequency dependent, a phenomenon called *chromatic* or *material dispersion*. The effect comes from the structure of the dielectric medium interacting at different strengths with the electromagnetic field depending on the frequency of the field. The function $n(\omega)$ can be well approximated by the Sellmeier equation, a function built from the dielectric's resonance frequencies and their strengths, see Agrawal [95, Ch. 1].

chromatic/material dispersion

The dispersion is often expressed as the lower-order coefficients in a series expansion of the propagation constant in terms of angular optical frequency in a medium. The *propagation constant β* is the *wavenumber $k = 2\pi/\lambda$* (sometimes referred to as the free-space propagation constant) multiplied by the frequency dependent refractive index $n(\omega)$, giving the Taylor expansion

propagation constant β

wavenumber k

$$\beta(\omega) = k\, n(\omega) = \frac{\omega}{c}\, n(\omega) \tag{2.20}$$

$$= \beta_0 + \beta_1(\omega - \omega_0) + \frac{\beta_2}{2}(\omega - \omega_0)^2 + \dots \tag{2.21}$$

for a central frequency ω_0 [95, Ch. 1], where the expansion coefficients are

$$\beta_0 = \frac{\omega_0}{c}\, n(\omega_0)\ ; \qquad\qquad \beta_{j>0} = \frac{d^j\beta}{d\omega^j}\bigg|_{\omega=\omega_0}\ . \tag{2.22}$$

The first-order dispersion β_1 is the inverse of the group velocity $v_g = d\omega/d\beta$. When working with pulsed experiments, the first-order dispersion results in group delay, whereas the second-order dispersion β_2 causes spatial pulse broadening. The accumulated phase of the field after propagating a length L is

$$\phi(L; \omega) = \beta(\omega)L = 2\pi \, \frac{n(\omega)L}{\lambda} \; . \tag{2.23}$$

For WGM resonators, the frequency-dependent refractive index causes different effective resonator lengths for different frequencies, resulting in a non-uniform free-spectral range over the transparency of the dielectric. Furthermore, the chromatic dispersion can be a limitation for nonlinear interactions in the resonator, as all the involved frequencies need to be phase matched for the contributions from the different parts of the resonator to add coherently – Section 5.3.3 discusses a similar phase matching challenge for Brillouin scattering in a resonator with mechanical anisotropy.

In addition to the material dispersion for a plane wave due to the response of the medium to different wavelengths, waveguiding gives rise to other forms of dispersion: *geometric dispersion* and *modal dispersion*.[iv] In an optical ray picture, these can be understood as different frequencies or spatial mode structures might take different spatial paths in the resonator, and thus affecting the effective radius of the WGM. For example, shorter wavelengths are reflected closer to the surface than longer wavelengths, resulting in different optical path lengths [96]. The next section covers the modal degeneracies resulting from the waveguide dispersion.

geometric dispersion

modal dispersion

[iv] See for instance Del'Haye [96, Ch. 4] for a comprehensive review on dispersion in WGM resonators.

2.2.2   *WGM field distribution and modal degeneracies*

Even before Richtmyer [63] introduced the idea of high-Q optical WGM resonators, analytical expressions for the field distribution of WGMs in dielectric spheres were known from solving the vector Helmholtz equation with a spatial dependence of the refractive index, as first done by Mie [97] and Debye [98] (see e.g. the review by Oraevsky [6]). Numerical finite-element-method approaches have been widely used since Oxborrow [99] introduced a method for using commercially available finite-element-method solvers to find eigenmodes of arbitrary axisymmetrical resonator shapes.

For each azimuthal mode number m, there is a number of degenerate modes with different spatial profiles. In addition to the fundamental mode with one maximum in the polar and radial directions, there is a set of higher-order modes with multiple maxima in the polar and/or radial directions. A finite-element-method simulation result showing one fundamental and higher-order mode for a silica rod resonator is shown in Fig. 2.3. Furthermore, applying Maxwell's equations for appropriate boundary conditions reveal two possible polarisations for each of the degenerate WGMs: Either the electric or the magnetic field is parallel to the surface, called transversal electric (TE) and transversal magnetic (TM) modes, respectively [100, 101].

Analytical approximations for the eigenfrequencies of the modes have been found [100, 102], and also analytical approximations for more generalised axisymmetric geometries [103–
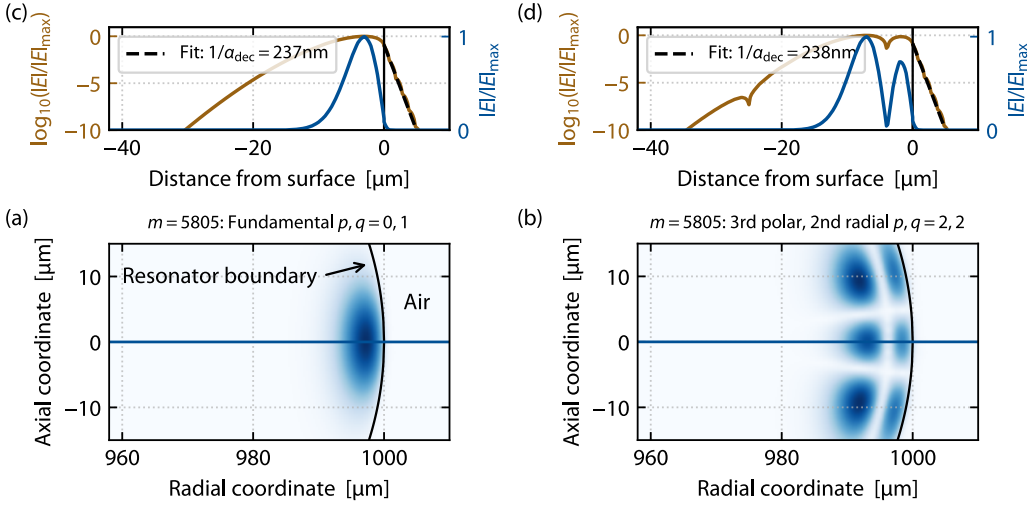
Figure 2.3. Example WGM profiles and their evanescent fields for a silica rod resonator. (a–b) Radial cross sections of the electric field norm of the fundamental and a higher-order optical mode of a silica rod resonator calculated using the finite-element-method solver COMSOL. The resonator has a (major) radius of 1000 μm and a confinement (minor) radius of 50 μm. Both modes are of the TE type have azimuthal mode number m = 5805, with the eigenfrequency of the fundamental mode $[(p, q) = (0, 1)]$ being v = 192.94 THz, and the higher-order mode $[(p, q) = (2, 2)]$ has v = 194.10 THz. The blue lines indicate the position of the cross sections in the top panels. (c–d) The normalised field magnitude ($|E|$ normalised by the maximum magnitude $|E|_{\mathrm{max}}$) along the resonator plane, plotted both linearly (blue) and logarithmically (golden) to better show the exponential decay of the evanescent field outside the resonator surface. The evanescent field is fitted with dashed black lines, giving penetration depths [Eq. (2.27)] for the field of 237 nm and 238 nm, respectively.

105]. The mode-number-degenerate modes typically have different resonance frequencies as their effective path-lengths in the resonator are different. For a disk structure in air with major radius r and minor radius ϱ, combining the approximation from Breunig *et al.* [104] and a polarisation correction term from Righini *et al.* [2], the resonance frequencies for mode with azimuthal mode number m, polar mode number p, and radial mode number q, and polarisation $\mathfrak{p}$, can be approximated by

$$\omega_{m,p,q,\mathfrak{p}} = \frac{mc}{n(\omega)r}\left[1 + \left(p + \frac{1}{2}\right)\frac{1}{m}\frac{\sqrt{r}}{\sqrt{\varrho}} + \frac{|\zeta_q|}{2^{1/3}m^{2/3}} - \frac{\xi(\mathfrak{p}, \omega)}{m\sqrt{n(\omega)^2 - 1}}\right] \equiv \frac{mc}{nr^{\mathrm{eff}}_{m,p,q,\mathfrak{p}}} \quad (2.24)$$

when $r/\varrho \ll m^{2/3}$. The symbol ζ_q is the argument of the q-th zero of the Airy function,[v] and the polarisation-dependent factor is

$$\xi(\mathfrak{p}, \omega) = \begin{cases} n(\omega) & \text{for } \mathfrak{p} = \text{TE} \\ n(\omega)^{-1} & \text{for } \mathfrak{p} = \text{TM} \end{cases}. \quad (2.25)$$

In the right-most part of Eq. (2.24), the corrections are absorbed into an effective radius, $r^{\mathrm{eff}}_{m,p,q,\mathfrak{p}}$ for the particular mode. The above equation reduces to the simpler Eq. (2.18) when the material dispersion is not taken into account [$n(\omega) \rightarrow n$], polarisation effects not

[v] The arguments for the first four zeros of the Airy function (to four digits): –2.338, –4.088, –5.520, –6.788 [106, Tab. 10.13].

taken into account ($\xi \to 0$), the geometric dispersion neglected [the radial structure is not accounted for ($\zeta_q \to 0$), and the resonator is a large sphere $r = \varrho$ with $m \gg p$].

Comparing the analytical expression Eq. (2.24) to the simulation result displayed in Fig. 2.3, the simulation gives a resonance frequency for mode $(m, p, q, \mathfrak{p}) = (5805, 0, 1, \text{TE})$ of 192.948 THz compared to 192.966 THz from the formula, which is a typical 10^{-4} relative error of the analytical expression compared to the simulation result [104]. The frequency shift from one polar mode order to the next is 154 GHz from the simulation versus 148 GHz from the analytic expression, and from one radial order to the next the shift is 831 GHz and 825 GHz from the simulation and the formula, respectively. The shift between the TE and TM polarisation modes for a particular mode (m, p, q) is typically much smaller: in the simulation the shift between them is 21 GHz, whereas from the analytical expression 24 GHz.

2.2.3   *Propagation-direction degeneracy and backscattering*

Light can propagate in either direction around the cavity, clockwise (CW) or counter-clockwise (CCW). Thus, for each mode (m, p, q) of a certain polarisation there is a pair of counterpropagating modes. Under time-reversal symmetry, these counterpropagating modes are normally frequency degenerate, exhibiting the same resonance frequency for both directions, but the degeneracy can be lifted through coupling of the counterpropagating modes. Coupling can occur as a result of nonlinearities such as the Kerr-effect [Section 2.6.3], optomechanical coupling [Section 4.1.1], or if the azimuthal symmetry is broken by a perturbation in polarisability such as surface roughness, material inhomogeneities or a scatterer introduced within the mode volume [107–109].

Coupling by scatterers can be understood by considering the scattered optical power: some of the scattered power is lost to the environment, and the remaining power is coupled back into the cavity. The back-coupled power can enter non-propagating modes, or scatter quasi-elastically into the counterpropagating mode, called *backscattering*. The coupling of the CW and CCW modes can be strong enough to cause appreciable build-up of power in both directions even when the resonator is pumped only in one direction, and can result in mode-splitting. Mode-splitting was first observed in WGMs by Weiss *et al.* [56] in silica sphere resonators (and the phenomenon was already well-known at the time in the context of ring resonators [e.g. 110, 111]).

backscattering

Since the first experimental discovery in WGM resonators, the literature has explored and exploited backscattering, with examples such as control over the mode-splitting [112, 113], using the mode-splitting for sensing [40, 114, 115], controlling the modal coupling through backscattering to manipulate light propagation [116, 117], sensing using the backscattered power [118], estimation of refractive index variation [119], and suppression of backscattering [57]. Chapter 4 of this thesis concerns backscattering control and demonstrates a near-field-scatterer technique for this purpose.

2.2.4   *The evanescent field and its penetration depth*

For any waveguide, a portion of the guided electromagnetic field extends outside the waveguide material. As the top panels of Fig. 2.3 show, WGMs are no exception, with an exponentially decaying field outside the resonator surface.

For a general waveguide, the *evanescent field*'s strength decreases in an exponential manner with the distance x from a waveguide's surface,

evanescent field

$$E(x) = E_{\text{surf}} \, e^{-\alpha_{\text{dec}} x} \,, \tag{2.26}$$

where E_{surf} is the field strength at the surface. For a waveguide in air, the decay constant α_{dec} is

$$\alpha_{\text{dec}} = k \sqrt{n^2 \sin^2 \vartheta - 1} \;\overset{\vartheta \to \pi/2}{=}\; \frac{2\pi}{\lambda} \sqrt{n^2 - 1} \,, \tag{2.27}$$

where k is the free-space wavenumber, n is the refractive index of the waveguide material, and $\vartheta \in (\vartheta_{\text{crit}}, \pi/2]$ the angle of incidence [120, Ch. 1]. For a WGM resonator, the angle is close to $\pi/2$, and the rightmost expression can be used with good approximation [121]. For high-order modes, the decay constant is typically smaller than what this approximation gives, which can be understood in a ray picture as the mode being deeper in the resonator requires a smaller angle ϑ, reducing the decay constant.

The inverse of the decay constant is called the *field penetration depth*, describing how deep into the surroundings the evanescent field extends before it is reduced by a factor of Euler's number. The penetration depth is smaller than one wavelength; for instance, for $\lambda = 1550\,\text{nm}$ and the approximation of Eq. (2.27), the penetration depth is $\alpha_{\text{dec}}^{-1} = 237\,\text{nm}$ for silica or $\alpha_{\text{dec}}^{-1} = 230\,\text{nm}$ for barium fluoride ($n_{\text{BaF}_2} = 1.4661$ [122]). The value for silica agrees with the finite-element-method simulation for a silica resonator shown in Fig. 2.3(c-d), where the the fitted penetration depths are 237 nm and 238 nm for a fundamental and first radial mode, respectively. The larger penetration depth for the higher-order mode is as expected due to its slightly lower decay constant.

field penetration depth

As the next section will show, the evanescent field provides coupling of the intra-cavity optical modes to the resonator's surroundings, allowing light to be transmitted into the cavity, and the cavity response to be studied. Furthermore, later chapters will show how external perturbations in the evanescent field, such as introducing a scatterer within the evanescent field, affects the intra-cavity field. If the intra-cavity field response to a perturbation is accurately monitored, the resonator can be used for sensing applications, often called near-field sensing [e.g. 8].

Coupling light efficiently and reliably to a resonator is critical for experiments. Because the total internal reflection generally reflects nearly all the light with no net energy flow across the boundary of the waveguide material, coupling fields efficiently in and out of the resonator was the most significant challenge Braginsky *et al.* [1] solved in their seminal paper from 1989. The coupling mechanism they used, which this work also uses, is based on *frustrated total internal reflection*, an effect seen when a medium with an evanescent field is sufficiently close to another dielectric material of high refractive index, for instance a WGM resonator. Normally, the evanescent field does not constitute a net flow of energy across the waveguide material boundary; however, with a dielectric material within the evanescent field of the waveguide, the evanescent field can be strong enough to drive electrons in the other dielectric, allowing energy to flow across the gap between the media [123, Ch. 4].

frustrated total internal reflection

Evanescent coupling for transmission of light from one waveguide to another is widely used, and there are multiple geometries that can be used for generating an evanescent field close enough to a WGM for coupling purposes, such as prisms [1], angle-cleaved fibres [124], or adiabatically tapered fibres [125, 126]. For chip based resonators integrated waveguides are often used for coupling [127, 128].

Little *et al.* [101] give a detailed description and analytical treatment of evanescent coupling into microresonators. For a tapered fibre, the three most important parameters for the achieved coupling are (a) the distance between the taper and the resonator, (b) the polarisation of the coupler matching the resonator mode, and (c) the phase matching of the coupling, i.e., the difference between the propagation constants of the desired WGM and the evanescent coupler. For tapered optical fibres, the evanescent field strength increases as the fibre diameter decreases, giving a stronger interaction with the WGM; however, as the propagation constant of the fibre decreases with a decreasing fibre radius, there is an optimum fibre radius for achieving maximum coupling to a resonator mode.

For a tapered fibre with radius $r_\text{f} < 3\,\mu\text{m}$, the propagation constant in the fibre for optical wavelengths can be approximated by

$$\beta_\text{f}^2 \approx \left[kn(\omega)\right]^2 - \left(\frac{2.405}{r_\text{f}}\right)^2 \tag{2.28}$$

(for SI units) [129], where the numerical factor represents the correction to the refractive index as a result of the reduced effective refractive index experienced by the mode as it increasingly extends into the near field with a smaller taper radius. The propagation constant of the resonator can be expressed as

$$\beta_{m,p,q,\mathfrak{p}} = \frac{m}{r_{m,p,q,\mathfrak{p}}^\text{eff}} \tag{2.29}$$

by inserting Eq. (2.24) into Eq. (2.20). The coupling-rate depends on the mismatch $\Delta\beta = \beta_\text{f} - \beta_{m,p,q,\mathfrak{p}}$ in an exponential fashion $\exp[-(\Delta\beta)^2/\alpha_\text{f}']$, where α_f' is the ratio of the fibre's evanescent field decay constant to the WGM radius, reducing the maximum possible coup-

ling rapidly with a propagation constant mismatch [101]. There are techniques for improving the propagation-constant/phase matching by for instance coating the tapered fibre with a liquid polymer to adjust its propagation constant [130].

As discussed in Section 2.2.2, for each mode given by (m, p, q), there is a pair of modes of orthogonal polarisations in the resonator. The coupling efficiency to a certain WGM is highly dependent on whether the polarisation of the light in the coupling region of the waveguide matches that of the WGM.

The coupling rate is usually controlled by tuning the gap between the coupling waveguide and the resonator [131]. Three different coupling regimes can be observed depending on the balance of the losses in the resonator to the coupling to the waveguide:

(i) *undercoupling*, where the internal losses per round trip are higher than the losses due to coupling out to the fibre;

(ii) *critical coupling* where the out-coupled field and internal losses per round trip are equal, leading to the highest intra-cavity power; and

(iii) *overcoupling*, where the field leaks out into the fibre at a faster rate than it dissipates in the resonator.

Well phase-matched tapers with diameters close to the wavelength are found to be able to provide overcoupling to a mode if the taper position is adjusted appropriately. The next section will give a quantitative treatment of the coupling and coupling regimes.

2.3.1 *The coupling equation and coupling regimes*

To describe the coupling quantitatively, consider a tapered fibre waveguide coupling to one resonator mode with an intrinsic roundtrip loss parameter α_{rt} ($\alpha_{\mathrm{rt}} = 1$ corresponds to zero losses[vi]) and electric fields as shown in Fig. 2.4. Following the description of Yariv [132], let the electric field amplitudes be complex and normalised so that $|\widetilde{E}|^2 = \mathcal{P}$, the optical power; the amplitudes are then described by

[vi] Cf. the description earlier, $\alpha_{\mathrm{rt}} = \exp(-\alpha_{\mathrm{att}}L)$.

$$\begin{pmatrix} \widetilde{E}_{\mathrm{t1}} \\ \widetilde{E}_{\mathrm{t2}} \end{pmatrix} = \begin{pmatrix} \mathrm{t} & \varkappa \\ -\varkappa^* & \mathrm{t}^* \end{pmatrix} \begin{pmatrix} \widetilde{E}_{\mathrm{i1}} \\ \widetilde{E}_{\mathrm{i2}} \end{pmatrix} , \qquad (2.30)$$

where z^* denotes the complex conjugate of z, given a coupling parameter $\varkappa$ and a transmission parameter t. The model assumes a lossless coupling mechanism,

$$|\varkappa|^2 + |\mathrm{t}|^2 = 1 , \qquad (2.31)$$

and no frequency dependence in the two parameters.

During one roundtrip in the cavity, the field acquires a phase $\phi = \beta L$ and it is attenuated according to the intrinsic losses of the resonator,

$$\widetilde{E}_{\mathrm{i2}} = \alpha_{\mathrm{rt}} \mathrm{e}^{\mathrm{i}\phi} \widetilde{E}_{\mathrm{t2}} . \qquad (2.32)$$

Figure 2.4. Model of evanescent coupling from a tapered fibre to a WGM resonator. The transmission parameters t, $\varkappa$ with subscripts i and t for incoming and transmitted field amplitudes to the coupling region in the taper and resonator. The fractional intrinsic roundtrip losses are given by α_{rt}.

Inserting this relation into Eq. (2.30) yields

$$\widetilde{E}_{t1} = \frac{-\alpha_{rt} + te^{-i\phi}}{-\alpha_{rt}t^* + e^{-i\phi}} \widetilde{E}_{i1} .\tag{2.33}$$

The transmission parameter can be expressed $t = |t| \exp(i\theta_t)$, where $|t|$ represents the amplitude of transmittance (i.e., $|t| = 1$ would correspond to the field being fully transmitted, and thus no coupling from the resonator to the waveguide and vice versa) and θ_t the coupling phase shift. Then, the following expression for the power transmitted in the fibre is obtained by squaring $\widetilde{E}_{t1}$:

$$\mathcal{P}_{t1} = \frac{\alpha_{rt}^2 - 2\alpha_{rt}|t|\cos(\phi + \theta_t) + |t|^2}{1 - 2\alpha_{rt}|t|\cos(\phi + \theta_t) + \alpha_{rt}^2|t|^2} \mathcal{P}_{i1} .\tag{2.34}$$

On resonance, the total phase acquired over the roundtrip and transmission inside the resonator must be an integer number of 2π, making $\cos(\phi + \theta_t) = 1$, and thus

$$\mathcal{P}_{t1}^{res} = \left(\frac{\alpha_{rt} - |t|}{1 - \alpha_{rt}|t|} \right)^2 \mathcal{P}_{i1} .\tag{2.35}$$

From this equation it is evident that when $\alpha_{rt} = |t|$, the transmitted power in the fibre at resonance is zero, which is the definition of *critical coupling*. It can be understood as a balance of the losses and coupling; the relation $\alpha_{rt} = |t|$ is equivalent to the coupling $|\varkappa|^2 = 1 - |t|^2$ (in power, thus squared) being equal to the power losses over one roundtrip, $1 - \alpha_{rt}^2$.   *critical coupling*

The per-roundtrip parameters $\alpha_{rt}, |t|$ are related to their rate counterparts κ_0, κ_{ex}, respectively. To find their relationship, consider the amplitude losses over a roundtrip, $1 - \alpha_{rt}$. As the roundtrip time of the cavity is v_{FSR}^{-1}, the angular amplitude rate of intrinsic losses is $(1 - \alpha_{rt})\omega_{FSR} = \kappa_0$. Similarly, the angular coupling amplitude rate is $|\varkappa|\omega_{FSR} = \kappa_{ex}$. Rearranging these gives

$$\alpha_{rt} = 1 - \frac{\kappa_0}{\omega_{FSR}} ; \qquad\qquad |t| = 1 - \frac{\kappa_{ex}}{\omega_{FSR}} ,\tag{2.36}$$

where $\kappa = \kappa_0 + \kappa_{\mathrm{ex}}$. Inserting these expressions into Eq. (2.35), the transmitted power can be expressed

$$\mathcal{P}_{\mathrm{tl}}^{\mathrm{res}} = \left(\frac{\kappa_{\mathrm{ex}} - \kappa_0}{\kappa_{\mathrm{ex}} + \kappa_0 - 2\kappa_0 \kappa_{\mathrm{ex}} / \omega_{\mathrm{FSR}}} \right)^2 \mathcal{P}_{\mathrm{il}} \, , \tag{2.37}$$

and assuming a resonator with a large mode-spacing and low loss, $\kappa_0 \kappa_{\mathrm{ex}} \ll \omega_{\mathrm{FSR}}$, the third term in the denominator can be discarded:

$$\mathcal{P}_{\mathrm{tl}}^{\mathrm{res}} \approx \left(\frac{\kappa_{\mathrm{ex}} - \kappa_0}{\kappa} \right)^2 \mathcal{P}_{\mathrm{il}} \, . \tag{2.38}$$

Figure 2.5(a) shows the relative power at the output of the tapered fibre as a function of the ratio of the coupling losses to the intrinsic losses, showing how the field in the taper vanishes when the ratio is one. The three coupling regimes can now be rephrased as

   (i) $\kappa_0 > \kappa_{\mathrm{ex}}$ undercoupling,
  (ii) $\kappa_0 = \kappa_{\mathrm{ex}}$ critical coupling, and
 (iii) $\kappa_0 < \kappa_{\mathrm{ex}}$ overcoupling.

The on-resonance transmission, i.e., the transmitted power in the fibre at resonance relative to the input power, can be expressed

$$\mathcal{T}^{\mathrm{res}} = \frac{\mathcal{P}_{\mathrm{tl}}^{\mathrm{res}}}{\mathcal{P}_{\mathrm{il}}} = \left(1 - \frac{2\kappa_0}{\kappa} \right)^2 \, . \tag{2.39}$$

Using the binomial expansion to the second-order and noting that $\kappa_{\mathrm{ex}} - \kappa_0 = \kappa - 2\kappa_0$, the transmission can be approximated to

$$\mathcal{T}^{\mathrm{res}} \approx 1 - \frac{4\kappa_0}{\kappa} + \frac{4\kappa_0^2}{\kappa^2} = 1 - \frac{4\kappa_0}{\kappa} \frac{\kappa - \kappa_0}{\kappa} = 1 - \frac{4\kappa_0 \kappa_{\mathrm{ex}}}{\kappa^2} \, , \tag{2.40}$$

which is unity if the taper is not coupled to the resonator, $\kappa_{\mathrm{ex}} = 0$, and is zero when critically coupled, $\kappa_{\mathrm{ex}} = \kappa_0 = \kappa/2$, as all the power is coupled into the resonator. Alternatively, the coupling contrast at resonance can be expressed

$$\mathcal{K}^{\mathrm{res}} = 1 - \mathcal{T}^{\mathrm{res}} = \frac{\mathcal{P}_{\mathrm{tl}}^{\mathrm{res}}}{\mathcal{P}_{\mathrm{il}}} \approx \frac{4\kappa_0 \kappa_{\mathrm{ex}}}{\kappa^2} \, , \tag{2.41}$$

which is unity when critically coupled and zero when there is no coupling.

   In terms of experimental parameters, the transmission and total linewidth are easy to measure from monitoring the transmitted light on a photodiode as a laser is swept across the resonance at low optical power. To calculate the extrinsic coupling rate from these two parameters, Eq. (2.39) can be rearranged to give

$$\kappa_{\mathrm{ex}} = \frac{\kappa}{2} \left(1 \pm \sqrt{\mathcal{T}^{\mathrm{res}}} \right) \, , \tag{2.42}$$

where the sign is chosen according to the coupling regime: plus for over-coupling and minus for under-coupling.
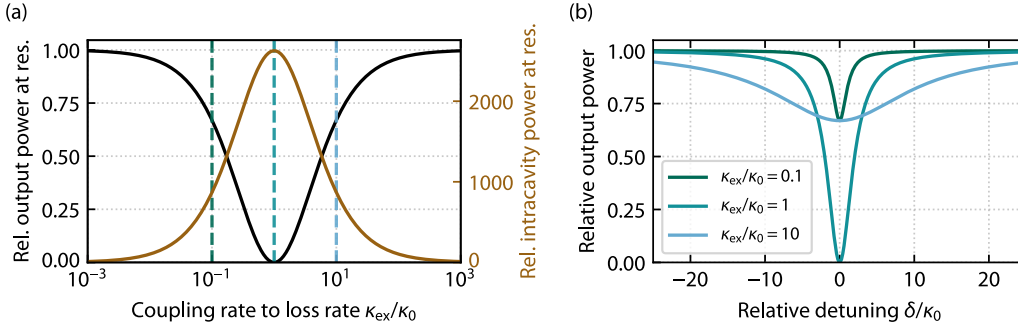
Figure 2.5. Coupling regimes, resonator buildup, and transmission profiles. (a) Left axis: The power in the tapered fibre output at resonance relative to the input power, $\mathcal{P}_{\mathrm{t1}}^{\mathrm{res}}/\mathcal{P}_{\mathrm{i1}}$, for varying coupling strength relative to intrinsic losses, as in Eq. (2.38). The transmitted power in the tapered fibre vanishes for critical coupling $\kappa_0 = \kappa_{\mathrm{ex}}$. The loss ratios for the resonances in panel (b) are indicated with dashed lines. Right axis: The intracavity buildup at resonance B^{res} [Eq. (2.47)] for a resonator with intrinsic Q factor $Q_0 = 1 \cdot 10^8$ [$\kappa_0/(2\pi) \simeq 1\,\mathrm{MHz}$] and FSR corresponding to a 1-mm-radius resonator (33 GHz). (b) Transmission profiles [Eq. (2.53)] for three selected ratios of extrinsic to intrinsic losses in the resonator, showing a resonance being undercoupled, critically coupled, and overcoupled.

2.3.2   *The intra-cavity power*

The time-domain dynamics of the intra-cavity field is typically described using rate equations, treating the resonator as a damped harmonic oscillator with resonance frequency ω_{cav} driven by the input optical field coupled into the resonator and simultaneously leaking to the waveguide causing losses κ_{ex}.

First, consider the non-driven case. Let the intra-cavity energy $\mathcal{E}_{\mathrm{cav}}(t) = |e(t)|^2$. Due to the intrinsic damping and leakage to the waveguide $\kappa = \kappa_0 + \kappa_{\mathrm{ex}}$, the time derivative of the energy amplitude e is [133, 134]

$$\dot{e}(t) = (\mathrm{i}\omega_{\mathrm{cav}} - \kappa)\, e(t)\,. \tag{2.43}$$

Now, adding also the driving term consisting of a normalised input power $\mathcal{P}_{\mathrm{i1}} = |p_{\mathrm{i1}}|^2$ and a coupling parameter $\tilde{\varkappa}$ (in units of $\sqrt{1/\mathrm{s}}$), the rate of change in the energy amplitude is

$$\dot{e}(t) = (\mathrm{i}\omega_{\mathrm{cav}} - \kappa)\, e(t) + \tilde{\varkappa} p_{\mathrm{i1}}(t)\,. \tag{2.44}$$

For a drive with frequency ω, the power term can be written $p_{\mathrm{i1}}(t) = |p_{\mathrm{i1}}| \exp(\mathrm{i}\omega t)$, and the solution to the differential equation (2.44) is

$$e(t, \omega) = \frac{\tilde{\varkappa} p_{\mathrm{i1}}(t)}{\mathrm{i}(\omega - \omega_{\mathrm{cav}}) + \kappa}\,. \tag{2.45}$$

From time reversibility considerations at zero intrinsic losses [134, Ch. 7], or a similar power conservation argument [129], it can be shown that $|\tilde{\varkappa}| = \sqrt{2\kappa_{\mathrm{ex}}}$. Noting that the circulating power in the cavity $\mathcal{P}_{\mathrm{cav}}$ is given by the intra-cavity energy $|e|^2$ divided by the

roundtrip time $T_{rt} = v_{FSR}^{-1}$, the circulating power in the resonator can be expressed

$$\mathcal{P}_{cav}(\omega) = \frac{2\kappa_{ex}v_{FSR}}{(\omega - \omega_{cav})^2 + \kappa^2} \mathcal{P}_{il} \;. \tag{2.46}$$

The *detuning* of the input field relative to the cavity resonance, $\omega - \omega_{cav} \equiv \delta$, giving the maximum circulating power for zero detuning.

detuning δ

BUILD-UP FACTOR. At zero detuning, $\mathcal{P}_{cav}(\omega = \omega_{cav}) = \mathcal{P}_{cav}^{res}$, the power enhancement of the cavity is

$$B^{res} = \frac{\mathcal{P}_{cav}^{res}}{\mathcal{P}_{il}} = \frac{2\kappa_{ex}v_{FSR}}{\kappa^2} = \frac{2\kappa_{ex}}{\kappa}\frac{1}{\pi}\frac{\omega_{FSR}}{2\kappa} = \frac{2\kappa_{ex}}{\kappa}\frac{F}{\pi} \;. \tag{2.47}$$

This quantity is called the (power) *build-up factor B*, and is proportional to the cavity finesse. The proportionality constant between the build-up factor and finesse is the coupling efficiency of the taper to the cavity,

build-up factor B

$$\eta_c = \frac{2\kappa_{ex}}{\kappa} \;, \tag{2.48}$$

which is unity at critical coupling, $\kappa_{ex} = \kappa_0 = \kappa/2$. At critical coupling the build-up factor simplifies to

$$B_{crit}^{res} = \frac{F}{\pi} \stackrel{crit}{=} \frac{F_0}{2\pi} \;, \tag{2.49}$$

where $F_0 = \pi v_{FSR}/\kappa_0$ is the intrinsic finesse of the cavity. Figure 2.5(a) shows the build-up at resonance for varying coupling to a $Q_0 = 1 \cdot 10^8$, 1-mm-radius resonator ($v_{FSR} = 33\,\text{GHz}$).

INTRA-CAVITY PHOTON NUMBER. The number of intra-cavity photons at resonance can be estimated from the intra-cavity energy divided by the photon energy $\hbar\omega$. The intra-cavity energy is the circulating power integrated over the round-trip time, $\mathcal{E}_{cav} = \mathcal{P}_{cav}/v_{FSR}$, and thus

$$N_{cav}\,\hbar\omega = \mathcal{E}_{cav} = \frac{B^{res}\mathcal{P}_{il}}{v_{FSR}} = \frac{2\kappa_{ex}}{\kappa^2}\mathcal{P}_{il} = \frac{\eta_c}{\kappa}\mathcal{P}_{il} \;, \tag{2.50}$$

giving

$$N_{cav} = \frac{1}{\hbar\omega}\frac{\eta_c\mathcal{P}_{il}}{\kappa} \;. \tag{2.51}$$

2.3.3 *The Lorentzian spectral shape of the resonance*

Neglecting thermal and nonlinear optical effects and backscattering,[vii] the transmission spectrum of a resonance from WGM resonator is approximately a Lorentzian. Modelling a resonator mode as a damped harmonic oscillator yields a Lorentzian lineshape. To motivate[viii] the transmission profile shape at the output of the tapered fibre based on the derivations so far, the Lorentzian expression for the circulating power (2.46) is gives the frequency dependence of the power coupled into the resonator $\mathcal{P}_{coup}$:

$$\mathcal{P}_{coup}(\omega) \propto \frac{1}{\kappa^2 + (\omega - \omega_{cav})^2}\mathcal{P}_{il} \propto \frac{1}{1 + \delta^2/\kappa^2}\mathcal{P}_{il} \;. \tag{2.52}$$

[vii] Broadening effects are considered later in this chapter, and Zhu *et al.* [135] give an in-depth treatment.

[viii] For a derivation of the below result directly from the rate equations in the previous section, see Sedlmeir [121].

From steady-state power conservation, $\mathcal{P}_{tl} = \mathcal{P}_{il} - \mathcal{P}_{coup}$ when assuming a lossless coupling mechanism, and from the relative on-resonance coupling contrast, (2.41) the normalised transmission spectrum for the steady-state resonance can then be expressed

$$\mathcal{T}(\delta) = \frac{\mathcal{P}_{tl}}{\mathcal{P}_{il}} = 1 - \frac{\mathcal{P}_{coup}}{\mathcal{P}_{il}} = 1 - \frac{\mathcal{K}^{res}}{1 + \delta^2/\kappa^2} , \qquad (2.53)$$

i.e., a background of one with a Lorentzian dip at ω_{cav} of contrast $\mathcal{K}^{res}$ and half-linewidth κ. Transmission profiles for a resonance with different coupling efficiency due to different ratios of extrinsic to intrinsic losses are shown in Fig. 2.5(b).

2.4 INTRINSIC RESONATOR LOSSES

The previous section treats the coupling of the resonator to a tapered fibre or some other waveguide, which represents losses for the intra-cavity field, and how the balance between the intrinsic and coupling losses is important for resonance build-up of optical power. So far the intrinsic losses have been assumed to be low, but the motivation for this assumption or the mechanisms for intrinsic losses have not been discussed.

Typically, the intrinsic loss mechanisms for WGM resonators are grouped into three categories [87, 108, 136]:

(i)   radiative losses due to the curved surface guiding the light;

(ii)   bulk material absorption and scattering from defects; and

(iii)   surface scattering due to surface roughness, and inhomogeneities and contaminants, such as material deposited on the surface during or after fabrication.

Similarly to how the total losses can be separated into intrinsic and extrinsic contributions, the intrinsic Q factor can be split into the contributing terms

$$Q_0^{-1} = Q_{rad}^{-1} + Q_{mat}^{-1} + Q_{scatt}^{-1} , \qquad (2.54)$$

where, for most WGM resonators, one of the two last terms is the main limitation of Q_0.

The radiation losses, sometimes called bending losses, arise due to the curved surface of the resonator. For a flat interface between materials, light incident at the critical angle [Eq. (2.17)] or greater is totally internally reflected, but for a curved interface the reflection is only quasi-total, with some of the field being transmitted. As the transmittance vanishes when the interface is straight, the larger the resonator is compared to the wavelength, the smaller the losses. The azimuthal mode number is proportional to the size–wavelength ratio, $m \propto r/\lambda$, i.e., with a large m the curved surface is closer to being straight over a wavelength. For $m \gg 1$, the order-of-magnitude quality factor associated with the radiation losses is given by [85]

$$Q_{rad} \sim m e^{2m} , \qquad (2.55)$$

which is an exponential function that increases rapidly for large mode numbers as shown in Fig. 2.6. For small mode numbers, the radiation losses are much larger than Eq. (2.55) predicts. Nevertheless, numerical work for low for mode numbers [137] shows that for
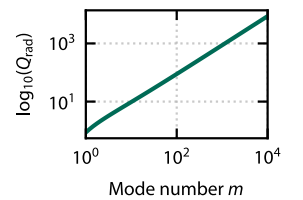
Figure 2.6. Approximate contribution to the Q factor from radiation losses as a function of the azimuthal mode number [Eq. (2.55)] valid for $m \gg 1$. Note that the y axis is $\log_{10}$ of the associated radiation Q, and then plotted on a logarithmic scale.

$m \geq 60$, the quality factor associated with the radiation losses is $\geq 10^8$, which corresponds to a WGM radius of roughly 12 µm for light of vacuum wavelength 1550 nm in silica. The resonators used in the work presented in this thesis have radiuses that are more than an order of magnitude larger than 12 µm and thus the radiative losses are very small compared to other loss mechanisms.

The material Q factor related to absorption and scattering off material defects can be estimated from the material's optical energy/power attenuation factor α_{mat} of relative losses per length at the resonance wavelength. When considering only material losses, the dissipated energy over a roundtrip $\Delta \mathcal{E}_{cav} \approx -\alpha_{mat} L \mathcal{E}_{cav}$, giving an approximate power dissipation of $\dot{\mathcal{E}}_{cav} \approx -\alpha_{mat} L \mathcal{E}_{cav}/T_{rt}$ over a round trip. Using the definition of the Q factor [Eq. (2.11)], the material contribution to the Q factor is then

$$Q_{mat} = \frac{\mathcal{E}_{cav}}{-\dot{\mathcal{E}}_{cav}} \, \omega \approx \frac{\mathcal{E}_{cav}}{\alpha_{mat} L \mathcal{E}_{cav}/T_{rt}} \, 2\pi v = \frac{1}{\alpha_{mat}} \frac{2\pi v T_{rt}}{L} = \frac{1}{\alpha_{mat}} \frac{2\pi n}{\lambda} \, , \qquad (2.56)$$

where it has been used that the resonator length over the round trip time is the phase velocity of the light field, $L/T_{rt} = v_{ph} = c/n$. At $\lambda = 1550$ nm the attenuation factor for fused silica is 0.2 dB km^{-1} = $1 \cdot 10^{-5}$ m^{-1} [2, 101], giving $Q_{mat}^{SiO_2} \sim 10^{11}$. For barium fluoride the attenuation factor $\sim 10^{-3}$ m^{-1} [89], giving $Q_{mat}^{BaF_2} \sim 10^9$.

Lastly, there are typically imperfections in the resonator surface or contamination that can limit the quality factor beyond the limit imposed by the material Q. Quality factors close to the material absorption limit have been reported for instance for silica microspheres ($Q = 3 \cdot 10^9$ [87]) and barium fluoride disk resonators ($Q = 1.3 \cdot 10^9$ [89]), noting that Gorodetsky *et al.* [87] found a 100-second timescale of adsorption of atmospheric water onto their silica spheres, reducing from the material limited Q to about 20 %. Keeping the resonators clean is critical to ensure that the Q is not reduced over time.

2.5   THE THERMO-OPTIC AND THERMOELASTIC EFFECTS

When the temperature of a WGM resonator changes, either through optical absorptive heating or external heat sources/cooling, the cavity modes are affected. There are two different temperature-related effects with different associated timescales: the fast thermo-optic effect that causes a local change in the refractive index as the temperature of the mode volume changes, and the slower thermoelastic effect that causes expansion or contraction of the bulk material, resulting in a geometrical path-length change [138, 139]. These effects will both contribute to a change in the resonance frequencies. As absorptive heating increases with optical power, these effects are thus nonlinear effects in field strength and often referred to as thermal nonlinearities.

The temperature dependence can be an issue for some applications for instance due to drifts in absolute frequency, but the temperature dependence is also a powerful tool; temperature control can be used for instance to tune resonance frequencies, and for materials with a positive thermo-optic coefficient it can provide a means for passive, thermal locking to a resonance, as covered in Section 3.6.1.

To first order, the frequency change of a mode due to a change in the refractive index or resonator radius can be expressed

$$\Delta\omega \simeq \frac{\partial\omega}{\partial n}\Delta n + \frac{\partial\omega}{\partial r}\Delta r \;. \tag{2.57}$$

Using the simplified resonance frequency expression (2.18), the relative shift is

$$\frac{\Delta\omega}{\omega_0} \simeq -\frac{\Delta n}{n} - \frac{\Delta r}{r} \;. \tag{2.58}$$

The change in refractive index due to the mode temperature change ΔT_m for a thermo-optic coefficient C_n of the resonator material is

$$\frac{\Delta n}{n} = \frac{1}{n}\frac{\mathrm{d}n}{\mathrm{d}T_\mathrm{m}}\Delta T_\mathrm{m} = \frac{C_n}{n}\Delta T_\mathrm{m} \;, \tag{2.59}$$

and the radius change as a function of bulk temperature change ΔT_b and the thermal expansion coefficient C_r is

$$\frac{\Delta r}{r} = \frac{1}{r}\frac{\mathrm{d}r}{\mathrm{d}T_\mathrm{b}}\Delta T_\mathrm{b} = C_r\Delta T_\mathrm{b} \;. \tag{2.60}$$

Together, this yields

$$\frac{\Delta\omega}{\omega_0} \simeq -\left(\frac{C_n}{n}\Delta T_\mathrm{m} + C_r\Delta T_\mathrm{b}\right) \;. \tag{2.61}$$

As the mode volume for a WGM is typically small compared to the resonator size, the thermo-optic effect is faster than the thermoelastic effect. The balance between the magnitudes and signs of C_r and C_n determines a resonator's frequency response to temperature changes. The response can be modified by coating the resonator surface with a polymer, see for instance He [140].

At room temperature, fused silica[ix] has a linear thermo-optic coefficient of $C_n = 1.05 \cdot 10^{-5}\,\mathrm{K}^{-1}$ at $\lambda = 1.55\,\mu\mathrm{m}$, and a particularly small thermal expansion coefficient $C_r = 5.4 \cdot 10^{-7}\,\mathrm{K}^{-1}$ [141]. In fact, the expansion coefficient is so small that fused silica is sometimes used as a reference material for thermal expansion. As n is of order unity, the thermo-optic effect is two orders of magnitude more pronounced than the thermal expansion, and the thermo-optic effect is typically also faster given the smaller relevant volume.

For barium fluoride, the coefficients are $C_n = -1.7 \cdot 10^{-5}\,\mathrm{K}^{-1}$ [142, 143] and $C_r = 2.0 \cdot 10^{-5}\,\mathrm{K}^{-1}$ [144] at room temperature and $\lambda = 1.55\,\mu\mathrm{m}$. Noting the negative sign of the thermo-optic coefficient, the two effects nearly cancel; however, the timescale difference can give rise to dynamic interplay effects [140].

The smaller the resonator, the smaller the heat capacity and thus the effect of heating is generally more pronounced. Note also that the thermo-optic and thermal expansion coefficients typically are temperature dependent. Figure 2.7 shows the temperature dependence for the coefficients from room temperature down to cryogenic temperatures for fused silica: C_n decreases by about an order of magnitude over the range 300 K to 30 K, whereas the thermal expansion coefficient decreases with a zero crossing at 175 K to $\simeq -8 \cdot 10^{-7}\,\mathrm{K}^{-1}$

[ix] The terms fused silica/quartz and vitreous silica are often used interchangeably to describe SiO_2 heated up to >1600 °C, causing a fused, amorphous structure.
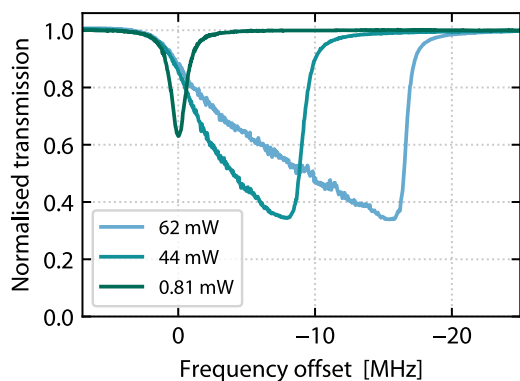
Figure 2.8. Spectral transmission profiles of a resonance ($\lambda_{cav} \simeq 1.55\,\mu m$) scanning downwards in frequency at a rate of $\simeq 90\,\mathrm{GHz\,s^{-1}}$. At low input power the resonance is close to a Lorentzian lineshape, whereas at higher powers thermal effects broaden the resonance. The coupling position is different for the low input power and the two higher power measurements.

at 40 K, and then approaches zero as the temperature approaches zero kelvin. In addition comes changes in the thermal conductivity, which can result in change of timescales and resonance shifts for the same input power at different temperatures.

2.5.1   *Thermal broadening of the resonance shape*

When coupling in an optical field to a resonator, the WGM volume heats up as the resonator material absorbs some of the light circulating in the resonator. As the heat diffuses into the resonator structure, the bulk temperature also changes. For resonators with high absorption, small heat capacity, or when using high input powers, the heating from absorption becomes significant enough to cause resonance frequency changes beyond the linewidth of the resonance, leading to the transmission spectrum changing from the normal Lorentzian profile when scanning the pump laser across the resonance.

Carmon *et al.* [138] derive a model for the dynamic response of the resonator, but the spectral response can be understood qualitatively from Eq. (2.61). If a silica WGM resonator is heated, the resonance shifts downwards in frequency (upwards in wavelength) because both the coefficients C_r and C_n are positive. If the heating increases with circulating power and the pump laser frequency is swept across the resonance, the resonance profile shows hysteresis with relation to the sweeping direction: as the frequency is approaching the resonance from above, the increased heating from a larger in-coupled optical power shifts the resonance frequency downwards along with the pump, whereas if the pump is sweeping upwards in frequency, the resonance frequency moves towards the pump laser.

The result is a broadened transmission shape when scanning downwards in frequency, or a compressed shape when scanning upwards. For the case of broadening: when the maximum in-coupled power is reached, the maximum heating is occurring and thus also maximum thermal shift, when the coupling then decreases this reduces the thermal shift of the resonance and causes a jump out of resonance. Transmission spectra for a resonance at different input powers for a silica rod resonator is shown in Fig. 2.8, showing a significant broadening at higher input powers.

Note that this form of thermal broadening, often called a thermal triangle, is not present in barium fluoride resonators as the thermo-optic coefficient is negative, thus shifting the resonance towards the pump as it is increasingly coupled in.
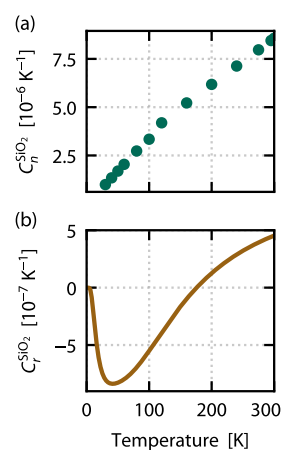
Figure 2.7. Temperature dependence for fused silica of (a) the thermo-optic coefficient at 1.5 µm wavelength (experimental values) [145], and (b) the thermal expansion coefficient (phenomenological model fit) [146].

When a sufficiently strong optical field is present in a dielectric material, the properties of the material might change as a consequence of the field's presence. When the material response depends on the optical field in a nonlinear manner, the material is said to have a nonlinear response. Many textbooks are devoted to this topic, see for instance Boyd [12] or others [13, 95, 147]. As WGM resonators have small optical mode volumes and the build-up of optical power is high, the input power needed to observe nonlinear effects is relatively small. Thus, WGM resonators have been a key platform of choice for many experiments in this domain for the last three decades, with examples given in the introduction chapter of this thesis.

This section explores the third-order optical nonlinearity resulting in an intensity-dependent refractive index and its consequences for WGM resonators. The third-order nonlinearity is often referred to as the Kerr nonlinearity, named after the Scottish physicist John Kerr who, in 1875, described the phenomenon now known as the DC Kerr effect [51] where the presence of a static electric field changes the optical properties of a dielectric. This section, however, will focus on the AC Kerr effect, where a time-varying optical field is changing the properties of the dielectric.

2.6.1   *The intensity-dependent refractive index*

In a semi-classical description, a time-varying, monochromatic electromagnetic field $\mathbf{E}$ induces an electric polarisation $\mathbf{P}$ (dipole moment per unit volume) in a dielectric. Normally, the induced polarisation is proportional to the field strength, $\mathbf{P} = \varepsilon_0 \chi \mathbf{E}$, where ε_0 is the vacuum permittivity. The proportionality factor χ is the *optical susceptibility*, from which the refractive index is defined by [12]

optical susceptibility χ

$$n^2(\omega) = 1 + \chi(\omega) \,, \tag{2.62}$$

where the frequency dependence of the susceptibility, the chromatic dispersion of the material, is indicated.

When the induced polarisation also has terms of higher-order dependence on the electric field, the medium's response is nonlinear. Assuming an instantaneous polarisation response,[x] the total polarisation induced in the dielectric as a result of the electric field is given by the Taylor expansion in powers of $\mathbf{E}$,

$$\mathbf{P} = \varepsilon_0 \big(\chi^{(1)} \cdot \mathbf{E} + \chi^{(2)} \colon \mathbf{E}\mathbf{E} + \chi^{(3)} \vdots \mathbf{E}\mathbf{E}\mathbf{E} + \dots \big) \,, \tag{2.63}$$

where $\chi^{(1)}$ is the linear susceptibility and $\chi^{(m)}$ the m-th order nonlinear susceptibility tensors [13]. Typically, the nonlinear susceptibilities are small so in most cases the equation can be linearised as the dominant contribution to the polarisation comes from the linear term $\mathbf{P}^{(1)} = \varepsilon_0 \chi^{(1)} \mathbf{E}$. However, if a the optical field is sufficiently strong, the nonlinear

[x]   Assuming an instantaneous response is effectively assuming a lossless and dispersionless medium, as can be seen from the Kramers–Kronig relations, see Boyd [12, Ch. 1].

contribution becomes important, as the nonlinear polarisation effectively acts as a source for the electric field within the dielectric.[1]

The higher-order susceptibilities are tensors as they detail the polarisation contributions from the fields from different directions. For instance, the third-order tensor is a rank four tensor $\chi^{(3)}_{ijkl}$ with 81 elements. Fortunately, due to a range of different symmetries, the number of independent elements in the tensor is typically much smaller [12, Ch. 1]. For optically isotropic media such as fused silica or barium fluoride, the linear susceptibility is a scalar quantity, and the number of nonzero elements of the third-order tensor is 21, with only four independent elements [13].

For amorphous dielectrics or crystalline dielectrics with crystallographic inversion symmetry, the even-order susceptibilities must be zero:[xi] for instance for the second order, $\mathbf{P}^{(2)} = \varepsilon_0 \chi^{(2)} \mathbf{E}\mathbf{E} = -\mathbf{P}^{(2)}$ by inversion symmetry, which for a nonzero field can only be satisfied by $\chi^{(2)} = 0$ [12, Ch. 1]. Fused silica is amorphous, thus exhibits inversion symmetry, and hence even-order nonlinear effects such as the second-order nonlinearity cannot be observed in the resonators used here. However, centrosymmetric materials do show odd-order nonlinearities, and particularly the third-order nonlinearity is important in this work.

A non-zero third-order susceptibility causes *nonlinear refraction*, i.e., an intensity dependent term for the refractive index,

$$n(\omega, I) = n_0(\omega) + n_2 I \,, \tag{2.65}$$

where I is the optical intensity in the medium [95, Ch. 2]. As the nonlinear refractive index coefficient n_2 is typically small compared to n_0, high optical intensities are needed for the nonlinear term to contribute significantly – for most materials n_0 is of order unity, whereas $n_2 \sim 10^{-20}\,\mathrm{m^2\,W^{-1}}$ for both fused silica [148] and barium fluoride [149] at near-infrared wavelengths.

The intensity-dependent refractive index, often called the optical (AC) *Kerr effect*, comes from the third-order polarisation term and is thus a third-order effect. To derive it, consider a monochromatic, linearly polarised electric field E in the spatial direction i: the only involved element of the third-order susceptibility tensor is $\chi^{(3)}_{iiii}$, which in the below is denoted simply as the scalar $\chi^{(3)}$. Writing the electric field as $E = E_0 \cos(\omega_0 t)$, the third-order polarisation term is

$$P^{(3)} = \frac{1}{4}\varepsilon_0 \chi^{(3)} E_0^3 \left[\cos(3\omega_0 t) + 3\cos(\omega_0 t)\right] \,. \tag{2.66}$$

Margin notes:

xi Note that also an instantaneous field response is required for the following argument, but it is in fact generally valid that centrosymmetric media do not exhibit a second-order susceptibility [12, Sec. 1.5].

nonlinear refraction

Kerr effect

---

[1] The effect of the nonlinear polarisation can be understood through Maxwell's equations, under the slowly varying amplitude approximation and assuming a dispersionless, isotropic dielectric, the wave equation for the electrical field can be expressed [12]

$$\nabla^2 \mathbf{E} - \frac{n^2}{c^2}\frac{\partial^2 \mathbf{E}}{\partial t^2} = \frac{1}{\varepsilon_0 c^2}\frac{\partial^2 \mathbf{P}_{\mathrm{NL}}}{\partial t^2} \,, \tag{2.64}$$

where $\mathbf{P}_{\mathrm{NL}} = \sum_m \mathbf{P}^{(m)} - \mathbf{P}^{(1)}$. The nonlinear polarisation term can be interpreted as a driving term in the differential wave equation.

The term represents third-harmonic generation, but for efficient conversion from ω_0 to $3\omega_0$, the phase velocities of the two waves must be equal [13]. Generally this is not the case because of material dispersion, $n_0(\omega) \neq n_0(3\omega)$, and thus the third-harmonic term can be neglected. The total polarisation up to the third order is then

$$P = P^{(1)} + P^{(3)} = \varepsilon_0 \left(\chi^{(1)} + \frac{3\chi^{(3)} E_0^2}{4} \right) E = \varepsilon_0 \chi_{\text{eff}} E , \tag{2.67}$$

where an effective susceptibility χ_{eff} has been introduced. Inserting the effective susceptibility into the definition of the refractive index (2.62), an expression for the refractive index including the nonlinear contribution is obtained:

$$n^2 = 1 + \chi_{\text{eff}} = \left(1 + \chi^{(1)}\right) + \frac{3\chi^{(3)} E_0^2}{4} = n_0^2 + \frac{3\chi^{(3)} E_0^2}{4} . \tag{2.68}$$

As the nonlinear contribution is assumed to be small, the approximation $(1+x)^{1/2} \approx 1+x/2$ for $x \ll 1$ can be used:

$$n = n_0 \left(1 + \frac{3\chi^{(3)}}{4n_0^2} E_0^2 \right)^{1/2} \approx n_0 + \frac{3\chi^{(3)}}{8n_0} E_0^2 . \tag{2.69}$$

The optical intensity is proportional to the square of the field amplitude, $I = c n_0 \varepsilon_0 E_0^2 / 2$, which gives a refractive index

$$n = n_0 + \frac{3\chi^{(3)}}{4c\varepsilon_0 n_0^2} I \equiv n_0 + n_2 I , \tag{2.70}$$

i.e., a nonlinear refractive index coefficient in units of $\text{m}^2\,\text{W}^{-1}$

$$n_2 = \frac{3\chi^{(3)}}{4c\varepsilon_0 n_0^2} . \tag{2.71}$$

2.6.2 Self-phase and cross-phase modulation

The nonlinear contribution to the refractive index can also be seen as an increased phase accumulation over a propagation length L: $\phi = (n_0 + n_2 I) kL$ [Eq. (2.23)]. The intensity-dependent term represents additional phase accumulation

$$\phi_{\text{SPM}} = n_2 kL\, I \tag{2.72}$$

to the linear phase. This effect is called *self-phase modulation* (SPM), as it is the field itself that is causing the additional phase accumulation. The term SPM is also often used referring to the self-induced refractive index change.

self-phase modulation

In addition to the self-induced phase shift, other fields spatially overlapping but at a different wavelength, in a different polarisation state or direction, can also cause phase shifts. This effect is called *cross-phase modulation* (XPM) and will also contribute to a refractive index change.

cross-phase modulation

In fact, the refractive index change from XPM is twice as strong as the SPM contribution. Following the approach of Kaplan [150], the factor of two can be shown for the case of two linearly polarised, counterpropagating fields considering the third-order polarisation term when the fields are at the same frequency ω and propagating along the x-axis, i.e., with wavevectors $\mathbf{k}_\rightarrow = -\mathbf{k}_\leftarrow = k\,\hat{\mathbf{x}}$. The total field is then

$$E(t, x) = E_\rightarrow(t, x) + E_\leftarrow(t, x) \tag{2.73}$$

$$= \left[A_\rightarrow e^{ikx} + A_\leftarrow e^{-ikx} \right] e^{-i\omega t} + \text{c.c.} , \tag{2.74}$$

where the slowly varying field amplitudes $A_\rightarrow, A_\leftarrow$ are complex and 'c.c.' denotes the complex conjugate. The third-order nonlinear polarisation $P^{(3)} \propto E^3$ will have 20 terms for this total field, some of which are components oscillating at 3ω or with wavenumbers $\pm 3k$. Because of material dispersion these frequency conversion processes are not phase-matched, meaning those terms can be neglected. Leaving those terms out, only eight remain:

$$P^{(3)} \propto 3 \Big[\left(|A_\rightarrow|^2 + 2|A_\leftarrow|^2 \right) A_\rightarrow e^{ikx}$$
$$\left(|A_\leftarrow|^2 + 2|A_\rightarrow|^2 \right) A_\leftarrow e^{-ikx} \Big] e^{-i\omega t} + \text{c.c.} . \tag{2.75}$$

The polarisation for the right-propagating component can be identified,

$$P_\rightarrow^{(3)} \propto \left(|A_\rightarrow|^2 + 2|A_\leftarrow|^2 \right) E_\rightarrow ,$$

where the factor of two in front of the counterpropagating squared amplitude term is what gives the twice as strong power dependence in the XPM compared to the SPM.

By similar arguments as in the case of only SPM in Eq. (2.67) to Eq. (2.70), one finds there is an additional XPM-induced refraction term for the field $\rightarrow$ due to the counterpropagating field $\leftarrow$ and vice versa. The refractive indices counting both the SPM and XPM terms are then

$$n_\rightleftharpoons(\omega, I_\rightleftharpoons, I_\leftrightharpoons) = n_0(\omega) + n_2(I_\rightleftharpoons + 2I_\leftrightharpoons) . \tag{2.76}$$

The nonlinear phase shifts resulting from the SPM and XPM interactions is therefore

$$\phi_\rightleftharpoons^{\text{NL}} = n_2 k L(I_\rightleftharpoons + 2I_\leftrightharpoons) . \tag{2.77}$$

From the full nonlinear refractive index in Eq. (2.76), it is apparent that in the case of two counterpropagating light fields of the same vacuum wavelength but different intensities outside a $\chi^{(3)}$ material, they will experience different refractive indices inside the material and thus different wavelengths, illustrated in Fig. 2.9. The wavelength difference can be seen as different optical path-lengths through the material, having important consequences in the context of counterprogating light in microresonators.
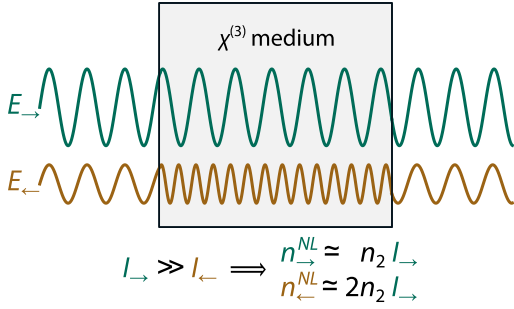
Figure 2.9. Illustration of the Kerr effect for counterpropagating electric fields. Two spatially overlapping (offset in the figure for clarity) fields of equal vacuum wavelength are counterpropagating in a $\chi^{(3)}$ material. When the intensities are unequal, the two beams experience different nonlinear contributions to the refractive indices (n^{NL}), giving different wavelengths within the material for the two propagation directions. Adapted from Del Bino *et al.* [16] under a CC-BY licence.

2.6.3   *The Kerr-induced resonance frequency shift*

For WGM resonators, the intensity-dependent refractive index results in a power-dependent resonance frequency. Considering only one propagation direction first, for an intra-cavity power $\mathcal{P}_{\mathrm{cav}} = IA_{\mathrm{eff}}$, where A_{eff} is the effective area of the mode cross section, the change in the refractive index can be found from the derivative of Eq. (2.65),

$$\frac{\partial n}{\partial \mathcal{P}_{\mathrm{cav}}} = \frac{n_2}{A_{\mathrm{eff}}} \, . \tag{2.78}$$

The refractive index change causes a shift in the resonance frequency away from ω_0 by

$$\frac{\partial \omega_0}{\partial \mathcal{P}_{\mathrm{cav}}} = \frac{\partial \omega_0}{\partial n}\frac{\partial n}{\partial \mathcal{P}_{\mathrm{cav}}} = -\frac{\omega_0}{n}\frac{n_2}{A_{\mathrm{eff}}} \, , \tag{2.79}$$

where the first partial derivative is calculated from Eq. (2.18). This resonance frequency shift is the *Kerr shift*. Normally the nonlinear contribution to the refractive index is small, $n_2 I \ll n_0$, and the shift can be approximated via

Kerr shift

$$\frac{\Delta \omega}{\omega_0} \approx -\frac{1}{n_0}\frac{n_2}{A_{\mathrm{eff}}}\mathcal{P}_{\mathrm{cav}} \, . \tag{2.80}$$

Similarly to how the thermo-optic and thermoelastic shifts changes the spectral shape of a resonance, the Kerr shift also distorts the resonance lineshape when scanning over the resonance:[xii] when scanning a probe field towards the resonance, the resonance shifts downwards in frequency due to increasing intra-cavity power. In contrast to the thermal effects, the Kerr effect is practically instantaneous for the work presented in this thesis [151].

2.6.4   *Resonance shifts for counterpropagating modes*

Due to cross-phase modulation between counterpropagating beams, the resonance frequency of the clockwise direction of a spatially degenerate WGM is not only dependent on the optical power in the CW direction, but also the power in the CCW direction, and vice versa. Because of the factor of two difference between the strength of SPM and XPM contributions in a dielectric, the initially frequency-degenerate counterpropagating modes frequency split when pumped at unequal intensities – and even when pumped with equal intensities for sufficiently high powers.

[xii] Cao *et al.* [17, supp.mat.] roughly estimates the ratio of the shift caused by thermal effects to the Kerr shift in a silica WGM microsphere, showing that the shift caused by thermal effects exceed the third-order nonlinear effects by one order of magnitude. He [140] reports two orders of magnitude for silica WGM microtoroids.

With the optical powers $\mathcal{P}_{cw}, \mathcal{P}_{ccw}$ counterpropagating in a WGM, the resonance frequency shift of the CW resonance of frequency ω_{cw} due to SPM and XPM can be found from the expression for the intensity-dependent refractive index for counterpropagating fields (2.76),

$$\frac{\partial \omega_{cw}}{\partial \mathcal{P}_{cw}} \approx -\frac{\omega_0 n_2}{n_0 A_{\text{eff}}} \; ; \qquad\qquad \frac{\partial \omega_{cw}}{\partial \mathcal{P}_{ccw}} \approx -2 \frac{\omega_0 n_2}{n_0 A_{\text{eff}}} \; , \qquad (2.81)$$

where ω_0 is the common, unshifted resonance frequency. The factor of two between the self-Kerr-induced and the cross-Kerr-induced shifts couples the two resonance frequencies with unequal weights, opening for several interesting effects. Ghalanos *et al.* [152][xiii] shows direct spectroscopy measurements of the shifted resonances, using beatnote measurements of a fixed, strong optical pump and weak co- and counterpropagating probes to detect the resonance shifts. This form of splitting can for instance be exploited for tuning the resonance frequency of a mode through pumping on the counterpropagating mode, and the authors demonstrate a 35-FWHM-linewidth splitting between the two propagation directions.

[xiii] The author of this thesis is a co-author on this work.

Furthermore, as a consequence of the imbalance between the SPM and XPM contributions, for higher powers, even equal-intensity pumping of the two directions can lead to frequency splitting. The solutions to the coupled steady-state equations for the optical power reveals an optical bistability for sufficient optical input powers. Phenomena such as spontaneous symmetry breaking [16, 153, 154] and self-switching [155] can be observed. Spontaneous symmetry breaking was utilised in Svela *et al.* [156] for enhancing the responsivity of near-field sensing with a WGM resonator.

CHAPTER 3

Fabrication methods and experimental techniques

The experimental work presented in this thesis relies on specialised optical devices, custom made to suit the particular experiments. The development of experimental techniques for reliable and reproducible fabrication processes for high-quality devices that meet necessary optical performance, but also with sufficient rigidity, lifetime, thermalisation for cryogenic experiments, et cetera, is key to this research programme. This typically requires an iterative approach with improvements to the design and construction of the setups or characterisation techniques. Sometimes these procedures involve hours and hours of trial and error in parameter hunting, troubleshooting, readjusting, and trying again. Thankfully, with the efforts put down by others in the past, not everything has to be reinvented or developed from scratch; many of the devices used in this thesis are well-known devices in the literature, but with their particularities and special requirements for the experiments presented here. All the important small details and tricks cannot be conveyed in a paper, and sometimes that magical pair of experienced hands is needed to get a setup working.

This chapter describes the fabrication procedures for the optical devices used in this work made by the author or collaborators. Additionally, some experimental techniques that are used extensively throughout this work are also described.

CHAPTER CONTENTS

3.1   FUSED SILICA OPTICAL ROD MICRORESONATORS

The rod resonators used for the work described in Chapter 4 were made from fused silica owing to its low optical losses at telecom wavelengths, ease of machining, and phase-matched evanescent coupling to silica tapered fibres. Fused silica is also optically isotropic,[i] ensuring optical properties do not vary over a roundtrip in the optical resonator. The silica rod resonators used in this thesis were machined in-house at the National Physical Laboratory on an existing machining setup.

The machining procedure is based on the method introduced by Del'Haye *et al.* [55], using a high-power CO_2 laser beam to mill silica glass rods. To reach the state-of-the-art optical quality factors of 10^9, the resonators are fabricated in a nitrogen atmosphere, seeking to avoid the formation of near-IR-absorbing OH groups from water vapour in ambient air being trapped in the resonator during fabrication [157, Ch. 4]. To the best of the author's knowledge, the nitrogen-atmosphere technique has not been demonstrated previously in the literature. Figure 3.2 shows a box plot for the intrinsic Q factors for 13 resonators of diameters in the range $[1.55, 1.87]\,$mm, where the medians suggest a $\simeq 3$ times improvement in the Q factor by fabrication in a nitrogen atmosphere. The Q factors measured for these resonators are amongst the highest reported in the literature for fused silica rod resonators.

The resonators' Q factors were measured under atmospheric conditions, therefore OH-absorption losses caused by post-fabrication adsorption of water to the resonator surface could have reduced the Q factor for the nitrogen-atmosphere-fabricated resonators compared to their initial state. The duration of this adsorption process is reported to be about 100 seconds [87] from the time the resonator comes into contact with atmospheric air, a time window during which the resonators were not measured. However, there was no significant reduction in the Q factor observed in the first few days of use, indicating that if there was a reduction in Q, the adsorption happens on a shorter timescale as reported in the literature. Operating the resonator in a nitrogen atmosphere or under vacuum without air exposure can possibly increase the Q factor even further. Normally, Q factors of a resonator

[i] *Optical isotropy* is defined as the refractive index (or, equivalently, the phase velocity of a wave) being the same in all spatial directions inside the material.
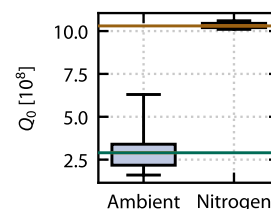
Figure 3.2. Effect on the Q factor of resonator given fabrication atmosphere. Box plot of the highest intrinsic Q factors obtained for ten resonators fabricated in ambient air and three resonators fabricated in a nitrogen atmosphere (box extends from first to third quartile, whiskers cover the whole data range). The medians are marked as horizontal lines. The median for the nitrogen-atmosphere fabricated resonators is approximately three times higher.
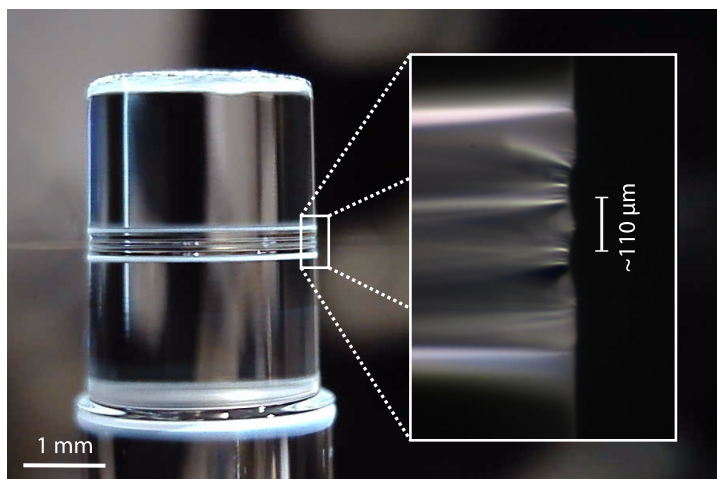
Figure 3.1. Micrograph of a fused silica rod resonator of diameter $2730(2)\,\mu$m, with inset of the resonator profile confining the WGM. The indicated distance between the grooves confining the optical field is $\simeq 110\,\mu$m.

degrade over timescales of weeks or months due to deposition of dust or other impurities on the surface unless under vacuum or other precautions are taken.

To fabricate a resonator, a 3-mm-diameter silica rod is fixed to a spindle motor, and set to spin at 2500 revolutions per minute. Gold-coated galvanometer mirrors provide a means to control the position of the laser beam during the three stages of the milling procedure. First, a laser beam of power in the range 5 to 8 W is swept along the rod surface to evaporate the silica in order to mill the rod to the required diameter. This creates a symmetrical rod with respect to the rotational axis and removes any surface contaminants or air bubbles. Next, the laser beam position is alternated between two points separated by ~0.1 mm along the axis of rotation, cutting grooves at these positions, creating the resonator bulge as shown in Fig. 3.1 in between them. Lastly, the laser power is reduced and swept along the rotation axis, melting the surface to ensure a smooth surface and a high-Q-factor resonator.

The resonators used in this work had diameters in the range 1.7 mm to 2.7 mm, with optical quality factors in the range 10^5 to 10^9.

3.2   CRYSTALLINE BARIUM FLUORIDE OPTICAL ROD MICRORESONATORS

The rod resonator used for the Brillouin optomechanical work described in Chapter 6 needed to comply with two additional requirements to low optical losses, namely, low acoustic losses and high isotropic elasticity to facilitate optomechanical coupling by electrostriction. Crystalline structures generally have lower phononic damping rates than amorphous ones [158, 159], making crystalline structures attractive to ensure low acoustic losses. Furthermore, crystalline materials also show reductions in mechanical damping rates at cryogenic temperatures [160, 161], as the material contribution phonon dissipation is reduced [162, 163].

However, in contrast to amorphous materials, crystalline materials are generally mechanically anisotropic, resulting in directional dependence of the speed of sound in the crystal. This is disadvantageous for Brillouin optomechanics as it reduces the coupling between light and mechanics and thus the Brillouin gain, see Section 5.3.2 for a detailed description. Generally, cubic and hexagonal crystals show the lowest mechanical anisotropy [164] and are also optically isotropic [12].

Based on these considerations, Enzian [165] identified crystalline barium fluoride, BaF_2, as a good candidate for cavity Brillouin optomechanics because of its low optical losses at 1550 nm and relatively high and low-anisotropy elasticity. Moreover, Enzian [165] found that a resonator plane normal to the [111] crystal axis would yield the smallest variation in the speed of sound over the course of a roundtrip along the azimuth,[ii] making this the optimal axis for resonator fabrication to avoid reduced optomechanical coupling.

Barium fluoride has opposite signs of the thermo-optic and thermo-elastic nonlinearities, which makes passive thermal locking unviable, see Section 3.6.1. Furthermore, the different timescales and signs of the Kerr and thermal nonlinearities can lead to oscillatory instabilities in the resonance frequency at high optical powers [96, 166].

[ii] For the [111] axis, the relative variation of the speed of sound is $\simeq 5 \cdot 10^{-6}$, compared to orders of magnitude higher relative variation for other crystal axes such as [001] or [121], see Section 5.3.2.
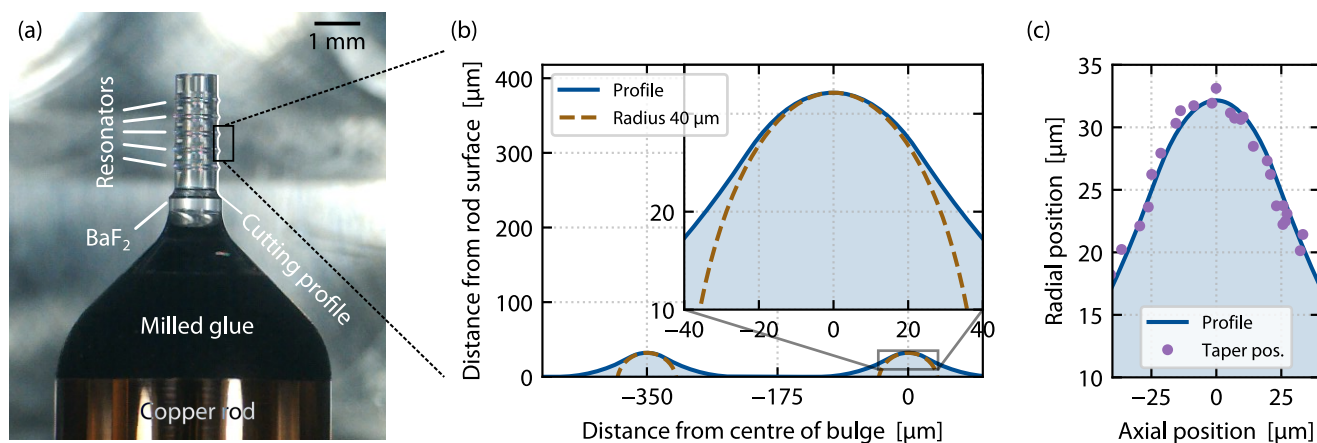
Figure 3.3. (a) Crystalline barium fluoride rod with diameter 0.9 mm with five microresonators. The machining profile (not to scale) is indicated in blue. (b) Plot showing the machined resonator profile for a single resonator bulge, with an orange dashed line indicating a its radius of curvature of 40 μm. (c) Positions of the optical fibre taper when light is coupled into the resonator in comparison to the machining profile, indicating a similar final shape of the resonator bulge as the machining profile.

The barium fluoride resonator used in this thesis [Fig. 3.3(a)] was machined by collaborators at the Ultra-precision machining facility at the Australian National University in Canberra. In order to keep the desirable crystalline structure, a mechanical machining setup is used rather than laser ablation as that would result in an amorphous material structure on the surface. Therefore, a nanometre precision diamond lathe[iii] is used to machine down commercially available barium fluoride single-crystal rods with the [111] crystal axis aligned with the cylinder's symmetrical axis.

In contrast to the machining procedure for the silica rods where grooves are cut and thereby creating a resonator 'bulge' between them, for the BaF_2 resonators, material is removed cylinder symmetrically along the rod, only leaving material to form a set of five resonator 'bulges' spaced by 350 μm on a crystal. The machining profiles of two resonators can be seen in Fig. 3.3(b), indicating the 40 μm radius of curvature of the bulge.

Before machining, the crystal is glued with a cryo-compatible epoxy[iv] onto the end of an oxygen-free copper cylinder to facilitate mounting in our cryostat setup and ensure good thermalisation of the crystal to the cryostat temperature. During machining, the crystal is rotated at 2000 revolutions per minute, and at a 3 mm min^{-1} feed rate in the axial direction, i.e., rate at which the diamond tool moves along the crystal. The particular machining speed is selected as it is sufficiently slow to ensure no slipping of the tool, and sufficiently fast to avoid large cracks in the crystal. The crystal is first machined to a perfect cylinder with the same axis as the lathe, then the lathe is set to trace out the custom path corresponding to the desired resonator shape, as shown in Fig. 3.3(b). The final lathe steps use a new diamond tool to ensure its sharpness for a smooth surface, making double cuts for each of the depths 10, 5, 2, and 1 μm.

After using the nano-lathe tool for the cutting the shape, diamond slurries of progressively fine particle sizes[v] are used for final polishing to provide the necessary surface smoothness needed for high optical Q factors. After polishing, the samples are shipped

to the UK in custom made aluminium boxes to protect the resonators in transit and keep them pristine.

The resonator used in this work has a major diameter of 953(1) μm and radius of curvature for the bulge confining the light field of 40.0(1) μm. The resonator machining profile matches recorded positions for which a tapered optical fibre couples to the WGMs, see Fig. 3.3(c). The resonators show optical quality factors up to 10^8.

3.3   MICRON-WAIST-SIZE TAPERED OPTICAL FIBRES FOR RESONATOR COUPLING

Tapered optical fibres have been used to couple into microresonators since Knight *et al.* [125] demonstrated the technique more than two decades ago. It is still a challenging device to make because of its thin, long nature and large parameter space with small tolerances for what yields a high-transmission, durable taper or a taper that does not exhibit these characteristics.

For the work described in the first part of this thesis, the tapered fibres for coupling to microresonators were produced in-house at the National Physical Laboratory using an existing setup. For the Brillouin optomechanics projects, a similar setup was replicated under a laminar flow box, to avoid any contamination on the tapered fibres during and after fabrication. The author played a significant role in building and optimising this setup, including contributions to writing a comprehensive graphical user interface controlling all the components, and providing convenient control over the involved components and automation of the whole pulling procedure.

3.3.1   *Hydrogen flame tapering setup*

To fabricate the fibres, a flame is placed close to the fibre, heating the silica whilst simultaneously the fibre is pulled symmetrically from both sides until the desired thickness is reached. A mass flow controller[vi] is used to control hydrogen flow through a 0.4-mm-diameter copper nozzle, with multiple flashback arrestors in the hydrogen piping. The hydrogen gas is ignited by an arc between two copper electrode tips, providing a clean ~2000 °C flame. To pull the fibre, it is clamped[vii] to two stepper motor stages.[viii] The HEPA-filter flow box[ix] over the setup provides a clean environment so that dust and other contaminants are prevented from sticking to the taper during and after fabrication. This is critical to ensure the tapered fibre will not heat when being pumped with milliwatt levels of laser power, as under vacuum this can cause the taper to break.

A 1550 nm laser source and a photodiode is used to monitor the transmission whilst the fibre is pulled to provide a means of determining when the fibre is single mode. As the fibre is pulled, the diameter of the high-index core changes, and the single-modedness of the fibre is lost. When the core becomes too small to support the optical mode, light leaks into the fibre cladding and light is lost to the environment or guided by the refractive index difference between the surrounding air and the cladding silica [125]. The changing diameter results in a varying ability to guide the light and interference, which can be observed as change in the transmission of the 1550-nm light passing through the taper as it

[vi] Bronkhorst EL-FLOW Base F-201CB

[vii] using Thorlabs T711/M-250

[viii] Thorlabs MTS50/M-Z8 with KST101 controllers

[ix] Spetec SuSi
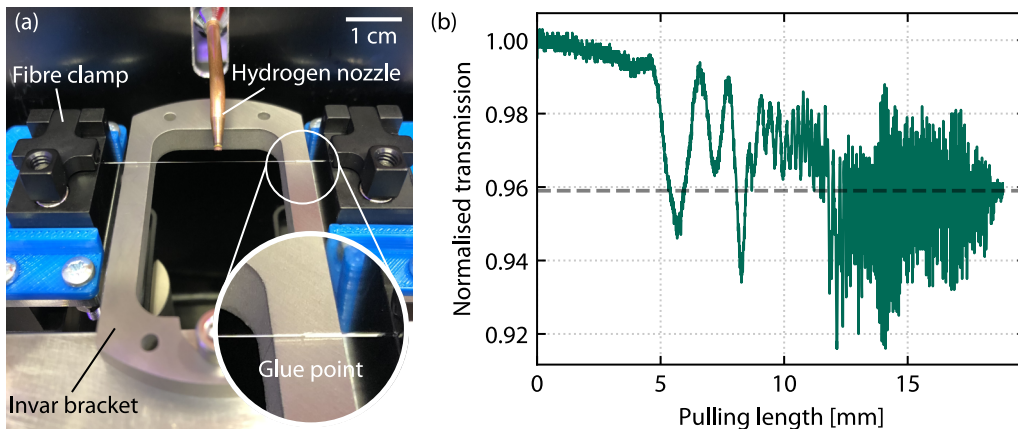
Figure 3.4. Tapered fibre fabrication. (a) Photo of a pulled fibre in the tapering setup before glueing onto the bracket. Note that since this photo was taken the nozzle has been rotated 180°, so the outlet of the nozzle is facing upwards. The fibre clamps are mounted onto stepper motors and the hydrogen gas flow rate is controlled by a mass flow controller. The copper electrodes providing the arc for igniting the hydrogen are removed in this photo. (b) Transmission of the fibre as it is pulled simultaneously from both sides.

is pulled thinner. When the taper-waist diameter is so small that only one mode propagates through, the oscillation in the transmission ceases and the pulling is stopped. At this fibre diameter, the evanescent field is significant and the fibre is well-suited for coupling into WGM resonators.

3.3.2   *Pulling procedure*

The fibres are made from a stripped 125-μm-diameter standard single-mode silica optical fibre (SMF-28). After stripping off the polymer coating using a a pair of manual strippers,[x] the exposed silica is cleaned with IPA and clamped in place. The flow box is turned off during the pulling procedure to avoid the flame shape being affected by the air flow.

A hydrogen flow of 80 to 110 mL/min is used. A delay of 15 s is used between when the hydrogen is ignited and the motors start pulling at a constant speed of 20 μm s^{-1}. The taper transmission is recorded throughout the pulling procedure. When a steady transmission is reached, the motors are stopped and the hydrogen flow is simultaneously cut off.

Due to the upwards push from the flame during pulling and the softness of the hot silica, the fibre is not straight when the flame is cut off. Therefore, a small tensioning of 80 μm to 160 μm is applied to ensure a straight and tensioned fibre to avoid taper vibrations, providing stable coupling control.

After tensioning, the fibre is glued in-place onto a custom designed metal bracket, making sure that both the exposed silica part and the polymer coating is glued onto the bracket for optimal tensioning and robustness. For room temperature experiments, a fast-curing glue is used,[xi] allowing for the taper be to used right away. For cryogenic experiments, however, a few additional factors must be considered. To avoid the tensioning of the fibre changing with temperature for cryogenic experiments, invar is chosen as the

[x] Thorlabs FTS4

[xi] Norland Optical Adhesive 81, cured by exposing to a 5 W ultraviolet handheld torch for 30 s.

bracket material.[2] As the fast-curing glue is not cryo-compatible, the UV glue is covered with a slow-curing two-component cryo-compatible epoxy.[xii] As we have observed that the epoxy typically releases from the bracket after a few thermal cycles between room temperature and 4 K regardless of whether UV glue or not is used underneath the epoxy, a different cryogenic glue better matched to the small thermal contraction of invar over the temperature range in question is now being tested.

[xii] Stycast 2850FT with 24LV catalyst, 18 hours curing time at room temperature.

Finally, the fibre ends are spliced onto SMF-28 pigtails with APC fibre connectors to interface with the optical setups.

3.4   SUB-WAVELENGTH-SIZE TUNGSTEN TIPS FOR NEAR-FIELD PERTURBATION

The tungsten tips used in this work's Chapter 4 were made in-house, based on an electromechanical etching method used for the fabrication of tips for scanning tunnelling electron microscopy and atomic force microscopy tips.[xiii] The author built a setup at the National Physical Laboratory for the fabrication of tips, and subsequently built another one with improved etching voltage cut-off control at the Max Planck Institute for the Science of Light.

[xiii] The works of Ibe *et al.* [168], Lucier [169], and Hagedorn *et al.* [170] in particular have shaped the procedure detailed below.

In this section, the fabrication principle, procedure, and effect of delayed etching-voltage cutoff is explored.

3.4.1   *Electrochemical reaction and etching setup*

The tips are made by electrochemically etching a piece of high-purity, polycrystalline tungsten wire. The process relies on capillary action and the aqueous electrochemical reaction

$$W(solid) + 2\,OH^- + 2\,H_2O \longrightarrow WO_4{}^{2-} + 3\,H_2(gas), \tag{3.1}$$

in which the solid tungsten (W) anode is etched through oxidation, as shown schematically in Fig. 3.5 and explained below.

When the tungsten wire is inserted into the solution, capillary forces cause an upwards meniscus to form around the wire. When a voltage is applied across the tungsten and some other electrode in the electrolyte, the etching reaction runs when the 1.43 V minimum potential difference for the reaction is overcome [170]. Importantly, the rate of the reaction varies along the wire: the etching rate is small at the top of the meniscus as the hydroxide influx is increasingly lower where the meniscus gets smaller, and similarly, further down the wire, there is also a gradient in the etching rate, but there because the tungstate ($WO_4{}^{2-}$) ions that fall along the sides of the wire form an increasingly dense laminar layer, protecting the lower end of the wire from being etched. The etching rate gradient causes a waist to be formed at the point of highest etching rate. When the waist diameter has decreased

---

[2]The relative thermal expansion of this iron-nickel alloy over a temperature change from 300 K to 4 K is $-40 \cdot 10^{-5}$ (all of which is attributed to the 100 K, from there on there is no change). For comparison, aluminium has a relative expansion of $-460 \cdot 10^{-5}$ over the same temperature range [167]. For a 36 mm bracket this corresponds to a change of $\simeq -14\,\mu m$ for invar or $\simeq -170\,\mu m$ for aluminium, which is substantial compared to the tensioning applied.
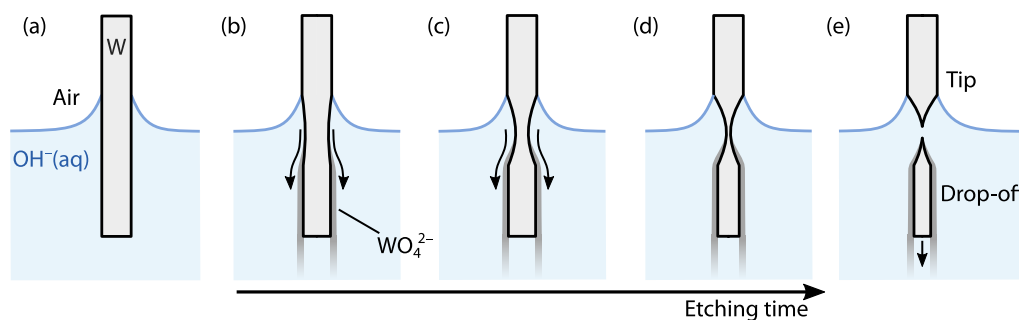
Figure 3.5. Tungsten tip etching process. (a) A meniscus is formed around tungsten wire due to surface tension. (b-d) When the voltage supply is turned on, the electrochemical etching starts, the concentration gradient of OH^- gives lower etching speed at the top of the meniscus; as WO_4^{2-} is formed, it slides down along the tungsten wire and protects it from being etched. (e) Drop-off of the lower tip happens due to gravity as the thin centre part of the wire ruptures.

sufficiently, gravity will break off the lower part of the wire, leaving a sharp tip on the tungsten wire.

The time between the lower wire drop-off and turning off the voltage across the two electrodes is critical for tip sharpness: as long as the voltage is sufficient for driving the reaction, the etching continues and the tip's shape changes, becoming less sharp. To control this voltage cutoff time delay on a millisecond level, a computer controlled setup was built using an Arduino, a shunt resistor, and a relay.

A diagram for the etching setup is shown in Fig. 3.6. A computer reads the voltages of the two Arduino pins at a sampling rate of 2.0 kS/s, calculating the etching current from the voltage drop across the shunt resistor. When gravity pulls off the lower part of the tungsten wire, the step change in the tungsten electrode area causes a step change in the current, falling to the noise limit of the current measurement. To stop the reaction completely, the current drop triggers the computer to send a command to the Arduino to set the relays to their normally closed state and thus the voltage across the electrodes drops to zero. The delay between wire drop-off and voltage cutoff can be controlled, allowing to study the tip radius of curvature in relation to the voltage cutoff delay.

3.4.2   *Fabrication procedure and cutoff-delay-radius relationship*

Temper-annealed, 250-μm-diameter, 99.95 % purity polycrystalline tungsten wire was used in the fabrication. The electrolyte is made by dissolving potassium hydroxide (KOH) in deionised water, creating a $7.5\,\mathrm{mol\,L^{-1}}$ concentration aqueous solution. A tinned copper electrical wire of diameter 0.3 mm is used as the cathode.

The tungsten wire is cleaned using a tissue with IPA and then inserted approximately vertically into the solution, 3.5 mm deep. A DC power supply set to output of 3.0 V is turned on to start the etching.[xiv] To further clean the part of the wire forming the final meniscus and to reduce the surface roughness, the wire is lifted by 1 mm after $\simeq 10\,\mathrm{s}$ of etching. The etching current falls as the contact area of the tungsten electrode to the electrolyte reduces as a result of the etching, and abruptly drops to the noise level of the current measurement when the part below the waist drops off, as can be seen in Fig. 3.7(a). The total etching time

[xiv] Alternatively, an AC voltage source can be used; however, in general, AC-etched tips are conically shaped and longer than the hyperbolically shaped and sharper DC etched tips [168].
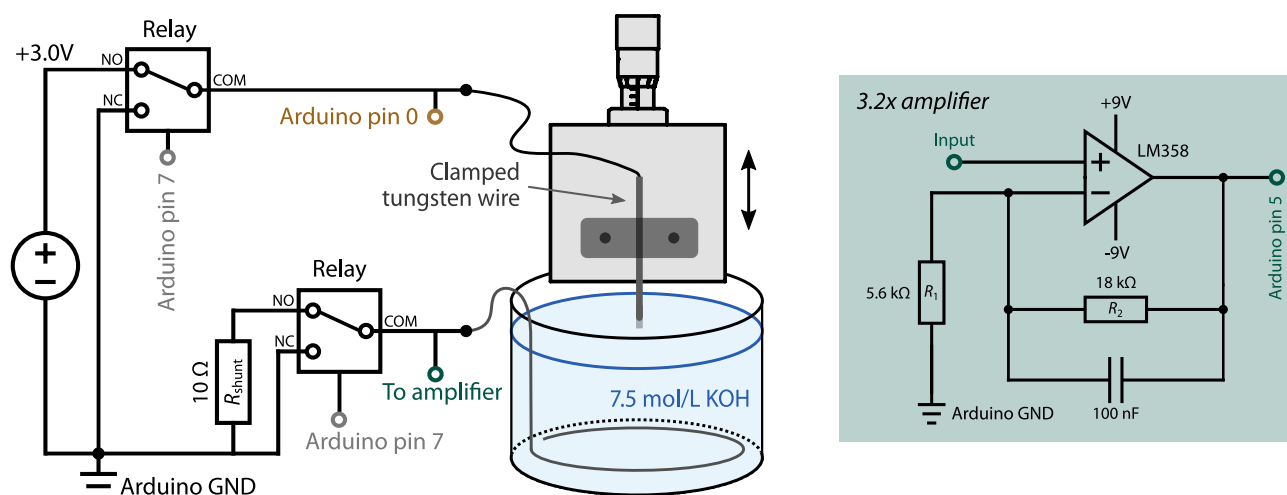
Figure 3.6. Schematic of the computer-controlled tungsten tip etching setup during etching. A tungsten tip is mounted on a translation stage to control its position in an OH^- solution. A 3.0 V power supply is connected to the tungsten tip via the normally open (NO) port of a relay. The relay is controlled by an Arduino, allowing millisecond-timescale control over the etching time. The Arduino measures the voltage drop across the solution by the difference between the voltages on its pins 0 and 5 (scaled for $R_2/R_1 = 3.2$ times amplification), and the current is measured by the (scaled) voltage drop over the 10 Ω shunt resistor: $I = V/R_{shunt}$. For better sensitivity, an op-amp is used to amplify the shunt resistor voltage drop, as shown in the righthand-side circuit diagram. The relays switch from the normally open (etching reaction driven) to the normally closed (no etching) when a computer sends a command to the Arduino, turning off its voltage output on port 7.

is typically two minutes. After etching, the tip is removed from the solution and cleaned with IPA and left to dry.

Scanning electron microscope[xv] (SEM) images of a tip fabricated using the setup are show in Fig. 3.8. From SEM imaging 10 tips, the relationship between the voltage cutoff delay and the size of the tip is explored in Fig. 3.7(b). A phenomenological power law relation is fitted to the data,[xvi] showing that the cutoff delay is a critical parameter in determining the radius of curvature of the final tip. A simple motivation for a power law relation is that the amount of material that has to be removed for a change in the radius of curvature is increasingly larger as the radius increases.

3.4.3   *Tip yield & reliability and sharpness improvements*

The method presented in this section is found to reliably produce sub-wavelength-size tips,[xvii] and the tip-size can be controlled by the etching-voltage cutoff delay. As long as the electrolyte is free of contaminants, the tips do not show signs of contamination and the yield of those tips selected for SEM imaging is close to 100 %.

Improvements that can be made to the setup include simple changes to increase the reproducibility and reliability further such as (i) inserting a bubble barrier to avoid H_2 gas bubbles disturbing the meniscus; (ii) covering the setup to avoid contaminants in the electrolyte; and (iii) using a better clamping mechanism to ensure the tungsten wire is perpendicular to the electrolyte. To improve tip sharpness beyond the 30 nm achieved here, implementing a shorter voltage cutoff delay [168] will probably have the most significant effect. Additionally, using crystalline tungsten wire [170], or employing post-etching

[xv] Hitachi S-4800 at the Max-Planck Institute for the Science of Light, Erlangen

[xvi] The logarithm of the radius and delay are used in a linear fit, i.e. $\log r = a_1 \log t_d + a_0 \implies r = 10^{a_0}(t_d)^{a_1}$, where a_0, a_1 are free parameters.

[xvii] Keeping in mind this statement by Ekvall *et al.* [171]: *Possibly there are as many tip-preparation procedures as there are people making tips.*
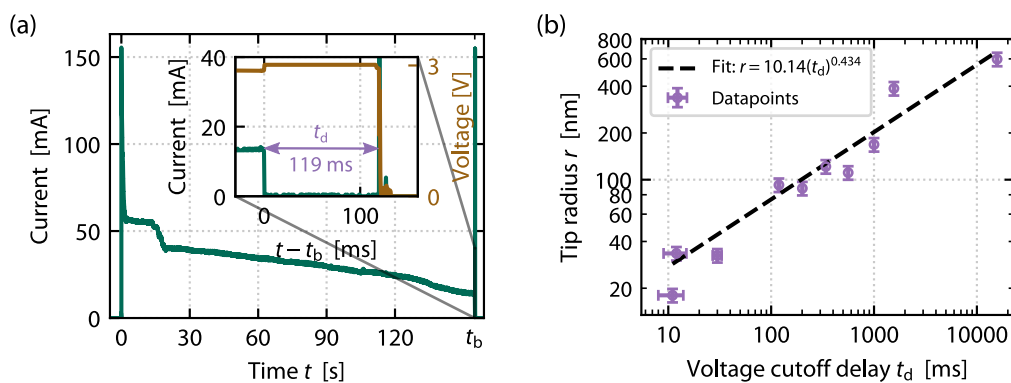
Figure 3.7. Tungsten tip etching current profile, and etching voltage-cutoff delay versus size. (a) The etching current over the course of an etching procedure. A reduction in the current around 15 s etching time can be observed, which is when the tip is moved 1 mm out of the electrolyte (end of pre-etching), reducing the etching area and thus the current. The tip drop-off occurs at $t = t_b$, and the inset shows the etching current and voltage drop across the solution in the time after the drop-off, where the delay time t_d between the drop-off and the voltage cutoff is annotated. (b) Radius of curvature of etched tips measured from SEM images plotted as a function of the delay time t_d between the tip drop-off and voltage cutoff. A linear fit to the logarithm of the radius and delay is shown (a power law fit). The uncertainties of 3 ms and 10 % on the radius is indicated.
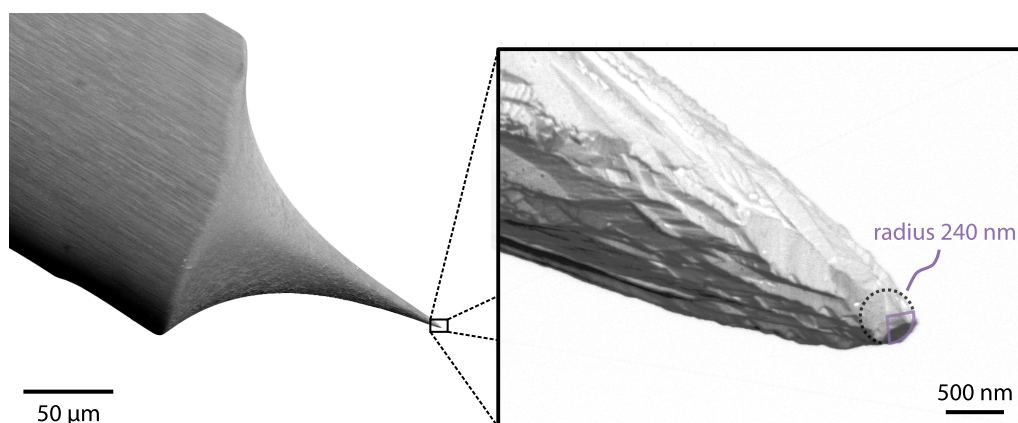
Figure 3.8. Scanning electron microscope images (inverted colours) of a tungsten tip. The tip's radius of curvature at the tip is annotated.

sharpening techniques such as heating [171], field-ion-microscope-driven reaction with nitrogen [172], or ion milling [173], can be considered.

3.5   MEASURING THE OPTICAL QUALITY FACTOR OF A RESONANCE

There are several approaches to measuring the Q factor of a resonance, for instance through cavity ring-down measurements [e.g. 174]. Here, however, a direct linewidth measurement is used, where the loaded Q factor is calculated from the ratio of the resonance frequency to the FWHM linewidth of the resonance [Eq. (2.16)].

To measure the linewidth of a resonance, a setup like the one shown in Fig. 3.9(a) can be used. The frequency of a narrow-linewidth, tuneable laser coupled to the resonator is swept over the resonance and the transmission is recorded on a photodiode (PD). To avoid Kerr or thermal broadening or compression of the resonances [Section 2.5.1], a low input
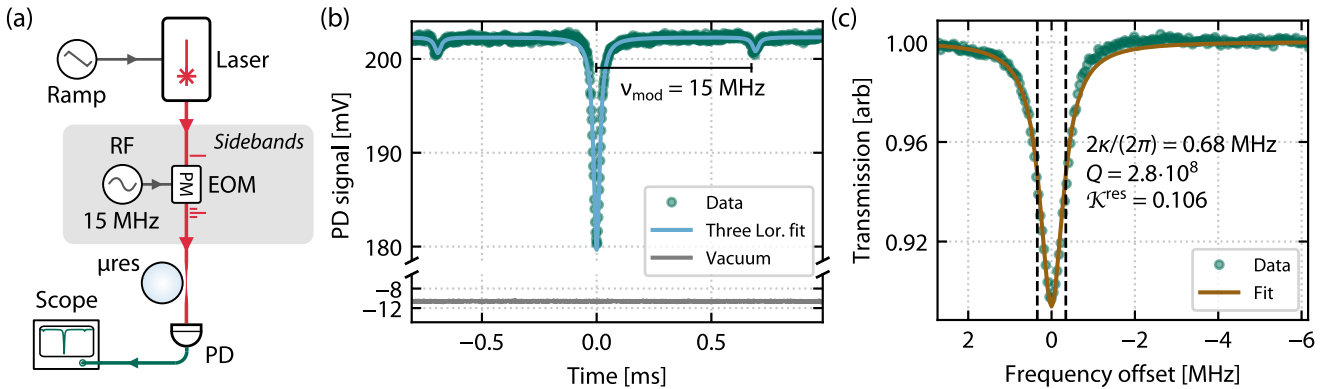
Figure 3.9. Frequency sweep calibration and optical Q factor measurement using sidebands. (a) Schematic of a setup for measuring the optical Q factor. The laser frequency is scanned as a linear ramp downwards in frequency and passed through a phase modulating (PM) EOM before it is coupled into the microresonator (μres). The transmission is recorded by a photodiode (PD). Polarisation controllers before the EOM and resonator, necessary to ensure correct polarisations for maximum transmission, are omitted from the schematic. The RF signal modulating the light causes sidebands spaced by the modulation frequency. (b) Sweeping the probe laser carrier (v = 193.38 GHz) downwards in frequency with EOM generated sidebands at $\pm v_{mod}$ = ±15.0 MHz across the resonance (dots). The data is fitted with the sum of three Lorentzian lineshapes (line) to determine the separation of the sideband resonances from the carrier, which is used to calculate a time–frequency calibration for the laser scan. To determine the optical coupling efficiency, the voltage for when there is no optical input to the PD is used (vacuum, grey line). (c) A fitted Lorentzian (line) gives a FWHM linewidth of 0.68 MHz for the resonance scan (dots), where the linewidth is indicated by dashed lines. From the optical coupling efficiency, the intrinsic Q factor can be calculated, giving Q_{in} = 2.9 · 10⁸. The uncertainty of these values can be around a percent level due to the nonlinearity of the piezo scan.

power must be used to obtain a Lorentzian resonance shape for an accurate linewidth to be measured. Alternatively, if intermediate input powers are needed, a sweep faster than the thermal effect will ensure a near-unbroadened linewidth.[xviii] To ensure that the effects of broadening or compression are negligible, the resonance profile should be equal for laser frequency scans in both directions.

In order to calibrate sweep of the laser, i.e., the frequency sweep per time, an electro-optical modulator (EOM) driven by an RF signal in the MHz range can be inserted before the tapered fibre. The laser probe acquires sidebands at the modulation frequency $\pm v_{mod}$, resulting in three resonances with a known separation equal to the EOM modulation frequency, as shown in Fig. 3.9(b). By fitting a sum of three Lorentzians to the transmission spectrum, the time separation between the sidebands is determined, which, together with the known sideband frequency, gives the time-to-frequency calibration for the laser sweep. Note that if using a piezo to scan the laser, one should preferably be scanning over a small part of the middle of the piezo range to avoid a nonlinear response from the piezo.

Alternatively, to sweep the output frequency of a diode laser and avoid the (small) nonlinearity of a piezo affecting the sweep, the current of the diode can be swept. The current across the junction effectively controls the junction temperature, and the output wavelength responds rapidly and linearly to changes in the junction temperature. To avoid changes in the optical power as a consequence of the current sweep, the laser output can be directed through an optical amplifier, such as an erbium doped fibre amplifier (EDFA), operating in saturation, which keeps the power stable. Figure 3.10 shows such a calibration for a Toptica CTL 1500, where the swept optical frequency per time and per scanned current

[xviii] A scanning frequency of for instance 1 kHz will ensure no thermal broadening for milliwatt input powers, but if the scanning frequency is too high, ringdown signals will distort the resonance shape.
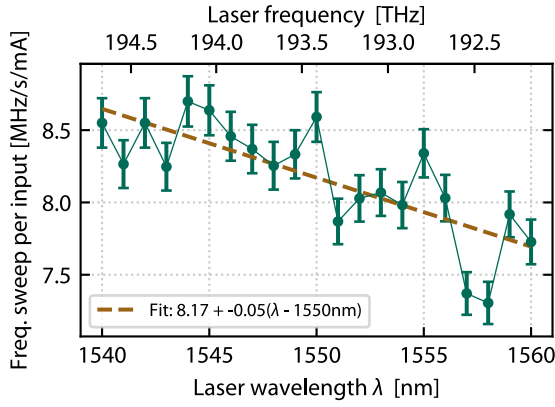
Figure 3.10. Measured laser current sweep calibration. Sweeping the current of the laser linearly at a frequency of 1007 Hz, the frequency sweep per time per current can be calculated from fitting spectra with EOM generated sidebands. The data points are given with a 2 % error.

for a particular scanning speed is given across some of the laser's output spectrum. The linear fit to the data points gives a sweep calibration of $8.17(6)$ MHz s^{-1} mA^{-1} at 1550 nm when the current is swept at 1007 Hz. The response of the junction can be different for a different speed of the current sweep, so similar calibrations can be made for different scanning speeds.

When the laser calibration has been obtained, another spectrum without modulation sidebands is taken to avoid any distortion of the resonance shape. From knowing the voltage reading of the PD when there is no incident light, the spectrum can be normalised to transmission values between 0 and 1. A Lorentzian dip from a background of 1, with depth η_{opt}, FWHM Δv, and central frequency v_0,

$$\mathcal{T}(v) = 1 - \frac{\mathcal{K}^{\mathrm{res}}}{1 + [2(v - v_0)/\Delta v]^2},$$

(3.2)

is then fitted, giving the linewidth of the resonance.

When measuring the Q factor, the coupling to the taper increases the losses as light leaks out of the cavity, thus the measured Q factor is the Q factor of the combined resonator-taper system, often called the *loaded Q factor*. The intrinsic Q_{in} can be deduced from the loaded $Q_{(\mathrm{tot})}$ for a known optical coupling contrast at resonance $\mathcal{K}^{\mathrm{res}}$:

$$Q_{\mathrm{in}} = \frac{2Q_{(\mathrm{tot})}}{1 \pm \sqrt{1 - \mathcal{K}^{\mathrm{res}}}},$$

(3.3)

where the sign is chosen according to the coupling regime: $+ (-)$ for an under(over)coupled resonator [16]. The coupling depth is the depth of the resonance in the transmission spectrum, where $\mathcal{K}^{\mathrm{res}} = 1$ corresponds to critical coupling when no light is transmitted at the resonance.

An example of a fitted Lorentzian is shown in Fig. 3.9(c), resulting in the linewidth $\Delta v = 2\kappa/(2\pi) = 0.68$ MHz, corresponding to a loaded $Q \simeq 2.8 \cdot 10^8$. The fit gives $\mathcal{K}^{\mathrm{res}} = 0.106$, and thus, by Eq. (3.3), $Q_{\mathrm{in}} \simeq 2.9 \cdot 10^8$ for this undercoupled resonance. The uncertainty of the linewidth and Q factor values can be around the percent level due to the nonlinearity of the piezo scan.

3.6   LOCKING TO OPTICAL MICRORESONATOR MODES

When working with optical resonances it is often desirable to fix the pump laser to a particular offset from a resonance frequency, typically zero offset for maximal intracavity build-up. Two different approaches can be chosen: either change the laser frequency to follow the resonance frequency, or change the resonance frequency to follow the laser.

For some materials and situations, the physics of the system allows for passive locking, where the resonator is self-stabilised to keep the particular coupled power for small perturbations. In other situations active locking techniques are used to keep the laser frequency offset from the resonance fixed. This section will briefly explain qualitatively the basis of two standard locking methods.

3.6.1   *Passive thermal locking*

For a resonator that has the same sign for the thermo-optic and thermoelastic coefficients, an equilibrium between the heating-induced resonance frequency shift and the laser frequency shifts can create a self-stable system where small perturbations to the laser frequency will make the resonance frequency follow the laser [138].

The qualitative description of the locking mechanism depends on the sign of the thermal nonlinearity. For a resonator with negative frequency shift for increasing temperature, $\partial\omega/\partial T < 0$, such as silica: if the laser is on the high-frequency side of the resonance, a slight decrease in the laser frequency leads to increased in-coupled power due to the decreased detuning, heating the resonator, which shifts the resonance frequency downwards [Eq. (2.61)], i.e., pushed in the same direction as the laser is moving. Conversely, if the laser frequency increases, the resonator cools down, shifting the resonance frequency up to match the laser's frequency increase. Thus, resonance frequency is locked to the laser for small perturbations.

Note that this form of locking of the resonator works only on one side of the resonance, and cannot be used to lock to the resonance point exactly, due to the turning point in coupled power versus frequency. Which side the locking can be used depends on the thermal coefficients: the laser must be blue (red) detuned for a resonator with positive (negative) thermal coefficients.

This experimentally simple, passive technique can be useful for experiments or quick tests without stringent lock-performance requirements.

3.6.2 *Active Pound–Drever–Hall locking*

For resonators with thermal coefficients of opposite signs, such as those made from barium fluoride, thermal locking is not possible. There might also be times where a passive lock is not an option for other reasons, for instance because it might be too slow[xix] or temperature fluctuations are causing instabilities. In these situations active locking techniques can be used, for instance the Pound–Drever–Hall (PDH) locking technique [175, 176] is widely used.

To implement an active lock of the laser to a cavity resonance, a feedback system is set up to adjust the laser frequency so that the frequency offset between the laser and resonance is stable. This is implemented by supplying an *error signal* – a signal proportional to the deviation from the chosen resonance lock point – to a servo like a proportional-integral-derivative (PID) controller, which continuously controls the laser frequency. For an external-cavity diode laser (ECDL), the frequency is typically tuned through applying a voltage to the piezo which adjusts the grating position, or by changing the laser current.

A canonical PDH lock uses the phase shift of the light transmitted through the cavity, shown in Eq. (2.33), as the error signal. It can be shown [176] that the phase shift is approximately linear around the resonance frequency, and zero at resonance, thus, fulfilling the two requirements for an error signal.

The phase shift information is obtained by modulating the phase of the laser carrier much faster than the cavity decay time and mixing down the electronic signal from the detected transmitted light with the modulation signal, extracting the relative phase of the input field with respect to the cavity field. If the phase of the modulation signal is shifted by $\pi/2$ before it reaches the mixer, the power in the mixed-down signal will be zero at resonance, giving the zero crossing for the locking point. An example error signal is shown in Fig. 3.11.

The specific hardware and modulation frequencies and powers used for the PDH locks used in the experiments described in this thesis have varied. For the example shown in Fig. 3.11, the RF signal was a 17.5 MHz, 1.2 Vpp sinusoid supplied by a function generator[xx] to a phase-modulating EOM.[xxi] The electrical signal of the PD measuring the transmitted light is mixed down[xxii] with the modulation signal phase-shifted by $\pi/2$. The phase shift to the modulation signal before the mixer was ensured by simply adding the appropriate amount of BNC cable for the signal to propagate. A low pass filter[xxiii] is used to filter out higher harmonics in the mixed-down signal. A proportional-integral controller[xxiv] is used to keep the resonator locked, allowing tuning of the locking point.

[xix] Carmon *et al.* [138] reports a few-milliseconds response time for the thermal shift in a 0.14-mm-diameter silica sphere.

error signal

[xx] Agilent 33250A

[xxi] Thorlabs LN65S-FC

[xxii] Minicircuits ZMF-3H+

[xxiii] Minicircuits BLP-1.9+

[xxiv] Newport LB1005-S
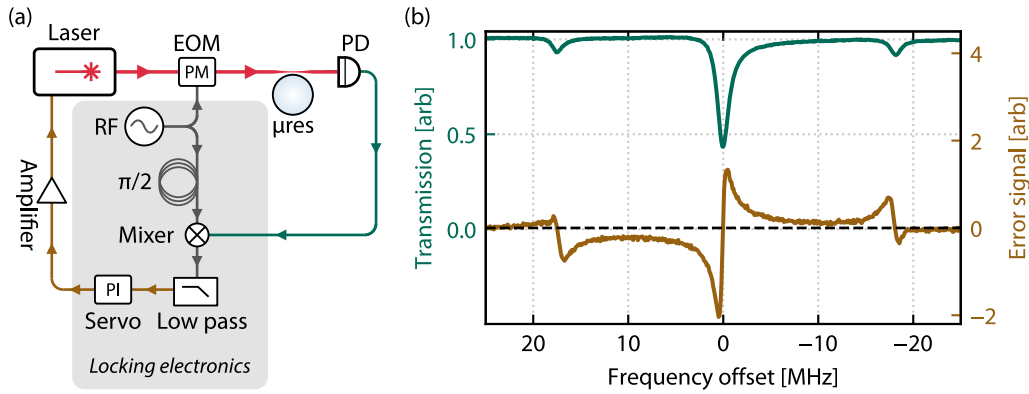
Figure 3.11. PDH locking to a cavity resonance. (a) Schematic of a setup for PDH locking of laser to a microresonator (μres). The laser light is phase modulated (PM) by an EOM before coupling into the cavity, and the transmission is recorded by a photodiode (PD). The RF signal modulating the light is offset in phase by a delay loop before the signal is mixed with the transmission signal to form the error signal. To filter out the harmonics in the mixed down signal, a low pass filter with cutoff lower than the first harmonic is used before feeding the signal to a proportional-integral (PI) servo, which controls the laser wavelength. Polarisation controllers to optimise the transmission of the EOM and coupling to the resonator are not shown. (b) Transmission spectrum for a resonance at low optical power with sidebands at the modulation frequency ±17.5 MHz. The PDH error signal is obtained by mixing the transmission spectrum with the RF modulation signal and shows a monotonically increasing signal within the central part of the resonance, a zero crossing at the resonance frequency.

3.7   BALANCED HOMODYNE AND HETERODYNE DETECTION

Balanced photo-ddetection is widely used in quantum optics as it is, in principle, a form of shot-noise-limited detection, where a field quadrature can be detected with an accuracy limited only by the vacuum fluctuations. The below is meant as a short summary outlining some important points related to how heterodyne detection is used in Chapter 6. Many textbooks treat dyne detection in detail, for instance Refs. 177–179.

3.7.1   *Homodyne detection*

The principle of homodyne detection is to interfere a weak signal of interest with a strong coherent field on a beamsplitter with equal transmittance and reflectivity, and then detecting the optical power at the two output ports of the detector. By taking the difference between the photodetector currents, the resulting signal is proportional to the difference in photon number at the two detectors (Fox [177] gives a practical description how such a detector can be made). To see this, consider a 50:50 beam splitter with inputs $\hat{a}_{\text{LO}}, \hat{a}_{\text{sig}}$ [Fig. 3.12(a)]. The field at the output ports follow the transformation [179, Ch. 4]

$$\hat{a}_{\text{o1}} = 2^{-1/2}\left(\hat{a}_{\text{sig}} - \hat{a}_{\text{LO}}\right), \tag{3.4a}$$

$$\hat{a}_{\text{o2}} = 2^{-1/2}\left(\hat{a}_{\text{sig}} + \hat{a}_{\text{LO}}\right). \tag{3.4b}$$
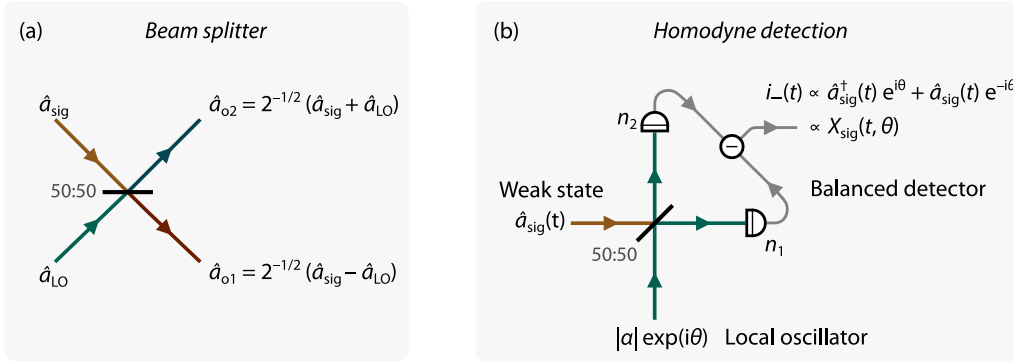
Figure 3.12. Homodyne detection schematic. (a) A lossless beam splitter with equal probability for reflecting as transmitting an incoming photon at one of its ports. (b) A homodyne detection setup where a weak state is interfered with a strong, coherent local oscillator, allowing a quadrature of the signal field to be measured.

The difference photocurrent is proportional to the difference in photon number at each detector

$$i_-(t) \propto \hat{n}_2(t) - \hat{n}_1(t) \tag{3.5}$$

$$\propto \hat{a}_{o2}^\dagger \hat{a}_{o2} - \hat{a}_{o1}^\dagger \hat{a}_{o1} = \hat{a}_{sig}^\dagger \hat{a}_{LO} + \hat{a}_{LO}^\dagger \hat{a}_{sig} , \tag{3.6}$$

where the time dependencies of the field operators have been omitted for compactness. Now letting the local oscillator be a strong coherent state with phase θ and power proportional to $|\alpha|^2$

$$\hat{a}_{LO} \rightarrow |\alpha| \exp(i\theta) , \tag{3.7}$$

then

$$i_-(t) \propto \hat{a}_{sig}^\dagger(t) |\alpha| e^{i\theta} + |\alpha| e^{-i\theta} \hat{a}_{sig}(t) \tag{3.8}$$

which, by Euler's formula can be written

$$i_-(t) \propto 2|\alpha| \left\{ \left[\hat{a}_{sig}^\dagger(t) + \hat{a}_{sig}(t) \right] \cos(\theta) + i \left[\hat{a}_{sig}^\dagger(t) - \hat{a}_{sig}(t) \right] \sin\theta \right\} \tag{3.9}$$

$$\propto \sqrt{2}|\alpha| \left\{ X_{sig}(t) \cos\theta + P_{sig}(t) \sin\theta \right\} \tag{3.10}$$

$$\propto \sqrt{2}|\alpha| X_{sig}(t, \theta) , \tag{3.11}$$

where the definition of the optical quadratures of the input signal X_{sig}, P_{sig} have been used. This shows that the balanced homodyne setup is able to measure the weak signal in an arbitrary rotated quadrature basis $X(\theta)$ as given by the local oscillator phase θ, and that the signal is amplified according to the strength of the local oscillator. The balanced setup removes the influence of classical noise sources compared to using a single detector where not only would the weak signal be very challenging to detect, and thus noise in the measurement is given by the uncorrelated quantum shot-noise of the light.

Through repeated measurements for a set of known θ, the homodyne measurement provides a means for tomography of the quantum state.

3.7.2 *Heterodyne detection*

When instead of using a local oscillator at the same frequency as the signal of interest, but at some detuning $\omega_{\text{het}} = \omega_{\text{sig}} - \omega_{\text{LO}} \neq 0$, the detection scheme is called heterodyne detection. In principle, this can be thought of as a homodyne detection setup where the measurement basis rotates at a speed ω_{het}, simultaneously measuring two field quadratures.

In the quantum optics theory framework, heterodyne detection projects the input optical state $\hat{\rho}$ entering the detector onto the local oscillator coherent state $|\alpha\rangle$. An outcome $\alpha = X_{\text{opt}} + iP_{\text{opt}}$ occurs with probability proportional to $\text{Tr}(|\alpha\rangle\langle\alpha|\hat{\rho}) = \langle\alpha|\hat{\rho}|\alpha\rangle$. This is proportional to the definition of the Husimi-Q function

$$Q(\alpha) = \frac{1}{2\pi} \langle\alpha|\hat{\rho}|\alpha\rangle \;, \tag{3.12}$$

which means that heterodyne detection measures the real-valued and non-negative Q function of the optical state $\hat{\rho}$ up to a proportionality factor. The Husimi Q function is a smoothened representation of the state's Wigner function due to the added vacuum noise from simultaneously measuring both optical quadratures [179]. In contrast, a homodyne setup projects the state onto a single chosen quadrature, and can thus measure the Wigner function of the state given a detection setup with unity efficiency.

The Wigner quasiprobability function fully describes the quantum state in phase space, and the expectation value of any observable can be computed from it. The Q function is equivalent to the Wigner function convolved with with a two-dimensional Gaussian representing the vacuum noise, and also provides a powerful tool to represent states and compute statistics. A more detailed description of the different distributions and what it means for the computed probability marginals, see Appendix B.

Backscattering control in microresonators
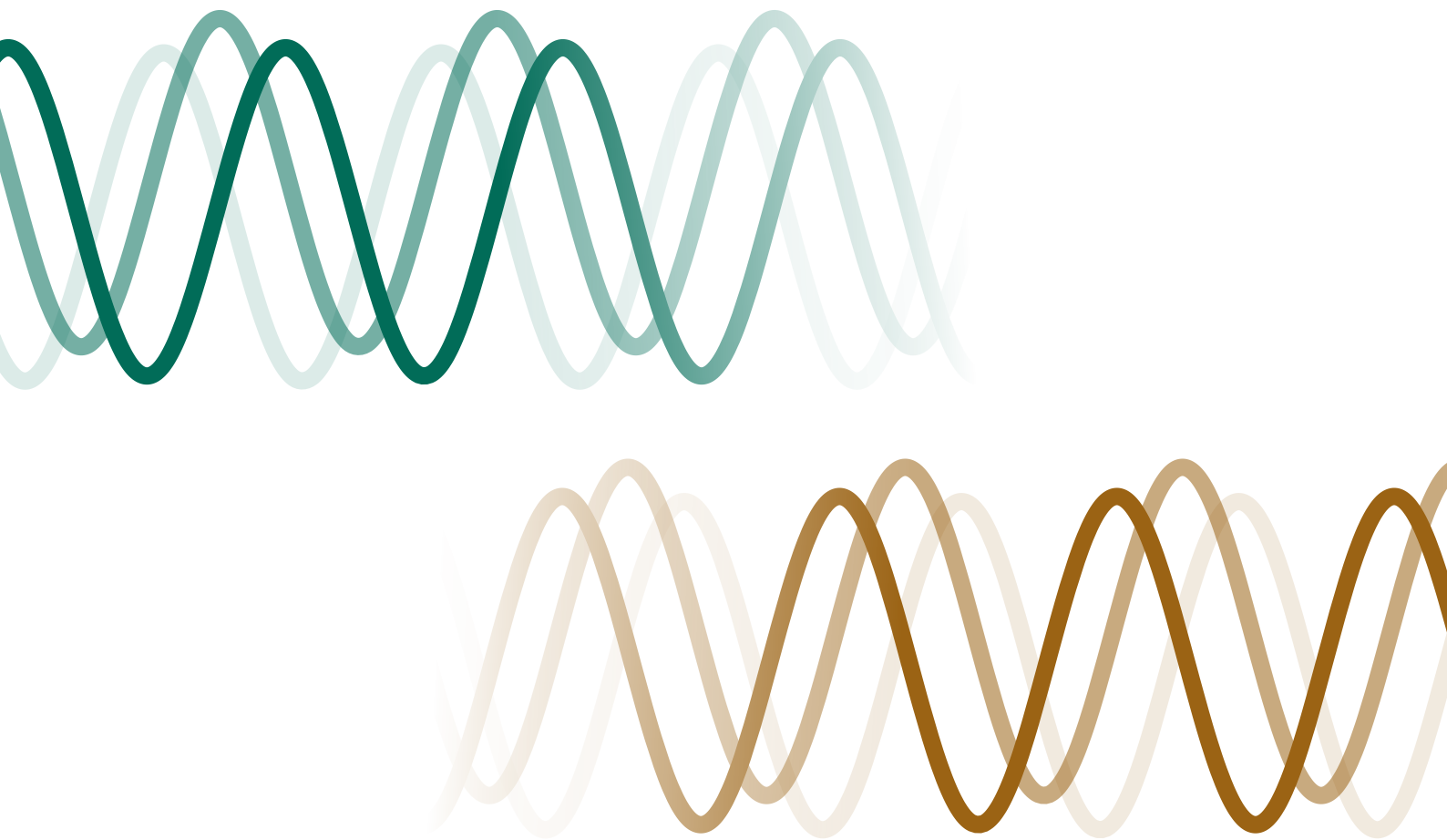
CHAPTER 4

Coherent backscattering control using a near-field probe

As light propagates in a waveguide, a fraction of the field can be reflected quasi-elastically by scatterers smaller than the wavelength of the light, known as Rayleigh scatterers. Given the name of these scatterers, it comes as no surprise that the omnipresent baron was involved in the early days of describing this form of scattering.

In the late 1860s, the colour and polarisation of light from the sky was a hot and unexplained topic. Scientist John Tyndall noted that *these questions constitute, in the opinion of our most eminent authorities, the two great standing enigmas of meteorology* [as quoted in 180]. As a young scientist at Cambridge in 1871, the same year as he got married, Rayleigh went on to essentially solve not one but both of these meteorological enigmas. Rayleigh did so by working through the maths of density variations in the elastic-solid "luminiferous aether" [181] that he and many colleagues at the time believed existed. It was ten years later that Rayleigh applied his calculations to variations in the electric permittivity following Maxwell's electromagnetic theory [182], arriving at the same conclusions, one of which was that the intensity of light scattered off sub-wavelength particles is inversely proportional to the incident light's wavelength to the fourth power. This relation explained the blue hue of the sky, as the smaller wavelength of blue light scatters at a much higher rate than larger-wavelength red light, diffusing more of the blue light over the sky making it appear blue. For a longer history lesson on Rayleigh's contributions to what we know about scattering of light see Young [180], or for a more comprehensive review see Twersky [183].

Back to optical waveguides: Rayleigh scattering can be problematic for various reasons. In optical whispering-gallery-mode microresonators, sub-wavelength imperfections and defects in the surface or bulk material act as Rayleigh scatterers, causing losses and reflections. When pumping the resonator in one direction, the scatterers cause some level of scattering from the pump direction to the opposite-direction WGM, referred to as backscattering. Controlling the amount of backscattering as a tuneable parameter can be useful for several types of microresonator-based experiments and applications, and in particular minimising backscattering is important for some applications like optical gyroscopes.

Optical WGM resonators were not something Rayleigh got to see in his lifetime, and he probably did not contemplate the effect of scattering in them or think about their near fields. When Rayleigh considered the problem of scattering, the experiments available to him were only those studying the far field – the field far away from the scatterer relative to the wavelength. Such far-field experiments could for instance be measurements of the polarisation of light passing through a vapour cloud, but studying the field around a single

scatterer in the vapour was unattainable to Rayleigh. With the significant advances in nanofabrication and detection techniques over the last three or so decades, experiments studying optical near fields have proliferated,[i] including those of whispering-gallery-mode resonators. The microresonators' near field is what couple them to their surroundings, making it possible to couple in light through for instance a tapered fibre, but this coupling can also be used to manipulate the properties of the WGM modes.

In this chapter, it is demonstrated that the controlled introduction of a Rayleigh scatterer into the near field of a high-quality-factor microresonator can coherently suppress the amount of backscattering in the microresonator by at least 34 dB. The method relies on controlling the scatterer's position such that the intrinsic and scatterer-induced backpropagating fields destructively interfere. This technique is useful in microresonator applications where backscattering is currently limiting the performance of devices, for instance ring-laser gyroscopes and dual frequency combs, which both suffer from injection locking. Moreover, these findings are of interest for integrated photonic circuits in which back reflections could negatively impact the stability of laser sources or other components.

This chapter is an adapted and expanded version of the main text and supplementary information of the publication Svela *et al.* [58]. The work has been presented by the author at several conferences with published abstracts [185–187]. The experimental work was carried out in Dr Pascal Del'Haye's group in the Time and Frequency department of the National Physical Laboratory in Teddington, UK. From the initial idea stage to the final publication, this research project was driven by the author of this thesis, with important contributions from the coauthors. This included device fabrication of microresonators and tapered fibres with S. Zhang, fabrication of tungsten tips, building and modifying the experimental setup with J. Silver and L. Del Bino, performing the measurements,[ii] and the data analysis. The theoretical model was developed by J. Silver with support from the author.

[i] Particularly the subject of nanoplasmonics [184], where electronic oscillations at the surface of metal nanoparticles are excited by optical fields, has received a lot of attention. The metal nanoparticles confine the electrical fields to volumes the size a fraction of a wavelength cubed. These surface plasmons have a multitude of applications, for example can they provide orders of magnitude sensing enhancements when coupled to WGM resonators [8].

[ii] In the process of the experimental work, the author developed an open-source Python package for *Keysight InfiniiVision* oscilloscopes – available under the name *keyoscacquire* on PyPi and Github [188] with a comprehensive documentation – which at the time of writing is downloaded >50 per month.

4.1   BACKGROUND, MOTIVATION AND PRINCIPLE FOR BACKSCATTERING CONTROL

Low optical losses is generally desirable for WGM resonators, for instance because the long photon lifetime gives a large intracavity buildup or because the field can interact over a larger number of oscillation periods. As outlined in Section 2.4, there are three main loss mechanisms for WGM resonators (typically ascending order of contribution): (i) radiative losses due to the curved surface guiding the light; (ii) bulk material scattering and absorption; and (iii) surface scattering or absorption due to surface roughness, material deposited on the surface during or after fabrication. Typically, low-loss resonators are sought, but low losses alone might not be sufficient for applications; it might also be crucial where the lost light travels.

The losses related to sub-wavelength imperfections in the surface or bulk material of the resonator can cause light to quasi-elastically Rayleigh scatter into non-propagating modes, to the environment, or to be reflected into the frequency- and polarisation-degenerate, counterpropagating mode. The latter of these categories are what is referred to as *backscattering*. These imperfections are typically distributed around the cavity, but for low scattering, as the coherence length of the circulating field is much longer than the cavity round-trip length, the imperfections scattering light into the counterpropagating mode can be approximated as a single scatterer, scattering light with a specific amplitude at a specific point along the cavity circumference (or equivalently with a specific phase in relation to the pump field) into the counterpropagating mode [189–191]. This coherent scattering effectively couples the two modes, causing light to build up in the counterpropagating mode [108].

backscattering

mode splitting

When the two counterpropagating, travelling-wave modes are coupled by scattering, the frequency degeneracy between the modes can be lifted, resulting in modes with different central frequencies and/or losses. For high levels of backscattering, this *mode splitting* may be spectrally resolvable, i.e., detected as two separate resonances as shown in Fig. 4.1. This was first observed in WGM resonators by Weiss *et al.* [56].

If the system of all scatterers breaks the mirror symmetry by unequal scattering amplitude for the two directions and introduce loss, this results in eigenmodes that are superpositions of unequal weight of the two travelling-wave modes [112, 192, 193],

$$E_\pm = aE_{\mathrm{cw}} \pm bE_{\mathrm{ccw}}, \tag{4.1}$$

where a and b are complex coefficients and the clockwise and counterclockwise travelling waves are E_{cw} and E_{ccw}, respectively. As, in general, $|a| \neq |b|$, the superposition modes $E_\pm$ modes are not standing waves, but non-orthogonal, chiral modes. By manipulating the scatterer, the coupling and thus the mode structure can change.

Backscattered light in WGM resonators can limit the performance of applications, for example by causing unwanted injection locking in laser gyroscopes operating at low rotational speeds [194–198], or in dual frequency combs [199, 200], as well as causing instabilities for frequency combs [201]. Backscattering also reduces the nonlinear enhancement

Figure 4.1. Illustrations of transmission spectra of mode split resonances. The examples have different combinations of splittings f_{s} and linewidths κ_1, κ_2.

and contributes to back-reflections in devices relying on symmetry breaking of counterpropagating fields [16] for sensing [202–204], optical logic [205], memory [206] or isolation/circulation [207] applications. Furthermore, control over backscattering permits tuning of the standing wave pattern to maximise coupling by moving an anti-node of the standing wave along the resonator perimeter, which can be beneficial for systems relying on evanescent coupling, such as evanescent optomechanics [208], or biomedical near-field sensors [8, 209]. In addition, telecom applications of WGM resonators [50, 210] or applications where WGM resonators are used in quantum state preparation can benefit from lower backscattering levels to ensure high fidelity [211].

In this chapter, an unprecedented ≥34 dB suppression of the backscattered light from a WGM resonator is shown, where the suppression figure is limited by the detection noise level. The suppression is achieved by manipulating the position of a sub-wavelength-size scatterer within the near field of a cavity mode, coherently controlling the effective backscattering. The effect is demonstrated in three silica rod microresonators with low intrinsic backscattering, meaning neither resonator shows resolved frequency mode splitting before the technique is applied.

4.1.1   *Existing literature on backscattering control*

Experimental work in the literature related to backscattering in WGM optical resonators has previously focussed on controlling and changing backscattering in resonators with relatively high intrinsic backscattering rates, tuning the resulting mode splitting with a near-field scatterer [112, 113, 212] or tuning chirality for light flow control [116, 117], without investigating backscattering suppression specifically. Monitoring backscattering as a sensing method has also been shown [118]. Now, the backscattering problem is attracting more interest in the community, with a recent publication showing suppression from resolved to unresolved mode splitting using a Brillouin-optomechanical method [57].[iii]

BRILLOUIN METHOD. Kim *et al.* [57] suppress backscattering by exploiting a Brillouin cavity mode-trio as explained in Section 5.3 (see in particular Fig. 5.7). The suppression is caused by breaking time-reversal symmetry[iv] for the two counterpropagating optical modes by optomechanically coupling the optical mode that is not of interest, say the CCW mode, to its Stokes mode through optically pumping on the Stokes mode. The hybridisation of the mechanical mode and the CCW mode effectively reduces the density of states of the CCW mode at its unperturbed frequency, resulting in a weaker backscattering coupling between the CW and CCW modes. Hence the backscattering from the CW mode of interest into the CCW mode is reduced.

This Brillouin-based method is elegant and can in principle be used for any resonator of any dielectric material, and with the convenience of simply turning on a pump. However, to use this technique, a number of relatively challenging experimental requirements must be satisfied. Firstly, a suitable mode-trio obeying Brillouin phase-matching conditions for momentum and energy conservation (see Section 5.3.1), in addition to a sufficient spatial mode overlap, must be identified, which in itself can be an experimental challenge.

[iii] Note also the recent publication on backscattering suppression in free-space ring resonators by polarisation engineering [213].

[iv] Two years prior to Kim *et al.*'s work, Miri *et al.* [214] had theoretically investigated optomechanical time-reversal symmetry breaking for introducing controlled chirality in different optomechanical systems. Optical circulation [215] and isolation [216] via radiation pressure optomechanics in WGM resonators had also been demonstrated prior.

Furthermore, this mode trio must also obey whatever other requirements the experimenter might need for a certain application, limiting the chances of finding a suitable mode-trio further. In addition comes the requirement for an extra pump frequency, which might have undesirable implications, such as thermal effects, interference, experimental complications for readout, et cetera.

When a suitable mode-trio has been identified, the suppression bandwidth and parameter coupling must be considered. As the bandwidth of suppression is set by the linewidth of the mechanical resonance, and the Brillouin linewidth is usually smaller than the optical linewidth even for high-Q resonators, the backscattering is suppressed only in a narrow band of the optical resonance. This might not be desirable, but there are also other implications: as the total optomechanical detuning of the mechanical and optical modes is optical-power dependent, the offset of where within the optical resonance bandwidth the suppression occurs will be linked to the optical power, and furthermore, so will also the optomechanical coupling strength, which effectively controls the amount of suppression achieved. This coupling of parameters can potentially be challenging to work with as for instance by increasing the pump to achieve a larger suppression from increased optomechanical coupling, the suppression decreases because the optomechanical detuning increases, and the suppression band moves.

The maximum suppression achieved by Kim *et al.* [57] is not explicitly given, but it can be estimated from the reduction in the measured reflection or from the theoretical model to approximately 13 dB and 7 dB for the two separate mode trios used. Plotting the theoretical suppression as a function of optomechanical coupling for the parameters of mode-trio of used in the highest suppression case, Fig. 4.2 shows that the optomechanical coupling would need to be increased by an order of magnitude to achieve a suppression similar to the one presented in this chapter. This higher coupling might not be unattainable in itself, but because of the strong thermal effect in the silica resonator, increasing the pump power to reach the sufficient optomechanical coupling would significantly change the optomechanical detuning, severely decreasing the suppression gain expected from the increased coupling. The method by Kim *et al.* can prove useful for some applications, but other methods that do not suffer from the complications outlined in the above give increased flexibility and should be explored.

MODE MANIPULATION LITERATURE. Other publications related to backscattering control in WGM resonators have explored the use of near-field probes for manipulation of the coupling between the counterpropagating modes. In the group of V. Sandoghdar, Götzinger *et al.* [217] first studied the effect sharp tip scatterers within the near field of a WGM resonator. In 2007, the group demonstrated control of mode splitting and linewidths using a single silica-tip near-field probe, studying the transmitted field as well as the field coupling to the fibre tip scatterer [112], but the backscattering was not studied.

The group of L. Yang at Washington University at St. Louis has worked on light flow manipulation in WGM resonators for more than a decade. In 2010, the group demonstrated mode-coupling control using two silica tip near-field scatterers [113], although not studying
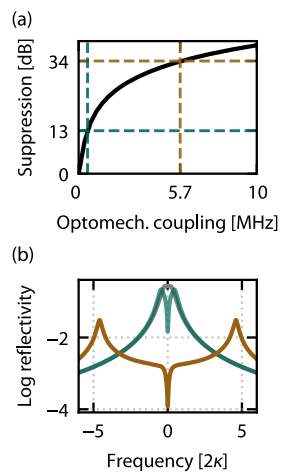
Figure 4.2. Performance of the Brillouin backscattering suppression method in Kim *et al.* [209]. (a) Theoretical suppression as a function of optomechanical coupling (black) for the mode trio used, assuming zero optomechanical detuning. Green dashed lines indicate the maximum coupling and suppression demonstrated in [209] (0.5 MHz, 13 dB), golden dashed lines indicate the necessary coupling to achieve the suppression as demonstrated here (5.8 MHz, 34 dB). (b) The logarithm of the reflection coefficient across the resonance at zero optomechanical coupling (grey), at the maximum coupling achieved in [209] (green), and for the coupling needed to achieve 34 dB suppression (golden).

the backscattering explicitly. The two scatterers tuned the resonator close to an exceptional point [218], which is briefly explained in the following. For a WGM resonator with no coupling between optical modes, for a given resonance frequency there are two perfectly frequency-degenerate optical modes, one for each direction of travel, i.e., the energy levels are twofold degenerate, but the associated eigenstates are not the same; this is sometimes referred to as a diabolic point [219]; however, by manipulation of the coupling and losses of the two optical modes, they can be brought to an exceptional point, which is when also the eigenstates coalesce, thus the system has only one direction of propagation, i.e., there can be no backscattering as light can only propagate in the forward direction.

This chiral symmetry breaking, where only one propagation direction is sustained can be used to suppress backscattering, similarly to how the optomechanical time-reversal symmetry breaking of Kim *et al.* [57] prohibits the propagation in the backwards direction. In 2016, the L. Yang group demonstrated that tuning a doped, lasing WGM resonator to an exceptional point using two silica tips, they could control its emission direction [116]. In 2020, the same group demonstrated that by tuning a passive WGM to an exceptional point using a nanoscatterer and coupling it to another WGM, the equivalent of what in the atomic physics community [220] is called electromagnetically induced transparency (EIT) can occur [117]. The broad definition of an EIT is a medium becoming transparent over a narrow spectral window within a wide absorption spectrum background – for a microresonator this would mean its transmission increases within a narrow band of a resonance – due to destructive interference between excitation pathways. The narrow transparency window gives a sharp phase change, which is equivalent to a large dispersion of the light within the narrow band, resulting in a small group velocity causing what is known as slow light [221].[3] When tuning the resonator to the exceptional point, the chiral symmetry between the pair of counterpropagating modes breaks, allowing only one propagation direction in that resonator. The chiral asymmetry is used by Wang *et al.* [117] to create a loop coupling between the two resonators, where the phase difference between the pump light coupled in from the taper and that making a loop-roundtrip can interfere destructively resulting in a transparency window of width given by the coupling rates. All of this to say, they successfully control the amount of backscattering in the resonator using nanotips, but there is no discussion on the achieved backscattering suppression.

---

[3]The optomechanical equivalent of EIT, called optomechanically induced transparency or OMIT, was first demonstrated by Weis *et al.* [222] and later shown to slow down light [223]. It can be achieved by pumping on the red side at a detuning equal to the mechanical frequency: a probe swept over the resonance will have a transparency window of width given by the mechanical linewidth at the mechanical frequency as photons are scattered from the pump into the probed resonance.

WAVEGUIDE RING RESONATORS. Also in WGM resonators' close cousin, waveguide ring resonators [133], modal coupling due to intrinsic scatterers also occurs [189, 224] and backscattering suppression is sought. Waveguide ring resonators are typically lithography-based micron-size structures on chips, making them attractive for compact, commercial applications. Previously, waveguide ring resonators would typically be made of silicon on insulator chips, not achieving similarly high Q factors as WGM resonators; however, development in fabrication techniques and the use of materials such as silicon nitride [225] and others [86] have changed this, and waveguide ring resonators are now on par with WGM resonators in terms of achieved Q factors. Backscattering is typically higher than in WGM resonators due to relatively higher surface roughness and other imperfections, which is affecting the performance of several types of ring-resonator applications [226–228]. In 2013, an extra-cavity interference technique, where the transmitted and reflected output of a waveguide ring resonator are combined on a beamsplitter with tuneable phase difference between them, was shown to selectively choose to transmit only one of the superposition modes, $E_{\pm}$ [229]. However, the intracavity backscattering is not directly cancelled with this technique, but rather masked to avoid a split resonance in the output spectrum. Furthermore, the linewidth of the selected superposition mode is generally broader than the intrinsic, unsplit linewidth. The method also results in significantly reduced output optical power and would not be suitable for high-Q WGM resonators due to the relatively low backscattering rates found in these resonators.

A more recent demonstration from 2017 showed suppression of backscattering in a waveguide resonator using a more similar method to the one presented in this chapter: Li and Bogaerts [230] introduced a tuneable reflector inside a silicon ring resonator to destructively interfere the intrinsic backscattering by controlling the reflector-induced backscattering. The intracavity reflector used is a tuneable Mach–Zehnder interferometer with a loop at one end, giving a controllable reflector. The maximum suppression demonstrated with this technique is approximately 10 dB, and with this suppression the authors recover unsplit modes of the resonator, bringing all the optical modes simultaneously back to the unsplit regime. There are some technical disadvantages with the method such as the increased complexity in fabrication (multiple lithography steps and materials) and operation (electrical drive), and that the Mach–Zehnder effectively increasing the resonator length by at least about 25 %, which increases losses and decreases the free spectral range, which is often undesirable as it decreases the finesse of the cavity. However, nanofabrication techniques and the state-of-the-art silicon-on-insulator resonators have improved since Li and Bogaerts carried out their work, and the integrated, on-chip method is convenient for suppression backscattering in waveguide ring resonators in the split to non-split regime.
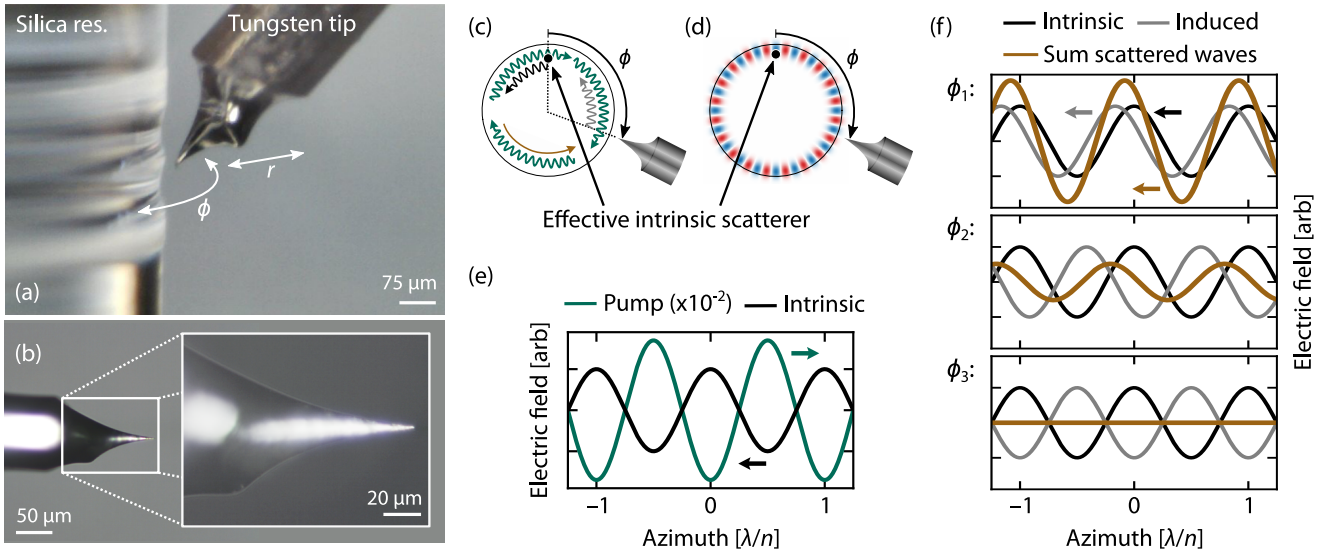
Figure 4.3. Principle for backscattering control using a near-field scatterer. (a–b) Micrographs of the microresonator and tungsten tip with the axes of tip movement annotated. (c) Cartoon of the propagation directions of the fields and scatterers. The green pump field circulates in the cavity, scattering off the effective intrinsic scatterer (black dot) and the near-field scatterer (tip), resulting in the scattered waves in black and grey, respectively. With an appropriate azimuthal position of the near-field scatterer, ϕ, the intrinsic and induced scattering destructively interfere (golden). (d) Illustration of the phase of the pump field around the cavity (cavity size and wavelengths not to scale). (e) Illustration of wave profiles along the azimuth when the tip scatterer is far away from the cavity, showing the counterclockwise-propagating backscattered waves due to the clockwise-propagating pump field. The backscattered field amplitudes are small compared to the pump as only a small fraction of the light is backscattered. (f) Wave profiles for the backscattered waves when the tip is *critically coupled* (equal amplitudes for intrinsic and induced backscattered waves) for different near-field scatterer positions ϕ_i. The different azimuthal positions correspond to phase offsets between the effective intrinsic scatterer and the induced scatterer $(2m + q)\pi$ for an integer m and $q = 1/3, 5/6, 1$, respectively, showing both constructive and destructive interference between the waves. The tip position ϕ_3 gives full backscattering suppression.

THIS WORK. The method presented in this chapter contrasts the methods described in the above, using a single near-field probe to control the backscattering in a WGM resonator. The method expands the toolbox for backscattering control and suppression, focussing on suppressing backscattering beyond recovery of unsplit modes. Unprecedented suppression levels are shown, limited by optical detector noise. The present implementation of the technique does require delicate fine positioning of a near-field scatterer, but it does not suffer from many of the complications and limitations other methods mentioned in the above are associated with, representing an alternative to other methods available.

4.1.2   *Principle for backscattering suppression via a near-field probe*

To control the backscattering in the WGM resonator, a sub-wavelength-size tungsten tip is positioned in the near field of the resonator [Fig. 4.3(a,b)]. The technique is based on interference, where the tip is coherently scattering light from the pumped optical mode into the counterpropagating mode [Fig. 4.3(c)], leading to interference between the intrinsic backscattering and that caused by the tip [192]. With sufficient induced backscattering and an appropriate phase offset between the intrinsic and induced backscatter, the net backscattering can be made to vanish.

The amplitude and phase of the induced backscattering can be controlled by the tip's position: the radial position of the tip, r, controls how strongly the tip couples the two propagation directions and thus the induced backscattering amplitude, whereas the azimuthal position, ϕ, governs the phase offset between the intrinsic and induced backscatter [Fig. 4.3(d)]. Thus, the tip position can coherently control the net backscattered field [Fig. 4.3(f)]. The situation when the tip is inducing backscattering of equal magnitude to the intrinsic backscattering is called *critical tip coupling*. As long the tip scatters sufficiently for critical tip coupling to occur, the method can be used for complete suppression of backscattering. By choosing the tip position, the backscattering can also be increased beyond the intrinsic backscattering level.

critical tip coupling

The presence of the tip will cause increased optical losses for the mode of interest, as the tip scatters also to free-space modes and other non-propagating modes in the resonator; however, for a small tip size, the reduction in the optical quality factor is relatively small, as is shown here and in Refs. 112, 217, 231.

The method presented in this chapter enables full control of the amplitude and phase of the backscattering in a microresonator, and it is shown experimentally that the total backscattering can be reduced by orders of magnitude below the unresolved frequency splitting level, whilst the optical quality factor is reduced by less than one order of magnitude.

4.2   THE NEAR-FIELD DECAY AND TIP-INFLUENCE ON THE OPTICAL LINEWIDTH

In this work, the interest is primarily to control the backscattering in the resonator; however, not only the backscattering changes when the probe is placed within the near field. Understanding the effect of the tip on the whispering-gallery modes, including their linewidth, will be important for interpreting the experimental data. This section presents a model for the WGM linewidth as a function of the tip-position. In short, given a linear coupling between the evanescent WGM near field and the tip, the linewidth of the WGM is expected to increase proportionally to the energy density in the near field at the tip position as the tip is moved closer to the resonator surface due to scattering and absorption.

SCATTERING AND ABSORPTION. When a light field is incident on a particle small compared to the wavelength, charges in the particle will to some extent be accelerated into oscillatory movement due to the electromagnetic oscillations that are the field. The accelerated charges reradiate some of this energy captured from the field into all spatial directions, called scattering. Many textbooks are devoted to describing light scattering, see for instance Refs. 232–235. Some of the energy that accelerates the charges is not reradiated but converted into other forms energy, for example via damping mechanisms of the movement of the charges to thermal energy. This non-reradiated energy is referred to as absorbed light.

How much of the incident light that is absorbed and scattered is dependent on the electric permittivity contrast of the particle compared to the surroundings, the shape and size of the particle. An experimental observable is often used to describe how much of

the incident light a scatterer removes from an incident beam: for a known intensity of incident light, power per area, the power detected on the shadow side of the particle can be measured, whose ratio with the incident intensity is called an *extinction cross section* – an area corresponding to the area of the beam that was effectively removed by the particle. The extinction cross section can be several times larger than the geometric cross section of the particle, this dimensionless ratio of the extinction to geometric cross section is often referred to as the extinction efficiency factor. The extinction cross section can be split into an absorption cross section and a scattering cross section, denoting the areas corresponding to the absorbed power and scattered power, respectively.

extinction cross section

The process of scattering can change both the direction and the wavelength of the light. Scattering due to small particles is responsible for a range of everyday phenomena, from the rainbow to zodiacal light. In the context of this work, the tip represents an element that will both absorb light from the near field and also scatter light into other propagation directions. Similarly to how intrinsic scatterers in the resonator cause optical losses due to scattering into modes that for the purpose of the experiment are considered losses – like non-propagating modes in the resonator structure and free-space modes, sometimes referred to as reservoir modes – also the tip will scatter into these lossy modes. Thus, the tip will contribute to increasing the losses both via absorption and scattering in the near-field.

NEAR-FIELD SCATTERS AND WGMS IN THE LITERATURE. The near field distribution of WGM resonators is well understood from analytical theory, numerical finite-element simulations, and experiments. Studies have also contributed to the understanding of the influence of scatters within the near field of WGM resonators. These studies are often presented in the context of sensing [e.g. 115, 118, 236–239], but also for other purposes such as optomechanical systems with dielectric beams near-field-coupled to WGMs [240, 241]; optoplasmonical systems with metal nanoparticles coupled to WGMs [242–246]; or for the inverse of sensing, namely deliberately manipulating properties of WGMs using near-field probes [112, 113, 116, 117, 217]. The work presented in this chapter falls into the latter category.

[v] In the following, assumptions made are explicitly stated in the spirit of Bohren and Huffman [232]: "Unfortunately, as so often happens in physics, each successive author in a chain extending from the source of a theory tends to omit more of the fine print underlying its validity."

When considering scattering and absorption of a probe, the size and material type of the probe is essential. When the probe is a dielectric particle smaller than the wavelength, Rayleigh's scattering theory where the scatterer is treated as a single dipole that is in equilibrium with an external field at any instant of time, is in general valid provided that the field intensity is uniform over the scatterer.[v] And as electrodynamics need not be considered under this approximation, this regime is sometimes called the *quasi-static approximation* [8, 247]. However, if the dielectric scatterer is large compared to the wavelength, (Lorentz–)Mie[vi] scattering theory should be used as the resonances in the scatterer itself should be taken into consideration, see for instance the reviews by Fan *et al.* [247] or Tzarouchis and Sihvola [248].

quasi-static approximation

[vi] Many scientists made important contributions to scattering theory, resulting in somewhat arbitrary and inconsistent naming by different authors. Bohren and Huffman [232] wrote the following about Rayleigh–Gans theory: "Any day now we can expect scholars to announce that the theory has been found scribbled in the margins of one of Gauss's unpublished manuscripts; or in the notebooks of Leonardo; or implicit in the writings of Aristotle; or painted in brilliant colors on the walls of a French cave by Paleolithic men."

For metal scatterers, however, the conductive nature can make the Rayleigh-scatterer model insufficient also for scatterers small compared to the wavelength. When a metal scatterer becomes sufficiently small so that the penetration depth of the electrical field is

comparable to its size, but larger than the distance an electron moves within an optical oscillation, electronic oscillations of conduction electrons at the surface of the scatterer can be excited by the optical incident field. These electronic resonances are called *localised surface plasmon resonances*, and the field of study is referred to as nanoplasmonics [184]. The size range of metallic particles for which nanoplasmonic phenomena can be observed is typically in the 2 nm to 20 nm range. Localised surface plasmons can be described with a Drude model of metals and Lorentz–Mie theory for the small-sphere resonance, and for instance the aforementioned reviews [247, 248] and Kolwas *et al.* [249] give introductions to localised surface plasmons and scattering.

localised surface plasmon resonances

When plasmonic nanoparticles are put close to a wgm, they can couple strongly to the resonator, leading to hybridised wgm-plasmonic modes. Doeleman [250] provides an instructive introduction to such hybridised modes, or see recent reviews of *optoplasmonic systems* [251] and wgm-optoplasmonic systems in particular [242]. Foreman and Vollmer [252] show that a silver nanoparticle will not only induce a larger wavelength shift than a silica nanoparticle of the same size due to the higher relative electric permittivity of silver, but the silver particle will also more easily induce frequency splitting, as plasmonic resonances hybridise with the optical modes. Experimental demonstrations have shown that depending on the size and pitch of an array of gold nanoparticles, the optical linewidth of a wgm resonator can broaden or narrow when it couples to the array [244], and that by tuning the azimutal offset between two nanoparticles, the resonance frequency and linewidth of the hybridised modes can be tuned [243]. Due to the very strong confinement of the electric field, plasmonic particles coupled to wgm resonators can act as high-efficiency optical antennas for increased coupling to for instance a quantum emitter [245, 246], or conversely, can provide electric field "hot spots," which can give orders of magnitude enhancements in near-field-sensing applications [8, 253].

optoplasmonic systems

Aside from the plasmonic literature, studies on the influence on a wgm of a scatterer in the near field typically use dielectric Rayleigh scatterers. Many of these studies use wgm resonators for sensing applications, particularly *biosensing*; early work in this field include an experimental demonstration of protein [114, 254], bacteria [255], and single-virus [40] detection, and theoretical work describing the resonance frequency shift and broadening by an arbitrarily shaped dielectric scatterer in the near field [256]. The reviews by Kim *et al.* [209] or Yu *et al.* [7], or the recent textbook by Vollmer and Yu [8] cover wgm-based biosensing in detail.

biosensing

KEY ASSUMPTIONS OF THIS WORK. Similarly to the majority of biosensing literature, the size of the near-field-probe tip in the work presented in this chapter is assumed be to sufficiently small compared to the wavelength for the Rayleigh/quasi-static approximation to be used. However, in contrast to most of the sensing and wgm manipulation literature listed so far, a metal tungsten tip is used in this work rather than a dielectric probe.

A metal tip is chosen not only for its relatively easy and reproducible fabrication, but also because metals generally scatter more effectively than dielectrics in air, and to maximise the scattering to absorption ratio: The scattering cross section is typically much

larger than the absorption cross section for metal particles of a diameter of $\gtrsim$100 nm [257]. The effect of a metal perturbation in the near-field is stronger than a dielectric as the contrast in the permittivity between the metal tip and the environment it displaces – air in this case – is larger since the permittivity of a metal like tungsten is orders of magnitude larger than a dielectric. Calculations by Foreman and Vollmer [252] on the influence of a silver nanoparticle on a WGM resonance give similar results when treating the silver particle as a dielectric with complex permittivity within the Rayleigh regime compared to a more fundamental Mie-theory approach considering the metallic nature of the particle.

As the tip diameter used in this work is >50 nm, plasmonic resonances are assumed to be negligible.[vii] Furthermore, Bohren and Huffman [232] note that surface charges affect the effective scattering and absorption cross sections only slightly for metallic particles that are small compared to the wavelength. Hence, the tip in this work is assumed to act as a single dipole scatterer making the theory of dipole scatterers in the Rayleigh regime available for use.

In the following, the WGM near-field decay is recapitulated, before the absorption and scattering losses in the WGM induced by the tip depending on its position in relation to the resonator surface will be explored. The purpose of the section is not to numerically predict the exact optical linewidth broadening due to the tip, but to understand the functional relationship between tip position and broadening. The section concludes with an expression for the optical linewidth's dependence on the distance between the tip and the resonator surface.

4.2.1   Whispering-gallery-mode near-field decay

The evanescent electric field from a waveguide decays exponentially with respect to the perpendicular distance from the surface – i.e., for a WGM resonator, the radial distance from the surface, r. As previously stated in Eqs. (2.26) and (2.27), the evanescent near field for a WGM can be expressed

$$E_{\mathrm{NF}}(r) = E_{\mathrm{surf}} \exp\left[-\alpha_{\mathrm{NF}}(r - r_0)\right] , \qquad (4.2)$$

where E_{surf} is the field strength at the surface (r_0), and the decay length is

$$\alpha_{\mathrm{NF}}^{-1} = \frac{\lambda}{2\pi\sqrt{n^2 - 1}} , \qquad (4.3)$$

for a field of vacuum wavelength λ in a resonator with refractive index n surrounded by air. Note that the evanescent field energy density is proportional to the squared magnitude of the field, $|E_{\mathrm{NF}}(r)|^2 \propto \exp[-2\alpha_{\mathrm{NF}}(r - r_0)]$, which means that

$$(2\alpha_{\mathrm{NF}})^{-1} \equiv d_{\mathrm{NF}} = 118.4\,\mathrm{nm} \qquad (4.4)$$

is the penetration depth into the surroundings of the optical energy density in the near field of a silica ($n = 1.444$) resonator at $\lambda = 1550\,\mathrm{nm}$.

[vii] As far as the author is aware, there is currently no literature on localised surface plasmons in metallic tungsten, only in so-called quasi-metallic tungsten oxide nanocrystals [e.g. 258]. For optically excited plasmonic resonances to be significant, the bulk plasma frequency must usually be in the UV or blue part of the spectrum as the plasma frequency typically reduces for nanoparticles [257]. The plasma frequency of bulk tungsten is reported to be 26 THz [259], i.e., significantly below optical frequencies.
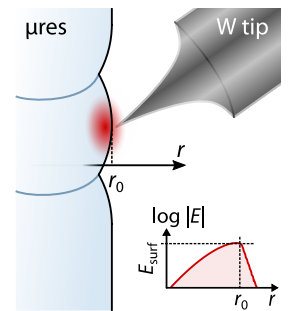
Figure 4.4. Cartoon of the near field decay from the resonator surface at r_0 and the tungsten tip.

4.2.2 *Tip-induced absorption losses*

When a probe is placed within the evanescent field of the WGM resonator, the probe can increase the rate of energy dissipation from a WGM by absorption. To calculate the increased absorption, an approach widely used in the biosensing literature for dipole scatterers called the *reactive sensing principle* can be used, which is based on theory originally developed for microwave cavities [260, 261]. The principle refers to the shift in the WGM resonance due to the change in the effective refractive index in the resonator's surroundings that probe represents: The relative frequency shift is the negative of the excess energy required to polarise the probe instead of the surrounding medium replaced by the probe, divided by the energy in the cavity [253].[viii] If the probe is metallic, the relative electric permittivity of the probe is a complex number[ix] where the imaginary part represents the Ohmic losses in the probe, and the increased losses from this absorption can be extracted from the imaginary part of the frequency shift [252].

reactive sensing principle

If the coupling between the probe and the resonator is weak – that is, the resulting shift in resonance frequency and linewidth is small – and the probe's size is smaller than the wavelength (quasi-static/Rayleigh approximation), a first-order perturbative approximation for the frequency shift of the resonance can be given: for a probe of relative electric permittivity ε_s, the relative shift from the complex unperturbed frequency

$$\Omega = \omega - i\kappa \,, \tag{4.7}$$

is given by [e.g. 8, 108, 240, 244, 256, 264, 265][x]

$$\frac{\Omega' - \Omega}{\Omega} \approx -\frac{1}{2} \frac{\int_{V_s} \mathbf{E}^*(\mathbf{r})(\varepsilon_s - \varepsilon_{env})\varepsilon_0 \mathbf{E}'(\mathbf{r}) \, d^3\mathbf{r}}{\int_V \varepsilon(\mathbf{r}) \, |\mathbf{E}(\mathbf{r})|^2 \, d^3\mathbf{r}} \,, \tag{4.8}$$

where $\Omega' = \omega' - i\kappa'$ are the perturbed frequency and linewidth, $\mathbf{E}(\mathbf{r})$ and $\mathbf{E}'(\mathbf{r})$ are the unperturbed and perturbed slowly varying WGM fields, V denotes all of space,[xi] V_s is the volume of the probe, and $\varepsilon(\mathbf{r})$ is the value of the electric permittivity at $\mathbf{r}$ without the probe present, i.e.,

$$\varepsilon(\mathbf{r}) = \begin{cases} \varepsilon_0 \varepsilon_{res} & \mathbf{r} \in \text{inside the resonator} \\ \varepsilon_0 \varepsilon_{env} & \mathbf{r} \in \text{outside the resonator} \end{cases} . \tag{4.9}$$

The integral in the denominator of Eq. (4.8) is constant for any probe shape or distance from the WGM, so for brevity let the energy stored in the unperturbed cavity field

$$\int_V \varepsilon(\mathbf{r}) \, |\mathbf{E}(\mathbf{r})|^2 \, d^3\mathbf{r} \equiv U_V \,. \tag{4.10}$$

To calculate the relative shifts in the real frequency and linewidth with respect to the real frequency, note that by the definition (4.7)

$$\frac{\Delta\Omega}{\Omega} = \frac{\omega' - \omega - i(\kappa' - \kappa)}{\omega - i\kappa} = \frac{-(\omega^2 + \kappa^2) + \omega'\omega + \kappa'\kappa}{\omega^2 + \kappa^2} + i\frac{\omega'\kappa - \kappa'\omega}{\omega^2 + \kappa^2} \,, \tag{4.11}$$

[viii] The reactive sensing principle was not derived from Maxwell's equations and Mie theory and has been criticised [262, 263], but it has later been shown that the principle does emerge from first principles considerations under the right approximations, see e.g. Deych and Shuvayev [264].

[ix] The complex dielectric function for metals

$$\varepsilon = \varepsilon_{Re} + i\varepsilon_{Im} \tag{4.5}$$

is related to the refractive index and the extinction coefficient (the latter often labelled κ but here K to avoid confusion with the optical linewidth) by [8]

$$\varepsilon = (n + iK)^2 \,. \tag{4.6}$$

[x] The listed references present different derivations of the result. Equation (4.8) is also used in the context of describing intrinsic scatterers, for instance in Srinivasan and Painter [266] and Borselli *et al.* [136].

[xi] When integrating over all of space the contributions from the whole WGM mode volume, both inside and outside the resonator material, is considered. Often, the approximation of only integrating over the volume in the resonator is made as this allows using a constant permittivity in the integral.

from which it follows that

$$\frac{\Delta\omega}{\omega} = +\mathrm{Re}\left(\frac{\Delta\Omega}{\Omega}\right) + \frac{\kappa}{\omega}\,\mathrm{Im}\left(\frac{\Delta\Omega}{\Omega}\right) \approx +\mathrm{Re}\left(\frac{\Delta\Omega}{\Omega}\right) , \qquad (4.12)$$

$$\frac{\Delta\kappa}{\omega} = -\mathrm{Im}\left(\frac{\Delta\Omega}{\Omega}\right) + \frac{\kappa}{\omega}\,\mathrm{Re}\left(\frac{\Delta\Omega}{\Omega}\right) \approx -\mathrm{Im}\left(\frac{\Delta\Omega}{\Omega}\right) , \qquad (4.13)$$

where the approximation can be made for high-Q resonators as the first factor will dominate because $\kappa/\omega = (2Q)^{-1}$. Thus, by calculating the shift in the complex resonance frequency, the change in the WGM losses due to the scatterer can be found by considering the imaginary part of the complex frequency shift. From Eq. (4.8) it can be seen that induced losses increase with a larger overlap between the scatterer and WGM mode volume, i.e., determined by the scatterer's geometric size relative to the mode volume and how close to the resonator surface the scatterer is. Numerical work [e.g. 252, 267] and experimental results [e.g. 112, 217] have shown how increasing size and increasing proximity results in increased broadening.

UNIFORM-FIELD APPROXIMATION. The probe is typically assumed to be small compared to the penetration depth of the WGM evanescent field into the surroundings, which means the field across the probe can be approximated uniform and constant, $\mathbf{E}_\mathrm{c}$. In the dipole approximation, the field within the probe is that of a dipole, which for a sphere in a uniform field is [232, 256, 257, 268, 269]

$$|\mathbf{E}(\mathbf{r} \in V_\mathrm{s})| = \frac{3\varepsilon_\mathrm{env}}{\varepsilon_\mathrm{s} + 2\varepsilon_\mathrm{env}}|\mathbf{E}_\mathrm{c}| . \qquad (4.14)$$

The proportionality constant between the field experienced by the dipole (local field) and the applied field is often called the *local-field correction factor* [269, 270]. Assuming the external field across the probe is equal to the unperturbed WGM field, the integral in the numerator of Eq. (4.8) then simplifies to

local-field correction factor

$$(\varepsilon_\mathrm{s} - \varepsilon_\mathrm{env})\varepsilon_0 \int_{V_\mathrm{s}} \mathbf{E}_\mathrm{c}^* \frac{3\varepsilon_\mathrm{env}}{\varepsilon_\mathrm{s} + 2\varepsilon_\mathrm{env}}\mathbf{E}_\mathrm{c}\, \mathrm{d}^3\mathbf{r} = \frac{3(\varepsilon_\mathrm{s} - \varepsilon_\mathrm{env})\varepsilon_0\varepsilon_\mathrm{env}}{\varepsilon_\mathrm{s} + 2\varepsilon_\mathrm{env}} V_\mathrm{s}|\mathbf{E}_\mathrm{c}|^2 , \qquad (4.15)$$

where the fraction is known from the Clausius–Mossotti relation as related to the *polarisability*[xii] of the perturbing element. For a sphere of radius ρ_s, the polarisability is defined [8, 232, 271]

$$\Upsilon_\mathrm{sphere} = 4\pi\rho_\mathrm{s}^3 \frac{\varepsilon_\mathrm{s} - \varepsilon_\mathrm{env}}{\varepsilon_\mathrm{s} + 2\varepsilon_\mathrm{env}}\varepsilon_0\varepsilon_\mathrm{env} , \qquad (4.17)$$

which means that Eq. (4.8) can be rewritten

$$\frac{\Delta\Omega}{\Omega} \approx -\frac{\Upsilon_\mathrm{sphere}}{2}\frac{|\mathbf{E}(\mathbf{r}_\mathrm{s})|^2}{U_V} \qquad (4.18)$$

when the probe is a sphere with radius $\rho_\mathrm{s} \ll \lambda$ at position $\mathbf{r}_\mathrm{s}$. If the probe is not a sphere, a tensorial treatment of the polarisability of the probe can be done to reflect a non-symmetric geometry, see e.g. Bohren and Huffman [232], Xu *et al.* [272], or the supplementary material

[xii] *Polarisability* expresses how easily an object is polarised in a uniform field – the proportionality constant between the total dipole moment (volume integral of the polarisation) and the applied field:

$$\mathbf{p} = \int \mathbf{P}(\mathbf{r})\mathrm{d}\mathbf{r}^3 \equiv \Upsilon\mathbf{E}_\mathrm{applied} . \qquad (4.16)$$

Note that here the polarisability includes the environment's permittivity, but some authors leave it out. The polarisability has units of $\mathrm{F/m} \cdot \mathrm{m}^3 = \mathrm{C/(Vm)} \cdot \mathrm{m}^3$.

of Baaske *et al.* [265].[4] Ruesink [273, Ch. 2] shows a detailed derivation of this expression including its approximations, limitations and a far-field correction term due to radiation seldom included in cavity perturbation analysis, and the backaction on the polarisability from the cavity has been investigated [274].

From the shift in the complex frequency, the relative WGM linewidth broadening can be found according to Eq. (4.13) by calculating the imaginary part of Eq. (4.18). Only the polarisability has a complex contribution due to the imaginary component of the electric permittivity of the scatterer material and therefore the relative broadening can be expressed

$$\frac{\Delta\kappa_{\text{abs}}}{\omega} \approx -\frac{\text{Im}(\Upsilon_{\text{sphere}})}{2}\frac{|\mathbf{E}(\mathbf{r}_{\text{s}})|^2}{U_V} .$$ (4.20)

Alternatively, the shift can also be expressed using the absorption cross section of the sphere, $\sigma_{\text{abs}} = n\omega\text{Im}(\Upsilon_{\text{sphere}})/(c\varepsilon_0)$ [232, 257], giving

$$\frac{\Delta\kappa_{\text{abs}}}{\omega} \approx -\frac{c\varepsilon_0\sigma_{\text{abs}}}{2n\omega}\frac{|\mathbf{E}(\mathbf{r}_{\text{s}})|^2}{U_V} .$$ (4.21)

In conclusion, under the uniform-field approximation for a spherical Rayleigh scatterer as outlined above, the relative broadening of the WGM related to absorption can be expressed

$$\frac{\Delta\kappa_{\text{abs}}}{\omega} \propto -\text{Im}(\Upsilon_{\text{sphere}})|\mathbf{E}(\mathbf{r}_{\text{s}})|^2$$ (4.22)

as a function of the scatter position $\mathbf{r}_{\text{s}}$, where the imaginary component of the polarisability comes from the imaginary component of the electric permittivity of the scatterer material; for tungsten $\varepsilon_{\text{W}} = -198 - 84\text{i}$ (<10 % uncertainty) [275]. As the broadening is proportional to the energy density of the near-field at the probe position, the near-field expression Eq. (4.2) can be inserted, giving

$$\Delta\kappa_{\text{abs}}(r_{\text{s}}) \propto \exp[-2\alpha_{\text{NF}}(r_{\text{s}} - r_0)] ,$$ (4.23)

for probe positions $r_{\text{s}} \geq r_0$, which shows that as the distance between the probe and the resonator surface at r_0 decreases, the linewidth will increase exponentially.

---

[4]For instance, in the description and notation of Bohren and Huffman [232, pp. 145–147], an ellipsoid of size $a > b > c$ has a polarisability along the j axis of

$$\Upsilon_j = \frac{4\pi abc}{3}\frac{\varepsilon_{\text{s}} - \varepsilon_{\text{env}}}{\varepsilon_{\text{env}} + L_j(\varepsilon_{\text{s}} - \varepsilon_{\text{env}})}\varepsilon_0\varepsilon_{\text{env}} ,$$ (4.19)

where L_j, known as the depolarisation factor, depends on the ratios between a, b, c. For a sphere, $L_j = 1/3$, consistent with Eq. (4.17).

ACCOUNTING FOR THE NON-UNIFORMITY OF THE NEAR-FIELD. Even though the probe size can be small compared to the wavelength and consequently be in the Rayleigh regime, the evanescent field of the WGM might decay significantly over the size of the probe, which the uniform-field approximation does not account for. To address the non-uniformity, for instance a displaced dipole model [276] could be developed, where the effective centre of the dipole is shifted as a result of the evanescent field decay; or a coupled dipole approximation model can be used, where the scatterer is divided into subunits and the scattered field from from all subunits considered, see e.g. Lakhtakia [277] or Novotny and Hecht [278, Ch. 15].

There are a couple of existing approaches in the literature for WGM resonators:[xiii] Kaplan *et al.* [267] presents a method for numerically solving these types of problems using finite-element-method simulations (but do not provide linewidth vs probe–resonator separation results). Keng *et al.* [237] multiplies the expression in Eq. (4.18) with a size-dependent geometry correction factor, whereas Anetsberger *et al.* [240] performs the overlap integral between the probe volume and the *un*perturbed evanescent field in Eq. (4.8). A more recent paper by Foreman *et al.* [285] performs the overlap integral between the *perturbed* field and the probe, comparing the typical dipole approximation to their more rigorous Green's function-based approach [e.g. 233, 278], showing there is a less than 10 % error in the frequency shift given by the dipole approximation for probe sizes $k\rho_s \lesssim 0.8$, corresponding to $\rho_s \lesssim 200$ nm at $\lambda = 1550$ nm.

For all of these cases, the unperturbed the evanescent field over the probe can be assumed to vary only in the radial axis passing through the centre of the probe when the size of the probe is much smaller than the minor radius of the resonator confining the light, see Fig. 4.5. Thus the expression for the evanescent field [Eq. (4.2)] can used for the unperturbed field in the integral in the numerator of Eq. (4.8) without having to account for polar or azimuthal variation in the field across the probe volume.

To explore if the near-field decay affects the probe's absorption as a function of the resonator surface–probe distance, the geometric volume overlap between the field intensity and the spherical probe can be calculated. For a typical penetration depth of the near-field energy density $d_{NF} = 118.4$ nm for silica, the near field decays significantly over a probe approximated as a sphere of radius of for instance $\rho_s = 300$ nm. Ignoring any local field corrections, i.e., using the unperturbed near field in the calculation, the numerator of Eq. (4.8) becomes

$$\int_{V_s} (\varepsilon_s - \varepsilon_{env})\varepsilon_0 |\mathbf{E}(\mathbf{r})|^2 \, d^3\mathbf{r} = (\varepsilon_s - \varepsilon_{env})\varepsilon_0 \, |E_{surf}|^2 \int_{r_1}^{r_2} e^{-2\alpha_{NF}(r-r_0)} 4\pi\rho^2(r) \, dr , \quad (4.24)$$

$$\equiv (\varepsilon_s - \varepsilon_{env})\varepsilon_0 \, |E_{surf}|^2 \, \mathcal{I}(r_1, \rho_s; r_0, \alpha_{NF}) , \quad (4.25)$$

when the probe is a sphere with its centre on the r axis with a cross-section radius from the axis of $\rho(r)$ over the interval $r \in [r_1, r_2] = [r_1, r_1 + 2\rho_s]$, see Fig. 4.6(a). The cross-section

[xiii] Note that corrections and alternative approaches to the approximations outlined in this chapter is an active field of research. Some recent papers in addition to the literature listed so far include Refs. 279–281. There is also theoretical [282, 283] and experimental [284] work on slab substrates perturbing WGMs.
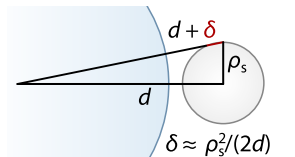
Figure 4.5. The near field decays only radially over the volume of a small scatterer when $d \gg \rho_s$: when a spherical scatterer is at some distance d from the centre of the minor circle of the resonator, the increased distance δ for the part furthest from the centre of the scatterer is negligible compared to the near field decay. By Pythagoras, $d^2 + \rho_s^2 = (d+\delta)^2$, which, to first approximation, means $\delta \approx \rho_s^2/(2d)$. For a typical resonator and scatterer combination $\rho_s \simeq 0.1\,\mu\text{m}$ and $d \simeq 100\,\mu\text{m}$, $\delta \simeq 0.05$ nm, which is much smaller than the near field decay.
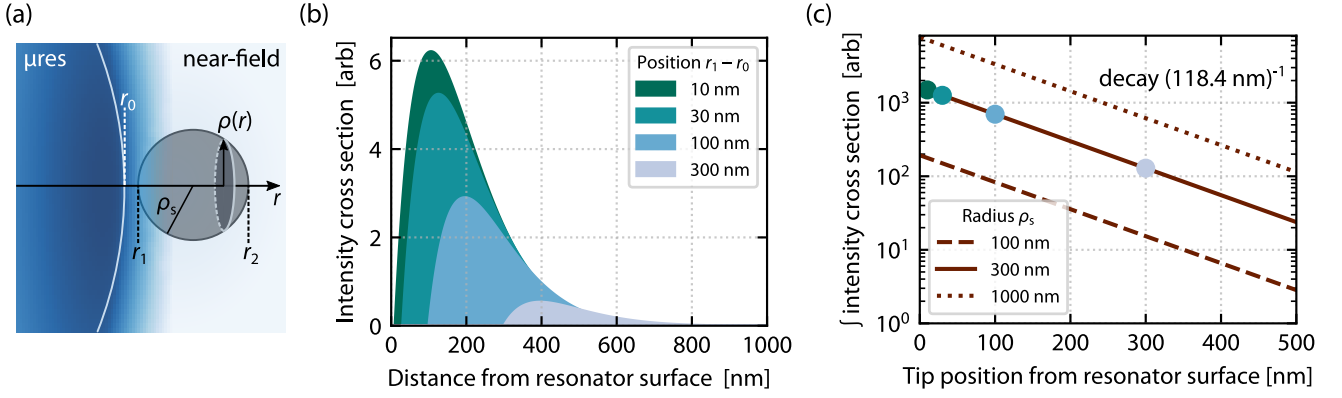
Figure 4.6. Numerical integration of field-intensity–sphere-volume overlap for various sizes and positions of a sphere. (a) Schematic of the sphere in the near-field with the relevant variables annotated. The field-intensity overlap is calculated from r_1 to $r_2 = r_1 + 2\rho_s$ for various sphere radii ρ_s, where the radius of the cross section at r is $\rho(r)$. (b) The integrand of Eq. (4.24): Product of the sphere's cross section and field intensity (intensity cross section) for a sphere with radius $\rho_s = 300$ nm at four different distances from the resonator surface. The distance is given from the point of the sphere closest to the resonator surface. The exponential field decay causes the intensity cross section to become exponentially smaller with increasing distance from the resonator. (c) The value of the integral (4.24) of the intensity cross sections given the distance from the resonator surface for spheres of three different sizes. The exponential decay of the integrated cross section is the same as the near-field decay for all three tip radii, indicating that the sphere size relative to the near-field decay does not change the overlap as a function of sphere position. Using other tip shapes such as a cone or half-sphere tip on a cone gives the same decay length.

radius is given by the equation for a circle of radius ρ_s centred at $r_1 + \rho_s$,

$$\rho^2(r) = \begin{cases} \rho_s^2 - [r - (r_1 + \rho_s)]^2 & \text{for } r_1 \leq r \leq r_2 \\ 0 & \text{otherwise} \end{cases} . \qquad (4.26)$$

In this work, it is primarily the functional dependence of the absorption on the tip–resonator distance that is of interest, not the particular proportionality factors. The imaginary part of Eq. (4.24) is proportional to the WGM linewidth change:

$$\Delta\kappa(r_s) \propto -\text{Im}(\varepsilon_s)\,\mathcal{I}(r_s, \rho_s)\,, \qquad (4.27)$$

where the point of the sphere closest to the resonator has been relabelled, $r_1 = r_s$. Performing the integration $\mathcal{I}$ for spheres of different sizes for positions approaching the resonator indicates if a sphere of size comparable to or larger than the near-field penetration depth will deviate from the uniform theory result (4.23), where the induced linewidth broadening follows the near-field intensity's exponential profile. Figure 4.6 shows the result of numerical integration in Eq. (4.24), where for three sphere sizes, the integral was performed for a range of positions within the closest 1 μm of the resonator surface (only 500 nm shown in the plot). The lines in Fig. 4.6(c) are proportional to the expected linewidth increase given a position of the sphere. The three lines all have slopes corresponding to exponential decay lengths 118.40(1) nm, which is the same as the penetration depth of the near-field intensity, suggesting that the uniform-field approximation holds also for probes larger than the near-field decay when the effect of the probe up to some proportionality factor is considered. To explore whether other scatterer shapes that more closely resembles the

tip used in the experiment, alternative expressions to Eq. (4.26) can be used to investigate other axisymmetric scatterers of various sizes. Using a cone or a half-sphere on a cone extending into the far-field gives the same decay length as a spherical scatterer, indicating that the decay of the near field over the probe volume makes little difference in the functional form of the linewidth broadening.

Note that local field effects such as a nonlinear field enhancement at the tip when moving closer to a resonator has been ignored in this calculation. Furthermore, the calculation builds on the first-order perturbation theory of the reactive sensing principle. The results of Foreman and Vollmer [252] show that the slope of the broadening induced by a silver nanosphere is in fact steeper for a (plasmonically non-resonant) silver sphere than what the perturbation theory result gives,[xiv] i.e., that the exponential decay length of the linewidth broadening with increasing probe–resonator distance is smaller than the decay length d_{NF} of the near-field intensity.

It should also be noted that it has been shown that in the case of even a 0.1 % deviation from a perfectly spherical resonator, the relative corrections to the predicted resonance frequency shifts from perturbation theory are orders of magnitude larger [281]; however, in this work it is not a goal to predict the absolute broadening caused by the tip, but understand its functional dependence on the probe–resonator distance, which should not be affected by such effects.

CONCLUSION FOR ABSORPTION LOSSES. For a non-plasmonically resonant scatterer of a size that is small compared to the wavelength, the dipole approximation result, Eq. (4.23), is expected to perform well for estimating the functional shape of the linewidth broadening with respect to the tip–resonator distance, also when the scatterer is large compared to the evanescent field's decay length.

4.2.3 *Tip-induced scattering losses*

As mentioned at the beginning of this section, the tip will not just contribute to broadening the resonator linewidth by absorption of light, but also scatter light in all directions. Some light can scatter back into the same mode, but from the forward-propagating mode's point of view, scattered light is largely lost and will contribute to broadening of the resonance. The consequence of the light scattering into the counterpropagating WGM – which is the very reason the tip is introduced into the near field – will be covered in the next section, Section 4.3. This section discusses the broadening of the forward-propagating mode caused by tip scattering.

Metals typically have a large negative electric permittivity at optical frequencies compared to free space. Generally, the larger the contrast between a scatterer and its surroundings, the more efficiently it scatters, resulting in a larger scattering cross section. For metal particles larger than around 100 nm in diameter the scattering cross section is much larger than the absorption cross section [257], and thus the effect of scattering is typically more important than absorption. This makes a metal tip a convenient choice for this experiment because the tip is introduced to tune the coupling between the forward- and backward-

[xiv] Foreman and Vollmer [252] do not give the numerical value of the discrepancy between the perturbation theory and Mie-theory result, but from extracting data from their plots (for a WGM of radius 4 μm with refractive index 1.59 perturbed by a silver sphere of radius 32 nm) and fitting the extracted values, the perturbation-theory result is show to over-estimate the inverse of the exponential decay factor by about 15 % for both TM and TE modes. This number may be different for other scatterer and WGM sizes.

propagating modes via scattering, and thus scattering is desired, whereas absorption only degrades the optical Q factor without making a difference to the backscattering.

Where does the scattered light go? Assuming quasi-elastic scattering, meaning that the scattered light from the tip has the same or close to the same frequency as the incident light, light does not couple into propagating WGM modes of different orders than the mode in question as these have different resonance frequencies.[5] Therefore, the tip-induced losses stem from coupling into free-space modes and into non-guided modes within the fused silica, as well as into the counterpropagating WGM.

There are a number of different approaches to deriving an expression for the induced broadening due to a scatterer, with some examples found in the supplementary materials of Refs. 112, 115, 265. Mazzei *et al.* [112] and Zhu *et al.* [115] use a Weisskopf–Wigner semiclassical approach, generalised by Yi *et al.* [212] for multiple scatterers, whereas Baaske *et al.* [265] base their derivation on Larmor's formula for the radiated power from an accelerated charge.

Following the same approach as Baaske *et al.* [265] to calculate the scattering losses, the optical Q factor of the WGM with the tip present can be expressed as the sum of all contributing Q factors [Section 2.1.2],

$$Q^{-1} = Q_0^{-1} + Q_{ex}^{-1} + Q_{tip\ abs}^{-1} + Q_{tip\ scatt}^{-1}\ , \tag{4.28}$$

namely the intrinsic, taper coupling, and two tip-related Q factors, respectively. From the definition of the quality factor as the energy in the mode per dissipated power [Eq. (2.11)], the total Q can be expressed by the dissipated power due to each contribution,

$$Q^{-1} = \frac{\mathcal{P}_0 + \mathcal{P}_{ex} + \mathcal{P}_{tip\ abs} + \mathcal{P}_{tip\ scatt}}{\omega U_V}\ . \tag{4.29}$$

Similarly, the total Q factor can be expressed in terms of the linewidth contribution for each loss channel,

$$Q^{-1} = 2\frac{\kappa_0 + \kappa_{ex} + \kappa_{tip\ abs} + \kappa_{tip\ scatt}}{\omega}\ , \tag{4.30}$$

which means that the scattering-related Q is

$$Q_{tip\ scatt}^{-1} = \frac{\mathcal{P}_{tip\ scatt}}{\omega U_V} = \frac{2\kappa_{tip\ scatt}}{\omega}\ . \tag{4.31}$$

---

[5]This so-called backscattering coupling picture has been criticised by some authors in a set of papers [262–264, 281, 286] for failing to capture the coupling to other WGMs than the counterpropagating mode. These authors are seeking to build first-principles models from Maxwell's equations valid for idealised spherical resonators rather than basing the models on observations and a simple experimental picture. They have shown that a first-principle model recovers that of the reactive sensing principle [264]. For the resonators used in this work, the geometry deviates drastically from a perfect sphere, and therefore the frequency spacing between resonances is larger than for a spherical resonator, and the coupling to modes of different orders can be ignored.

From this expression, the contribution to the linewidth from the tip scattering in terms of the power dissipated through tip scattering is

$$\kappa_{\text{tip scatt}} = \frac{\mathcal{P}_{\text{tip scatt}}}{2U_V} \,. \tag{4.32}$$

Now, by relating the scattered power to known quantities such as the polarisability of the tip, the broadening due to scattering can be expressed in a similar fashion as the tip absorption. The scattered power from the tip is caused by the oscillation of the charges in the tip due to the WGM field. Under the dipole approximation, the scatterer is treated as a dipole with dipole moment $\mathbf{p} = \Upsilon\mathbf{E}(\mathbf{r}_s)$ [Sidenote xii] where all quantities are slowly varying with respect to the optical frequency. Considering the time-dependence $e^{-i\omega t}$ of the WGM field, the time-dependent dipole moment is $\tilde{\mathbf{p}}(t) = \Upsilon\mathbf{E}(\mathbf{r}_s)e^{-i\omega t}$, giving a charge–acceleration product

$$\ddot{\tilde{\mathbf{p}}}(t) = \frac{\mathrm{d}^2}{\mathrm{d}t^2}\left[\Upsilon\mathbf{E}(\mathbf{r}_s)e^{-i\omega t}\right] = (-i\omega)^2\Upsilon\mathbf{E}(\mathbf{r}_s)e^{-i\omega t}\,, \tag{4.33}$$

The Larmor formula gives the radiated power due to an acceleration of a charge as proportional to the square of the product of the charge and its acceleration [268]. For a dipole, the Larmor formula is

$$\mathcal{P}_{\text{tip scatt}} = \frac{n^3|\ddot{\mathbf{p}}|^2}{6\pi\varepsilon_0 c^3} = \frac{n^3\omega^4|\Upsilon|^2}{6\pi\varepsilon_0 c^3}\,|\mathbf{E}(\mathbf{r}_s)|^2 \tag{4.34}$$

when inserting Eq. (4.33) and moving back to slowly varying quantities. Inserting this result into Eq. (4.32), the relative linewidth broadening due to the tip scattering can be expressed

$$\frac{\Delta\kappa_{\text{scatt}}}{\omega} = \frac{n^3\omega^3|\Upsilon|^2}{12\pi\varepsilon_0 c^3}\frac{|\mathbf{E}(\mathbf{r}_s)|^2}{U_V}\,, \tag{4.35}$$

where the Δ denotes that this quantity is the change in the linewidth compared to when the tip is not present. The scattering cross section of a sphere is $\sigma_{\text{scatt}} = n^4\omega^4|\Upsilon|^2/(6\pi\varepsilon_0^2 c^4)$ [278, 287], thus the broadening can be expressed

$$\frac{\Delta\kappa_{\text{scatt}}}{\omega} = \frac{c\varepsilon_0\sigma_{\text{scatt}}}{2n\omega}\frac{|\mathbf{E}(\mathbf{r}_s)|^2}{U_V}\,, \tag{4.36}$$

which is the same expression as for the absorption broadening, Eq. (4.21), except replacing the absorption cross section with the scattering cross section.

This finally shows that, similarly to the absorption broadening, the scattering-related broadening is also proportional to the near-field energy density at the tip's position:

$$\Delta\kappa_{\text{scatt}}(r_s) \propto \exp\left[-2\alpha_{\text{NF}}(r_s - r_0)\right]\,. \tag{4.37}$$

The derivation above does not take into account that some of the radiated power can reenter the forward-propagating mode, but this is assumed to be a linear correction with respect

to the resonator–tip distance and thus only changes the prefactors, not the functional dependence.

4.2.4   *The resulting tip-position dependent optical linewidth*

As discussed in the previous two sections, the presence of the tip within the near field will broaden the optical linewidth by absorption and scattering to free-space and other modes than the WGM of interest. In short, the discussion shows that when there is a linear coupling between the evanescent near field and the tip, both the absorption (4.23) and scattering (4.37) contributions to the linewidth broadening will exponentially increase as the tip is approaching the resonator surface, following the same functional dependence as the energy density in the near field.

In the experiment, a piezo with the tip attached is raster scanned over a grid of positions, including positions corresponding to the tip being inside the resonator. For these piezo positions, the tip will hit the resonator surface and bend and/or slide along the resonator surface. For these piezo positions, the linewidth will not change exponentially as the tip is nominally moved deeper into the resonator, but the linewidth may change as the tip is sliding along the surface and its effective extinction cross section changes. This linewidth change for tip positions nominally inside the resonator can be approximated to be linear.

Based on the expected behaviour in the two domains of tip positions outside and nominally inside the resonator, the linewidth change $\Delta\kappa$ from the intrinsic, unperturbed linewidth κ_0 can be expressed as a piecewise function comprising an exponential decay from the resonator surface and a linear plateau for the tip positions where it is touching the resonator surface. In a coordinate system where r is pointing outwards from the resonator in the radial direction and the resonator boundary is at r_0, the function describing the scatterer-influenced linewidth is then

$$\kappa\left(r\right) = \kappa_{\mathrm{in}} + \begin{cases} a_{\mathrm{p}} + s(r - r_0) & \text{for } r - r_0 < 0 \\ a_{\mathrm{p}} \exp[-(r - r_0)/d_\kappa] & \text{for } r - r_0 \geq 0 \end{cases}, \tag{4.38}$$

where d_κ the decay length of the tip influence, a_{p} the amplitude of the exponential decay, and s a linear slope of the plateau at the resonator surface. This model is consistent with the experimental results of Azeem *et al.* [284] where the optical linewidth of an WGM resonator is monitored as the mode is approached by a slab substrate.

After presenting in the previous section how the expected optical linewidth broadening as the probe is approaching the resonator, the focus now turns to the tip's influence on the backscattering in the resonator.

As covered in Section 2.4, the intrinsic scatterers in the resonator contribute to optical losses by scattering light from a WGM into non-propagating and free-space modes, but they also scatter some light into the counterpropagating mode, coupling the WGM pair by scattering. Similarly, when a tip scatterer is present in the near field of a resonator, the light scattering off it increases losses as covered in Section 4.2.3, but also couples the two counterpropagating optical modes in the resonator. The coupling strength will depend on the scattering cross section of the tip, which increases with the overlap between the tip's geometrical cross section with the WGM's near field.

In order to model the effect of the tip, the spectral line shape of the back-reflected signal due to the coupling between the modes is first established, then the tip-position-dependent backscattered optical power at resonance is hypothesised.

4.3.1   *The coupled pump and backscatter line shapes*

Given some coupling between two resonances, the line shapes of the resonances might differ from their normal Lorentzian line shapes. In the following the line shapes of two coupled resonances are derived following a time-dependent rate-equation approach (see for instance Refs. 109, 133, 192, 266, 288 for examples of literature discussing coupling in WGM resonators using the rate-equation approach).

Let the clockwise mode e_{cw} of a WGM resonator be pumped by a field $E_{\mathrm{cw}}^{\mathrm{in}}$ at some frequency detuning δ from its resonance frequency. Introducing coupling between the mode and its counterpropagating, frequency-degenerate mode e_{ccw}, optical power builds up in both modes. Using the complex scattering coefficients g_{jk} to describe the coupling from mode j to k, the steady-state equations of motion for the two circulating fields can be expressed

$$\begin{pmatrix} \dot{e}_{\mathrm{cw}} \\ \dot{e}_{\mathrm{ccw}} \end{pmatrix} = \begin{pmatrix} -\kappa - \mathrm{i}\delta + \mathrm{i}g_{11} & \mathrm{i}g_{21} \\ \mathrm{i}g_{12} & -\kappa - \mathrm{i}\delta + \mathrm{i}g_{22} \end{pmatrix} \begin{pmatrix} e_{\mathrm{cw}} \\ e_{\mathrm{ccw}} \end{pmatrix} + \begin{pmatrix} E_{\mathrm{cw}}^{\mathrm{in}} \\ 0 \end{pmatrix} = 0 \qquad (4.39)$$

where $E_{\mathrm{ccw}}^{\mathrm{in}} = 0$ as there is no pumping on the CCW mode. The coupling between the two counterpropagating modes can in general be non-symmetric $|g_{12}| \neq |g_{21}|$ but are typically assumed to be equal [112, 272]. Inverting the matrix gives

$$\begin{pmatrix} e_{\mathrm{cw}} \\ e_{\mathrm{ccw}} \end{pmatrix} = \frac{E_{\mathrm{cw}}^{\mathrm{in}}}{(\kappa + \mathrm{i}\delta - \mathrm{i}g_{11})(\kappa + \mathrm{i}\delta - \mathrm{i}g_{22}) + g_{12}g_{21}} \begin{pmatrix} \kappa + \mathrm{i}\delta - \mathrm{i}g_{22} \\ \mathrm{i}g_{12} \end{pmatrix}. \qquad (4.40)$$

In the small-backscattering regime, $|g_{jk}| \ll \kappa$, this gives

$$e_{cw} = \frac{E_{cw}^{in}}{\kappa + i\delta} \; ; \qquad\qquad e_{ccw} = \frac{ig_{12}E_{cw}^{in}}{(\kappa + i\delta)^2} \, , \qquad (4.41)$$

where $|e_{cw}|^2, |e_{ccw}|^2$ are proportional to the powers circulating in the respective directions.

As the measurements obtained in the experiment are of the optical power in the tapered fibre, the output fields in the taper from the cw and ccw directions must be found. These can be expressed using the taper coupling rate κ_{ex} [133]:

$$E_{cw}^{out} = E_{cw}^{in} - 2\kappa_{ex}e_{cw} \; ; \qquad E_{ccw}^{out} = E_{ccw}^{in} - 2\kappa_{ex}e_{ccw} = -2\kappa_{ex}e_{ccw} \, , \qquad (4.42)$$

where $E_{ccw}^{in} = 0$ as there is no pumping in the ccw direction. To find the line shapes of the output fields, insert Eq. (4.41) and take the modulus squared to obtain

$$|E_{cw}^{out}|^2 = |E_{cw}^{in}|^2 \left[1 - \frac{4\kappa_{ex}(\kappa - \kappa_{ex})}{\kappa^2 + \delta^2} \right] \; ; \qquad |E_{ccw}^{out}|^2 = |g_{12}|^2 |E_{cw}^{in}|^2 \frac{4\kappa_{ex}^2}{(\kappa^2 + \delta^2)^2} \, . \qquad (4.43)$$

Expressing the total losses as the sum of the intrinsic losses κ_{in} and the taper coupling κ_{ex}, $\kappa = \kappa_{in} + \kappa_{ex}$, and using the coupling contrast $\mathcal{K}^{res} = 4\kappa_{ex}\kappa_{in}/\kappa^2$ [Eq. (2.41)],

$$|E_{cw}^{out}|^2 = |E_{cw}^{in}|^2 \left[1 - \frac{\mathcal{K}^{res}}{1 + \delta^2/\kappa^2} \right] \; ; \qquad |E_{ccw}^{out}|^2 = |g_{12}|^2 |E_{cw}^{in}|^2 \frac{4\kappa_{ex}^2/\kappa^4}{(1 + \delta^2/\kappa^2)^2} \, . \qquad (4.44)$$

These expressions for the optical power in the fibre taper shows that the transmitted clockwise pump spectrum is a normal Lorentzian line shape dip, whereas the backscattered spectrum will exhibit a peak with a squared Lorentzian line shape with its amplitude given by the coupling parameters and the input pump power.

4.3.2   *Backscattering power given the position of the near-field probe*

Knowing the line shape of the backscattered light Eq. (4.44), the expected backscattered power at resonance when the tip is present can be modelled. As will be shown, the backscattered power is dependent on the tip's radial and azimuthal position in relation to the resonator surface.

Assuming a constant taper coupling κ_{ex} and input power $|E_{cw}^{in}|^2$, the on-resonance backscattered power exhibits the proportionality relation

$$A_b \propto \frac{|g_{12}|^2}{\kappa^4} \, . \qquad (4.45)$$

The complex coupling coefficient g_{12} has two contributions, an intrinsic coupling g_0 between the two modes due to intrinsic scatterers and inhomogeneities and an additional tip-induced coupling g_{tip} [288].

TIP-INDUCED COUPLING. The tip-induced coupling is expected to be proportional to the tip scattering considered in Section 4.2.3 and therefore exponentially increase as the tip is approaching the resonator. However, the phase of the light coupled from the CW to CCW mode by the tip will vary with the azimuthal position of the tip, as the phase is a function of the phase of CW mode at that position. By a suitable choice of the relative phase between the CW and CCW basis states, the intrinsic coupling g_0 can be made to be real, and the phase relationship between the light coupled from the intrinsic (effective) scatterer and the light coupled by the tip is described by a complex phase factor in g_{tip}. In the polar coordinate system where $R = r - r_0 \geq 0$ is the distance of the tip from the resonator surface and the azimuthal position is ϕ, the tip-induced coupling can be expressed as a function of the tip's position:

$$g_{\text{tip}}(R, \phi) = a_{\text{tip}} \exp(-R/d_{\text{b}}) \exp[i\Theta(R, \phi)] , \tag{4.46}$$

where the tip-position-dependent coupling phase

$$\Theta(R, \phi) = k_{\text{fr}}\phi + \theta_0 + \theta_R R \tag{4.47}$$

accounts for how the phase of the light in the mode being scattered from changes as the tip is moved. As the next paragraphs will show, when the tip is close enough to the resonator for the tip coupling to be significant, this phase causes an azimuthal fringe pattern in the backscattered power due to the interference between the tip-induced and intrinsic backscattered light, where the constant k_{fr} represents the wavenumber of the fringe pattern. In addition to the azimuthal phase dependence $k_{\text{fr}}\phi$, a parameter for a fixed offset θ_0 is included, and a radially dependent, linear phase contribution θ_R accounting for phase drift over the course of the measurement and any tip-shape effects (discussed in Section 4.6.3).

The effective backscattering in the resonator can be tuned by controlling the coupling phase and amplitude of the light scattering via the tip from the forward- to the backward-propagating mode. When the radial position of the tip is sufficiently close for the tip to couple the two modes as strongly as the intrinsic scatterer does, $|g_{\text{tip}}| = g_0$, a suitable phase offset between the light coupled by the two mechanisms makes the light destructively interfere, resulting in zero effective backscattering. This phase offset is governed by the azimuthal position of the tip, see Eq. (4.47).

Assuming there is a tip position for which $|g_{\text{tip}}| = g_0$, the notion of a *critical tip-coupling distance* R_{crit} can be introduced by forcing the coupling amplitude to be equal to the intrinsic coupling at this position:

critical tip-coupling distance

$$g_{\text{tip}}(R, \phi) = g_0 \exp\left[-(R - R_{\text{crit}})/d_{\text{b}}\right] \exp\left[i\Theta(R, \phi)\right] , \tag{4.48}$$

which evaluates to g_0 at R_{crit}.

The total coupling can be found by coherently adding the two coupling contributions

$$|g_{12}|^2 = |g_0 + g_{\text{tip}}|^2 = g_0^2 \left[1 + 2e^{-R'/d_b} \cos(\Theta) + e^{-2R'/d_b} \right] . \qquad (4.49)$$

where $R - R_{\text{crit}} \equiv R'$ for compactness of notation. When the tip is critically coupled ($R' = 0$), this expression becomes

$$|g_{12}|^2_{\text{crit}} = g_0^2 \left[2 + 2\cos(\Theta) \right] , \qquad (4.50)$$

where it is clear that for $\Theta = \pm\pi$, the total coupling from the CW to the CCW mode is zero when the tip is critically coupled. If the tip coupling is insufficient for any position in the near field to match that of the intrinsic coupling, the critical tip-coupling position will be negative, corresponding to an (unrealisable) tip position inside the resonator.

Inserting the tip-coupling parameter (4.49) into Eq. (4.45), the expected proportionality of the on-resonance backscattered power can be expressed

$$A_b(R \ge 0, \phi) \propto \frac{g_0^2}{\kappa^4(r)} \left\{ 1 + 2e^{-R'/d_b} \cos\left[\Theta(R, \phi)\right] + e^{-2R'/d_b} \right\} , \qquad (4.51)$$

where only the tip positions up to where the tip touches the resonator are considered, $r - r_0 = R \ge 0$, and in which $\kappa(r)$ is the tip-position-dependent linewidth from Eq. (4.38). Figure 4.7 shows an example of how the backscattered power varies with the tip position. The intrinsic backscattered power corresponds to when the tip is far away, $A_b(R \to \infty, \phi) \equiv A_{b,0}$, and in this work the intrinsic backscattered power is normalised to 1.

4.3.3 *Period of the fringe pattern in the backscattered power*

The fringe pattern in the backscattered power arises as consequence of the interference between the tip-induced and intrinsic backscattering, expressed by the $\cos(\Theta)$ term in Eq. (4.51), where $\Theta(R, \phi) \propto k_{\text{fr}}\phi$ represents the phase of the backscattered light from the tip relative to the phase of the intrinsically scattered light. Note that if the phase of the pump light changes, the phase difference between the intrinsic and tip-induced light should stay constant as their phases are both given by the pump phase at their respective scattering points.

Such a fringe pattern in the backscattered power from a microresonator has previously been observed in a context of scanning near-field microscopy (SNOM) [e.g. 289], where Schmidt *et al.* [290] presented measurements of the reflected power from a WGM resonator as a metal-coated fibre-SNOM tip was scanned in the resonator's near field.[xv] Also Mazzei *et al.* [112] essentially observed a fringe pattern of the same origin, but did so by measuring the transmitted field in a mode-split regime where they measured the relative peaks of the hybridised modes as a tip was scanned azimuthally.

To calculate the periodicity of the fringe pattern with respect to the azimuthal position of the tip, ϕ, the change in the phase difference between the induced and intrinsic light as a function of tip position must be considered. The periodicity is by definition given by the
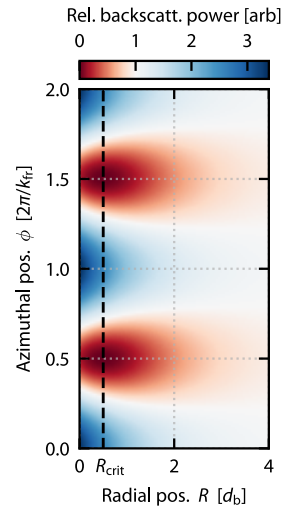
Figure 4.7. The on-resonance backscattering power as a function of tip position calculated by evaluating Eq. (4.51) when the critical tip coupling is at $R_{\text{crit}}/d_b = 0.5$ (dashed line), and the linewidth broadens by 10 % as the tip approaches the resonator.

[xv] Another notable prior paper by Blaize *et al.* [291] studied the phase and amplitude of the field scattered into the far-field as a SNOM tip was scanned within a microresonator's near field.

fringe wavenumber in Eq. (4.47), $\Lambda_{\mathrm{fr}} = 2\pi/k_{\mathrm{fr}}$. By relating the fringe pattern wavenumber k_{fr} to the optical propagation constant, the fringe pattern period can be expressed in terms of the vacuum wavelength of the pump light.

First, consider the change in the phase of the scattered light as the tip is moving: the phase of the tip-induced backscattered light is given by the phase of the pump light at the tip's position, which varies along the azimuth by $\beta_{\mathrm{opt}}\phi$, where $\beta_{\mathrm{opt}} \approx 2\pi n/\lambda$ is the propagation constant of the pump light. The change in the phase of the light reflected by the tip *at the tip's position* as the tip moves from position ϕ_1 to ϕ_2 is

$$\Delta\Theta_{\mathrm{p}} = \beta_{\mathrm{opt}}(\phi_2 - \phi_1) . \qquad (4.52)$$

However, the change in the phase difference between the intrinsic and scatterer-induced light is not just $\Delta\Theta_{\mathrm{p}}$, because the change in the tip's position in relation to the intrinsic scatterer must also be accounted for. Assuming that the phase of the intrinsic backscattered light is unchanged as the tip moves, the phase-difference change due to the tip's movement is an additional $\beta_{\mathrm{opt}}(\phi_2 - \phi_1)$. Thus, the total change in the phase difference between the tip-induced and intrinsic backscattering when the tip moves from one position to another is

$$\Delta\Theta = 2\Delta\Theta_{\mathrm{p}} = 2\beta_{\mathrm{opt}}(\phi_2 - \phi_1) . \qquad (4.53)$$

From this result and the definition of the coupling phase, Eq. (4.47), the fringe pattern wavenumber can be identified to be $k_{\mathrm{fr}} = 2\beta_{\mathrm{opt}}$, and thus $\Lambda_{\mathrm{fr}} = 2\pi/(2\beta_{\mathrm{opt}})$.

Alternatively, consider the tip moving the distance equivalent to the fringe separation distance Λ_{fr}, for example from one backscattering maximum ϕ_m to a subsequent maximum in the fringe pattern ϕ_{m+1}, the change in Θ is

$$\Theta_{m+1} - \Theta_m = 2\beta_{\mathrm{opt}}(\phi_{m+1} - \phi_m) = 2\beta_{\mathrm{opt}}\Lambda_{\mathrm{fr}} . \qquad (4.54)$$

where, by definition, the phase difference between subsequent maxima is

$$\Theta_{m+1} - \Theta_m = 2\pi . \qquad (4.55)$$

Thus, for a resonator of material with refractive index n, the fringe period is

$$\Lambda_{\mathrm{fr}} = \frac{2\pi}{2\beta_{\mathrm{opt}}} \approx \frac{\lambda}{2n} . \qquad (4.56)$$

4.4 EXPERIMENTAL SETUP AND MEASUREMENT PROCEDURE

To experimentally investigate the effect of a near-field probe on the backscattering from a resonator, the reflected power and resonance linewidth are studied as functions of the distance of a tungsten tip from the resonator surface r and its azimuthal position ϕ [coordinates as shown in Fig. 4.3(a)]. The tungsten tip is fabricated as described in Section 3.4. The experiment was performed with three different silica rod resonators with diameters of 2.7 mm, 1.72 mm, and 1.74 mm, and Q factors of various resonances in the 10^8 to 10^9 range. The laser-lathe technique described in Section 3.1 is used to fabricated the resonators, with two higher-Q resonators fabricated in a nitrogen atmosphere to increase the Q by reducing the formation of light-absorbing hydroxide [292, 293]. In the following, results from a measurement using the 2.7-mm resonator will be discussed first.

A schematic of the experimental setup is shown in Fig. 4.8(a). The setup allows the resonator to be pumped whilst taking spectral measurements of the transmitted and back-reflected signals simultaneously, and controlling the position of the near-field scatterer.

The optical setup is all-fibre and single mode. The microrod resonator is pumped with a 1.55-μm, continuous-wave, external-cavity diode laser[xvi] using a tapered optical fibre mounted on a translation stage[xvii] controlling the coupling of light into the cavity. A polarisation controller[xviii] is used for further optimising the coupling to a particular resonator mode. An optical circulator[xix] directs the backscattered light from the cavity onto an amplified photodetector,[xx] so the optical power can be recorded with an oscilloscope.[xxi] The cavity transmission is simultaneously recorded using a photodetector connected to the oscilloscope.

In order to obtain optical transmission and backreflection spectra, the frequency of the light source is scanned by modulating the laser current with a triangular wave signal supplied by a waveform generator.[xxii] To avoid power fluctuations, the light is subsequently fed into an erbium-doped fibre optical amplifier[xxiii] operating in saturation, and a variable optical attenuator[xxiv] is then used to set the input optical power to the cavity to 20 mW. The laser frequency is scanned at a rate of $-330\,\mathrm{GHz\,s^{-1}}$ to avoid thermal broadening of the resonance [Section 2.5.1]. The nonlinear Kerr effect is practically instantaneous, which means it is faster than the scanning rate and hence causing some broadening; however, with low input powers, this broadening is small and Lorentzian line shapes are observed for both directions of scanning.

The part of the setup with the resonator, tapered fibre, tungsten tip and translation stages is kept in an acrylic box to protect the components against contamination and draughts. A photograph of the components can be seen in Fig. 4.9. The tungsten tip near-field probe was fixed to a polylactic acid (PLA) plastic mount, attached to a computer-controlled, three-axis piezoelectric positioner.[xxv] A manual translation stage underneath provides coarse positioning.

When performing the measurements, the tip position is raster scanned in steps of 50 nm (results presented in Fig. 4.10) or 25 nm (results presented in Fig. 4.14) over a 1 μm × 1.5 μm area in the resonator plane. As the tip position is raster scanned, at each pos-

[xvi] Toptica CTL 1500

[xvii] Thorlabs NanoMax 300

[xviii] Thorlabs FPC562

[xix] Haphit FCIR-1550-3

[xx] Thorlabs PDA10CF-EC

[xxi] Keysight DSOX2024A

[xxii] Agilent 33250A

[xxiii] Pritel FA-33-IO

[xxiv] Haphit PMVA-1550-M

[xxv] PI P-611.3 NanoCube
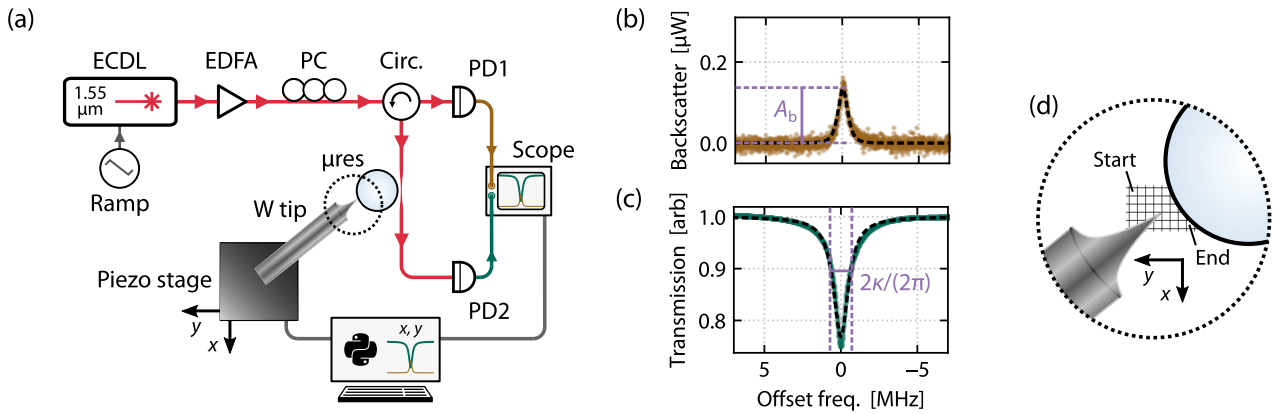
Figure 4.8. Experimental setup for backscattering measurements. (a) Schematic of the setup: A 1.55-µm, fibre-coupled external cavity diode (ECDL) laser amplified by an erbium-doped fibre amplifier (EDFA), a polarisation controller (PC) optimises the coupling to the desired resonator mode, a circulator separates the light based on its propagation direction, and photodetectors monitor the backscattering (PD1) and transmission of the resonator (PD2). An optical isolator at the ECDL output, variable attenuators, EOM for laser frequency scan calibration are not shown for simplicity. The tungsten tip near-field probe is fixed to a computer-controlled piezo nano-positioner. The automated measurement procedure moves the tip and acquires spectral measurements using an oscilloscope for each tip position. Spectra of the backscattered light (b), and transmitted light (c) for when the tip is far away from the resonator is shown, with fitted Lorentzians (dashed). The Lorentzian amplitude of the backscattering A_b and transmission linewidth $2\kappa/(2\pi)$ are annotated. (d) The measurement procedure defines a grid of tip positions to raster scan over (figure not to scale), where at each position, optical spectra are obtained.
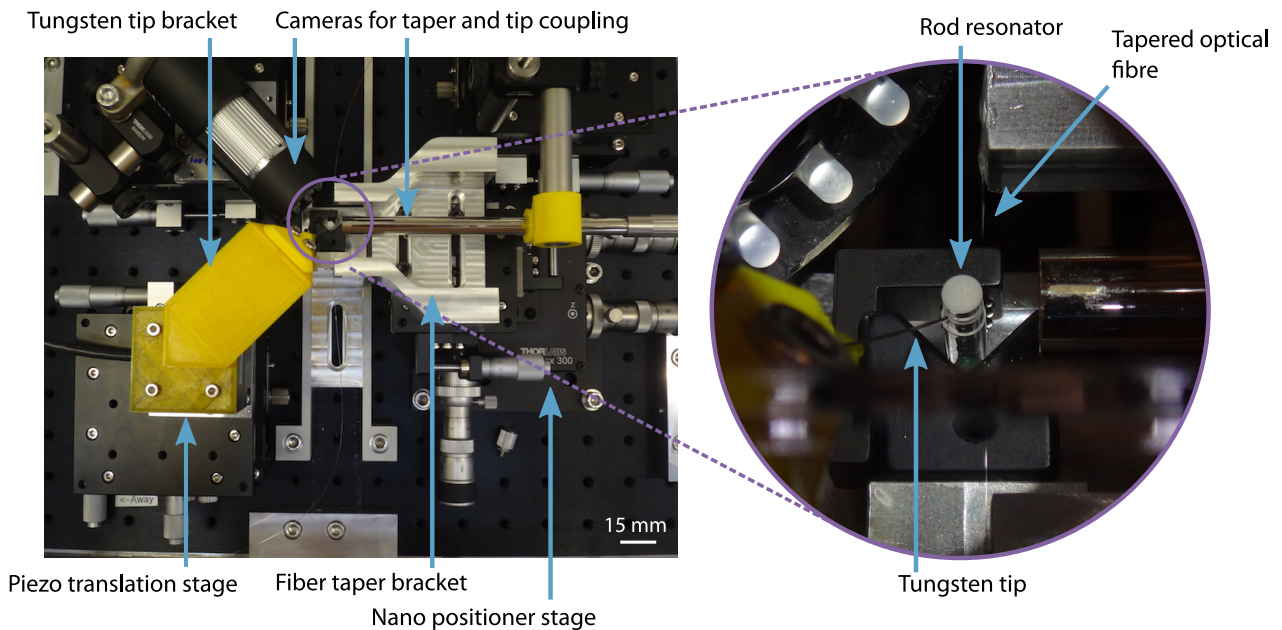
Figure 4.9. Photograph of the experimental setup inside the protective acrylic box to shield the setup from dust, contaminants and draughts. The box contains the optical resonator, a tapered optical fibre for coupling into the resonator, and the tungsten tip. The tapered fibre and tungsten tip are mounted on coarse and fine translation stages for control over their optical coupling to the resonator. The tungsten tip bracket is 3D printed with a PLA filament. The scale bar indicates the size in the plane of the resonator and tungsten tip. The remaining optical components and electronics are outside the acrylic box. This part of the setup was originally designed by L.DB. and M.T.M.W.; the author built the optical and electronic circuitry and modified the setup with changes and additions to perform the measurements of this chapter. The resonator, fibre taper, and tungsten tip were all fabricated by the author.

ition, transmission and backscattering spectra are simultaneously recorded, with example spectra shown in Fig. 4.8(b,c). By computer control of the tip positioner and oscilloscope, the capture time for a measurement set of 600 different tip positions, corresponding to pixels in Fig. 4.10, is only a few minutes. The short measurement time reduces the impact of slow drifts that can occur due to for example temperature changes causing thermal expansion of parts in the setup.

To extract the backscattered power and pump-resonance half-linewidth κ given each of the positions of the tip, the obtained spectra are fitted with Lorentzian functions, as given in the next section, Section 4.5. The resulting grids of on-resonance backscattering power and linewidth data over the two spatial coordinates are then numerically fitted with functions also described in the next section. Using these datasets, the position of the resonator surface in the grid is determined, the tip coupling positional dependence is studied, and the periodicity the backscattered power with azimuthal tip movement as well as the achieved backscattering suppression are calculated.

4.5   DATA ANALYSIS METHODS AND NUMERICAL FITTING

To extract the parameters of interest from the dataset, least squares fitting procedures are applied to the spectra obtained for each tip position in the raster-scan measurement. For the pump transmission spectra, the half-linewidth κ and on-resonance Lorentzian amplitude A_p are of interest to determine the resonator boundary and the optical coupling for Q factor calculations. For the reflection spectra, the on-resonance backscattered power A_b is of interest to determine the backscattering level. No spectrally resolvable mode splitting was observed for any of the measurements in this work.

To fit the the pump transmission resonance, a normal Lorentzian dip from a background B is used,

$$\mathcal{P}_p(\delta) = B_p - \frac{A_p}{1 + \delta^2/\kappa^2} \,, \tag{4.57}$$

where the detuning with respect to the resonance angular frequency ω_0 is $\delta = \omega - \omega_0$. However, the spectral shape for the backscattering is distorted as it is effectively pumped by a Lorentzian (the pump resonance), resulting in a line shape,

$$\mathcal{P}_b(\delta) = B_b + \frac{A_b}{(1 + \delta^2/\kappa^2)^2} \,, \tag{4.58}$$

in the limit of small backscattering, as shown in Section 4.3.1.

Subsequent to fitting the individual spectra to extract the parameters with estimated errors for each tip position, the grid data of linewidth and backscattering amplitude measurements are fitted. The functions used for the grid data fitting are expressed in a rotated (cartesian) coordinate system (r, ϕ) at an angle ϑ to the measurement coordinate system

(x, y), where the coordinate transformation is given by

$$
\begin{pmatrix} r \\ \phi \end{pmatrix} = \begin{pmatrix} \cos \vartheta & -\sin \vartheta \\ \sin \vartheta & \cos \vartheta \end{pmatrix} \begin{pmatrix} x \\ y \end{pmatrix}.
\tag{4.59}
$$

In this coordinate system, the r axis is normal to the resonator surface, and ϕ can be approximated as the azimuthal position over a short distance compared to the resonator's radius of curvature.[xxvi] The rotation angle ϑ is determined as one of the free parameters of the linewidth grid fit, where the linewidth function expressed in the (r, ϕ) coordinate system as shown in Eq. (4.38),

$$
\kappa(r) = \kappa_0 + \begin{cases} a_\mathrm{p} + s(r - r_0) & \text{for } r - r_0 < 0 \\ a_\mathrm{p} \exp[-(r - r_0)/d_\kappa] & \text{for } r - r_0 \geq 0 \end{cases},
\tag{4.60}
$$

with the unperturbed linewidth κ_0, decay length d_κ, amplitude of the exponential decay a_p, linear slope of the plateau at the resonator surface s, and the coordinate system offset r_0 as free parameters. The fitted parameter r_0 determines the resonator surface.

The on-resonance backscattered power grid data is subsequently fitted with the coordinate system rotation parameter ϑ and resonator surface parameter r_0 fixed to the values obtained from the linewidth fit. Only the portion of data outside the resonator boundary, $r - r_0 = R \geq 0$, is fitted according to Eq. (4.51):

$$
A_\mathrm{b}(R, \phi) = \begin{cases} \text{not fitted} & \text{for } R < 0 \\ |g|^2/\kappa^4(r) & \text{for } R \geq 0 \end{cases},
\tag{4.61}
$$

where $\kappa(r)$ is the fitted linewidth function, and the coupling from the forward- to the backward-propagating mode

$$
|g|^2 = g_0^2 \left[1 + 2 \exp(-R'/d_\mathrm{b}) \cos(\Theta) + \exp(-2R'/d_\mathrm{b}) \right],
\tag{4.62}
$$

where g_0 the intrinsic backscattering coupling, $\Theta = k_\mathrm{fr}\phi + \theta_0 + \theta_R R'$ the position-dependent phase responsible for the fringe pattern, in which θ_R is a radially dependent phase accounting for drifts, which will be justified in Section 4.6.3. The tip-critical-coupling distance is given by $R_\mathrm{crit} = R - R'$, and can be negative if critical tip coupling is not achieved in the near field. From the fit, the period Λ_fr of the fringe pattern can be calculated from $k_\mathrm{fr} = 2\pi/\Lambda_\mathrm{fr}$, as shown in Section 4.3.3.

[xxvi] For a resonator of radius $\mathcal{R} = 2.7\,\mathrm{mm}/2$, the maximum radial correction between the cord and arc for a cord of length $1.5\,\mu\mathrm{m}$ can be found using first the law of cosines to find the angle γ_arc over which the arc spans (0.064°), then calculating the max correction by $\mathcal{R}[1 - \cos(\gamma_\mathrm{arc}/2)] = 0.2\,\mathrm{nm}$.

4.6   EXPERIMENTAL RESULTS AND DISCUSSION

To investigate the experimental viability of the backscattering suppression technique and compare results to the theory, the tip-position raster-scan experiment was performed with three different microresonators and two different tungsten tips. The microresonators varied in diameters and optical quality factors. Multiple datasets were obtained and are presented in this section.

The measurement set presented in Fig. 4.10 was obtained with a 2.7-mm-diameter resonator, raster-scanning the tip in steps of 50 nm. The resulting linewidth and backscatter optical power grids from fitting the transmission and backscattering spectra from each tip position are shown in Fig. 4.10(a) and (b), respectively, where each pixel of the images corresponds to a position on the raster-scan measurement grid. This measurement set has a maximum backscattering suppression of a moderate 12 dB, limited by the detection noise level,[xxvii] but the measurement serves as a clear example of how the tip influences the WGM and displays a prominent fringe pattern.

The second measurement set, presented in Fig. 4.14, achieves a higher suppression in a 1.72-mm-diameter resonator. Because the suppression changes by orders of magnitude over small distances near the minimum backscattering points, this measurement set was obtained with a higher spatial resolution (steps of 25 nm) to increase the chance of getting a measurement in a position that results in higher suppression. Furthermore, this measurement allows a larger suppression to be measured because the photodetector noise level relative to the intrinsic backscattering level is lower: the standard deviation of the off-resonance signal is −34 dB of the on-resonance intrinsic scattering, resulting in a maximum noise-limited suppression of 34 dB.

4.6.1   *Linewidth broadening caused by the tip*

By extracting the Lorentzian linewidth for the transmission spectra for each tip position, the transmission linewidth data grid, such as the one shown in Fig. 4.10(a) is assembled. This grid is used for three purposes: (i) to determine the resonator surface from the exponential-to-linear transition, (ii) to fit the backscattering amplitude [Eq. (4.51)], and (iii) to calculate the optical coupling efficiency of each position in order to calculate the intrinsic optical quality factor of the resonance.

By fitting the linewidth data with Eq. (4.60), the resonator surface $R = 0$ is determined by the fitted interface between the plateau and the exponential decay. The surface is shown as solid black lines in Fig. 4.10(a,b,e). For comparing cross sections of the fit to the measured data, the relatively low resolution grid data is interpolated linearly in order to sample arbitrary lines in the two-dimensional grid of measurement data. Figure 4.10(e) shows cross sections of the fit (solid lines) and interpolated measured values (circles) for the linewidth data along the radial direction. The error bars show the linewidth error estimated by the least-squares fitting of the spectrum for that tip position. The standard deviation in the residual between the position of the tip as given by the piezo-positioner's

[xxvii] The detection noise level is taken to be the standard deviation of the photodetector output when the pump is far off resonance.
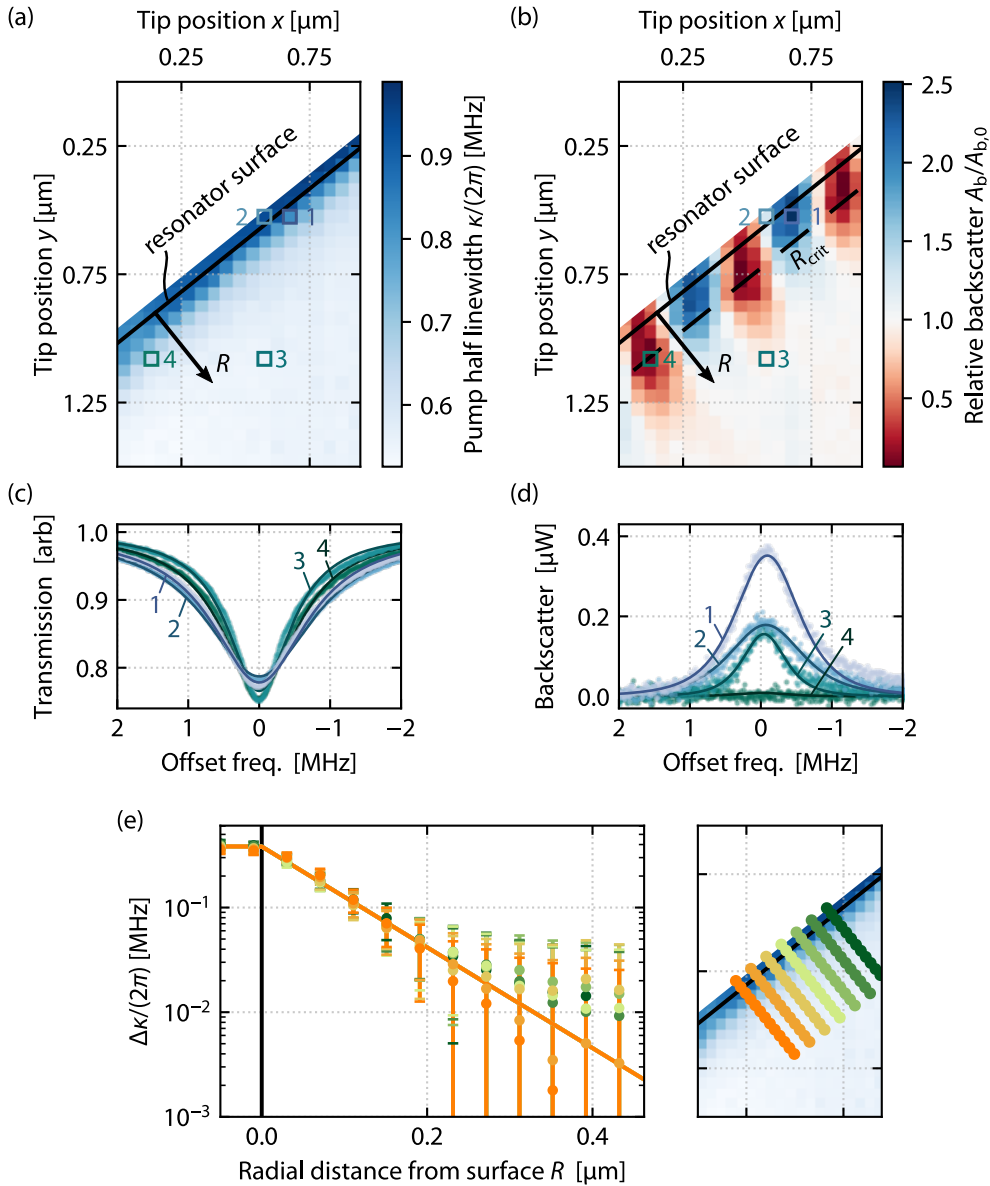
Figure 4.10. The whispering-gallery mode's response to the tungsten tip in the near field. (a,b) Grids of (a) fitted linewidths of the transmission and (b) backscatter power for tip positions in the resonator plane. The black lines ($R = 0$) indicate the fitted resonator surface based on the transition from exponential to linear change in the linewidth; measurements shown as $R < 0$ were obtained while the tip was touching the resonator surface, resulting in the tip sliding along the surface. Maximum backscattering suppression occurs at the dashed line representing the critical tip coupling distance R_{crit}. The backscattered power is normalised by the intrinsic backscattering power $A_{b,0}$. (c,d) Optical spectra of the (c) transmission and (d) backscattering for four selected tip positions, as annotated in panels (a) and (b). (e) Radial cross sections of the transmission linewidth change. The lines show the fitted tip-dependency over the full grid, and the circles are interpolated from the grid with errors given by the estimated linewidth fits for the transmission spectra.
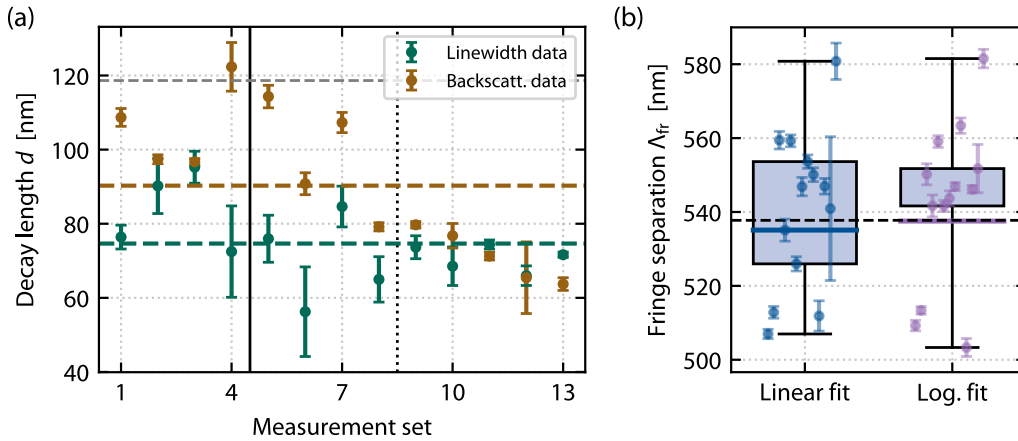
Figure 4.11. Comparisons of fitted parameters for thirteen different measurement sets using three different resonators and two different tungsten tips. (a) Comparison of the fitted decay lengths for the change in linewidth (d_κ) and change in backscattering (d_b) as the tip moves away from the resonator surface with errors as estimated from the least squares fitting. The value of the near-field intensity penetration depth d_{NF} is shown as a dashed grey line, and the solid black line marks the point at which the resonator was changed from a 2.7- to a 1.72-mm-diameter resonator, the dotted line is where a new 1.74-mm resonator was installed. Note that the decay lengths from different measurement sets are not expected to be the same due to differences in mode profiles and polar positions. (b) Boxplot of the values of the fitted fringe distance in the backscattering data for the same thirteen measurement sets as in panel (a). The fitted value per measurement set is overlaid. The boxes extend from the first to the third quartile, with weighted, best-estimate lines shown, and whiskers spanning the full data range. The fringe pattern is fitted both for the linearly scaled data and for the logarithmically scaled suppression. The dashed line indicates the expected value $\lambda/(2n)$ from theory.

sensor compared to the target of the raster grid is 7.2 nm, and thus small compared to the uncertainty in the linewidth.

The fit of the perturbed linewidth expression Eq. (4.60) to the linewidth data gives the exponential decay length for the linewidth dependence on the tip position as $d_\kappa =$ 92(3) nm for the measurement set presented in Fig. 4.10(a). Repeating the experiment with different resonances in the two resonators, the decay length of the linewidth dependence can be extracted for each measurement set. Figure 4.11(a) shows the fitted decay lengths across thirteen different measurement sets with errors as estimated from the least-square fits. The variation in the fitted decay length is expected because the measurement sets involved different resonances and resonators with a variation in their mode profiles, two different tungsten tips, and variation in the polar position as well as variations in the tip angle. Nevertheless, even not directly comparable, the mean at $\bar{d}_\kappa = 75$ nm is indicated by a dashed line.

Similarly to the numerical findings of Foreman and Vollmer [252], the fitted decay lengths are all smaller than the calculated near-field intensity decay length $d_{NF} = 118.6$ nm using Eq. (4.3) for silica, $n = 1.444$, at $\lambda = 1553$ nm. Any drift in the tip position whilst the measurement is running can also artificially reduce or increase the decay length, this will be treated in Section 4.6.3.

4.6.2 *Analysis of the backscattered power and optical quality factor*

The on-resonance backscattered power for each tip position is shown in Fig. 4.10(b). The data for up to when the tip is touching the resonator ($R \geq 0$, as defined by the linewidth grid data fit) is fitted by Eq. (4.61), which is effectively a function comprising an exponential decay length d_b multiplied with a fringe pattern. Radial and azimuthal cross sections of the data and fit of the measurement set can be seen in Fig. 4.13.

The radial cross sections in Fig. 4.13(a) show the intrinsic backscattering level when the tip is far away from the resonator. As the tip approaches, the effect of the tip becomes apparent, reducing or increasing the total backscattering depending on its azimuthal position. The fitted decay length of the influence of the tip as given by Eq. (4.61) for this measurement set is $d_b = 97(2)$ nm. A comparison of the fitted decay lengths for the backscattering power across all the measurement sets is shown in Fig. 4.11(a), giving a mean of $\bar{d}_b = 90$ nm. Similarly to the decay lengths for the linewidth influence, the backscattering decay lengths are expected to vary between measurement sets due to differences in the mode profile of the modes and change in the scatterer geometry, and also temperature drifts as will be discussed in the next section. Because the linewidth change is driven by both tip absorption and scattering, whereas the backscattering change is purely due to scattering and thus have different physical origins, two decay lengths d_b and d_κ are not expected to be the same.

The grid in Fig. 4.10(b) shows minima in the backscattering when the tip is at some distance from the resonator. This distance, referred to as the critical tip-coupling distance R_{crit}, is where the amplitudes of the induced and intrinsic scattering are the same and a suitable phase offset leads to destructive interference. For distances closer to the surface than R_{crit}, the tip is *over-coupled* – i.e., the induced backscattering due to the tip exceeds the intrinsic backscattering. As the critical tip-coupling distance depends on the coupling strength of the tip to the WGM, it will vary between different modes and scatterers. For the measurement set presented in Fig. 4.10, $R_{\mathrm{crit}} = 111(1)$ nm, i.e., the critical tip coupling is at comparable distance to the near-field penetration depth. The R_{crit} value for all the measurements are shown in Fig. 4.12. For some measurement sets, $R_{\mathrm{crit}} < 0$, meaning the induced coupling due to the tip was not sufficient to match the intrinsic coupling for any position in the near field, meaning complete backscattering suppression could not be realised for these measurement sets. The reason the tip coupling was not sufficient in these cases can be due to the spatial profile of the chosen WGM or slight variations in the polar (z) position of the tip.

The azimuthal cross sections in Fig. 4.13(b, c) show a fringe pattern in the backscattered power. The fringes are a result of the relative phase change of the induced backscattering relative to the intrinsic backscattering as the tip is translated parallel to the surface (along the azimuthal direction). The expected periodicity of the fringe pattern can be calculated from Eq. (4.56), which yields

$$\Lambda_{\mathrm{fr}}^{\mathrm{theory}} = \frac{\lambda}{2n} = 537.7 \text{ nm} , \qquad (4.63)$$
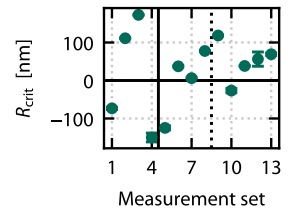
Figure 4.12. Fitted critical tip-coupling distances, i.e., the distance from the resonator surface at which the amplitude of the induced backscattering is equal to the intrinsic backscattering. The negative values represent measurements in which critical tip coupling was not achieved.
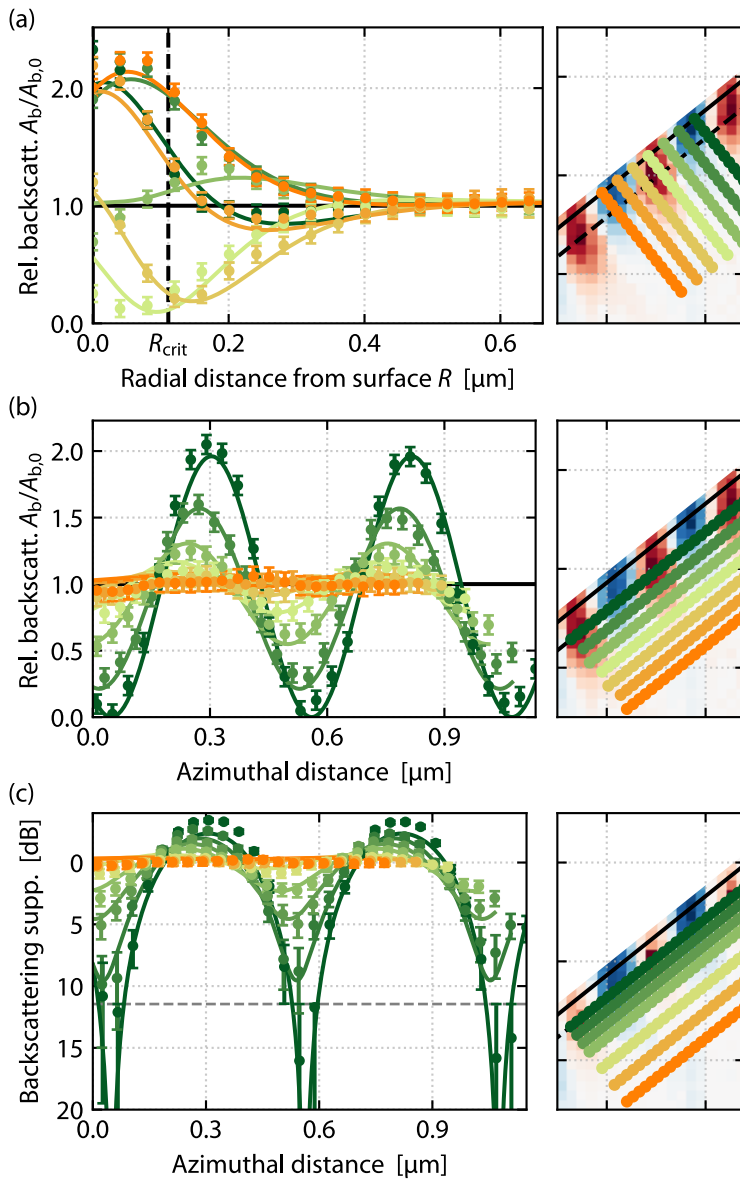
Figure 4.13. Cross sections through the backscattered power measurement grids of Fig. 4.10. The lines show the fitted backscattering dependence on the tip position, and the circles are interpolated from the grid data, with error bars given by the vacuum noise on the photodetector. The data is normalised by the intrinsic backscattering $A_{b,0}$. The insets show the positions of the cross sections in the data grid.

(a) Backscattered power as a function of the radial tip-position at some azimuthal positions. Maximum backscattering suppression occurs at the dashed line representing the critical tip coupling distance R_{crit}, for positions closer to the resonator surface, the induced backscattering is larger than the intrinsic scattering and thus the suppression decreases from its maximum value.

(b,c) Backscattered power as a function of the azimuthal tip-position at given some radial positions $R > R_{crit}$. The two panels show the data on a linear scale (a), and a logarithmic scale (b) given in terms of suppression compared to the intrinsic value, and the fits are performed on their respective scales. The dashed line represents the photodetector noise level.

for silica at the pump wavelength used. The fit for the measurement set presented in Fig. 4.10 gives a fringe separation of $\Lambda_{fr} = 513(2)$ nm, where the error given is estimated from the least squares fit. This error is small compared to the discrepancy from its theory value, and looking at this measurement in isolation it could suggest that some systematic error is present in this measurement set. When comparing the fitted values of the fringe separation across all thirteen measurement sets, as shown in the box plot of Fig. 4.11(b), this hypothesis is reinforced; the large spread of the fitted values compared to the magnitude in their estimated errors indicates that the statistical error in the fit for each set is underestimating the real error of each measurement set. The random errors between the measurement sets can be explained by random difference in systematic drift for each measurement set, such as different thermal expansion for each measurement set, as considered in Section 4.6.3.

Using the fitted fringe separation from all thirteen measurement sets, an error-weighted combined estimate[xxviii] is calculated to be $\Lambda_{fr}^{lin} = 535.1(6)$ nm. This combined estimate is close to the theoretical value of 537.7 nm, further strengthening the interpretation that there are random errors between the measurement sets. Note that the ± 0.6 nm uncertainty given for the best estimate is based on the artificially small errors as given by the fits of the measurement sets; the estimated standard error[xxix] is 20.8 nm$/13^{1/2} = 6$ nm.

Because this work focuses on the suppression aspect of this experiment, it is desirable to emphasise the small backscattering values corresponding to high suppression. A least-squares fit minimises the absolute residuals, and thus normally, a small relative residual for a higher backscattering value will be emphasised much more than the same relative residual for a smaller value. Therefore, the logarithmic suppression is fitted to optimise the fit for the high-suppression part of the fringe pattern. These logarithmic fits give a smaller spread in the fringe separation parameter, with a combined estimate $\Lambda_{fr}^{log} = 537.5(5)$ nm, which contains the theoretical value for the fringe separation within its error.

HIGHER-SUPPRESSION MEASUREMENT SET. Figure 4.14 shows data from a measurement set with higher spatial resolution in the tip-position grid. This measurement is obtained using a smaller resonator of diameter 1.74 mm with a higher-optical-Q resonator of $9.8(2) \cdot 10^8$. Because of the extraordinary high Q factor, the measurement is performed with a lower scanning speed of the optical frequency of the pump laser (-8.96 GHz s^{-1}) to avoid ring-down signals.[xxx] To avoid thermal broadening [Section 2.5.1] at this lower scanning speed, the optical input power is reduced to $\simeq 40$ μW.

The relative suppression compared to the intrinsic level is presented in Fig. 4.14(a-d), as a grid corresponding to the tip raster-scan positions as well as cross sections through the grid. The maximum backscattering suppression is measured to $44_{-10}^{+\infty}$ dB, which is below the 34 dB noise floor, blowing up the upper limit on the error and limiting the suppression claim to 34 dB. In contrast to the measurement set presented earlier, the backscattered power here decreases compared to the intrinsic level for all azimuthal positions as the tip approaches the resonator. This is because the backscattering level is linewidth dependent (see Section 4.3.2) and for this measurement set, the linewidth decreases relatively more compared to its intrinsic level than for the measurement set shown in Fig. 4.10. However,

[xxviii] The combined estimate for a parameter given a set values ξ_i with errors σ_i is the normalised, weighted sum [294, Ch. 4],

$$\xi_{est} = \frac{\sum_i w_i \xi_i}{\sum_i w_i} \quad (4.64)$$

where the weights $w_i = \sigma_i^{-2}$. The error in the combined estimate is $\sigma_{est} = \left(\sum_i w_i^{-2}\right)^{-1/2}$.

[xxix] The standard error can be estimated from the (estimated) standard deviation divided by the square root of the number of samples.

[xxx] If the input light frequency is swept faster than the cavity lifetime, the cavity is not pumped in steady state and temporal phenomena are exhibited as a consequence of the different phases of the light that have undergone different number of roundtrips [174, 295]. The result is an overshoot in the transmission signal due to the constructive interference with a decaying, oscillatory structure.
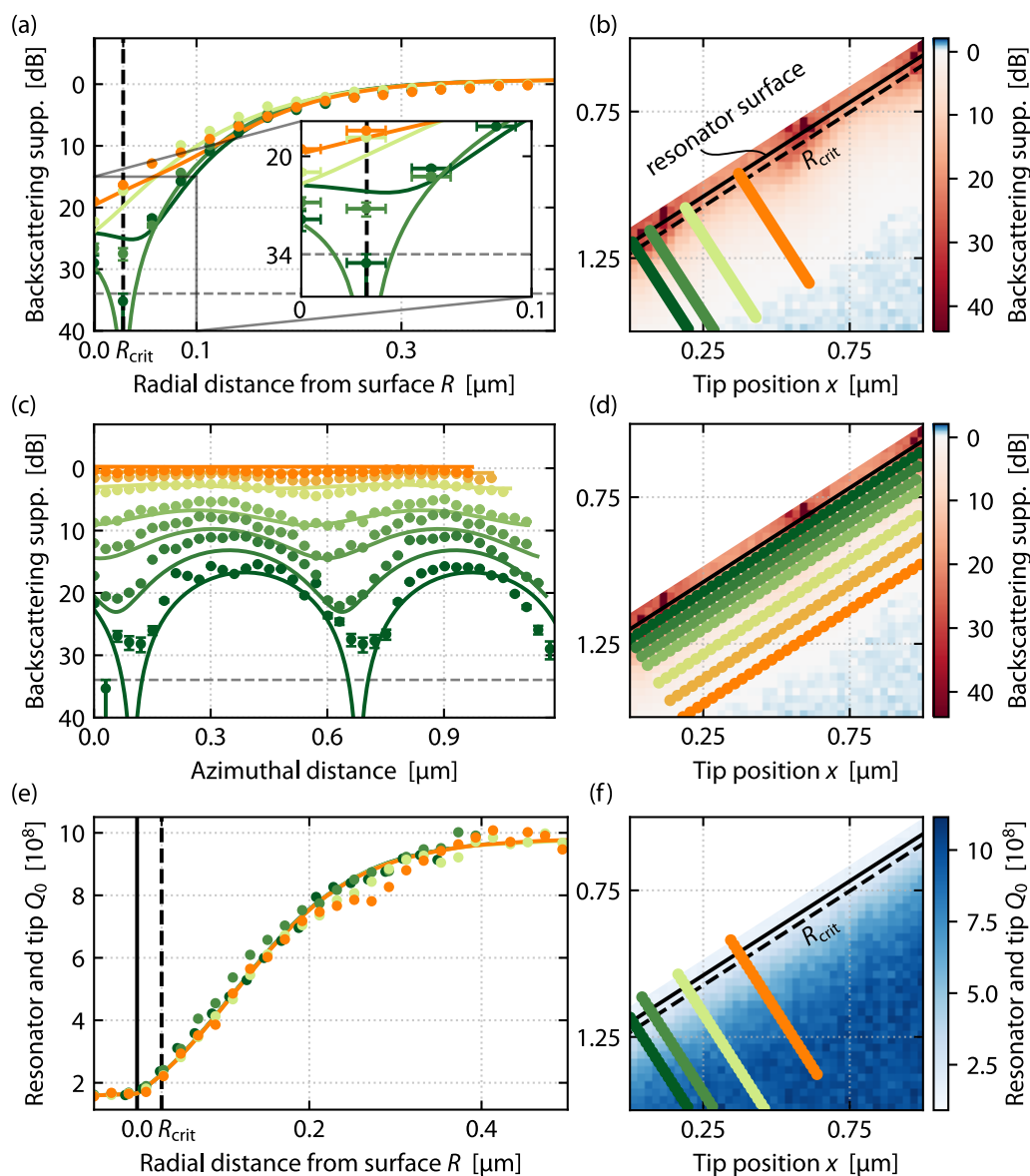
Figure 4.14. Backscattering suppression and Q_0 in a high-suppression measurement. (a) The suppression along radial lines (circles, interpolated measurement; lines, fit), with a zoom-in inset on the high suppression area. The photodetector noise level is indicated by the dashed grey line, and error bars are estimated by the photodetector noise. The inset also shows error bars in the R direction given by standard deviation of the piezo-stage actual versus target position. (b) Measured backscattering suppression for all tip positions, with the radial lines in (a) shown, as well as the resonator boundary line and critical tip-coupling distance. (c) The same plots for the suppression along azimuthal lines as shown in (d). (e,f) The optical quality factor of the combined resonator–tip system along radial lines calculated from the transmission linewidth. The Q at the critical tip coupling can be inferred from the intersection with R_{crit}.
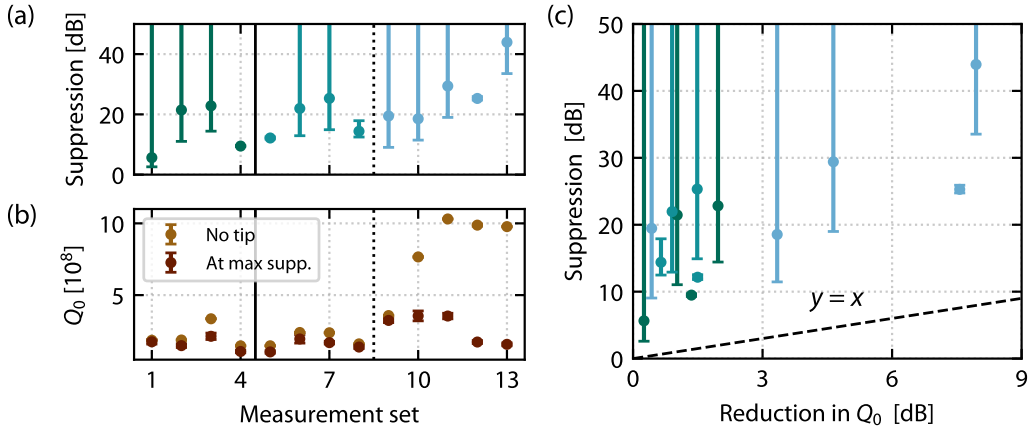
Figure 4.15. Comparison of the optical quality factor and the maximum measured backscattering suppression across the measurement sets. (a) Maximum suppression measured for each measurement set, with error bars given by the photodetector noise level. For measurements where the Lorentzian amplitude is below the noise level, the error bar extends to infinity as the measured suppression is limited by the detector noise. (b) Corresponding Q factors for the measurement sets, where the Q factor with no tip present and at maximum measured suppression are shown. (c) The maximum measured backscattering suppression compared to the relative reduction in the Q factor from its value when the tip is not present. This plot is not suggesting a functional relationship between the two parameters, as the errors in the suppression are far too large, but it shows significant reduction in the backscattering compared to the reduction in the Q factor. All experimental values are above the dashed line representing equal suppression to reduction in the Q factor.

the relative reduction in backscattering surpasses the reduction in the optical quality factor of the resonance by orders of magnitude.

For each tip position, the total and corresponding intrinsic Q factors of the system can be calculated using the expressions given in Section 2.1.2. The total Q factor is

$$Q(r, \phi) = \frac{\omega_{\text{pump}}}{2\kappa(r, \phi)} , \tag{4.65}$$

where κ denotes the total optical half-linewidth and the pump frequency used is $\omega_{\text{p}} = 2\pi \times 193.1\,\text{THz}$. Given the coupling contrast $\mathcal{K}^{\text{res}}$ extracted from the Lorentzian amplitude of the transmission spectra [Eq. (2.41)], the quality factor Q_0 of the resonator with the tip present excluding the extrinsic taper coupling losses can be estimated

$$Q_0(r, \phi) = \frac{2Q(r, \phi)}{1 + \sqrt{1 - \mathcal{K}^{\text{res}}(r, \phi)}} . \tag{4.66}$$

This Q factor is calculated and shown in Fig. 4.14(d,e). At the tip position for which the maximum suppression occurs, the intrinsic Q factor is calculated to be $Q_0 = 1.6(1) \cdot 10^8$ from the fitted linewidth of that position. That is a reduction by approximately 80 % or 7.7 dB from the unperturbed Q_0 value, however, this reduction is small compared to the $\geq 34\,\text{dB}$ reduction in the backscattered optical power.

The maximum suppression achieved and the change in the Q factor from when the tip is not present to the point of maximum suppression are shown in Fig. 4.15 for all obtained

measurement sets. Figure 4.15(c) shows that for several measurements >20 dB reduction in the backscattering is possible with only a <3 dB (<50 %) reduction in the optical Q. As most measurement sets are noise limited, the true suppression achieved can be significantly higher. Furthermore, there is a potential for optimising the scatterer material, shape and size for low absorption and high scattering to minimise the linewidth broadening for a given suppression.

4.6.3 *Stability considerations*

To control the backscattering over time, stability in the tip position is required. This work has not experimentally addressed this issue, but a few points are discussed below, particularly temperature stability.

In the measurement sets performed for this work, the longest time duration of a measurement set was approximately 45 minutes for a raster scan of the tip and obtaining spectra, but most lasted a few minutes. Any drift happening over the timescale of the measurement will influence the result, so the measurement results indicate how stable the current experimental setup is. The stability beyond these <1 hr measurement time scales has not been investigated in these experiments, neither has the reproducibility in achieving the same suppression for a given tip position at some later time after an initial measurement set is obtained.

PUMP AND INTRINSIC SCATTERER DRIFTS. The required azimuthal position of the tip for suppressing backscattering should stay unchanged for any drifts in the phase of the optical pump, as the relative optical phase between pump light at the intrinsic and tip scatterer positions will remain the same, and thus also the destructive interference of the intrinsic and tip-induced scattering.

However, a change in the effective intrinsic scatterer will require to move the tip to compensate in order to keep the backscattering level unchanged. Such a change can be caused by for example temperature fluctuations, changes in the resonator's environment, or contaminants attaching or releasing from its surface, as these affect the position and amplitude of the effective intrinsic scatterer. If the effective intrinsic scatterer position changes, the relative phase between the intrinsic and tip-induced scattering changes, and to keep the suppression stable, the azimuthal tip position must be adjusted. Similarly, if the effective intrinsic scatterer's amplitude changes, the critical tip-coupling distance will move and the tip must move accordingly to compensate for the altered intrinsic backscattered power.

TIP POSITION DRIFT. Temperature is not only a possible source of instability for the resonator itself: drift in the ambient temperature can affect the tungsten tip position. In fact, this is likely to be the limiting factor in the current experimental setup, because the thermal expansion of the bracket holding the tungsten tip is large compared to the scale of the features of the fringe pattern. Figure 4.11(b) shows a relatively large spread in the fitted fringe separations (approximately ±40 nm) compared to the statistically estimated error of each measurement set (approximately ±2 nm), suggesting that some systematic error is affecting the measurements within each measurement set. As the next paragraphs will show, a linear drift in the tip position will systematically affect the fitted parameters such as fringe separation and decay lengths because the perceived fringe pattern differs from the actual fringe pattern.

To understand how ambient temperature changes impacts the setup, consider the item with the largest thermal expansion and estimate its impact. The tungsten tip holder is 3D printed from PLA filament. The linear thermal expansion coefficient of 3D printed PLA of a density comparable to the one used here is $C_{\mathrm{PLA}} = 4.36 \cdot 10^{-4}\,\mathrm{K}^{-1}$ at room temperature [296], almost 20 times larger than that of aluminium ($0.255 \cdot 10^{-4}\,\mathrm{K}^{-1}$ [297]), which most of the other components of the setup is made from. From the definition of the thermal expansion coefficient for a piece of material of length ℓ and temperature denoted T,

$$C_\ell = \frac{1}{\ell}\frac{\mathrm{d}\ell}{\mathrm{d}T} \implies \Delta\ell \approx \ell_0 C_\ell \Delta T \,, \tag{4.67}$$

to first order. For the tip-holder bracket, which has a nominal length of $\ell_0 = 41\,\mathrm{mm}$ from the edge of the piezo positioner to the position of the tip, for example a 1.0 mK temperature change causes a 18 nm change in the bracket length, and thus also the tip position, ignoring the much smaller contribution from the aluminium parts. This change in the tip position is significant compared to the size of the fringe-pattern features such as the fringe separation and decay length.

To estimate the order-of-magnitude rate of the temperature-related tip-position change in the experiment, a temperature measurement is carried out. Using a thermocouple and digital thermocouple input module[xxxi] for digitisation, the temperature at the piezo positioner on which the PLA tip-holder bracket is mounted, and is measured over the course of three days of normal lab occupancy. The cold-junction reference of the thermocouple is stabilised, but can slowly drift over time making the absolute temperature measurement over long times uncertain; however, the derivative over short timescales should not suffer much from this drift.

[xxxi] National Instruments NI9211

To analyse the obtained temperature data and estimate the resulting tip drift, the data is first filtered. The 2-Hz absolute temperature data is downsampled by averaging to a rate of 2 min^{-1}, and then the approximate per-minute time derivative of the temperature is calculated by the discrete difference between consecutive elements. Scaling the time derivative by $\ell_0 C_\ell$ gives the approximate per-minute bracket-length time derivative [Eq. (4.67)], as presented in Fig. 4.16. It is evident that the presence of people in the lab during the daytime and evening causes fluctuations in the temperature. With a bracket length change

Figure 4.16. Estimate of the length fluctuations of the tungsten tip bracket over three days with normal lab occupancy. The temperature of the metal body on which the tip holder bracket sits is measured with a thermocouple, providing the data for the two panels. (a) The right axis shows the calculated time derivative of the temperature for each minute of the day. By scaling the right axis by the expansion coefficient of the material and the nominal length of the tungsten tip bracket, the bracket's length change per minute is estimated. To suppress the noise in the temperature measurement, the temperature data is smoothened using a centred moving average before the time derivative is calculated. (b) The cumulated temperature change (right axis) and length change (left axis) during each day. Note that changes in the cold-junction reference temperature for the thermocouple can cause drifts in the absolute temperature, but the derivative over a short time window is less impacted by this.

of tens of nanometres per minute, the cumulative bracket-length change may be as much a few hundred nanometres over the time corresponding to the duration of a measurement.

A drift in the tip position of tens of nanometres during a measurement can significantly impact the results. In Fig. 4.17, an example of tip-drift effects is shown qualitatively. To first order, the drift can be assumed to be linear, which effectively skews the raster-scan measurement grid, meaning spectral data is obtained at different positions than intended, and thus the attributed position to a datapoint is wrong. This skew in the measurement grid due to a drifting tip causes the perceived fringe separation distance to change from its actual value, and introduces an angle between the fringe pattern phase and perceived resonator surface, as can be seen in Fig. 4.17. This angle is equivalent to a radial dependence of the phase in the fringe pattern Θ [Eq. (4.47)]. Thus, to allow for drift effects in the fitting of the measured data, a radial dependence in the fringe pattern phase is introduced by adding a radially dependent, linear term $R\theta_R$, where θ_R is a free parameter.

Furthermore, these drifts will also impact the fitted decay lengths of the tip influence on the optical linewidth and backscattering, contributing to the large spread in the fitted decay lengths as the temperature drift could have varied between the measurements. Generally, if the tip drifts towards the resonator, the perceived decay length would be smaller than its real value as the tip is moving further than the data analysis expects. However, fitting the decay length along the axis normal to the perceived resonator surface, which can be at an angle with respect to the real radial axis $R^{\dagger}$, can make the perceived decay slope less steep than it is in reality, and thus result in a longer decay length.

Linear drift can be parametrised by two independent parameters, for instance the drift in x and y, or the magnitude of the drift and angle with respect to the real resonator surface. From the parametrised distortion, the resulting rest-frame-interpreted coordinate system
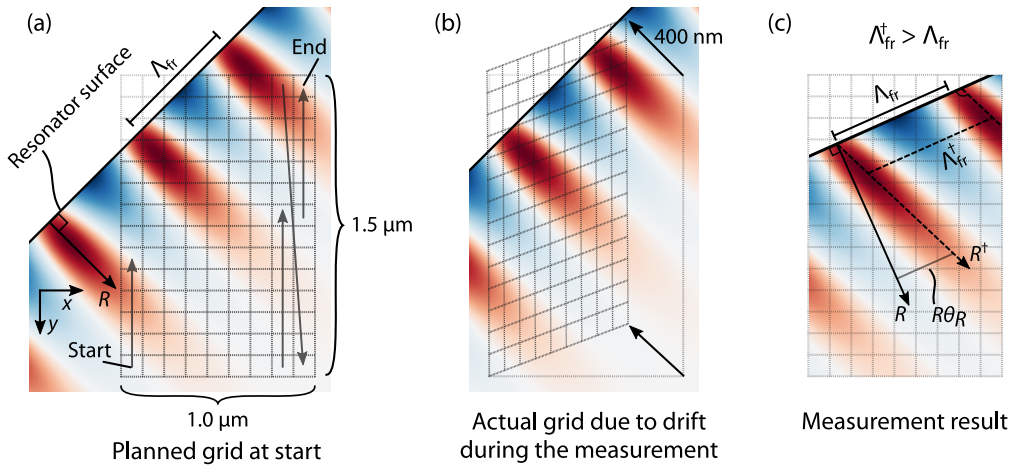
Figure 4.17. A qualitative analysis of the effect on a measurement of drift in the tip position. Here the effect on the backscattering measurement is considered, but a similar analysis for the linewidth measurement can be done. (a) The backscattering pattern resulting from a tip at that position with the planned measurement grid overlaid. (b) Over the course of a 10-minute measurement, drift in the tip position of 40 nm/min changes the shape of the actual measurement grid, causing the measured backscattering values to be according to the values in the distorted grid. Here shown for a tip drifting towards the resonator. (c) The result from the measurement as interpreted in the non-drift reference frame. The fringe pattern separation in the data $\Lambda_{\mathrm{fr}}^{\dagger}$ is larger than the real fringe separation Λ_{fr}, and the fringe pattern is not normal to the perceived resonator surface (the normal axis denoted R is not parallel to the fringe pattern, but the modified axis $R^{\dagger}$ is). To best fit the backscattering pattern to the measured data allowing for drift effects, a radial dependence in the fringe pattern phase Θ can be introduced by adding a radially dependent term $R\theta_R$, where θ_R is a free parameter.

can be found, and the drift can then be estimated from the experimental data. This will not be attempted here because from the present data, any estimated tip drift cannot be verified by other data, and secondly because a better strategy would be to rather experimentally reduce this drift in later experiments.

Temperature measurements were not performed whilst obtaining the optical measurements presented in this chapter and thus cannot be used to correct for any possible temperature related effects for those measurement sets. The measurement sets were typically obtained late in the evening or night when the building and lab were quiet, but inevitably, to operate the experiment, the author would be present in the lab, representing a thermal load moving in the vicinity of the experiment.

To mitigate the temperature effects, the bracket material can easily be changed to for instance aluminium, which would reduce the temperature effect to approximately a twentieth. Furthermore, the current setup was not built with high temperature stability in mind, and simple improvements in the thermal isolation of the setup can be made. A more substantial change can be to move to a chip-based resonator with a scatterer integrated on the chip, eliminating the distance between the tip mount and resonator.

4.7 SUMMARY AND OUTLOOK

Optical microresonators provide prospects for miniaturised sensing and communications systems; however, backscattering compromises the performance of some microresonator-based systems. This problem has attracted more attention over the last years, with publications showing suppression techniques for waveguide ring resonators and WGM resonators. In this chapter, a method for coherently suppressing the intrinsic backscattering in an optical WGM microresonator has been presented, demonstrating a record suppression exceeding 34 dB (noise limited) from an already low level where frequency splitting is not resolved.

Backscattering control enables chiral, pure travelling-wave resonators, where optical power flows in one direction only in the cavity and there is no standing-wave-mode component, without the challenge of tuning the system to an exceptional point. For some microresonator applications, backscattering is a factor limiting the performance. These applications include symmetry-breaking-based sensing, optomechanics applications, laser gyroscopes and dual frequency combs. The backscattering suppression technique demonstrated here can both improve existing systems and enable the development of new high-accuracy, portable optical spectroscopy systems, gyroscopes, and other sensors.

Multiple measurements across three different resonators demonstrate the experimental viability of the presented technique, and the results align with the theoretical framework and model. The measured impact on the optical quality factor due to the presence of the tip is orders of magnitude smaller than the achieved suppression, and optimisation of the scatterer size and material can help to improve this ratio even further.

Longer term stability of the suppression and reproducibility for a given scatterer position has not been investigated as a part of this work. A more suitable mounting of the scatterer for higher precision and to mitigate thermal-expansion effects is desirable and will be important for a stability study. Active feedback on the scatterer position in order to keep the suppression at a desirable level can be implemented.

The technique presented is of particular interest for on-chip WGM and waveguide ring resonators, where a scatterer can be permanently integrated on the chip to coherently suppress back reflections. Waveguide ring resonators designs and fabrication procedures have been rapidly improved over the past decade as they are favoured for commercial applications due to their so-called all-waveguide structures where the coupling waveguide is integrated on the chip with the resonator. The all-waveguide structure gives fewer moving parts and full chip-integration, as well as compatibility with existing commercial silicon electronics manufacturing technology, see e.g. Puckett *et al.* [225] for a state-of-the-art example of such resonators or Gao *et al.* [86] for a discussion on materials for these resonators.

For these mass-produced on-chip resonators, a scatterer can be permanently integrated either during fabrication or in post. This will give improved stability by reducing any thermal-expansion effects to a minimum and because the miniaturised system allows

better vibrational and environmental isolation. An integrated MEMS-based scatterer for tuneable backscattering suppression and control can also be envisaged.

Towards quantum applications with Brillouin cavity optomechanics
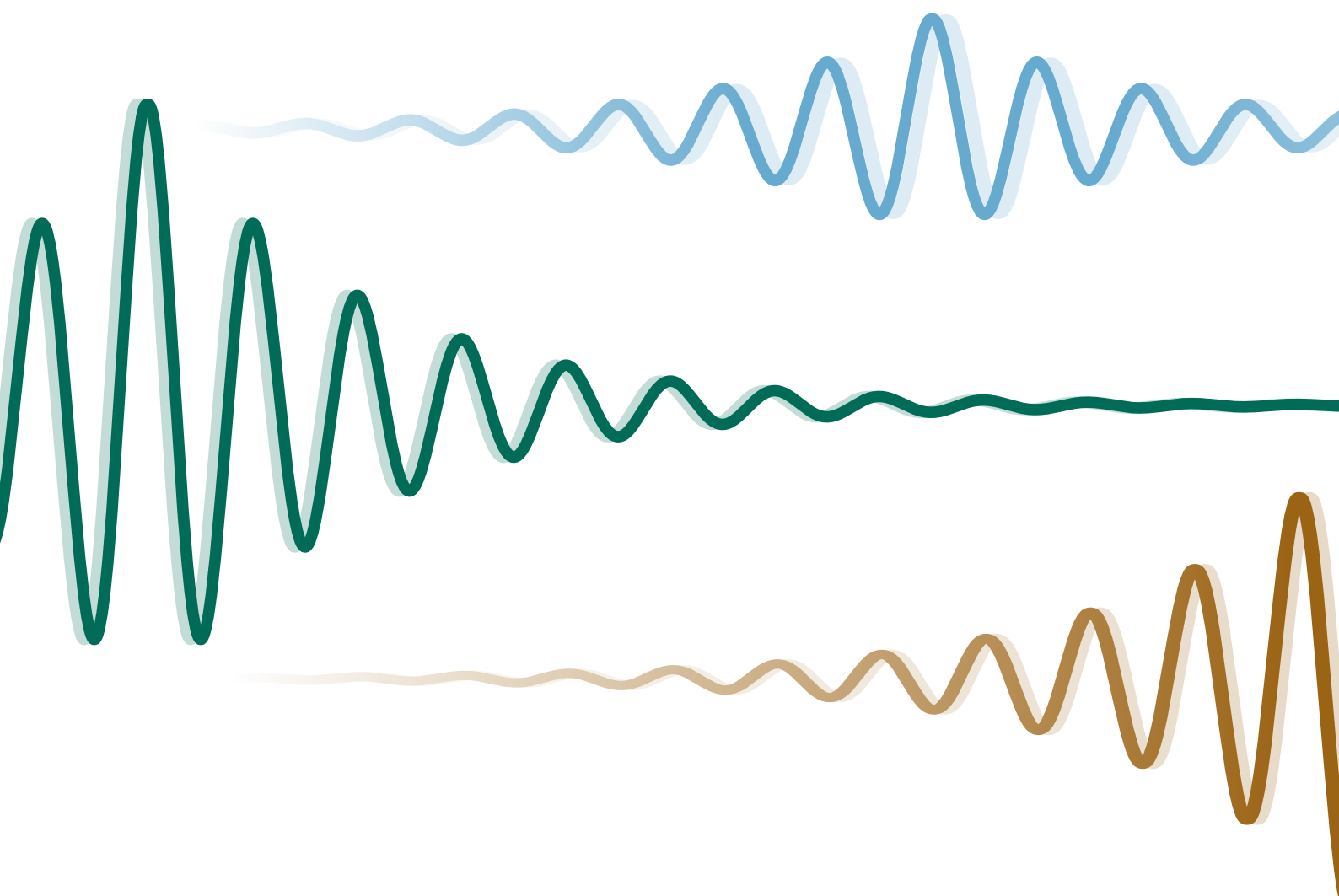
CHAPTER 5

A brief introduction to cavity quantum optomechanics

As early as the seventeenth century, Johannes Kepler speculated whether sunlight was exerting a force on comets' tails, causing the tails to point away from the sun [298, 299], and even speculated on the possible use of solar propulsion in correspondence with his contemporary, Galilei: *[..] provide ships or sails adapted to the heavenly breezes, and there will be some who will brave that void* [as quoted in 300]. Although many scientists worked on showing the radiation pressure force from light experimentally, it was not until centuries later, in the early nineteen-hundreds, that experiments by Lebedew [302] and others were able to show that light does carry momentum (the historical background and early experiments are covered by Nichols and Hull [303]). Solar sails for space travel have since become reality, being used as a secondary propulsion system for certain missions [300], but there are other areas where radiation pressure has been of much larger significance.

[concentrated rays from an electric lamp] falling on a thin metallic disc, delicately suspended in a vacuum, might perhaps produce an observable mechanical effect.
— Maxwell [301]

After Lebedew conducted his experiments in the early 1900s, it would take another half century before the introduction of the laser made coherent light sources available, enabling experimentalists to pursue further studies and to exploit the momentum carried by light for applications. A prominent example of such an application is optical trapping of dielectric particles first demonstrated by Ashkin [59] – a now-ubiquitous technique called optical tweezers, enabling research in labs around the world, with its significance highlighted by a Nobel Prize awarded in part to Ashkin for his work. About a decade prior, a Nobel Prize had been awarded to another use of the photon momentum: researchers Chu, Cohen-Tannoudji and Phillips received the prize for the development of methods to cool and trap atoms with laser light [304] where the momentum transfer from photons to atoms can slow down the atoms' movement [305]. Later, even another Nobel Prize was awarded in part to Wineland for his work involving laser cooling of ions [306]. These techniques are all commonly used, especially in many quantum science experiments.

In the late 1960s, Braginsky and colleagues began their pioneering work in studying the coupling between electromagnetic radiation and mechanical degrees of freedom in cavities [e.g. 307], the very beginning of what is today called cavity optomechanics. In the decades to follow, cavity optomechanics for displacement sensing was a hot topic, laying the foundation for the recent detection of gravitational waves with optomechanical displacement sensing using interferometers with suspended mirrors in the LIGO experiment [61]. Using squeezed light for beyond-standard-quantum-limit sensitivity, LIGO reaches a maximum sensitivity of below 10^{-19} m Hz$^{-1/2}$, corresponding to resolving displacements of about a ten-thousandth of the diameter of a proton at its most sensitive frequency [308, 309]. The importance of this experiment has also been recognised with a

Nobel Prize shared between three of the most significant contributors to LIGO's achievements.

What exciting science can be built on these achievements? Beyond optical trapping, cooling, and mind-blowing displacement sensitivity, the coupling of coherent light fields and mechanical degrees of freedom allows to generate and probe quantum states of mechanical motion. In this lies a potential for tests of fundamental physics, such as the very interpretation of quantum mechanics, exploring the interface between gravity and quantum physics, as well as a range of possible advances for quantum technologies. The first section of this chapter will expand on the motivation for continued research on optomechanics and quantum acoustics with technological impact in mind.

Quantumness has also shifted from being the very reason why experiments are constructed to becoming a resource for the investigation of fundamental physics and the creation of quantum technologies.
— Barzanjeh *et al.* [65]

Cavity optomechanics [15, 310], a term typically covering systems based on both microwave and optical frequencies of electromagnetic radiation, has developed quickly over the last decades, fuelled by advances in microfabrication techniques, and cryogenic systems being more widely available, amongst other drivers. Whispering-gallery-mode resonators have been used as a platform for optomechanics experiments: the canonical radiation-pressure coupling to vibrational modes has been studied [e.g. 24–26], and also other light-matter coupling mechanisms such as Brillouin scattering [12, 28, 311], where light scatters off density waves in the WGM resonator [27, 29, 31]. Since the first Brillouin optomechanical experiments in WGM resonators were reported in 2009 [32, 33], strong optomechanical coupling via Brillouin scattering has been demonstrated in WGM resonators [64], and a range of theoretical and experimental work has been published, see for instance Refs. 29, 30, 57, 74, 312–315 and references therein.

Brillouin-based optomechanics is a promising platform for quantum science as it can provide long-lived, high-frequency phonons in materials with low optical absorption: long life times means longer coherence times and GHz frequencies means there is a low mean thermal phonon occupation for finite temperatures, which makes it easier to reach the quantum ground state, an essential first-step for quantum control and engineering.

In this chapter, key concepts and theory for cavity optomechanics with focus on Brillouin-based systems will be presented to serve as a foundation for the following chapter on generation and measurement of non-Gaussian mechanical states realised by phonon subtraction from a thermal state. As an introduction, this chapter motivates the quantum optomechanical research programme briefly, then summarises a classical description of a radiation-pressure-based device and important figures of merit for an optomechanical system, before describing Brillouin optomechanics in whispering-gallery-mode resonators.

CHAPTER CONTENTS

5.1   A BROAD MOTIVATION FOR QUANTUM OPTOMECHANICS

The prelude of this chapter lists some achievements of optomechanical systems, such as optical trapping and the detection of gravitational waves. Looking forward, coherent coupling between photons and phonons is a useful process also in the context of the current rapid advance in so-called quantum technologies for sensing, metrology, and information transfer and processing. Over the last decades, research in the direction of quantum technologies has flourished, with advances in microfabrication methods, cryogenics, and experimental control as important drivers – and perhaps some geopolitical risk mitigation[i] by governments [317], significantly increasing research funding programmes in these areas [e.g. 318].

The ill-defined term quantum technology[ii] typically refers to the application of quantum science for practical purposes within and beyond research, leveraging quantum phenomena such as superposition, entanglement, and teleportation of quantum states. Some areas of research with various degrees of demonstrated results, expected potential, and technical and fundamental challenges ahead, are quantum metrology [320, 321] and sensing [322, 323], quantum communication [324], and quantum simulation [325, 326]. In addition comes what is seen by many as the ultimate goal since its inception some forty years ago: harnessing quantum technology for computation [327]. The idea of quantum computing is often attributed to Feynman, and in particular his 1981 talk at the conference *Physics of Computation* [328], but many other prominent physicists and computer scientists were central in the birth and early days of quantum computing [329].

Much has happened in physics and engineering since the 1980s, and the goal posts for quantum computing have moved from simulating physics to a universal, fault-tolerant, meaningfully scalable quantum computer [330–333], able to take advantage of the enormous parallel computing capacity qubits can provide. The advantage over classical computers has famously been theoretically demonstrated with examples such as Shor's seminal algorithm for factoring large prime numbers [334] or Grover's algorithm for searching in unsorted databases [335]. It has proven challenging to realise the vision of a quantum computer, partially because of challenges related to scalability of potential experimental platforms, but fundamentally because quantum states easily couple to their environment, changing their state in what is practically an irreversible manner, losing their quantum superpositions providing the quantum parallelism. This effect, called (environmental) decoherence, can be addressed by better isolating the quantum states from their environment – but isolating the quantum system perfectly from the environment makes it increasingly harder to interact with it for performing the necessary manipulations and result readout needed for meaningful computing. Therefore, hybrid quantum systems are expected to be important, where resilient systems for transferring quantum information are linked with systems that are convenient for manipulation and computation [336, 337]. Optomechanical systems are well suited to be such a mediator [338].

[i] The 2016 demonstration of satellite-based entangled-photon distribution by Yin *et al.* [316] has by some been labelled a *sputnik moment*, equating it with the surprise and change in military thinking in especially the US after the USSR's launch of the first artificial Earth satellite into orbit in 1957.

[ii] Dowling and Milburn [319] used this definition in 2003: *Quantum technology allows us to organize and control the components of a complex system governed by the laws of quantum physics.*

[n]ature isn't classical, dammit, and if you want to make a simulation of nature, you'd better make it quantum mechanical, and by golly it's a wonderful problem, because it doesn't look so easy.
— Feynman [328]

5.1.1 *Quantum-coherent transduction and other quantum technologies*

Photons are excellent information carriers for a number of reasons, including their speed and bandwidth, because they typically interact little with their environment and each other, and their many degrees of freedom that can be used to encode information, spatially, spectrally, polarisation and intensity. Fibre optics has enabled internet as we know it today and will, for the same reasons, also most likely underpin quantum networks [68, 339]. But as the previous chapter of this thesis notes, photons interact weakly with each other – in fact not at all in vacuum [340] – and achieving nonlinear effects associated with computation with photons requires a suitable medium and generally high optical intensities. A quantum computer will need capabilities to process, store, and transmit quantum information. Similarly to a classical computer whose chip processing the information is based on electronic transistors, whereas the choice of platform for information transmission is photons either in the radio frequency or optical bands, a quantum computer and other quantum technologies will most likely employ hybrid combinations; for example, a system can use superconducting qubits for computation [69] and photonic interconnects [341].

Mechanical motion can couple coherently with light through for instance radiation pressure, and the coupling can be enhanced by an optical cavity. The mechanical and optical frequencies, as well as the coupling between light and mechanics, can be engineered and tuned to various degrees depending on the implementation of an optomechanical system. This makes optomechanical systems attractive as interfaces between different quantum systems – between those that can be easily manipulated, like mechanical or radio-frequency electronic systems, and those that are more robust, like photons. Promising results have already been demonstrated in optomechanical experiments for transduction of quantum information from optical frequencies to microwave frequencies compatible with electronics (review on quantum transduction [66]; selected optomechanical experiments [23, 341–350]), as well as transduction between different optical frequencies mediated by optomechanics [67]. The fidelity of the transduction, i.e., the likeness of the input state to the output state, of such conversion must be high for a quantum network to work efficiently and reliably, and there is still a long way to go to boost the fidelity and operation rates.

In addition to providing coherent transduction, optomechanical systems can also process quantum information [351, 352], and are a promising candidate for quantum memories. Quantum memories are far from trivial not only because of decoherence, but amongst other reasons also because a quantum state cannot be directly copied (by the no-cloning theorem [353]), and upon measurement a state can collapse to a state different from the initial state. To implement long-lived quantum memories, the long coherence times of mechanical oscillators can be exploited with for instance a photonic quantum state transferred onto a mechanical oscillator, storing the quantum information, and then the state can be retrieved at a later time by transferring the state back onto an optical mode [342, 354–356]. This type of quantum memory is expected to play an important role in quantum networks in what are called quantum repeaters used in the famous DLCZ

protocol [339], where entanglement [357] is used to transmit quantum information over long distances to overcome the exponential loss associated with optical fibres and other media [339, 358, 359].

Beyond quantum information applications, optomechanics is employed in research in all the other major areas of quantum technology; a recent review by Barzanjeh *et al.* [65] discusses optomechanics as an experimental platform for quantum technologies. Within sensing, LIGO is a prominent example, achieving below-shot-noise sensitivity using squeezed light [309], but also examples of table-top optomechanical experiments showing sensitivities close to or below the standard quantum limithave been shown for sensing mechanical motion [41, 240, 360, 361], force [362], torque [363], and acceleration [364]. The high sensitivity of optomechanical sensors has also been used for biosensing applications [8, 365, 366].

Other recent demonstrations related to quantum acoustics and optomechanics notable for their potential technological use are for example squeezed light generation from an optomechanical experiment [367, 368], mechanical solitons [369], and phononic circuits [71–73] with phonon-number-resolving detectors [370–372] and optomechanical interfaces [70].

5.1.2   *Where the field is coming from and where it might be headed*

Quantum cavity optomechanics as an area of research was born from cavity optomechanics when Braginsky and others started considering the quantum limits to the sensitivity of gravitational wave detectors [373]. Subsequently, much of the development within the field was focusing on exploring quantum physics itself, especially on exploring superpositions and entanglement of macroscopic objects towards probing the quantum-to-classical transition.

In the late 1990s, seminal proposals how to generate non-classicality between a cavity field and a mechanical oscillator were published [374, 375]. After the turn of the millennium, proposals for optomechanical experiments that via radiation pressure can create and study superposition states of a mechanical oscillator [376] and entanglement between oscillators [377] were also published. Furthermore, proposals for quantum state transduction [378, 379] and teleportation of a quantum state via entanglement of light and mechanics [380] were also published at the time. For a review discussing the early theoretical developments see Genes *et al.* [381].

The 2010s saw several important experimental milestones in optomechanics being achieved. The first experimental demonstration of optomechanical strong coupling[iii] was reported [382], and later also quantum coherent coupling [23, 383]. The quantum ground state was reached for various macroscopic mechanical oscillators, first via dilution refrigeration [384] and then via sideband cooling, both in the optical [385, 386] and microwave [387] domains; demonstrations of entanglement between mechanical motion and microwave [388] and optical [389] fields, as well as between mechanical oscillators [390, 391] and optical fields [392, 393] via optomechanics; quantum-coherent transduc-

[iii] Optomechanical strong coupling and quantum coherent coupling is defined in Section 5.2.2.

tion was shown [23, 346]; and non-classical quadrature-squeezed states of motion [394] and light [367, 368], as well as Fock states of motion were prepared in both optomechanical [395] and quantum acoustical [396] systems.

So what will the 2020s bring? The main focus on creating and measuring non-classical states of macroscopic mechanical oscillators[iv] will still be an important direction for the field, with further developments towards using these tools for probing fundamental physics [15, 398, 399]. Proposals for such experiments include exploring the interface between quantum mechanics and gravity [400, 401], collapse models [402, 403] and the measurement problem, and improve the understanding of quantum decoherence [65]. In addition to further pursuing gravitational wave detection as a tool for astronomers, also proposals for dark-matter detection using optomechanical systems exist [404].

Even though the many promising results listed in the section on quantum technologies show the breadth of potential use of quantum optomechanical systems for technological advances, it should be noted that these results are mostly early demonstrations, and even with the field rapidly advancing, there are years of work to come to engineer more robust, more compact systems with better performance, moving the systems from research labs to customers. Thus, the coming years will likely see improvements to many of the first-time demonstrations of the 2010s, improving control, measurement efficiencies, and other performance parameters, as well as some of the same milestones reached for different experimental realisations.

When it comes to improving experimental control, the rise of so-called measurement-based control [74, 208, 405–410] is promising, which is one of the two main approaches for quantum control of mechanical motion. Typically, coherent control is used, where the mechanical oscillator is coupled to an engineered controller system, ensuring the system of interest converges to the quantum state sought. An example of coherent control is sideband-cooling where the mechanical oscillator is coupled to a coherent light field in such a way that it is effectively coupling the thermally excited mechanical motion to the essentially zero-temperature thermal bath of the light field, and thus cooling the mechanical oscillator. Alternatively measurement-based techniques, where a combination of measurements and feedback on the quantum system is used to bring the system to the desired state. As better measurement efficiencies are realised, measurement-based techniques can more easily be used.

As the milestones listed above show, progress has been made in regard to non-classical state generation, but there are still outstanding goals both in generation and measurement of non-classical mechanical states. Many proposals for generation of more complex non-classical states such as Schrödinger-cat states exist [409, 411–417]. Schemes for measuring non-classical motional states of mechanical oscillators via optomechanics has been proposed [418], but it is still an outstanding goal in optomechanics (it has been achieved for the motion of a trapped ion [419, 420]). Over the last years, steps have been taken in the direction of phase-space characterisation of a mechanical quantum state via tomography in both quantum acoustics with superconducting qubits [396] and optomechanics [75, 418, 421, 422] – Chapter 6 of this thesis describes the work in Ref. 75 in detail.

[iv] Recently, Whittle *et al.* [397] demonstrated cooling of a 10-kg mirror in one of LIGOs interferometer arms down to an average of 10.8 phonon occupancy in its centre-of-mass mode. Approaching the motional ground state of a mass of this scale is unprecedented, representing a 13-orders-of-magnitude increase in the mass compared to previous ground state cooling works.

5.1.3 *Summary*

Quantum cavity optomechanics has developed rapidly over the past decades. The interaction between light and mechanics is a powerful tool providing insight into fundamental physics and access to many of the quantum resources that make quantum technologies quantum, such as entanglement. The research is thus motivated both by the valuable insight gained form probing quantum motion, as well as demonstrated and potential technological applications.

Over the previous decade a plethora of different experimental realisations of optomechanical systems with different properties and advantages have been demonstrated. Several experimental milestones have been reached, showing increasingly better control over these experimental realisations. With the many building blocks demonstrated – cooling to the mechanical ground state, preparation of non-classical states, entanglement between oscillators, et cetera – optomechanical systems will most likely see uses in all areas of quantum technology. However, even with the field rapidly advancing, there are years of work to come to engineer more robust, more compact systems with better performance, moving the systems from research labs to customers.

5.2   THE CANONICAL CAVITY OPTOMECHANICS DEVICE, AND VARIANTS

The canonical example of a cavity-optomechanical device is a Fabry–Pérot optical cavity, where one end mirror is fixed and the other suspended, see Fig. 5.1. The suspended mirror is allowed to move in a damped, harmonic fashion along the x dimension, such that when an optical field of angular frequency ω_{cav} is coupled into the cavity, the moving end mirror of the cavity will modulate the light field, and simultaneously, the radiation-pressure force[v] imparted by the light field on the suspended end mirror will change the movement of the mirror. This coupled system leads to non-trivial dynamics, opening the rich field of cavity optomechanics.

[v] The force imparted on a mirror by an incoming beam of optical power $\mathcal{P}$ is $F = 2\mathcal{P}/c$.

Leaving aside the backaction from the light on the mechanics for now, consider the effect of the moving end mirror for a single cavity mode with angular frequency ω_{cav}: the cavity frequency can be expanded in terms of the mechanical displacement $x(t)$ from the
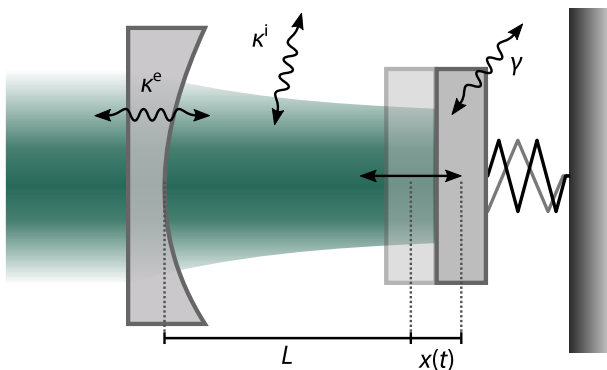
Figure 5.1. A canonical Fabry–Pérot-type optomechanical system: a light field is coupled into a cavity of length L where one end mirror is suspended. The optical coupling losses κ^{e}, cavity losses κ^{i} and mechanical damping rate γ are annotated.

equilibrium position of the end mirror,

$$\omega_{\mathrm{cav}}(x) = \omega_{\mathrm{cav}}(0) + x \left.\frac{\partial \omega_{\mathrm{cav}}}{\partial x}\right|_{x=0} + \frac{x^2}{2} \left.\frac{\partial^2 \omega_{\mathrm{cav}}}{\partial x^2}\right|_{x=0} + \dots , \tag{5.1}$$

where $\omega_{\mathrm{cav},\,x=0}$ is the unperturbed cavity frequency. Typically for radiation-pressure based optomechanics, the expansion can be linearised by only considering the first-order frequency shift per mirror displacement,

$$d = -\left.\frac{\partial \omega_{\mathrm{cav}}}{\partial x}\right|_{x=0} , \tag{5.2}$$

where the sign is chosen so that an increase in cavity length ($x > 0$) for a cavity with positive coupling ($d > 0$) results in a frequency decrease. For a simple Fabry–Pérot-type cavity of length L, Eq. (5.2) yields $d = \omega_{\mathrm{cav}}/L$.

The product of the frequency shift per displacement and the zero-point motion of the mechanical resonator is called the (bare) optomechanical coupling, $g_0 = d x_{\mathrm{zp}}$, where the zero-point fluctuations for an oscillator at angular frequency ω_{m} and with effective mass m_{eff} is $x_{\mathrm{zp}} = \sqrt{\hbar/(2 m_{\mathrm{eff}} \omega_{\mathrm{m}})}$. The optomechanical coupling is thus how much the cavity frequency shifts if the mechanics is displaced by its zero-point motion. The coupling rate is typically much smaller than the optical and mechanical decay rates of the system, the coupling rate can be enhanced by increasing the number of photons in the cavity. The cavity enhanced coupling $G = g_0 \sqrt{N_{\mathrm{cav}}}$ where N_{cav} is the number of intracavity photons.

5.2.1 *Different optomechanical systems*

In addition to suspended mirror cavities [423, 424], a large range of other systems differing from the canonical Fabry–Pérot-type example can exhibit optomechanical coupling between high-Q optical and mechanical modes. For instance different types of WGM microresonators have mechanical vibrational modes that can interact with an optical field [23, 26, 64, 360]. A non-exhaustive shortlist of other examples include different types of photonic-phononic nano-beam crystals [425] such as single-beam [385, 426], double-beam zipper cavities [427], split-beam [428], or single-beam-double-cavity crystals [429]; different types of so-called membrane-in-the-middle systems [430] such as a semi-transparent dielectric membrane suspended in a FP cavity [362, 405, 431], a levitated particle [432, 433] or atoms [434] in a cavity; bulk crystalline resonators [163]; and shell-resonators [435]. Also pressure-waves in superfluid helium in a FP cavity [436] and as a coating layer on a WGM resonator [437] has been used for optomechanical experiments. A similar example of the oscillator being external to the WGM resonator is a nanoscale dielectric oscillator placed within the evanescent field of a WGM resonator [240]. See Fig. 5.2 for images and illustrations of selected examples from the literature.

These systems show different implementations of coupling of optical fields with mechanical vibrations. For the WGM resonators coupling can be mediated by the radiation-pressure force at the resonator surface due to the internal reflection [24–26], similarly to
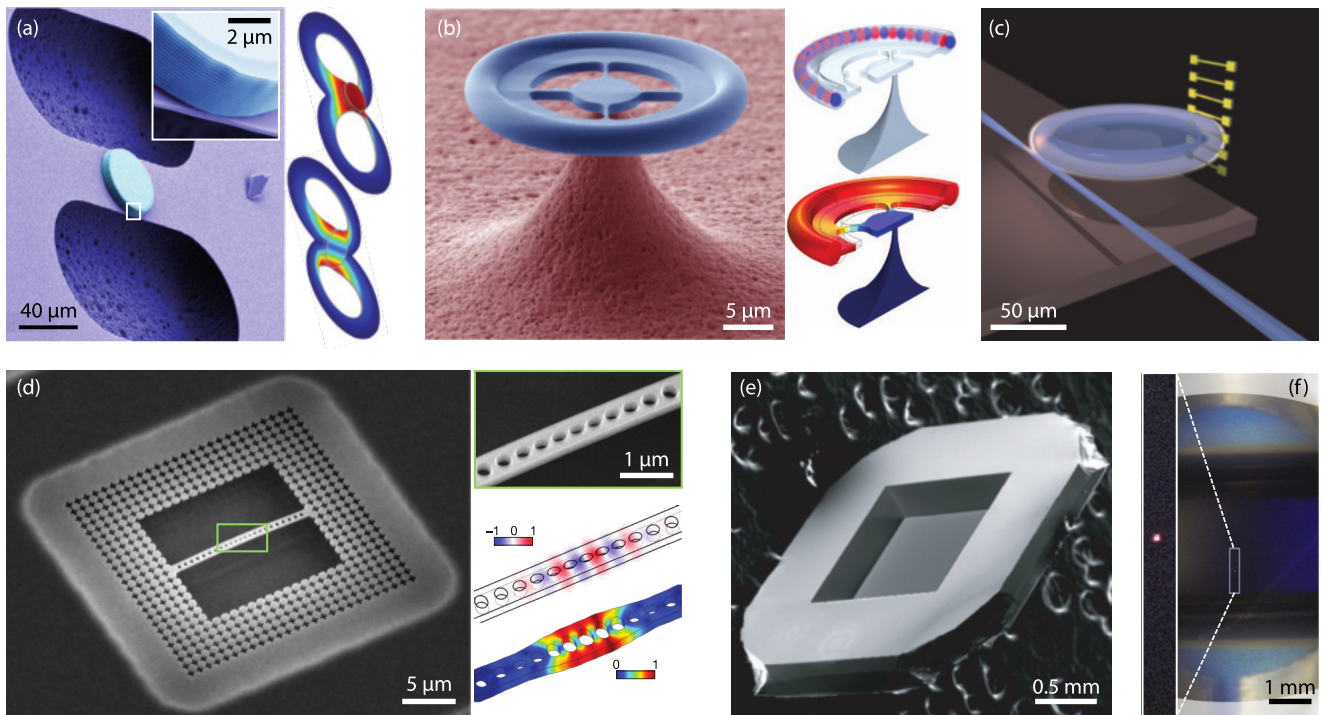
Figure 5.2. Examples of micro-optomechanical systems. The selected systems are early demonstrations, and Qf products are not necessarily state-of-the-art for similar systems today. (a) Gröblacher *et al.* [438]: A suspended Bragg mirror (stack of alternating Ta_2O_5 and SiO_2) mounted on a Si_3N_4 beam forms one side of a FP cavity: $\omega_m/(2\pi) \simeq 1\,MHz$, $Q_m \simeq 10^4$, $Q \simeq 10^6$. Exaggerated fundamental and first higher-order vibrational modes shown in the right top and bottom, respectively. (b) Verhagen *et al.* [23]: A 31-μm-diameter silica-on-silicon WGM toroidal resonator with vibrational modes excited by radiation pressure. The fundamental breathing mode is shown exaggerated in the bottom right panel, the top right indicates the phase of the light field: $\omega_m/(2\pi) \simeq 100\,MHz$, $Q_m \simeq 10^4$, $Q \simeq 10^8$. (c) Anetsberger *et al.* [240]: A 110-nm-thick nano-beam in the evanescent field of a WGM resonator $\omega_m/(2\pi) \simeq 10\,MHz$, $Q_m \simeq 10^5$, $Q \simeq 10^7$. (d) Chan *et al.* [385]: A silicon nano-beam optomechanical crystal with $\omega_m/(2\pi) \simeq 4\,GHz$, $Q_m \simeq 10^5$, $Q \simeq 10^5$. Bottom right panel illustrates the normalised electric field of the optical cavity (top) as well as the normalised displacement co-located mechanical breathing mode (bottom). (e) Thompson *et al.* [431]: A 50-nm-thick SiN membrane placed inside a FP cavity: $\omega_m/(2\pi) \simeq 130\,kHz$, $Q_m \simeq 10^6$, $Q \simeq 10^6$. (f) Kiesel *et al.* [439]: A levitated silica sphere of radius 130 nm trapped in an optical FP cavity: $\omega_m/(2\pi) \simeq 170\,kHz$, $Q_m \simeq 25$, $Q \simeq 10^9$. *Copyrights:* (a–d) Macmillan Publishers, each panel reprinted with permission from Springer Nature; (e) Nature Publishing Group, reprinted with permission from Springer Nature; (f) The article authors, reprinted according to PNAS guidelines.

the canonical case where the coupling strength is determined by the frequency shift due to mechanical displacement; or it can be due to Brillouin scattering [27–30, 32, 33], where the optical field scatters off a high-frequency acoustic wave due to the refractive index change caused by the acoustic wave's mechanical deformation of the material (which is the basis for the work in this thesis, see Section 5.3). For nano-beam optomechanical crystals, different mechanical displacement modes (breathing, accordion, pinch) couple to the co-localised photonic-crystal modes via radiation pressure, and the mechanical displacement in turn modulates the light field. For the membrane-in-the-middle systems, the coupling is, similarly to the canonical case, caused by the light field's momentum transfer caused by the semi-transparency of the membrane; and it is the membrane's position in relation to the cavity nodes that determines the coupling. [vi] Lastly, for the nanomechanical beams coupled to a WGM it is the evanescent field driving the oscillator and the effective refractive index change induced by the beam that causes the coupling; the coupling is determined by the distance separating the beam and the resonator.

5.2.2 *Figures of merit and optomechanical coupling regimes*

As for optical resonators, an important figure of merit for a mechanical resonator is the quality factor. It is defined similarly to an optical resonance's quality factor,

$$Q_{\mathrm{m}} = \frac{\omega_{\mathrm{m}}}{2\gamma} \, , \tag{5.3}$$

where ω_{m} is the angular frequency of the mechanical oscillation and γ is its amplitude decay rate. The state-of-the-art mechanical Q factors in optomechanical experiments are in the billions, with $Q_{\mathrm{m}} = 5 \cdot 10^{10}$ achieved for an optomechanical-crystal nano-beam at milli-kelvin temperatures [161]. Recent experimental work with crystalline strained silicon nano-beams showed a mechanical Q of $1 \cdot 10^{10}$ at 7 K [443], and a mechanical Q of $3 \cdot 10^{10}$ at room temperature has been shown for so-called perimeter modes of silicon nitride polygons vibrating at frequencies approaching megahertz [444].

STRONG AND WEAK COUPLING REGIMES. When comparing the mechanical and optical decay rates to the optomechanical coupling, two regimes are identified, called the strong and weak coupling regimes. When the optomechanical coupling is stronger than the optical and mechanical loss rates, $G > \{ \kappa, \gamma \}$, the system is in the *strong coupling regime*. The strong coupling makes it possible to manipulate the mechanical oscillator at a faster rate than it dissipates energy which is important for some experimental protocols. The cavity enhancement available can increase the coupling via $G \propto \sqrt{N_{\mathrm{cav}}}$, but for many systems, optical heating makes reaching the strong coupling regime impractical. The first experimental demonstration of optomechanical strong coupling was performed by Gröblacher *et al.* [382], and ten years later it was demonstrated also in a Brillouin optomechanical system by Enzian *et al.* [64].

[vi] The interest in nonlinear optomechanics, where the second-order position-coupling term in Eq. (5.1) is significant, makes these membrane-in-the-middle systems attractive, because they effectively couple two optical cavities with the mechanical motion, but affecting the cavities with opposite signs, see for instance Burgwal *et al.* [440]. Also other systems such as levitated optomechanical [432] or nano-beam systems [441, 442] have demonstrated nonlinear optomechanical coupling.

strong coupling regime

DECOHERENCE. In the quantum domain it is not just the dissipation of the mechanical oscillator that is of importance, but also its quantum decoherence [445] – a measure of how long the resonator keeps its quantum properties and correlations before they are lost via coupling to the environment. The key to many quantum applications is to isolate the state sufficiently from the environment to keep the quantum coherence but still be able to perform measurements and manipulate the state.

The quantum decoherence rate is state dependent, but in optomechanics, because the mechanical oscillator is coupled to a thermal bath at a finite temperature, the *thermal decoherence rate* is a key parameter. It describes the rate at which quanta are flowing into the mechanical oscillator from the thermal environment:

thermal decoherence rate

$$\Gamma_{\text{th}} = \gamma \bar{n}_{\text{th}} , \tag{5.4}$$

where $\bar{n}_{\text{th}}$ is the mean occupation of the thermal bath the mechanical oscillator is coupled to. Considering the decoherence contribution also from vacuum fluctuations, the total decoherence can be written

$$\Gamma = \gamma \left[\bar{n}_{\text{th}} + \frac{1}{2} \right] , \tag{5.5}$$

where for $\bar{n}_{\text{th}} \gg 1/2$, the thermal decoherence dominates and for $\bar{n}_{\text{th}} \ll 1/2$ vacuum fluctuations dominate.

Like photons, quanta of vibration are bosons, and the mean occupation of the mechanical bath is given by the Bose–Einstein distribution,

$$\bar{n}_{\text{th}} = \left[\exp\left(\frac{\hbar \omega_{\text{m}}}{k_{\text{B}} T} \right) - 1 \right]^{-1} \approx \frac{k_{\text{B}} T}{\hbar \omega_{\text{m}}} , \tag{5.6}$$

where k_{B} is Boltzmann's constant, and the approximation can be made for the classical limit in which $\bar{n}_{\text{th}} \gg 1$. For a 1 GHz mode at room temperature the mean occupation is $\bar{n}_{\text{th}} \simeq 6 \cdot 10^3$, which decreases to $5 \cdot 10^2$ for typical pulse-tube cryocooler temperatures (4 K) and 0.1 for dilution refrigeration temperatures (20 mK).[vii]

From Eqs. (5.5) and (5.6) it also becomes apparent why the thermal decoherence rate is not relevant for optical modes at room temperature, as $\bar{n}_{\text{th}} \sim 10^{-20}$, which is much smaller than the vacuum fluctuations.

QF PRODUCT. A figure of merit for comparing robustness to thermal decoherence for mechanical oscillators is the product of the mechanical quality factor and mechanical frequency, called the Qf *product*, as it essentially determines the ratio of the mechanical frequency to the thermal decoherence rate and thus captures the number of coherent mechanical oscillations:

[vii] In electromechanical systems, where RF oscillators are coupled to mechanical motion, the ground state has been reached using passive cooling for GHz mechanical oscillators [384]. A recent demonstration even showed reaching the ground state for its 15 MHz fundamental vibrational mode using passive cooling down to 500 μK via nuclear adiabatic demagnetisation cooling [446].

$$\frac{\omega_{\text{m}}}{2\Gamma_{\text{th}}} = \frac{\omega_{\text{m}}}{2\gamma \bar{n}_{\text{th}}} = \frac{\omega_{\text{m}}}{2\gamma} \frac{\hbar \omega_{\text{m}}}{k_{\text{B}} T} = Q_{\text{m}} \omega_{\text{m}} \frac{\hbar}{k_{\text{B}} T} \propto Q_{\text{m}} f_{\text{m}} . \tag{5.7}$$

Qf product

Note that Qf product is not independent of the temperature, and should be compared to the value of $k_{\text{B}} T/\hbar$ for a given operating temperature. For the state-of-the-art work by

MacCabe *et al.* [161], a mechanical Qf product of 10^{20} Hz was demonstrated, compared to $k_\text{B}T/\hbar \sim 10^9$ Hz. Brillouin optomechanical systems show state-of-the-art Qf products of 10^{17} Hz at cryogenic temperatures [163, 447].

QUANTUM COHERENT COUPLING REGIME. In addition to distinguishing between the strong and weak coupling regimes, also the more challenging *quantum coherent coupling regime* where $G > \{ \kappa, \Gamma_\text{th} \}$ is used as a term to describe a regime where the quantum state can efficiently be transduced from mechanical oscillator to the light field, and vice versa. This has been achieved for radiation-pressure-based optomechanics by Verhagen *et al.* [23] and electromechanics by Teufel *et al.* [383].

quantum coherent coupling regime

5.3   BRILLOUIN CAVITY OPTOMECHANICS

A 100 years ago this year, the French physicist Brillouin predicted that light can inelastically scatter off density waves in a medium [311]. Today this phenomenon is referred to as Brillouin scattering. The density waves in the medium act as a moving diffraction grating for the propagating light, changing the light's momentum and energy. Since its prediction in the early 20th century, and subsequent mid-century discovery [448], the process has been extensively studied in the nonlinear optics community [12, 95], mostly as a troublesome effect for optical fibre communications. However, over the last decade or so the Brillouin coupling between the light field and mechanical movement has been utilised for cavity optomechanical experiments.

Brillouin scattering has some properties making it attractive for optomechanics. The nonlinearity is present in any medium that exhibits a photoelastic response, which is most media. The acoustic waves involved in Brillouin scattering are typically in the GHz-frequency-range, which means bulk thermal cooling of high-frequency mechanical modes is possible with commercial cryogenics. Furthermore, the system has an intrinsically large frequency separation between the drive field and scattered light, and directional separation makes it easier to distinguish the optical pump from the generated light at the Stokes or anti-Stokes frequencies.

The first Brillouin optomechanical experiments were realised in 2009, where the Stokes scattering was studied in calcium fluoride [32] and silica [33] WGM microresonators. A quantum theory of cooling by Brillouin scattering was published in 2011 [449] and subsequently shown experimentally the year after [315]. Recently, Brillouin optomechanical strong coupling was shown for a 11 GHz mechanical mode in a silica WGM resonator [64]. An early review by Bahl and Carmon [29] gives an overview over the first experiments, and a more recent review, Wiederhecker *et al.* [27], shows the development since.

5.3.1 *Brillouin scattering*

Brillouin scattering is a three-wave nonlinear interaction, coherently coupling two optical fields and one acoustic field. The coupling is mediated by photoelasticity and electrostriction: acoustic waves in the material locally changes the density and thus the refractive index (photoelasticity), affecting the electromagnetic field; and the presence of a light field locally changes the density of the material via electrostriction (Fig. 5.3). Brillouin scattering is different from the formerly described Rayleigh scattering as the density modulation in the material is a travelling wave in the case of Brillouin scattering, not stationary as in Rayleigh scattering, which is an elastic process.[viii] Because the density fluctuations move, the Brillouin scattering process is inelastic (as can be understood via the Doppler effect), and results in higher and lower frequency light depending on the scattering conditions.

[viii] And to complete the optical scattering family: Raman scattering is when light scatters off phonons at optical frequencies [95, Ch. 1].

A classical derivation using the equation of motion for a pressure wave and an electromagnetic wave equation can be shown (e.g. Boyd [12, Ch. 9]), where the time-varying density modulates the polarisation of the material and gives rise to sidebands in the optical field spaced by the mechanical frequency,

$$\omega_\pm = \omega_\mathrm{p} \pm \omega_\mathrm{m} , \tag{5.8}$$

where $\omega_\pm$ is the anti-Stokes and Stokes sidebands, respectively. The pump light can scatter off either co- or counterpropagating acoustic waves, called forwards or backwards scattering. This gives rise to four possible interactions: forward or backward scattering resulting in either frequency up- or down-converted light. Conservation of momentum sets the following requirements for the wave vectors

$$\mathbf{k}_\pm^\mathrm{fw} = \mathbf{k}_\mathrm{p} - \mathbf{k}_\mathrm{m} , \tag{5.9a}$$

$$\mathbf{k}_\pm^\mathrm{bw} = \mathbf{k}_\mathrm{p} \mp \mathbf{k}_\mathrm{m} , \tag{5.9b}$$

where the superscripts fw and bw indicate forward and backward scattered light (with respect to the pump light) and plus and represent anti-Stokes and Stokes scattering, respectively. The conservation equations (5.8) and (5.9) are often referred to as phase-matching conditions. Figure 5.3(a) illustrates the phase matching for backwards anti-Stokes scattering via the optical dispersion relation.

The density waves in the medium can be excited thermally (also referred to as spontaneous Brillouin scattering in the literature), or stimulated optically via electrostriction: a strong pump optical field beats with the thermally Brillouin scattered optical field, causing increased density waves at the Brillouin frequency. The pump field will in turn scatter off the stronger refractive index modulation caused by the stronger density waves, which adds to the already scattered light, amplifying the process. How effectively light scatters can be described by a Brillouin gain parameter, see Boyd [12].
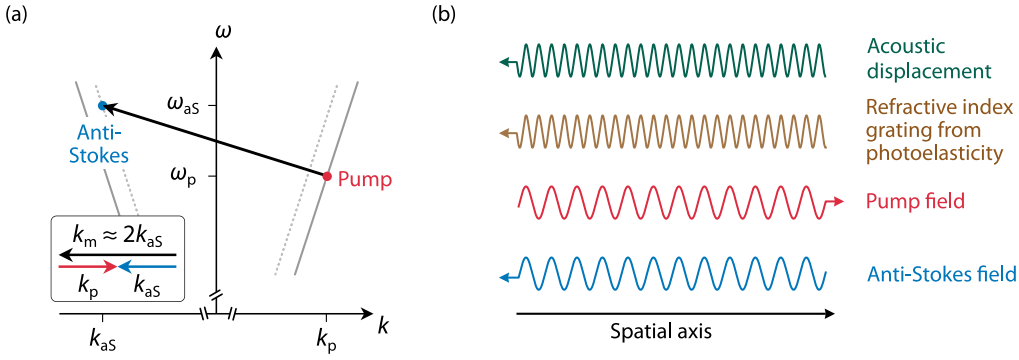
Figure 5.3. The Brillouin anti-Stokes backwards scattering process. (a) Dispersion relation for the two involved optical modes, showing the phase matching condition for the backwards scattering between the two where a phonon is absorbed in the process. (b) Illustration of thermal anti-Stokes scattering, where a thermally excited density wave via photoelasticity changes the refractive index of the medium, creating a propagating, Bragg mirror-like modulation. The optical pump field non-elastically scatters off the refractive index modulation, resulting in a counterpropagating anti-Stokes field. The waves are offset in the figure but in reality they overlap. Panel (a) is adapted from Price [450] (CC BY-NC licence).

THE BRILLOUIN FREQUENCY. The Brillouin frequency can be deduced from the momentum conservation requirement Eq. (5.9) and the mechanical and optical dispersion relations

$$\omega_m = |\mathbf{k}_m| v_{ph} , \tag{5.10}$$

$$\omega_i = |\mathbf{k}_i| \frac{c}{n} , \tag{5.11}$$

For the backwards anti-Stokes scattering, inserting Eq. (5.9b) into Eq. (5.10)

$$\omega_m = |\mathbf{k}_p - \mathbf{k}_{aS}| v_{ph} \approx 2|\mathbf{k}_p| v_{ph} , \tag{5.12}$$

where the approximation is valid for $\omega_m \ll \{ \omega_{aS}, \omega_p \}$. Inserting the energy conservation (5.8), gives the Brillouin frequency as a ratio of the phase velocities of sound to light in the medium

$$\omega_m = \frac{2 v_{ph}}{c/n} \omega_p , \tag{5.13}$$

which is typically in the GHz-range for Brillouin optomechanical systems [29].

INTERACTION HAMILTONIAN. In the quantum domain, Brillouin scattering is a three-wave process coupling a phonon and two photons. The interaction Hamiltonian can be written [449]

$$\hat{H}_{int} = \hbar g_0 (\hat{a}_{blue} \hat{a}_{red}^\dagger \hat{b}^\dagger + \hat{a}_{blue}^\dagger \hat{a}_{red} \hat{b}) , \tag{5.14}$$

where g_0 denotes the single-photon coupling strength of the interaction, and $\hat{a}$, $\hat{b}$ are the bosonic annihilation operators for the optical modes and mechanical mode, respectively, and † is used to denote their creation operator counterparts. The coupling rate g_0 is related to the Brillouin gain, see Van Laer *et al.* [28]. The Hamiltonian shows how lower-frequency photons (red) are swapped for higher-frequency (blue) photons by absorbing a phonon, or the reverse process where a red photon and a phonon is created from a blue photon.
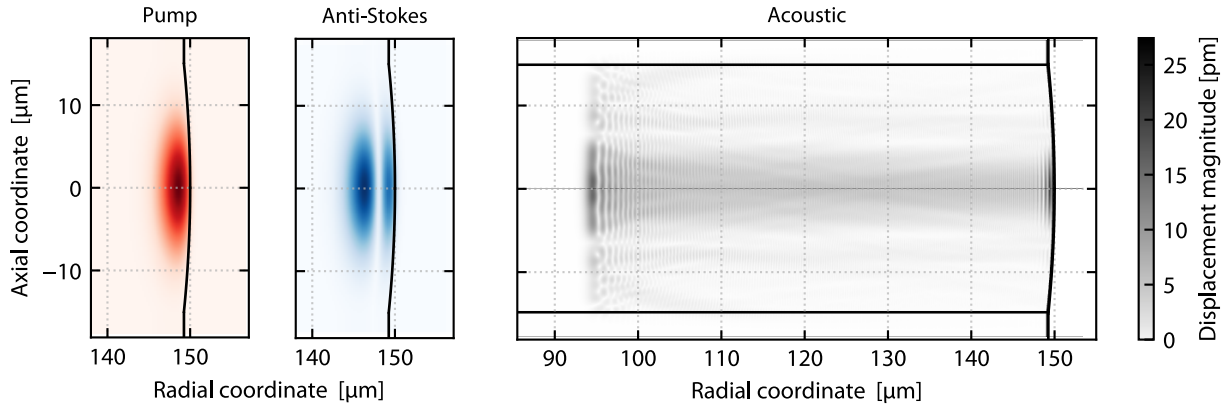
Figure 5.4. Profiles of coupled optical and mechanical modes. Finite-element-method simulation of mode profiles for a 150-μm-radius silica sphere. The pump mode is a fundamental mode and the anti-Stokes mode the first radial order mode, with darker colours corresponding to a larger electric field norm. The quasi-longitudinal acoustic mode providing the coupling between them is distributed over a much larger area, going deep into the silica sphere. The high displacement magnitude at around 95 μm is not an artefact of the simulation, but can be understood as the transversal component of the wave propagates along a cord through the sphere, and with the deepest point set by the central angle of the cord. At the deepest point, the density of overlapping cords is high giving a high total displacement. Finite-element-method simulation data courtesy of L. Freisem.

5.3.2   *Mechanical whispering-gallery modes*

The opening of Chapter 2 described Rayleigh's[ix] acoustic whispering-gallery modes in St. Paul's Cathedral, and now the acoustic domain features again. Optical WGM microresonators can also support acoustic WGM modes, such that optical and mechanical WGMs can interact if they overlap spatially and satisfy the imposed phase-matching conditions.

Analytical treatment of acoustic WGMs in optical microresonators reveals three different wave polarisations, one pseudo-longitudinal and two transversal modes, where the polar transverse is fast and the radial transverse (also called Rayleigh type) is slow [312, 451]. The pseudo prefix is because the longitudinal modes are in fact hybrid transverse-longitudinal as they are slightly reflected inwards in the resonator structure as they propagate. Similarly to the optical WGMs, the acoustic WGMs also have families of modes, with higher radial and polar orders. A finite-element-method simulation of a pseudo-longitudinal WGM is shown in Fig. 5.4.

Knowing the speed of sound for a longitudinal wave, the approximate Brillouin frequency for a quasi-longitudinal mode can be found using Eq. (5.13). In barium fluoride at room temperature, the speed of sound for the pseudo-longitudinal modes is $v_{\mathrm{ph}} = 4.38\,\mathrm{km\,s^{-1}}$ [314], which for 1550 nm light means that the approximate Brillouin frequency is $\omega_{\mathrm{m}}/(2\pi) \simeq 8.3\,\mathrm{GHz}$.

[ix] It should be noted that also Raman and Sutherland [79, 80] made important contributions to understanding the acoustic whispering-gallery mode phenomenon.

5.3.3   *Mechanical anisotropy and the Brillouin gain*

If Brillouin scattering is occurring in a WGM resonator made from an optically isotropic medium, the beat note of the two optical modes is constant with the azimuthal angle over a round trip of the resonator. However, if the medium is acoustically anisotropic and exhibits any variation in the speed of sound along the azimuth, this corresponds to a varying Brillouin frequency shift along the azimuth. When the Brillouin frequency is changing, the mechanical excitations at different azimuthal angles will to some extent cancel each other out, resulting in a reduced Brillouin gain and thus a reduced optomechanical coupling. Therefore, a low mechanical anisotropy in the resonator material is important to ensure good optomechanical coupling. Cubic and hexagonal crystals typically show the lowest mechanical anisotropy [164] and are also optically isotropic [12].

Based on these considerations, Enzian [165] identified crystalline barium fluoride, BaF_2, as a good candidate for cavity Brillouin optomechanics due to its low optical losses at 1550 nm and relatively high and isotropic elasticity, and low acoustic losses [89]. Moreover, Enzian [165] and Diallo *et al.* [313] independently found that a resonator plane normal to the [111] crystal axis would yield the smallest variation in the speed of sound over the course of a roundtrip along the azimuth, making this the optimal axis for resonator fabrication to avoid dephasing along the azimuth.

To show that the [111]-axis plane is the optimal resonator plane, the velocity variation for any chosen resonator plane is computed. The phase velocity for a given crystal direction can be found via solving the the Christoffel equation for a given stiffness/elasticity tensor and material density [452]. The equation gives three solutions corresponding to the three acoustic wave polarisations, one pseudo-longitudinal and two transversal, fast and slow. As BaF_2 is a cubic crystal, there are only three independent entries in the stiffness tensor, c_{11}, c_{12}, c_{44}, the two first of which show a temperature change of about $-10\,\%$ from cryogenic to room temperature, see Fig. 5.5.

The Christoffel equation can be conveniently solved using the published software by Jaeken and Cottenier [452]. The stiffness tensor values used in these calculations are taken from Jain *et al.* [454] as found in de Jong *et al.* [455] – the values are for the material at 0 K, which are practically the same as close to the 4 K cryostat operating temperature [453, 456]. Solving the eigenvalue problem, the phase velocity along any crystallographic direction can be calculated, as shown in Fig. 5.6(a) for the phase velocity of pseudo-longitudinal waves. From the phase velocities from crystal all directions, the variation across a WGM path for a given resonator–crystal orientation can be calculated from the phase velocities at the intersection between a resonator plane with normal vector (a, b, c) and the unit circle, and the alignment of the crystal axis resulting in the smallest variation can be chosen.

To parametrise the intersection circle along its roundtrip angle $\beta \in [0, 2\pi)$, two normal unit vectors in the resonator plane $\mathbf{v}_1, \mathbf{v}_2$ can be used,

$$\mathbf{r}(\beta) = \mathbf{v}_1 \cos(\beta) + \mathbf{v}_2 \sin(\beta). \tag{5.15}$$
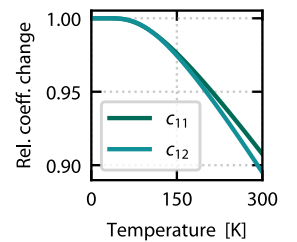
Figure 5.5. Temperature dependence of the stiffness tensor elements of BaF_2 relative to 0 K according to Varshni [453]. The change of the third independent tensor element, c_{44}, is negligible over the temperature range considered.

To find the unit vectors, start by choosing $\beta = 0$ so that $\mathbf{v}_1 = \mathbf{r}(0) = (0, y_1, z_1)$. Then note that the resonator plane can be expressed

$$ax + by + cz = 0 \quad \Leftrightarrow \quad z = -\frac{ax + by}{c} \tag{5.16}$$

using the entries from its normal vector. Together with the unit circle equation $x^2 + y^2 + z^2 = 1$, z can be eliminated whilst simultaneously plugging in $x = 0$:

$$y_1^2 + \left(-\frac{b y_1}{c}\right)^2 = 1 \quad \Rightarrow \quad y_1 = \frac{c}{\sqrt{b^2 + c^2}}. \tag{5.17}$$

Then $z_1 = -b/\sqrt{b^2 + c^2}$, resulting in $\mathbf{v}_1 = (0, c, -b)/\sqrt{b^2 + c^2}$, which is of unit length. To obtain the other unit vector in the resonator plane, calculate the cross product $(a, b, c) \times \mathbf{v}_1$ and normalise it to obtain $\mathbf{v}_2 = (b^2 + c^2, -ab, ac)/\sqrt{b^2 + c^2}$.

A few intersection rings for selected crystal orientations can be seen in Fig. 5.6(a), and the velocity variation along these circles plotted in Fig. 5.6(b) and (c). Figure 5.6(d) shows the maximum phase velocity for a resonator plane for all orientations, showing that the [111] orientation is the most favourable. Note also that the [111] direction is the resonator plane with the least variation in the phase velocity also for the fast transversal waves, but has a higher relative variation of $3 \cdot 10^{-3}$.

5.3.4 *Brillouin scattering in a cavity and selective driving*

For Brillouin scattering to occur in a cavity, not only do the phase-matching conditions need to be satisfied, but to have an appreciable rate of the scattering, the resonator must have an appreciable density of optical states at the optical frequencies involved in the interaction. If the cavity is in the *resolved sideband regime* where the Brillouin frequency is much larger than the cavity linewidth, $\omega_{\mathrm{m}} \gg \kappa$, this means that the spacing between the involved optical resonances must be approximately equal to the Brillouin frequency. Unless the free-spectral range of the resonator matches the Brillouin frequency, a pair of modes spaced by the Brillouin frequency will not have a third, equidistant optical mode available to scatter into, see Fig. 5.7. This allows to selectively drive the Stokes or anti-Stokes interaction by pumping on the higher or lower frequency mode in the pair, respectively.

resolved sideband regime

When selectively driving the anti-Stokes process with a strong, coherent pump field at the red resonance, the quantum fluctuations in the pump field can be neglected and the pump field operator is swapped for a coherent amplitude $\hat{a}_{\mathrm{red}} \to |\alpha|$. In this linearised regime, the interaction Hamiltonian Eq. (5.14) can be rewritten

$$\hat{H}_{\mathrm{bs}} = \hbar g_0 |\alpha| (\hat{a}_{\mathrm{aS}} \hat{b}^\dagger + \hat{a}_{\mathrm{aS}}^\dagger \hat{b}), \tag{5.18}$$

where the pump-enhanced optomechanical coupling rate can be identified,

$$G = g_0 |\alpha| = g_0 \sqrt{N_{\mathrm{cav}}}. \tag{5.19}$$
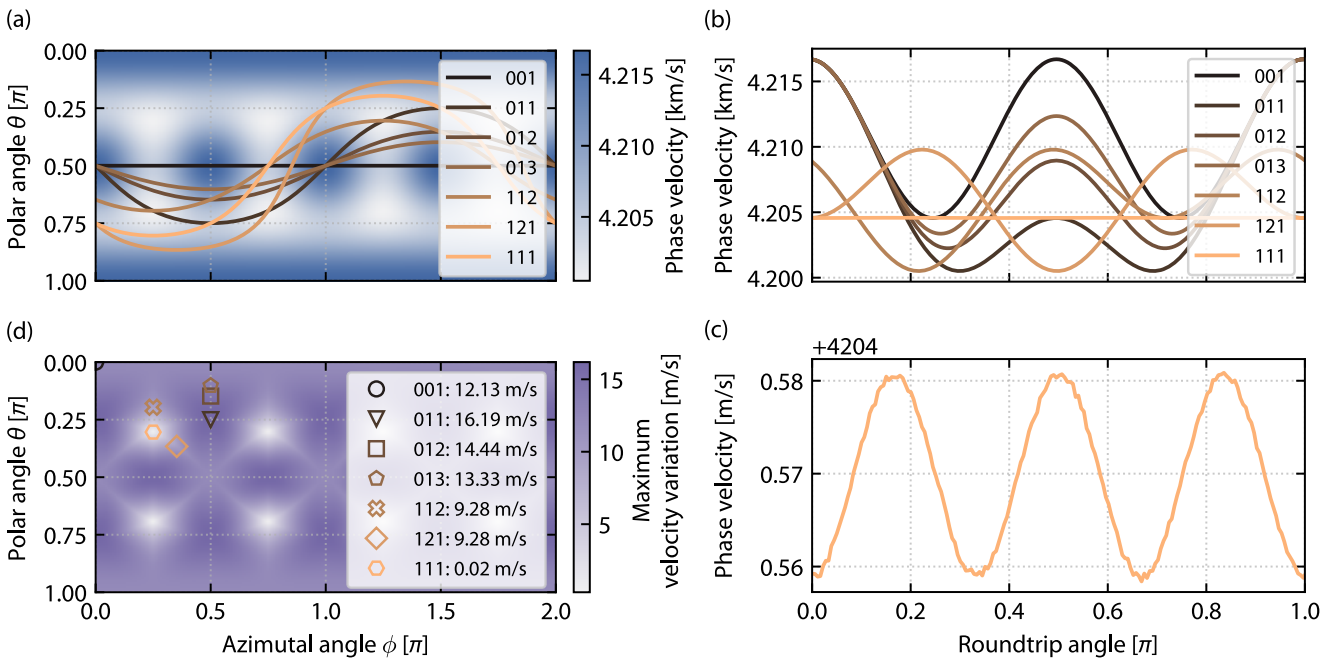
Figure 5.6. Phase velocity variation of quasi-longitudinal pressure waves along crystallographic axes in barium fluoride at 0 K. (a) Phase velocity for a pressure wave along a direction given in spherical coordinates on a unit sphere – for instance the speed along the [001] crystallographic direction corresponds to the value found at $(\theta, \phi) = (0, 0)$. The lines indicate the paths of WGMs traversing a crystal oriented so that the resonator plane is normal to the given crystallographic directions (i.e., the line plotted is the intersection between a plane whose normal vector is pointing in the crystallographic axis specified and the unit circle). Due to symmetry, the octants are equal, but all octants are shown to better visualise the paths. (b) The phase velocities sampled over a half-roundtrip for a few selected resonator plane choices (it is symmetric about π), and (c) zoomed in on the [111] resonator orientation line. (d) Maximum phase velocity variation over the course of a roundtrip of a resonator plane with a normal vector pointing in the (θ, ϕ) direction. The markers show the crystallographic directions of the lines drawn in the other panels. The smallest variation is found for the [111] (= [–111] = [1–11] = ...) direction, varying only by $0.02 \,\mathrm{m\,s^{-1}}$ over the course of a roundtrip, corresponding to a $4.8 \cdot 10^{-6}$ relative variation. At 300 K, the variation increases by an order of magnitude to $0.37 \,\mathrm{m\,s^{-1}}$ (relative variation $9.1 \cdot 10^{-5}$) for the [111] axis.
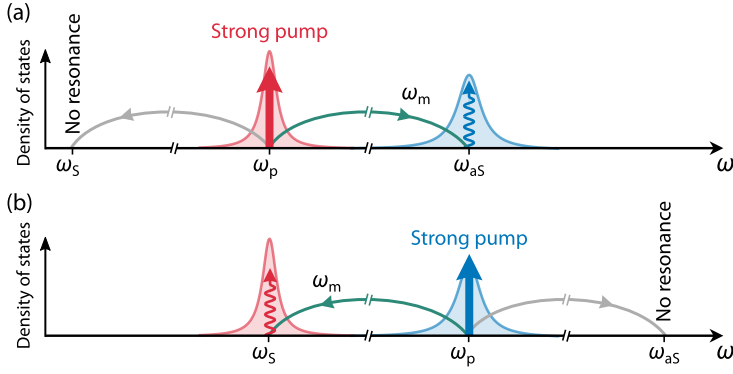
Figure 5.7. Cavity Brillouin optomechanics in the resolved sideband regime. Selectively driving the (a) anti-Stokes or (b) Brillouin interaction in a cavity in the resolved sideband regime.

This interaction is similar to that of an optical beam splitter [179, Ch. 4], and is therefore called a beam-splitter-type Hamiltonian. Phonons and pump photons are swapped for anti-Stokes photons, which means the mean occupancy of the mechanical mode is reduced, corresponding to an effective reduced temperature of the mechanical mode. To understand the time dynamics of the optical and mechanical state, the full Hamiltonian should be identified and the quantum Langevin equations of motion can be solved.

CAVITY HAMILTONIAN. Equation (5.14) gives the interaction Hamiltonian, but also the harmonic oscillator terms contribute to the full Hamiltonian. When Stokes resonance is pumped with a strong coherent field $|\alpha|e^{i\omega_p t}$, the full Hamiltonian can be written [450]

$$\hat{H}_{\text{full}} = \hbar \left[|\alpha|g_0(\hat{a}_{\text{aS}}\hat{b}^\dagger e^{-i\omega_p t} + \hat{a}_{\text{aS}}^\dagger\hat{b}e^{i\omega_p t}) + \omega_{\text{aS}}\hat{a}_{\text{aS}}^\dagger\hat{a}_{\text{aS}} + \omega_{\text{m}}\hat{b}^\dagger\hat{b} \right] . \qquad (5.20)$$

By moving to a rotating frame and defining $\Delta = \omega_{\text{aS}} - \omega_{\text{p}} - \omega_{\text{m}}$, the Hamiltonian is [450]

$$\hat{H}_{\text{rot}} = \hbar \left[G(\hat{a}_{\text{aS}}\hat{b}^\dagger + \hat{a}_{\text{aS}}^\dagger\hat{b}) + \Delta\hat{b}^\dagger\hat{b} \right] . \qquad (5.21)$$

5.3.5   *Quantum Langevin equations of motion*

The time evolution of the coupled optical and mechanical system can be described in the Heisenberg picture where the operators are time dependent. The quantum Langevin equations govern the time evolution of the operators [457, 458]. For a closed, dissipation-free system they read

$$\dot{\hat{a}} = -\frac{i}{\hbar}\left[\hat{a}, \hat{H}_{\text{bs}}\right] = -iG\hat{b} , \qquad (5.22a)$$

$$\dot{\hat{b}} = -\frac{i}{\hbar}\left[\hat{b}, \hat{H}_{\text{bs}}\right] = -iG\hat{a} . \qquad (5.22b)$$

The solution to the coupled equations show that the time evolution of the beam splitter anti-Stokes interaction swaps the the initial optical anti-Stokes state and the mechanical states in an oscillatory manner, with complete swaps at $Gt = 2\pi m$ for $m \in \mathbb{N}$.

However, the optical resonator is not a closed, dissipation-free system. The mechanical state is coupled to a thermal bath and the coupling of the optical mode to the tapered fibre for interacting with the resonator influences the occupation and adds noise. Using input–

output theory [457] the system can be described by

$$\dot{\hat{a}} = -\frac{i}{\hbar}\left[\hat{a}, \hat{H}_{\text{rot}}\right] - \kappa_{\text{aS}}\hat{a} + \sqrt{2\kappa_{\text{aS}}^{\text{e}}}\,\hat{a}_{\text{in}} \, , \tag{5.23a}$$

$$\dot{\hat{b}} = -\frac{i}{\hbar}\left[\hat{b}, \hat{H}_{\text{rot}}\right] - \gamma\hat{b} + \sqrt{2\gamma}\,\hat{b}_{\text{in}} \, . \tag{5.23b}$$

where $\kappa_{\text{aS}}^{\text{e}}$ is the extrinsic coupling rate of the optical resonance and $\hat{a}_{\text{in}}, \hat{b}_{\text{in}}$ are stochastic noise operators in units of $s^{-1/2}$, with expectation values

$$\begin{aligned}
\langle\hat{a}_{\text{in}}^{\dagger}(t)\hat{a}_{\text{in}}(t')\rangle &= 0 & \langle\hat{b}_{\text{in}}^{\dagger}(t)\hat{b}_{\text{in}}(t')\rangle &= \bar{n}_{\text{th}}\delta(t - t') \\
\langle\hat{a}_{\text{in}}(t)\hat{a}_{\text{in}}^{\dagger}(t')\rangle &= \delta(t - t') & \langle\hat{b}_{\text{in}}(t)\hat{b}_{\text{in}}^{\dagger}(t')\rangle &= (\bar{n}_{\text{th}} + 1)\delta(t - t')
\end{aligned} \tag{5.24}$$

The full solutions to Eq. (5.23) in both the time and frequency domains are calculated in Refs. 165, 450 and the lengthy calculation and will not be repeated here.

To find the power spectrum of the heterodyne signal, the definition of the power spectrum of a Fourier transform of the operator $X(t)$, $\tilde{X}(\omega)$, is used [459, Ch. 1]:

$$S_{XX}(\omega) = \int_{-\infty}^{\infty} d\omega' \, \langle\tilde{X}^{\dagger}(\omega')\tilde{X}(\omega')\rangle \, . \tag{5.25}$$

From this definition and the known quadrature of the optical field on the heterodyne detector, $\tilde{X}(\omega) = 2^{-1/2}[\tilde{\hat{a}}^{\dagger}(\omega + \omega_{\text{het}}) + \tilde{\hat{a}}(\omega + \omega_{\text{het}})]$ the spectrum can be calculated from the Fourier transformed solution to Eq. (5.23) [165]

$$S_{XX}(\omega) = 1 + 2\eta_{\text{det}}\kappa_{\text{aS}}^{\text{e}}\gamma G^2 \bar{n}_{\text{th}}\left[|D(-\omega - \omega_{\text{het}})|^2 + |D(\omega - \omega_{\text{het}})|^2\right] \, , \tag{5.26}$$

in which η_{det} represents the efficiency of the detection and

$$D(\omega) = \frac{1}{(-i\omega + \kappa_{\text{aS}})\left[-i(\omega + \Delta) + \gamma\right] + G^2} \, . \tag{5.27}$$

CHAPTER 6

Non-Gaussian mechanical motion via phonon subtraction from a thermal state

The broad motivation for optomechanics in the beginning of the previous chapter touches on many examples of optomechanics advancing as a platform for quantum experiments and for quantum technology. From both a scientific and technological standpoint, preparing and characterising states of mechanical motion exhibiting non-classical behaviour, is an important goal, enabling development of mechanical-oscillator-based quantum technology components as well as tests of fundamental physics.

It is more than two decades ago that the first proposal for using optomechanics as a means for preparation of non-classical mechanical states was published by Bose *et al.* [374]. Since then many schemes for optomechanical generation of such states have been proposed, for instance Refs. 413, 414 and references therein. One approach is to subtract one or several phonons from a mechanical squeezed state to generate non-classical states that closely approximate a Schrödinger cat state [416] – a quantum superposition of macroscopically distinguishable states [460]. In quantum optics, a similar technique for generating optical cat states via heralding photon subtraction events from a squeezed-vacuum state impinging on a weak beamsplitter was proposed [461] just before Bose *et al.*'s optomechanical proposal. This technique and other methods[i] were demonstrated a decade later [464–466], but generating such states is still an outstanding goal within optomechanics.[ii]

When it comes to measuring non-classical states, quantum optics experiments have also led the way, from early Wigner function reconstruction of squeezed states [470] to cat state reconstruction [462]. Building on this quantum optics state characterisation work, a promising route to perform mechanical quantum state characterisation is to efficiently transfer the mechanical state to the optical field via an optomechanical interaction, then use optical homodyne or heterodyne tomography to characterise the optical state. The tomography is performed by measuring the phase space quadratures for an ensemble of identically prepared states.

Experimentally determining the phase-space distribution for the mechanical states is valuable as it fully characterises the state, allowing any statistic or measurement probability to be determined, and will aid greatly in mechanical quantum state engineering research directions.

In this chapter, a combination of photon counting and optical heterodyne measurement is utilised to subtract phonons from a thermal mechanical state and measure the resulting

[i] Other techniques demonstrated for generating optical cat-like states include squeezing of number states [462, 463].

[ii] Note that non-classical states of mechanical motion have been generated in for instance trapped ions [467], including cat-like states [468, 469].

mechanical phase-space distribution via tomography. The experiment prepares heralded non-Gaussian mechanical states in a laser-cooled, Brillouin optomechanical system at room temperature. The experimental techniques developed advance the state of the art for optics-based tomography of mechanical states and will be useful not only for Brillouin-based cavity optomechanics, but for a broad range of both applied and fundamental studies of mechanical quantum-state engineering and tomography.

The work presented in this chapter is based on the main text and supplementary information of the published manuscript Enzian, Price, Freisem, Svela *et al.* [75] – where the first four authors contributed equally and are listed alphabetically. The author of this thesis has also presented the work at a conference with a published abstract [471]. The experimental work was carried out at the Department of Materials and the Clarendon Laboratory, Department of Physics at the University of Oxford, as well as in the Blackett Laboratory at Imperial College London. The project involves both experimental and the-oretical advances. The idea for the experiment was conceived by M. Vanner and G. Enzian before I joined the team. As a joint-first author in a team of both experimentalists and theorists, my contributions to this project have primarily concerned the experimental side, including jointly designing and implementing the experimental protocols to run the experiment and to obtain the data, and developing the data analysis methods and software. Furthermore, I contributed to rebuilding and making additions and improvements to the experimental setup, building the setup for and fabrication of tapered optical fibres, and experimental engineering such as instrument interfacing and control software.[iii]

[iii] As a part of the project, the author developed an open-source Python module for Tektronix function generators; it is available under the name *tektronix-func-gen* on Github [472], with API documentation.

6.1   BACKGROUND AND MOTIVATION FOR THIS EXPERIMENT

Throughout facets of quantum optics, non-Gaussian state preparation of a bosonic mode followed by phase-space characterisation has been performed with a wide spectrum of different experimental platforms. As an early notable example, a single-phonon Fock state of motion of a trapped ion was prepared and reconstructed [419], and further work with trapped ions has generated multi-component superposition states of motion for quantum-information applications [473]. In optics, heralded single-photon addition and subtraction followed by homodyne tomography has been utilised to generate and reconstruct several different quantum states that are now being explored for quantum science and technology applications. For instance, the Wigner function of a heralded single-photon state has been reconstructed [474], single-photon subtraction to squeezed states has been performed to generate small superposition states [464, 465], which have a superposition separation size that is enhanced by multi-photon subtraction [475], and the non-Gaussianity of photon-added and photon-subtracted thermal states has been studied [476–478]. Other notable examples of non-Gaussian quantum states with other physical systems include: studying the decoherence of a superposition state of a microwave field inside a cavity [479], generating non-Gaussian states of atomic-spin ensembles [480], creating and reconstructing arbitrary quantum states in a microwave superconducting circuit [481], and creating non-classical states of high-frequency acoustic waves coupled to superconducting qubits [396, 482].

Within optomechanics there have been several recent developments in this direction, with different experimental approaches being utilised to take advantage of the parameters and capabilities provided by fully engineered optomechanical devices. For instance, experiments exploiting quantum measurements with single-photon detectors include generating non-classical states of high-frequency vibrations in diamond crystals [483–485] and photonic-crystal structures [389], second-order-coherence measurements of mechanical modes [371, 372], the generation of mechanical interference fringes [486], and single-phonon addition or subtraction to a thermal state that results in a doubling of the mean thermal occupation [74].

There is also significant progress towards developing the experimental tools needed for mechanical phase-space tomography or reconstruction [421, 486–489]; however, none of these experiments have sufficient sensitivity to resolve features below the mechanical zero-point motion, and phase-space characterisation [418] of a mechanical quantum state remains as an outstanding goal in optomechanics. One promising route to achieving this goal in the resolved sideband regime is to perform single-phonon addition or subtraction for quantum state preparation and then utilise a red-sideband drive and optical state tomography with a balanced detector, such as homodyne or heterodyne detection.

This work is contributing towards the goal of non-classical mechanical state characterisation by advancing the state of the art in the overall measurement efficiency of the mechanical state. Via photon counting and simultaneous optical heterodyne detection, the s-parameterised Wigner phase-space distribution of non-Gaussian phonon-subtracted mechanical thermal states is measured. The measurements show that the initial thermal

state is transformed by the phonon subtraction events from an initial Gaussian in phase space into a ring shape with a diameter that increases with the number of phonons subtracted. The experiment is the first observation of the effect that the mean phonon occupation triples when a two-phonon subtraction is performed to the thermal mechanical state.

The work presented in this chapter expands the toolkit for optical control and readout of mechanical states, and can be applied to future room-temperature or cryogenic experiments to exploit and characterise the non-Gaussian and non-classical properties these operations generate. Pursuing this line of research will facilitate the development of mechanical-oscillator-based quantum technology such as quantum memories exploiting the long coherence times available [161–163], coherent transducers [341, 346], and sensors [363, 364, 404]. Additionally, such state generation and characterisation capabilities will help explore fundamental physics including the quantum-to-classical transition [376, 402, 490] and even the interface between quantum mechanics and gravity [401, 491, 492].

6.2 SINGLE- AND MULTI-QUANTA SUBTRACTION FROM A THERMAL STATE

The state of a bosonic system at equilibrium with a thermal reservoir of finite temperature is called a thermal state. When performing single- or multi-quanta subtraction such a state of large mean thermal occupation, one may expect very little change to the state. However, as this section will show, these operations significantly change the mean occupation of the state and also give rise to highly non-Gaussian distributions in phase space. Towards the end of the section the implementation of a phonon subtraction operation in a Brillouin optomechanical system is discussed.

6.2.1 *Quanta subtraction from a thermal state*

For a harmonic oscillator of frequency ω in equilibrium with a bath at temperature T, the mean occupation of the oscillator is given by

$$\bar{n} = \left[\exp\left(\frac{\hbar\omega}{k_{\mathrm{b}}T} \right) - 1 \right]^{-1} , \tag{6.1}$$

and the state can be described by a diagonal density matrix in the number basis $|m\rangle$,

$$\hat{\rho}_{\bar{n}} = \sum_{m=0}^{\infty} \Pr(m|\bar{n}) \, |m\rangle \langle m| , \tag{6.2}$$

where the probability for each number state is given the Bose–Einstein distribution [493, Ch. 3]

$$\Pr(m|\bar{n}) = \frac{\bar{n}^m}{(\bar{n}+1)^{m+1}} . \tag{6.3}$$

When n quanta are subtracted from an initial thermal state $\rho_{\bar{n}}$, the state following a subtraction operation is given by

$$\hat{\rho}_{n-} \propto \hat{b}^n \hat{\rho}_{\bar{n}} \hat{b}^{\dagger n} , \tag{6.4}$$
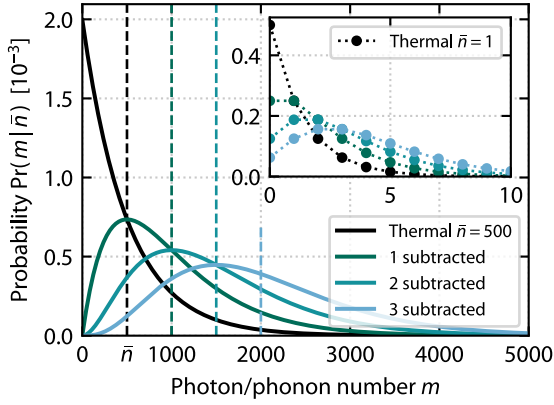
Figure 6.1. Occupation probability distributions for thermal and subtracted thermal states for an initial thermal state with mean occupation $\bar{n} = 500$. The mean occupation increases by $(n + 1)$-fold for n subtractions as shown by the vertical dashed lines. The inset shows the distributions for a smaller initial thermal state with $\bar{n} = 1$. Note that the ordinate axis in the inset is in units of unity, not scaled like the main axis.

Calculating the normalised density matrix of the n-subtracted state in the number basis (shown in Appendix A) gives

$$\hat{\rho}_{n-} = \sum_{m=0}^{\infty} \Pr(m|n, \bar{n}) \, |m\rangle \langle m| \, , \qquad (6.5)$$

where the number-state probabilities are given by

$$\Pr(m|n, \bar{n}) = (1 - q)^{n+1} q^m \binom{m + n}{n} \, , \qquad (6.6)$$

in which $q \equiv \bar{n}/(\bar{n} + 1)$ and the binomial coefficient[iv] is used.

Figure 6.1 shows the number distributions for the thermal and first three n-subtracted thermal states. Curiously, the mean occupations of the subtracted states *increase* when quanta are subtracted, even increasingly with the number of subtracted quanta!

CHANGE IN MEAN OCCUPATION AFTER SUBTRACTION. To calculate the new mean occupation number after n-quanta subtraction, the expectation value for the number operator must be calculated. Considering a mode with annihilation operator $\hat{b}$, the number operator is $\hat{b}^\dagger \hat{b}$ and the expectation value of the n-subtracted state is

$$\langle \hat{b}^\dagger \hat{b} \rangle_{n-} = \mathrm{Tr}\left(\hat{\rho}_{n-} \hat{b}^\dagger \hat{b}\right) = \frac{\mathrm{Tr}\left(\hat{b}^n \hat{\rho}_{\bar{n}} \hat{b}^{\dagger n} \, \hat{b}^\dagger \hat{b}\right)}{\mathrm{Tr}\left(\hat{b}^n \hat{\rho}_{\bar{n}} \hat{b}^{\dagger n}\right)} \, . \qquad (6.8)$$

It can be shown that the trace over the n-subtracted state is [Appendix A]

$$\mathrm{Tr}\left(\hat{b}^n \hat{\rho}_{\bar{n}} \hat{b}^{\dagger n}\right) = \frac{n!}{(1 - q)^n} q^n \, , \qquad (6.9)$$

and thus, with cyclical permutation of the operators in Eq. (6.8) and some algebra,

$$\langle \hat{b}^\dagger \hat{b} \rangle_{n-} = (n + 1)\bar{n} \, , \qquad (6.10)$$

showing that for n-quanta subtraction from a thermal state, the mean occupation transforms as

$$\bar{n} \to (n + 1)\bar{n} \, . \qquad (6.11)$$

[iv] Definition of the binomial coefficient

$$\binom{x}{y} = \frac{x!}{y!(x - y)!} \qquad (6.7)$$

A similar change is observed for n-quanta addition, where $\bar{n} \to (n+1)\bar{n} + n$. In the limit where the initial thermal state is much larger than the number of subtracted quanta, $\bar{n} \gg \sqrt{n}$, the expressions for the mean occupation approach the same values for both subtraction and addition operations [74]: the mean occupation doubles for both single-quantum subtraction and addition. This has been experimentally observed for thermal optical fields [476, 478, 494] and recently for a mechanical thermal state [74].

The surprising result that the mean occupation increases by $(n+1)$-fold for an n quanta subtraction can be understood via Bayesian inference, where the information obtained by heralding a subtraction event gives a conditional probability of the occupation of the conditioned state. Put differently, subtracting a quantum is more likely if there are many quanta to subtract, thus successfully subtracting a quantum makes it *a posteriori* more likely that the initial state had a high occupation.

Barnett *et al.* [495] use the following toy example to motivate the increase in the quantum number due to subtraction. A mode is prepared in a mixture (or superposition) of the ground state and the 100-quanta Fock number state such that there is a 50 % probability associated with each of the two outcomes if the state was measured:

$$\hat{\rho} = \frac{1}{2} |0\rangle \langle 0| + \frac{1}{2} |100\rangle \langle 100| \, , \tag{6.12}$$

which has a mean occupation number $\bar{n} = \mathrm{Tr}(\hat{b}^\dagger \hat{b} \hat{\rho}) = 50$. If a single subtraction is successfully performed and heralded, 100 quanta were present initially, and the conditioned state has a mean occupation of $99 \approx 2\bar{n}$, i.e., approximately double of the initial expectation value. A similar redistribution of the probability associated with the ground state happens for a thermal state that undergoes subtraction.

Moreover, in addition to the significant change to the mean occupation, the states generated by subtraction from a thermal state show non-Gaussian ring-shape features in phase space [478, 496]. The radius of the ring for a n-quanta subtraction is approximately proportional to the increased occupation $\sqrt{(n+1)\bar{n}}$ in zero-point units [478]. The non-Gaussian states are phase-invariant, meaning they are symmetric about the origin in phase space, because the initial thermal state itself is phase-invariant, and so is the subtraction operations, preserving the phase-independence (as shown by computing the Glauber–Sudarshan P function of the state in Appendix B).

In the limit where the initial occupation $\bar{n}$ is low, addition and subtraction operations can generate not only non-Gaussian states but also non-classical states [495]. This has been shown for addition and subtraction of single quanta from squeezed [464, 465, 497] and Gaussian states [498].

6.2.2   *The quadrature variance as a measure of the mean occupation*

For a thermal state, the variance of the quadrature $\hat{x} = 2^{-1/2}(\hat{b}^\dagger + \hat{b})$, where $\hat{b}$ is the annihilation operator of the mode, is related to the mean occupation. In general, the quadrature variance is defined

$$\sigma_{\hat{x}}^2 = \langle \hat{x}^2 \rangle - \langle \hat{x} \rangle^2 \, , \tag{6.13}$$

where for the thermal state, the expectation value

$$\langle \hat{x} \rangle_{\bar{n}} = \mathrm{Tr}(\hat{\rho}_{\bar{n}} \hat{x}) = \frac{1}{\sqrt{2}} \sum_{m=0}^{\infty} \Pr(m|\bar{n}) \, \langle m|(\hat{b}^\dagger + \hat{b})|m \rangle = 0 \, , \tag{6.14}$$

when using the cyclical property of the trace. To calculate the second moment, $\langle \hat{x}^2 \rangle$, use the commutation relation $[\hat{b}, \hat{b}^\dagger] = 1$ to express $\hat{x}^2 = 1/2(\hat{b}^{\dagger 2} + 1 + 2\hat{b}^\dagger \hat{b} + \hat{b}^2)$, and thus

$$\mathrm{Tr}(\hat{\rho}_{\bar{n}} \hat{x}^2) = \frac{1}{2} \sum_{m=0}^{\infty} \Pr(m|\bar{n}) \, \langle m|(\hat{b}^{\dagger 2} + 1 + 2\hat{b}^\dagger \hat{b} + \hat{b}^2)|m \rangle \tag{6.15}$$

$$= \frac{1}{2} \sum_{m=0}^{\infty} \Pr(m|\bar{n}) \, (1 + m) = \frac{1}{2} + \bar{n} \, . \tag{6.16}$$

Which means that the quadrature variance for a thermal state is

$$\sigma_{\hat{x}}^2 = \langle \hat{x}^2 \rangle_{\bar{n}} = \frac{1}{2} + \bar{n} \, , \tag{6.17}$$

in which the $+1/2$ is due to the zero-point fluctuations. By the same calculation for the subtracted state using Eq. (6.10), its quadrature variance is

$$\sigma_{\hat{x}}^2 = \langle \hat{x}^2 \rangle_{n-} = \frac{1}{2} + (n + 1) \, \bar{n} \, . \tag{6.18}$$

Thus, measuring the quadrature variance gives a means to verify the change to the mean occupancy of the subtracted state.

6.2.3   *Implementation of subtraction operations in Brillouin cavity optomechanics*

In this work, n-quanta subtraction from the mechanical motion of a Brillouin acoustic mode is performed by driving an optomechanical anti-Stokes interaction, swapping phonons for energy-upconverted photons. To herald the subtraction operations, single-photon detection of the resulting anti-Stokes photons is utilised. The scheme is a multi-phonon generalisation to the single-phonon subtraction (and addition) operation(s) considered theoretically by Vanner *et al.* [487] and later demonstrated experimentally by Enzian *et al.* [74] shortly before the author of this thesis joined the team.

Figure 6.2 shows a schematic of the process, where the Brillouin optomechanical interaction is resonantly enhanced by using an optical microresonator. A pair of optical cavity modes that are spaced by approximately the mechanical Brillouin frequency is used. Each optical mode has a linewidth much narrower than the mechanical frequency, which
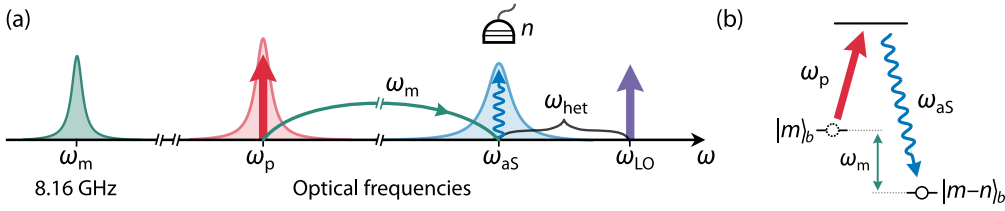
Figure 6.2. Optical pumping and heralding scheme for multi-phonon subtraction via Brillouin optomechanics. (a) A pair of optical resonances spaced by the mechanical angular frequency ω_m are used to resonantly enhance the optomechanical three-wave interaction: A pump field drives the mode at ω_p creating an anti-Stokes signal at ω_{aS}. An n-photon detection scheme (here simply represented by one detector) is then used to herald n-phonon subtraction to the mechanical motion. The same scheme can be used for n-phonon addition by instead pumping on the high-frequency optical mode, driving the Stokes interaction, and detecting photons in the lower-frequency mode for heralding addition operations. The local oscillator tone at ω_{LO} used for heterodyne detection is also illustrated. (b) The corresponding Λ-type schematic.

means that the experiment operates deep within the resolved sideband regime. By optically pumping the lower-frequency mode of the pair, at ω_p, the anti-Stokes scattering process is selected, with a high probability for pump photons to scatter off a mechanical excitation and thus generate a signal field in the higher-frequency cavity mode, ω_{aS}, where $\omega_{aS} - \omega_p = \omega_m$. Importantly, there is no optical mode spaced by the mechanical frequency on the lower frequency side of the pump mode, ensuring the Stokes interaction is suppressed.

The anti-Stokes scattering process is described by a light-mechanics beamsplitter-type interaction with Hamiltonian [Eq. (5.18)]

$$\hat{H}_{bs} = \hbar G(\hat{a}^\dagger \hat{b} + \hat{a}\hat{b}^\dagger),\qquad(6.19)$$

where $G = g_0\sqrt{N_{cav}}$ is the pump-enhanced, linearised optomechanical coupling rate, $\hat{a}$ is the field operator of the optical anti-Stokes signal field, and $\hat{b}$ is the mechanical annihilation operator. The Hamiltonian shows that this interaction can subtract a phonon via $\hat{b}^\dagger$, which results in a higher-frequency anti-Stokes photon being created $\hat{a}$. For weak optomechanical coupling, meaning the coupling rate between the light and mechanics is smaller than the optical and mechanical loss rates ($G < \{\kappa_{aS}, \gamma\}$), detecting n anti-Stokes photons heralds an n-phonon subtraction operation to the mechanical state. As the mechanical state is initially in a thermal state due to its coupling to a finite-temperature bath, the resulting state can be described by $\hat{\rho}_{n-} \propto \hat{b}^n \hat{\rho}_{\bar{n}} \hat{b}^{\dagger n}$.

Note also that by optically driving the upper-frequency mode of the pair, the phonon-adding Stokes scattering process is instead selected. This process corresponds to a two-mode squeezing Hamiltonian,

$$\hat{H}_{tms} = \hbar G(\hat{a}\hat{b} + \hat{a}^\dagger \hat{b}^\dagger),\qquad(6.20)$$

which means that detecting n photons in the frequency-down-shifted Stokes signal heralds an n-phonon addition process, $\hat{\rho}_{n+} \propto \hat{b}^{\dagger n} \hat{\rho}_{\bar{n}} \hat{b}^n$. In this work, only the n-phonon subtraction operation is considered as the anti-Stokes process is the best suited for mechanical

state readout because it does not give rise to lasing and instability when the interaction is strongly driven, and the optical field is a high-fidelity proxy for the mechanical state in the limit of high efficiency.

6.3   MECHANICAL STATE CHARACTERISATION VIA HETERODYNE MEASUREMENT

As the previous section describes, detecting n simultaneous anti-Stokes photons heralds an n-subtraction operation to the mechanical state. To characterise the subtracted mechanical state, heterodyne measurements of the anti-Stokes light around the heralding time is performed. The quadrature components of the time-domain heterodyne signal are extracted and can then be used for two types of analysis for characterising the mechanical state. Firstly, the quadrature variance of the ensemble of measurements for each time about the herald event is computed, which is a proxy for the change in the mean occupation of the mechanical state. Secondly, a two-dimensional histogram of the quadrature distribution at the heralding time is obtained, which, due to measurement inefficiencies, corresponds to a smoothened Wigner function of the mechanical state.

6.3.1 *The impact of measurement inefficiencies*

In the experiment, there is no access to measure the mechanical state directly. However, the light-mechanics-beam-splitter interaction maps the mechanical state onto the anti-Stokes light field, which can be used to infer an approximate phase-space distribution of the mechanical state via tomography.

In the absence of optical losses and inefficiencies, if an ensemble of optical homodyne measurements are performed on the anti-Stokes field, the obtained marginals allow the mechanical Wigner function to be tomographically reconstructed by varying the homodyne angle [179]. If a heterodyne measurement is performed instead, owing to the vacuum noise introduced with the simultaneous measurement of the two conjugate optical quadratures, it is the Husimi Q function of the impinging light field that is determined, which in the limit of perfect efficiencies is the same as the Q function of the mechanical state, as discussed in Appendix B.

However, in practice, losses and inefficiencies are present, and these affect how accurately the phase-space distribution of the mechanical state can be obtained. More specifically, optical losses result in the state of interest being convolved in phase space with vacuum noise, thus degrading the signal. The added noise can eliminate any non-classical or non-Gaussian features present if the efficiency is poor, see Fig. 6.3. This fact has been highlighted by many quantum optics experiments, and for instance, an overall efficiency of greater than 50 % was required to see the Wigner negativity of a single-photon Fock state in work by Lvovsky *et al.* [474]. A high overall measurement efficiency is therefore a key ingredient for state tomography experiments.

In this work, the efficiency is imperfect due to the limited efficiency of the state swap at the optomechanical beamsplitter, and because of subsequent optical losses as the anti-Stokes light travels from the resonator to the heterodyne detector, as illustrated in Fig. 6.4.
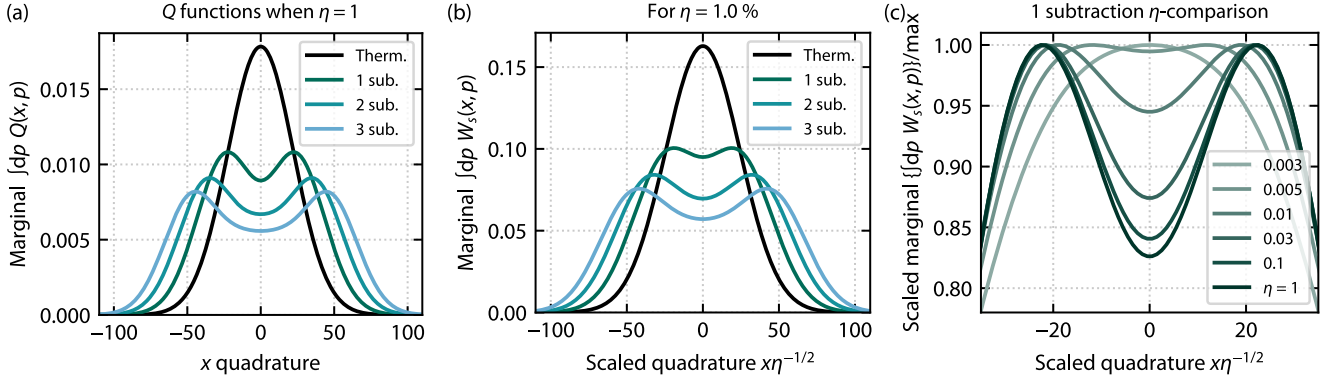
Figure 6.3. Phase-space marginals for varied measurement efficiency. The plots show marginals of the obtained phase space via heterodyne detection for the thermal and first three subtracted states. (a) When $\eta = 1$ the obtained phase space corresponds to the Q function of the respective states. Note the increasingly non-Gaussian shape of the subtracted states. (b) For $\eta < 1$ the obtained phase space corresponds to the s-parameterised Wigner function W_s with $s < -1$, here shown for $\eta = 0.01$ ($s = -199$), which is approximately the efficiency achieved in this experiment. Note the lower contrast in the non-Gaussian features compared to (a) due to the smoothening from the added noise. The quadrature is also scaled due to the associated amplitude losses. (c) A comparison of marginals computed from W_s for varying η where the each marginal is scaled to its maximum for comparable scales. For the lowest efficiencies the bimodality cannot be resolved.

The reconstructed phase space determined by the heterodyne measurement of the anti-Stokes light field corresponds to an s-parametrised Wigner function of the mechanical state, with further details presented in Appendix B.

The remainder of this section will briefly explain how the signal on the heterodyne detector is related to the mechanical state for the purpose of characterising the prepared mechanical states.

6.3.2 *Dynamics of the mechanical state and the measured heterodyne signal*

As shown in Eqs. (6.17) and (6.18), the quadrature variance of the mechanical state corresponds to the mean occupation of the state ($+1/2$ from the zero-point fluctuations). However, this quadrature cannot be measured directly, and it is instead the optical anti-Stokes quadrature that is measured by heterodyne detection, from which the dynamics of the mechanical state can be inferred. By considering the optical and mechanical state after heralding n anti-Stokes photons, the dynamics can be calculated via the Langevin equations governing the evolution of the mechanical and anti-Stokes field operators. The calculation for the one-phonon subtraction (and addition) case was performed by Enzian *et al.* [74] before it was subsequently expanded to the two-phonon case in Enzian *et al.* [75]. An outline of the calculation following that of Price [450] is presented in the following.
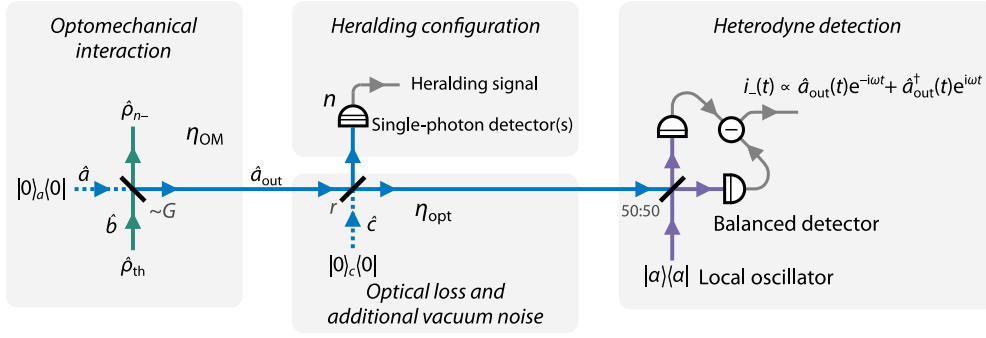
Figure 6.4. Heterodyne detection scheme for state characterisation. The optomechanical light-mechanics-beamsplitter interaction in the cavity weakly couples the mechanical mode ($\hat{b}$) and the anti-Stokes light field ($\hat{a}$) up to some efficiency set by the optomechanical coupling G. The anti-Stokes field is inefficiently coupled out of the optical cavity and further attenuated due to lossy optical components, which can be treated as a single beam splitter introducing additional vacuum noise (optical mode $\hat{c}$) and attenuation. When the attenuated field reaches the heterodyne detector it is mixed with a strong local oscillator, allowing the Husimi Q function of the optical state $\hat{a}_{\text{out}}$ to be determined, which is a smoothened Q function of the mechanical state.

THE HERALDED STATE. To express the heralded optical state consider first the initial state of the system. The initial thermal state of the mechanics $\hat{\rho}_{\text{th}}$ and the anti-Stokes vacuum $|0\rangle \langle 0|_a$ can be described as the bipartite system

$$\hat{\rho}_{\text{init}} = \hat{\rho}_{\text{th}} \otimes |0\rangle \langle 0|_a \ . \tag{6.21}$$

In the Schrödinger picture, the initial state evolves as governed by the light-mechanics beam splitter unitary $\hat{U}_{ab}(t)$

$$\hat{\rho}_{\text{evolv}}(t) = \hat{U}_{ab}(t)\hat{\rho}_{\text{init}}\hat{U}_{ab}^\dagger(t) \ . \tag{6.22}$$

The single photon heralding process can be expressed via a measurement operator applied to this initial state. The beam splitter used for heralding in Fig. 6.4 with reflectivity r can be described by the Hamiltonian $\hat{H}_{ac}/\hbar = r(\hat{a}\hat{c}^\dagger + \hat{c}\hat{a}^\dagger)$, whose unitary $\hat{B}_{ac}$ is

$$\hat{B}_{ac} = \exp(-i\hat{H}_{ac}/\hbar) = \sum_{k=0}^{\infty} \frac{(-i\hat{H}_{ac}/\hbar)^k}{k!} \approx 1 - ir(\hat{a}\hat{c}^\dagger + \hat{c}\hat{a}^\dagger) \ , \tag{6.23}$$

where higher order terms are not relevant as this derivation is restricted to the case of single-photon heralding. The heralding of one photon at time t_0 in the output mode $\hat{c}$ for vacuum input on the open ports can be expressed as a non-unitary measurement operator

$$\hat{Y}_{t_0} = \langle 1|_c \hat{B}_{ac} |0\rangle_c = -ir\hat{a} \tag{6.24}$$

where the $\langle 1|_c$ is the detector measuring one photon, and $|0\rangle_c$ represents the vacuum entering at the unused port of the beam splitter.

Applying the measurement to the evolving state, the full light-mechanics heralded state can be expressed

$$\hat{\rho}_{\text{herald}}(t, t_0) = \frac{1}{\mathcal{N}} \hat{Y}_{t_0} \hat{\rho}_{\text{evolv}}(t) \hat{Y}_{t_0}^\dagger = \frac{r^2}{\mathcal{N}} \hat{a} \hat{\rho}_{\text{evolv}}(t) \hat{a}^\dagger , \qquad (6.25)$$

where the normalisation $\mathcal{N} = r^2 \langle \hat{a}^\dagger \hat{a} \rangle$ is the trace over the heralded state, i.e., the heralding probability.

INTRACAVITY DYNAMICS. To describe time dynamics of the occupation of the mechanical state around the heralding time, the quadrature variance of the optical anti-Stokes field can be used as proxy. Similarly to the mechanical field, the intracavity field itself is not directly accessible, as it needs to be coupled out of the cavity, but this is left aside for now. The time evolution of the variance of the intracavity quadrature $\hat{X}_{\text{cav}} = 2^{-1/2}(\hat{a}^\dagger + \hat{a})$ can be found by the expectation value of the time-dependent heralded state and moving to the Heisenberg picture,

$$\langle \hat{X}_{\text{cav}}^2(t) \rangle = \text{Tr} \left[\hat{\rho}_{\text{herald}}(t) \hat{X}_{\text{cav}}^2 \right] \qquad (6.26)$$

$$= \frac{r^2}{\mathcal{N}} \text{Tr} \left[\hat{\rho}_{\text{init}} \hat{a}^\dagger(t_0) \hat{X}_{\text{cav}}^2(t) \hat{a}(t_0) \right] , \qquad (6.27)$$

where the cyclical property of the trace has been used. Working in time relative to the heralding time, $\tau = t - t_0$, the quadrature variance can be expressed

$$\langle \hat{X}_{\text{cav}}^2(\tau) \rangle = \frac{r^2}{\mathcal{N}} \langle \hat{a}^\dagger(0) \hat{X}_{\text{cav}}^2(\tau) \hat{a}(0) \rangle . \qquad (6.28)$$

where the time dependence of the operators is governed by the Langevin equations [Eq. (5.23)]. With the shorthand $\hat{a}(\tau) = \hat{a}_\tau$,

$$\langle \hat{X}_{\text{cav}}^2(\tau) \rangle = \frac{\langle \hat{a}_0^\dagger \hat{X}_{\text{cav}}^2(\tau) \hat{a}_0 \rangle}{\langle \hat{a}_0^\dagger \hat{a}_0 \rangle} = \frac{\langle \hat{a}_0^\dagger \hat{a}_\tau^\dagger \hat{a}_\tau \hat{a}_0 \rangle + \langle \hat{a}_0^\dagger \hat{a}_\tau \hat{a}_\tau^\dagger \hat{a}_0 \rangle}{2 \langle \hat{a}_0^\dagger \hat{a}_0 \rangle} , \qquad (6.29)$$

when substituting in the squared quadrature. It can be shown [165] via the Isserlis–Wick theorem that Eq. (6.29) can be written

$$\langle \hat{X}_{\text{cav}}^2(\tau) \rangle = \frac{1}{2} + \langle \hat{a}_0^\dagger \hat{a}_0 \rangle + \frac{|\langle \hat{a}_0^\dagger \hat{a}_\tau \rangle|^2}{\langle \hat{a}_0^\dagger \hat{a}_0 \rangle} . \qquad (6.30)$$

By inserting the solutions to the Langevin equations into this expression, it can be shown [165] that

$$\langle \hat{X}_{\text{cav}}^2(\tau) \rangle = \frac{1}{2} + \bar{n}_{\text{th}} \frac{G^2}{\kappa_{\text{aS}}(\kappa_{\text{aS}} + \gamma)} \left[1 + \left(\frac{\kappa_{\text{aS}} e^{-\gamma|\tau|} - \gamma e^{-\kappa_{\text{aS}}|\tau|}}{\kappa_{\text{aS}} - \gamma} \right)^2 \right] , \qquad (6.31)$$

giving an expression for the intracavity variance with time about the single-phonon subtraction heralding event $\tau = 0$ with system parameters that can be characterised: G is the cavity-enhanced optomechanical coupling, κ_{aS} optical decay rate of the of the anti-

Stokes resonance, γ the intrinsic mechanical decay rate, and $\bar{n}_{\text{th}}$ the initial mean phonon occupation. Evaluating the expression at the heralding event and far away from the event gives

$$\langle \hat{X}^2_{\text{cav}}(\tau = 0) \rangle = \frac{1}{2} + 2\bar{n}_{\text{th}} \frac{G^2}{\kappa_{\text{aS}}(\kappa_{\text{aS}} + \gamma)} , \tag{6.32}$$

$$\langle \hat{X}^2_{\text{cav}}(\tau \to \pm\infty) \rangle = \frac{1}{2} + \bar{n}_{\text{th}} \frac{G^2}{\kappa_{\text{aS}}(\kappa_{\text{aS}} + \gamma)} , \tag{6.33}$$

showing that the quadrature variance grows as the mechanical occupation doubles at $\tau = 0$, as expected from Eq. (6.18).

EXTRACAVITY QUADRATURE VARIANCE AND THE HETERODYNE SIGNAL. It is the light leaking out from the cavity that can be measured. The out-coupled anti-Stokes light is related to the intracavity light via cavity quantum input–output theory. Considering a situation with no optical losses, the coupling is [499]

$$\hat{a}_{\text{out}}(t; \eta_{\text{opt}} = 1) = \sqrt{2\kappa^{\text{e}}_{\text{aS}}}\hat{a}(t) - \hat{a}_{\text{in}}(t) , \tag{6.34}$$

where $\hat{a}(t)$ is the dimensionless intracavity field operator with evolution described by the solution to the Langevin equations, and $\hat{a}_{\text{out}}, \hat{a}_{\text{in}}$ are in units of $\text{s}^{-1/2}$. The operator $\hat{a}_{\text{in}}$ is a stochastic noise operator[v] representing vacuum noise input to the cavity as a result of the coupling. Accounting for the optical losses to the field before it reaches the detector can be done by adding a virtual beam splitter [179] with transmission η_{opt}, which adds more added noise due to the unused port (in Fig. 6.4 these losses are captured by the real beam splitter used for the heralding):

$$\hat{a}_{\text{out}}(t) = \sqrt{\eta_{\text{opt}}}\left[\sqrt{2\kappa^{\text{e}}_{\text{aS}}}\hat{a}(t) - \hat{a}_{\text{in}}(t)\right] + \sqrt{1 - \eta_{\text{opt}}}\hat{c}_{\text{in}}(t) , \tag{6.35}$$

where $\hat{c}_{\text{in}}(t)$ represents the vacuum entering through open beam splitter port.

This result is related to the voltage signal from the heterodyne detector via Eq. (3.10), noting that the voltage signal is proportional to the difference current $i_-(t)$. Letting $\theta \to \omega_{\text{het}}t$ for a heterodyne measurement, the difference current is

$$i_-(t) \propto a^\dagger d_{\text{out}} \cos(\omega_{\text{het}}t) + a_{\text{out}} \sin(\omega_{\text{het}}t) , \tag{6.36}$$

which corresponds to a rotating quadrature of the optical field impinging on the heterodyne detector

$$i_-(t) \propto X_{\text{out}} \cos(\omega_{\text{het}}t) + P_{\text{out}} \sin(\omega_{\text{het}}t) . \tag{6.37}$$

As both the initial thermal and subtracted states are symmetric in phase space about the origin and thus not phase dependent, the rotation does not need to be considered to calculate the quadrature variance as any rotated quadrature will yield the same answer. Therefore,

[v] The noise operator has zero average occupation and thus the expectation values [457]

$$\langle \hat{a}^\dagger_{\text{in}}(t)\hat{a}_{\text{in}}(t') \rangle = 0$$
$$\langle \hat{a}_{\text{in}}(t)\hat{a}^\dagger_{\text{in}}(t') \rangle = \delta(t - t')$$

the variance in the heterodyne difference current for a ensemble of measurements is

$$\sigma_{i_-}^2(t) \propto \langle X_{\text{out}}^2(t) \rangle - \langle X_{\text{out}}(t) \rangle^2 . \tag{6.38}$$

By inserting Eq. (6.35) and the solution to the Langevin equation, and performing a similar calculation to the one for the intracavity variance, it can be shown [165] that when normalised to the optical vacuum noise on the heterodyne detector, the heterodyne signal ensemble variance is

$$\sigma_{i_-}^2(\tau) = 1 + \eta\bar{n}_{\text{th}}\left[1 + \left(\frac{\kappa_{\text{aS}}e^{-\gamma|\tau|} - \gamma e^{-\kappa_{\text{aS}}|\tau|}}{\kappa_{\text{aS}} - \gamma}\right)^2\right], \tag{6.39}$$

where the parameter η captures the overall measurement efficiency, both the optomechanical state transfer onto the anti-Stokes field and the optical losses. The ensemble variance increases from the far-away value of $1 + \eta\bar{n}_{\text{th}}$ to the value $1 + 2\eta\bar{n}_{\text{th}}$ at $\tau = 0$, showing the doubling in the mechanical mean occupation. The supplementary material in Enzian *et al.* [75] shows the extension to two-phonon subtraction, giving

$$\sigma_{i_-}^2(\tau; n) = 1 + \eta\bar{n}_{\text{th}}\left[1 + n\left(\frac{\kappa_{\text{aS}}e^{-\gamma|\tau|} - \gamma e^{-\kappa_{\text{aS}}|\tau|}}{\kappa_{\text{aS}} - \gamma}\right)^2\right] \tag{6.40}$$

for $n \in \{1, 2\}$, where at $\tau = 0$ the variance increases to $1 + (n+1)\eta\bar{n}_{\text{th}}$, i.e., an $(n+1)$-fold increase in the occupation.

6.3.3 *Tomography of the mechanical state: the s-parametrised Wigner function*

Measuring the variance and calculating the ensemble variance gives a means for verifying the increase in the mechanical occupation at the time of subtraction. To see the non-Gaussian nature of the subtracted states, the state is characterised via tomography at the heralding time.

Lossless homodyne detection can measure an optical quadrature with quantum-limited accuracy. In this experiment, however, a heterodyne measurement is used, which via simultaneous measurement of two quadratures adds noise compared to a homodyne measurement. In addition, the state swap from the mechanics to the anti-Stokes light is imperfect and subsequent optical losses adds more noise as expressed by the overall efficiency parameter η in Eq. (6.39).

A versatile way to mathematically quantify the performance of a tomography experiment is to use the *s*-parameterised Wigner function W_s [500], as it captures the unwanted effects of noise and inefficiency in a single parameter. The *s*-parametrised Wigner function can be written as a two-dimensional convolution between the Glauber–Sudarshan *P* function of the state of interest and and a Gaussian. Thus for the *n*-phonon subtracted state, the *s*-parametrised Wigner function can be written:

$$W_s(X_{\text{m}}, P_{\text{m}}) = (P_{n-} \star \mathcal{G}_s)(X_{\text{m}}, P_{\text{m}}) . \tag{6.41}$$

where X_m, P_m are the mechanical state quadratures, and the n-phonon subtracted state's P function is [Appendix B]

$$P_{n-} = \frac{2^{-n}\bar{n}^{-n-1}}{\pi n!} \left(X_m^2 + P_m^2\right)^n \exp\left[-\frac{X_m^2 + P_m^2}{2\bar{n}}\right] , \qquad (6.42)$$

$$\mathcal{G}_s = \frac{1}{\pi(1-s)} \exp\left[-\frac{X_m^2 + P_m^2}{1-s}\right] \qquad (6.43)$$

The Gaussian represents the smoothening from the added noise. For heterodyne detection, the s-parameter is defined as [179]

$$s = \frac{\eta - 2}{\eta} , \qquad (6.44)$$

where η is the overall measurement efficiency of the mechanical state including the mechanics-light transduction efficiency, out-coupling efficiency and subsequent losses.

From the expression (6.44) for s, it is clear that for $\eta = 1$ one obtains $s = -1$, which corresponds to the Husimi Q function, and $\eta < 1$ implies $s < -1$, corresponding to a distribution that is smoothed more than the Q function. Experimentally determining W_s for the mechanical state is valuable as it fully characterises the state, allowing any statistic or measurement probability to be determined.

MEASURED MARGINAL DISTRIBUTIONS. The quadrature marginal distributions taking into account the measurement efficiency are calculated in Appendix B, where the expressions for the quadratures are given for an arbitrary overall measurement efficiency. Figure 6.3(b) shows plots of the marginals for an overall measurement efficiency of 1 %, which is approximately the efficiency achieved in the experiment presented in this chapter, showing the non-Gaussian shape of the expected obtained marginal.

6.4   EXPERIMENTAL SETUP AND SYSTEM CHARACTERISATION

The n-phonon subtraction is investigated experimentally in a barium fluoride optical microresonator (Fig. 6.5) at room temperature, building on earlier work from the group [64, 74]. A number of upgrades to the resonator design, the experimental setup, and the control capabilities were necessary to perform the measurements in this work compared to the previous publications. In particular, the increased overall measurement efficiency compared to earlier experiments is what allows this work to resolve the non-Gaussian features of the phonon-subtracted mechanical thermal states.

The first part of this section gives an overview of the setup. The following parts are more detailed descriptions of different aspects about the setup, experimental procedures and characterisation. The section covers how a suitable optomechanical mode-trio is found and characterised, presents the heralding and heterodyne parts of the setup in detail, and lastly, covers some additional experimental techniques for stabilisation of the setup for increased performance.

6.4.1   *Overview of the setup*

Figure 6.6 gives a stripped down overview of the experimental setup, and Fig. 6.7 shows a more detailed schematic of the setup. The experiment is mainly divided into three parts: the optical microresonator in which the optomechanical interaction happens, the heralding of the interaction, and the heterodyne measurement. Key system and experimental parameters are found in Tables 6.1 and 6.2.

The barium fluoride resonator is fabricated as described in Section 3.2, where the motivation for using a resonator fabricated from this crystalline material are also described in detail. In brief, the low optical [89] and acoustic losses [160, 163] enable significant enhancement of Brillouin optomechanical interaction. The mechanical losses in a crystalline material will be even lower at cryogenic temperatures [162], promising for future experiments. This experiment, however, is performed at 300 K, corresponding to a mean mechanical thermal occupation of $\bar{n}_{\mathrm{th}} \simeq 766$. Note that via the optomechanical coupling, the initial thermal state is sideband-cooled to $\bar{n} = 4.5(1) \cdot 10^2$, as described in Section 6.4.3.

A suitable pair of a pump and anti-Stokes optical resonances spaced by the mechanical frequency is identified as explained in Section 6.4.2. To drive the anti-Stokes interaction, a tuneable continuous-wave, fibre laser[vi] is locked to the pump resonance via a PDH lock [Section 3.6.2]. The pump field of wavelength $\simeq$1550 nm is evanescently coupled to the resonator via a tapered silica fibre with 89 % transmission. Measurements to characterise the system are described and discussed in Section 6.4.3. In summary, the linewidth of the optical mode at the anti-Stokes frequency is $2\kappa_{\mathrm{aS}}/(2\pi) = 93.7(1)$ MHz, the mechanical linewidth is $2\gamma/(2\pi) = 6.6(2)$ MHz, and the single-photon optomechanical coupling is $g_0 = 0.29(8)$ kHz. Using an input pump power of $\simeq$9 mW, the corresponding intra-cavity pump photon number is $N_{\mathrm{cav}} = 1.19(3) \cdot 10^9$, resulting in a pump-enhanced optomechanical coupling rate of $G/(2\pi) = 10.2(4)$ MHz. Hence, the the system is operated well within the weak coupling regime ($2G < \kappa_{\mathrm{aS}} + \gamma$).

The backscattered anti-Stokes Brillouin light is coupled out of the cavity by the tapered fibre and separated from the forwards-propagating pump field using an optical circulator. The back-reflected light is then split into two optical arms using a 25:75 beamsplitter: one for heralding via photon counting and one for heterodyne detection, see Fig. 6.6.

[vi] NKT Koheras Adjustik E15
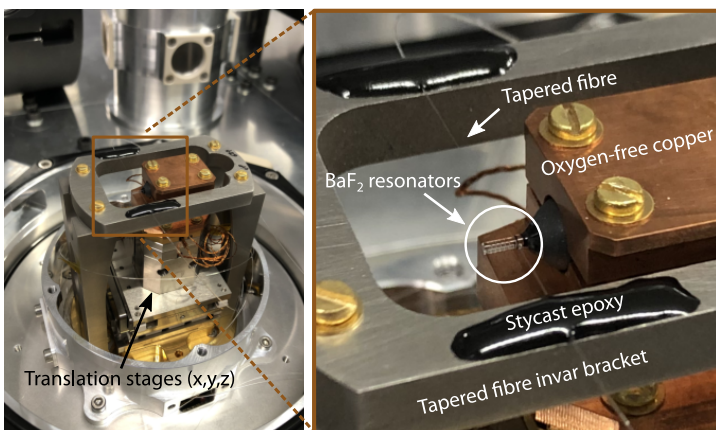
Figure 6.5. Photograph of the resonator and tapered fibre mounted inside a 4 K cryostat (open for sample swap). The resonator is mounted on a stack of translation stages providing control over the coupling to the tapered fibre. The diameter of the resonator is $\simeq$1 mm.
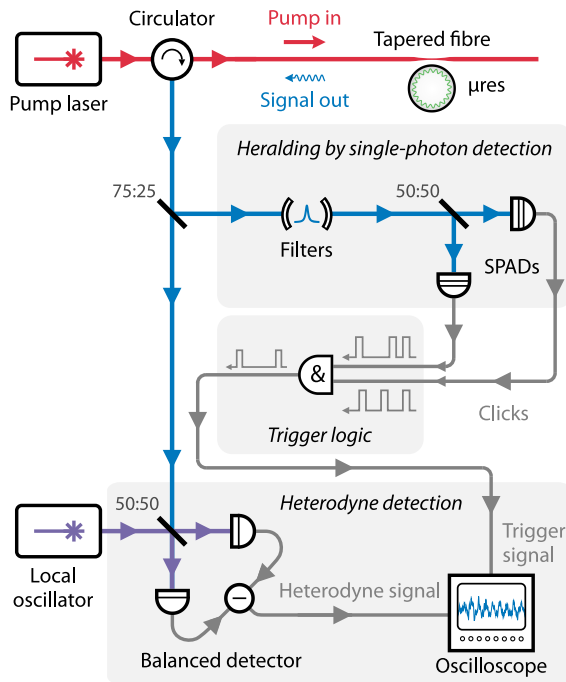
Figure 6.6. Overview schematic of the experimental setup. A tuneable laser drives the anti-Stokes interaction in a microresonator. The backscattered anti-Stokes signal is separated from the pump with an optical circulator. The signal is split into two arms for heralding and characterisation purposes. In the heralding arm, single-photon avalanche detectors (SPADs) detect anti-Stokes photons, heralding one- or two-phonon subtraction events. In the characterisation arm, an oscilloscope captures a time-domain measurement of the heterodyne signal when triggered by SPAD detection events. The two-phonon subtraction case is shown here, using a two-photon-coincidence triggering setup.

In the 25 % arm, single- and two-phonon subtraction events are heralded via single-photon detection using two single-photon avalanche detectors[vii] (SPADs). Two Fabry–Pérot optical filters are used in series before the detectors to filter out any backscattered pump light, ensuring that only anti-Stokes photons reach the SPADs. The rate of single photons measured at a detector when driving the anti-Stokes interaction is about 0.28 kHz, significantly higher than the measured dark count rate of ~1 Hz. When a one detector clicks, this heralds a single-phonon subtraction event, and when both detectors click simultaneously, this heralds a two-phonon subtraction event.

The 75 % arm is directed to a heterodyne detection setup to estimate the quadrature components of the conditioned mechanical states. The anti-Stokes signal interferes with a strong local oscillator, frequency-detuned by $\omega_{\mathrm{het}}/(2\pi) = 214$ MHz with respect to the signal, on a 50:50 beamsplitter, and the output is measured using a balanced photodetector.[viii] To obtain time domain data of the heterodyne signal around phonon-subtraction events, the single-photon and two-photon coincidences in the heralding arm trigger a high-bandwidth oscilloscope[ix] to record a time trace of the output from the balanced detector. In order to acquire sufficient statistics to characterise the phase-space distributions and temporal dynamics of the mechanical states for the unconditioned, single-phonon subtracted, and two-phonon subtracted thermal states, $2.4 \cdot 10^5$ time traces are recorded for each case.

[vii] ID Quantique id210

[viii] Insight BPD-1 (400 MHz bandwidth)

[ix] Tektronix MSO64 (4 GHz bandwidth)
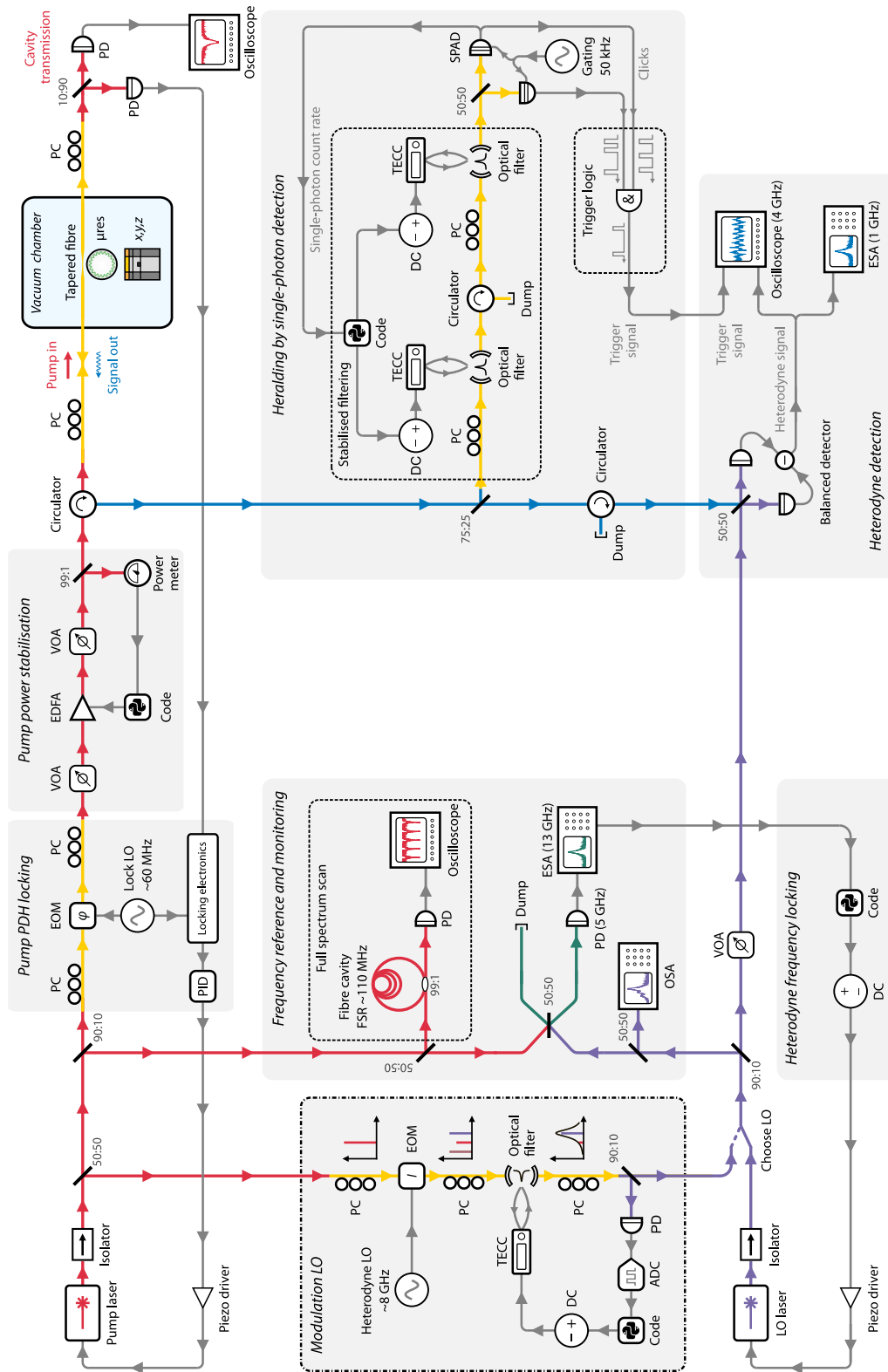
Figure 6.7. Simplified schematic of the experimental setup, with the constituent parts described in the text. Abbreviations can be found in the text and the list of abbreviations at the beginning of the document. Some abbreviations have so far not been used: polarisation controller, PC; variable optical attenuator, VOA; and thermoelectric-cooler controller, TECC. The optical fibre in the setup is mostly polarisation maintaining fibre, but some components are normal single mode as indicated by yellow lines. The modulated local oscillator has been set up after the data presented here was captured, but gives increased frequency stability for the LO with respect to the pump frequency. Adapted from Price [450] (CC BY-NC licence).

Table 6.1. Summary of the key system and experimental parameters.

Parameter	Symbol	Value
Pump wavelength	λ_p	1549.79 nm
Pump mode linewidth	$2\kappa_\mathrm{p}/(2\pi)$	14.1(1) MHz
Pump mode external coupling	$2\kappa_\mathrm{p}^\mathrm{e}/(2\pi)$	5.3(1) MHz
AS mode linewidth	$2\kappa_\mathrm{aS}/(2\pi)$	93.7(1) MHz
AS mode external coupling	$2\kappa_\mathrm{aS}^\mathrm{e}/(2\pi)$	11.7(1) MHz
AS mode taper coupling efficiency	$\eta_\mathrm{c}^\mathrm{aS}$	0.250(4)
Mechanical frequency	$\omega_\mathrm{m}/(2\pi)$	8.16(1) GHz
Mechanical linewidth	$2\gamma/(2\pi)$	6.6(2) MHz
Mechanical Qf product	$Q_\mathrm{m}f_\mathrm{m}$	10^{13} Hz
Optomechanical coupling rate	$g_0/(2\pi)$	0.29(8) kHz
Input pump power	$\mathcal{P}_\mathrm{in}$	9.00(5) mW
Intra-cavity pump photon number	N_cav	$1.19(3) \cdot 10^9$
Pump-enhanced coupling rate	$G/(2\pi)$	10.3(3) MHz
Optomechanical cooperativity	C	0.69(4)
Resonator temperature	T	300(1) K
Mean initial phonon number	$\bar{n}_\mathrm{th}$	766(2)
Sideband-cooled mean phonon number	$\bar{n}$	$4.5(1) \cdot 10^2$
Overall measurement efficiency	η	0.908(2) %

Table 6.2. Measurement and additional system parameters.

Parameter	Value
Resonator major diameter	936(1) μm
Resonator minor radius	40.0(1) μm
Optical fibre taper transmission	0.89
Filtering arm transmission	0.15
Heterodyne arm detection efficiency	0.365
FP filter FWHM linewidth	120 MHz
FP filter free spectral range	25 GHz
SPAD quantum efficiency	0.125
SPAD gate rate	50 kHz
SPAD gate length	3.5 ns
SPAD dead time	18 μs
SPAD dark count rate	$\simeq 1\,\text{Hz}$
Single-photon count rate	0.28 kHz
Two-photon coincidence rate	$\simeq 2\,\text{Hz}$
Heterodyne frequency $\omega_{\text{het}}/(2\pi)$	214 MHz
Balanced detector bandwidth	400 MHz
Recorded time trace length	4000 ns
Oscilloscope sampling rate	$3.125\,\text{GSs}^{-1}$
Number of time traces per operation	$2.4 \cdot 10^5$

6.4.2 *Mode trio-identification*

Identifying a suitable pair of optical resonances separated by the Brillouin frequency and with appreciable optomechanical coupling is a time consuming and probabilistic exercise. Significant time has been put into streamlining this procedure by writing software for making it easy and quick to identify mode pair candidates and test their properties. The approach is to obtain a spectrum of the resonator over the full laser bandwidth and look for optical modes separated by the Brillouin frequency, and pump on the lower-frequency mode to see if the modes optomechanically couple.

First, the spectral landscape for a chosen tapered fibre position is obtained for the full ~1 nm (~125 GHz) range of the pump laser, as shown in Fig. 6.8(a). The laser range covers just over two free-spectral ranges of the microresonator, $v_{\text{FSR}} \simeq 69.5\,\text{GHz}$, giving an overview of the densely populated spectrum, with optical modes of varying linewidths and degrees of coupling to the taper. The full spectrum is obtained by slowly temperature tuning the pump fibre laser frequency over its entire frequency range (a process that takes approximately 2.5 minutes, corresponding to $\sim 0.74\,\text{GHz}\,\text{s}^{-1}$) whilst simultaneously scanning its piezo at a much faster rate ($\sim 0.73\,\text{THz}\,\text{s}^{-1}$) and continuously obtaining transmission spectra at a rate of 75 Hz using an oscilloscope. The 12 500 obtained spectra overlap significantly, and by correlation, their overlaps can be determined to form one continuous spectrum of the resonator.[x]

To find potential mode pair, the optical modes with an appreciable taper coupling that are spaced by roughly the Brillouin frequency are identified by inspection of the full

[x] To ensure the performance of this technique, the algorithm also uses the simultaneously obtained spectrum of a fibre-loop cavity with multiple FSRs within the piezo scanning range, representing a frequency ruler with spacing equal to the fibre cavity's FSR. The fibre cavity is formed by a 99:1 beamsplitter with two ports connected to a loop.
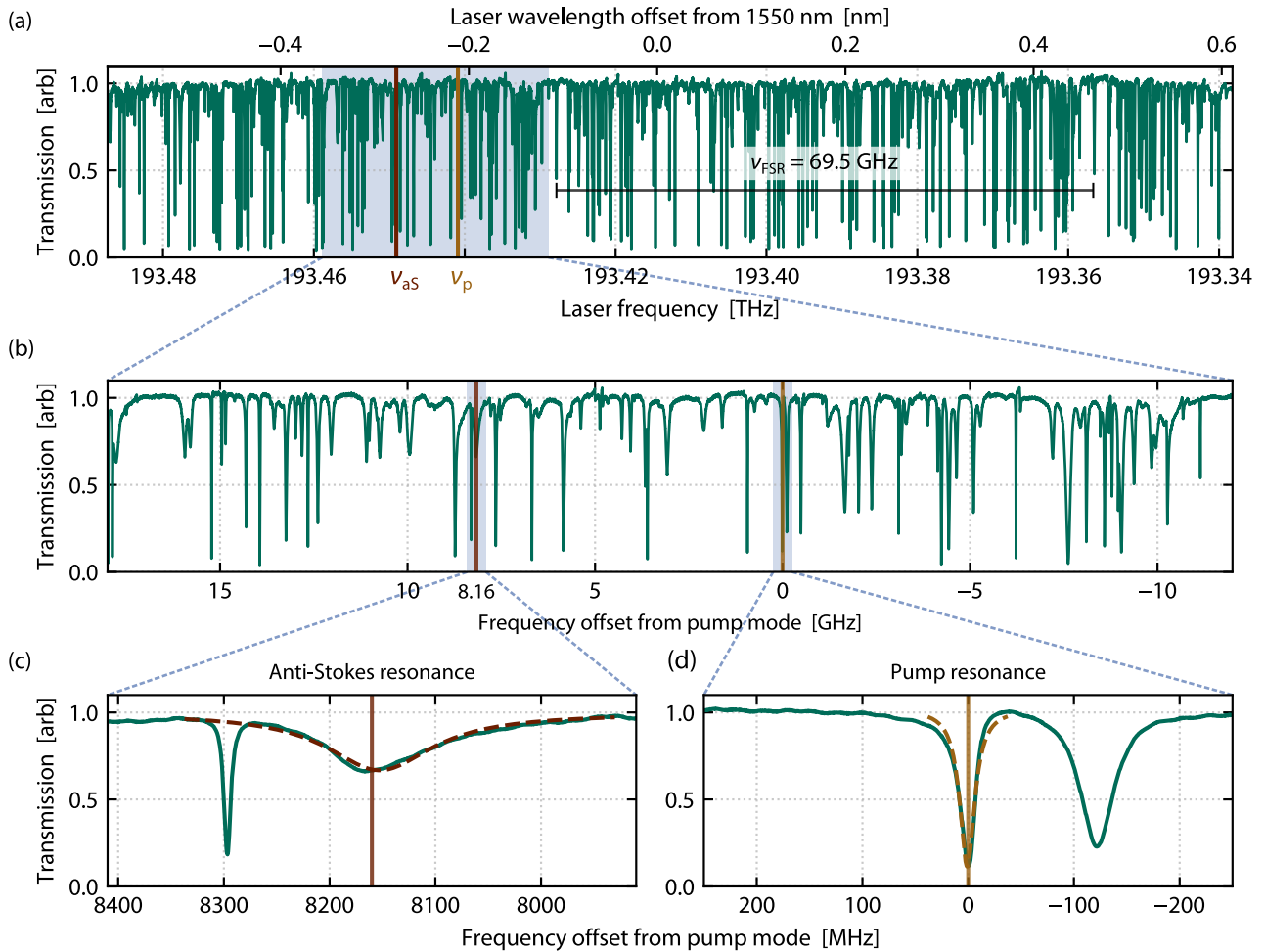
Figure 6.8. Optical spectrum of the microresonator with the pump–anti-Stokes mode pair. (a) The spectrum of across the full pump laser bandwidth, stitched together from 12 500 partially overlapping spectra obtained whilst the laser is thermally tuned over its full range. The pump and anti-Stokes resonances used are marked in (b) Zoomed in view on a section of the spectrum. (c,d) The anti-Stokes (c) and pump (d) modes with fitted Lorentzian lineshapes. Note that for an accurate linewidth measurement, a short-range, more accurately calibrated spectrum is obtained and fitted to extract the linewidths.

spectrum. One such pair is the pair shown in Fig. 6.8(b). The optomechanical coupling of the pair candidates is then investigated by optically pumping the lower-frequency mode and directing the backscattered light from the cavity to the heterodyne detector. If the backscattered light has frequency components shifted by the Brillouin frequency from the pump, the modes couple via Brillouin scattering. By inspecting the heterodyne spectrum using an electronic spectrum analyser[xi] (ESA) connected to the balanced detector, the strength of the coupling can be gauged from the signal-to-noise of the feature in the heterodyne spectrum and an estimate for the mechanical linewidth is given by the spectral feature's width, see Fig. 6.9. If the optomechanical coupling is small or the mechanical mode is broad, the mode trio is discarded. For the modes that seem favourable, the optical pump power is increased whilst the heterodyne spectrum is monitored to see the characteristic mechanical linewidth broadening to confirm it is indeed a Brillouin signal.

[xi] Rohde & Schwarz FPC1000 (1 GHz bandwidth)
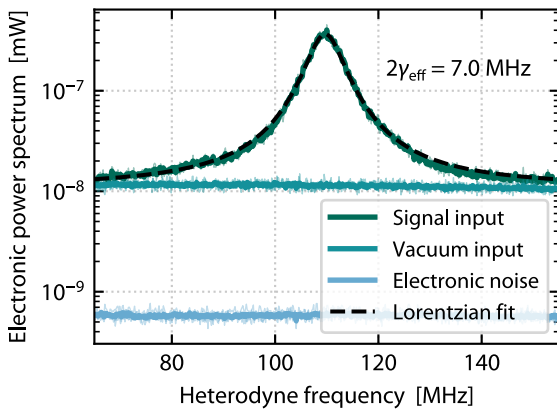
Figure 6.9. Example heterodyne spectrum and noise levels as obtained by an ESA (with resolution BW 30 kHz and video BW 100 Hz). The electronic noise (spectrum obtained with no input to the ESA) is far below the optical spectra and not the principal noise source. Instead, the noise floor is given by the shot noise of the LO laser, as shown by the spectrum obtained when optical vacuum is input to the heterodyne beam splitter instead of the anti-Stokes signal. The fitted effective mechanical linewidth is annotated.

6.4.3 *System characterisation*

In order to analyse and understand the experimental results, relevant optical, mechanical and optomechanical properties of the system must be characterised. The characterisation measurements and results are described below. A summary of the results can be found in Table 6.1.

OPTICAL LINEWIDTHS AND SEPARATION. The linewidths of the optical resonances are determined as described in Section 3.5, i.e., by sweeping the pump laser across the resonances at low power to avoid broadening, and fitting the resulting spectra. Figure 6.8(c,d) shows the anti-Stokes and pump optical lines, respectively. The pump mode's amplitude decay rate is fitted to $\kappa_{\mathrm{p}}/(2\pi) = 7.1(1)$ MHz, and for the anti-Stokes mode the decay rate is fitted to $\kappa_{\mathrm{aS}}/(2\pi) = 46.9(1)$ MHz. The uncertainties are given by the fit and uncertainty in the laser calibration. The separation of the two optical modes is pump-power dependent due to the Kerr effect, but is approximately equal to the mechanical frequency – which is measured as described in the next paragraph.

MECHANICAL FREQUENCY. The mechanical frequency can be determined from the frequency separation between the pump light and anti-Stokes light. Naïvely, one could interfere the light backscattered from the cavity directly with the pump and measure the beat note between the two; however, as the anti-Stokes signal is very weak, this is not directly feasible. Another approach could be to use heterodyne detection between the pump and anti-Stokes light, but the ~8 GHz spectral separation between the two fields is far beyond the bandwidth of the balanced detector. Therefore, a more convoluted measurement is instead performed: the strong local oscillator laser is ensured to be at the same frequency as the anti-Stokes light with optical modes, and then comparable powers of LO and pump light are interfered to produce a clean beat note on a high bandwidth photodiode, determining the optical frequency separation between the two.

In detail, the measurement works as follows. The frequency of the LO is tuned so it is roughly the same as the anti-Stokes light, then interfering the two at the heterodyne beam splitter, the difference current is within the balanced detector's bandwidth. The LO can then be brought to exactly the anti-Stokes frequency by tuning the LO frequency so that the heterodyne signal is at zero frequency. Then, by interfering the pump light with

the LO on a beam splitter and detecting the resulting light on a high-bandwidth photode-tector,[xii] the optical beat note can be measured by a high-bandwidth ESA.[xiii] The detected beat note is equal to the frequency separation between the pump and anti-Stokes light, which corresponds to the mechanical frequency. The measured mechanical frequency is $\omega_{\mathrm{m}}/(2\pi) = 8.16(1)$ GHz, corresponding to a pseudo-longitudinal mechanical whispering-gallery mode. The uncertainty is set by the ability to keep the laser beat notes stable.

MECHANICAL LINEWIDTH AND OPTOMECHANICAL COUPLING. The characterisation meas-urements to find the mechanical linewidth and the optomechanical parameters are more involved because the access to the mechanics is not direct, but via the optical coupling.

To determine the mechanical linewidth, the linear scaling of the effective mechanical linewidth with an increasing number of intracavity photons (due to increasing optomech-anical coupling) can be used. By extrapolating the effective linewidth to zero pump photons, the intrinsic mechanical linewidth can be found.

In the limit of weak coupling, it can be shown that the power spectral density of the anti-Stokes signal is given by [Eq. (5.26)]

$$S_{XX}(\omega) = \int_{-\infty}^{\infty} \mathrm{d}\omega \, \langle \widetilde{X}^\dagger(\omega)\widetilde{X}(\omega)\rangle \tag{6.45}$$

$$\propto |\chi_{\mathrm{bb}}(\omega - \omega_{\mathrm{het}})|^2 + |\chi_{\mathrm{bb}}(-\omega - \omega_{\mathrm{het}})|^2 \, , \tag{6.46}$$

where $\widetilde{X}$ is the Fourier transform of the X quadrature, ω_{het} is the heterodyne frequency, and the mechanical susceptibility is

$$\chi_{\mathrm{bb}}(\omega) \approx \frac{\sqrt{2\gamma}}{\mathrm{i}\omega + \gamma_{\mathrm{eff}}} \tag{6.47}$$

in the limit where $\gamma \ll \kappa_{\mathrm{aS}}$. This limit is crucial for this measurement and can be un-derstood by considering the frequency domain overlap between the optical mechanical resonances: if the optical mode is narrower than the mechanical mode, it effectively filters the anti-Stokes light generated across the mechanical resonance's linewidth due to the lack of optical density of states in the optical resonator, resulting in a heterodyne signal of linewidth limited by κ_{aS}. In this experiment $\gamma/\kappa_{\mathrm{aS}} \simeq 0.07$, and thus it is the mechanical linewidth that determines the linewidth of the heterodyne power spectrum.

In the weak coupling regime, the effective mechanical amplitude decay rate scales with the optomechanical cooperativity C:

$$\gamma_{\mathrm{eff}} = \gamma(1 + C) \, , \tag{6.48}$$

which is given by

$$C = \frac{G^2}{\kappa_{\mathrm{aS}}\gamma} = \frac{g_0^2 N_{\mathrm{cav}}}{\kappa_{\mathrm{aS}}\gamma} \propto N_{\mathrm{cav}} \, . \tag{6.49}$$

Therefore, as this experiment is operated in the weak-coupling regime and $\gamma \ll \kappa_{\mathrm{aS}}$, the spectrum of the backscattered anti-Stokes signal can be approximated by a Lorentzian function with FWHM given by $2\gamma_{\mathrm{eff}}$ [Eq. (6.46) and Eq. (6.47)]. As the effective linewidth

scales linearly with the number of intra-cavity pump photons, the effective linewidth can be extrapolated to zero optical pump to extract the intrinsic mechanical linewidth.

The measurement is performed comparing power density spectra of the heterodyne signal at different pump powers. The spectra are obtained by Fourier-transforming time traces from the output of the balanced heterodyne detector at eleven input powers in the approximate interval 1 mW to 10 mW. The resulting spectra are shown in Fig. 6.10(a) and the fitted effective linewidths in Fig. 6.10(b). By fitting a linearly increasing γ_{eff} to the effective linewidths, an intrinsic mechanical decay rate of $2\gamma/(2\pi) = 6.6(2)$ MHz by extrapolating to zero. This linewidth is in agreement with room-temperature Brillouin linewidths reported in similar crystalline materials [501].

To also estimate the bare optomechanical coupling rate g_0, the intra-cavity pump photon number is calculated [Eq. (2.51)]:

$$N_{\text{cav}} = \frac{1}{\hbar \omega_{\text{p}}} \frac{\eta_{\text{c}} \mathcal{P}_{\text{in}}}{\kappa_{\text{p}}} = 1.19(3) \cdot 10^9 \,, \tag{6.50}$$

where the taper coupling $\eta_{\text{c}} = 2\kappa_{\text{p}}^{\text{e}}/\kappa_{\text{p}}$ [Eq. (2.48)]. The pump mode's extrinsic optical decay rate, $\kappa_{\text{p}}^{\text{e}}$, is calculated from the mode's on-resonance transmission and total linewidth, see Eq. (2.42).[xiv] The single-photon optomechanical coupling rate can be calculated from Eqs. (6.48) and (6.49):

$$C = \frac{\gamma_{\text{eff}} - \gamma}{\gamma} \quad \Longrightarrow \quad \frac{g_0^2}{\kappa_{\text{aS}}} = \frac{\gamma_{\text{eff}} - \gamma}{N_{\text{cav}}} \,. \tag{6.51}$$

The term on the right-hand side of the right equation can be identified as the gradient of the linear fit in Fig. 6.10(b), $\partial\gamma_{\text{eff}}/\partial N_{\text{cav}}$. Thus

$$g_0 = \sqrt{\frac{\partial\gamma_{\text{eff}}}{\partial N_{\text{cav}}} \kappa_{\text{aS}}} = 2\pi \cdot 0.29(8) \text{ kHz} \,. \tag{6.52}$$

From the single-photon coupling rate and the intracavity photon number for the pump power used in the experiment, the optomechanical coupling rate and cooperativity are calculated to be

$$\frac{G}{2\pi} = 10.3(3) \text{ MHz} \,, \qquad C = 0.69(4) \,. \tag{6.53}$$

A MODEL INCORPORATING KERR DETUNING. Alternatively, a more comprehensive model can be used to extract the mechanical linewidth and coupling rate, a model describing not only the mechanical broadening but also the change in the optomechanical detuning change due to the Kerr effect. With increasing pump power, the pump resonance shifts in frequency relative to the readout resonance, and thus the detuning Δ between the readout resonance (referred to as the anti-Stokes resonance) and the frequency of the anti-Stokes light changes:

$$\omega_{\text{aS}} = \omega_{\text{p}}(P_{\text{in}}) + \omega_{\text{m}} = \omega_{\text{p}}^{\text{res}} + \Delta(P_{\text{in}}) + \omega_{\text{m}} \,. \tag{6.54}$$

[xiv] A note about uncertainties given for this and other calculated parameters: the uncertainties are calculated by using a first-order approximation and propagating the errors of the values used in the calculation. For example for a function $y(a, b)$ with uncorrelated variables a, b, to first order, the uncertainty in y given the uncertainties $\Delta a, \Delta b$ is

$$\Delta y^2 = \left[\left|\frac{\partial y}{\partial a}\right| \Delta a\right]^2 + \left[\left|\frac{\partial y}{\partial b}\right| \Delta b\right]^2 \,.$$

See for instance Hughes and Hase [294, Ch. 4] for more on error propagation.
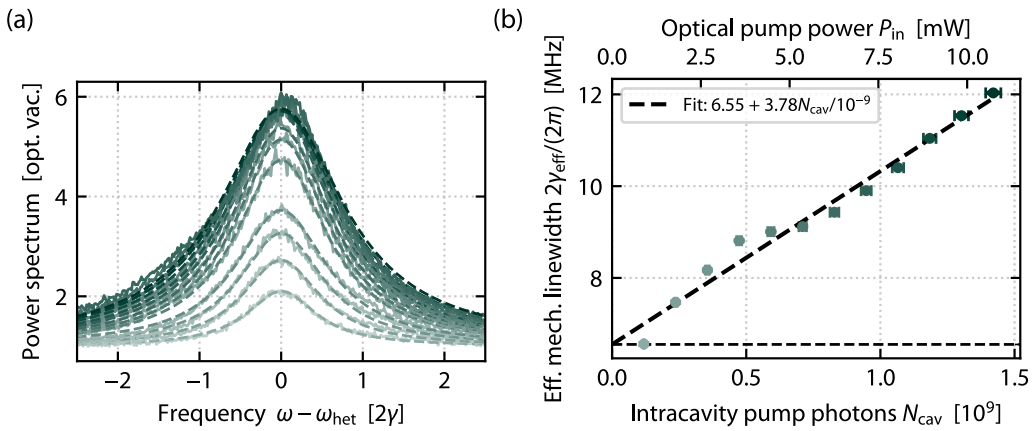
Figure 6.10. Determining the mechanical linewidth and optomechanical coupling from comparing spectra for increasing pump powers. For each pump power, 2000 heterodyne spectra are obtained. (a) The median spectrum for each pump power (normalised to vacuum noise), with darker shades corresponding to higher input powers, up to a maximum of $\simeq 11$ mW. The spectra are offset to the same centre frequency and plotted in units of the fitted intrinsic mechanical linewidth 2γ, as determined by panel (b). (b) The effective mechanical linewidth of the spectra in (a) given as a function of the intra-cavity pump photon number. The intercept of the linear fit gives the intrinsic mechanical linewidth $2\gamma/(2\pi) = 6.6(2)$ MHz, and the slope is used to calculate $g_0/(2\pi) = 0.29(8)$ kHz.
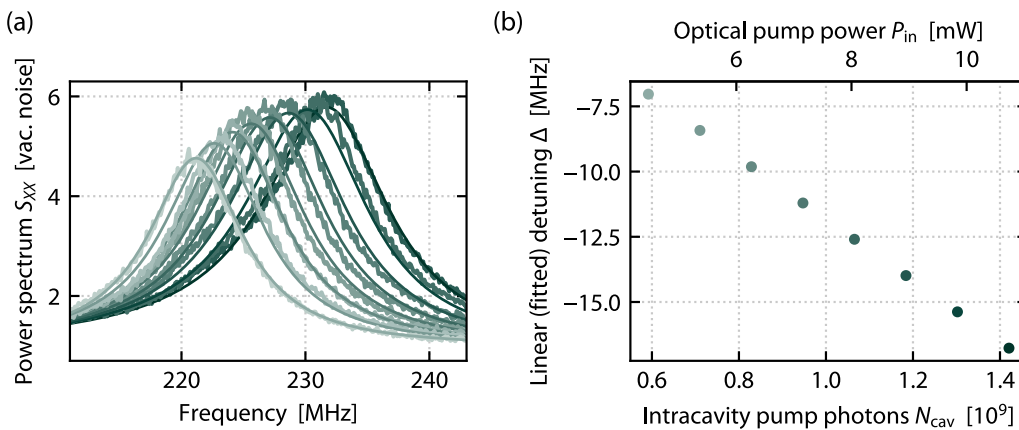
Figure 6.11. Full power spectrum model with detuning for obtaining mechanical linewidth and optomechanical coupling, using a subset of the data in Fig. 6.10. (a) A power spectrum model accounting for the change in detuning with increasing power is fitted simultaneously to the eight highest powers (the dataset is truncated due to drift in the local oscillator laser for the lowest powers). The fit gives both the intrinsic linewidth and coupling rate directly, $2\gamma/(2\pi) = 6.68(3)$ MHz and $g_0/(2\pi) = 309(1)$ Hz. (b) .

This change in the optomechanical detuning affects the centre frequency of the power spectra, as shown in Eq. (5.26). Note that any thermal shift can be assumed to affect the two modes equally as they have significant spatial overlap in the resonator.

If the heterodyne local oscillator is kept at a constant frequency, the change in the optomechanical detuning can be extracted from the change in the heterodyne carrier frequency, which changes as it is the difference between the frequency of the static LO and the changing anti-Stokes light. As the Kerr effect is linear with power [Eq. (2.80)], optomechanical detuning can be expressed as

$$\Delta(P_{\text{in}}) = \Delta_0 + \Delta_1 P_{\text{in}} \,, \tag{6.55}$$

where the proportionality constant Δ_1 is negative, as can be seen from Eq. (2.80), which gives $\Delta_1 \propto -n_2/n$, where n_2 is the non-linear refractive index of the material.

With this method, all the power spectra are simultaneously fitted, with the result shown in Fig. 6.11. The fit gives both the intrinsic linewidth and coupling rate directly, $2\gamma/(2\pi) = 6.68(3)$ MHz and $g_0/(2\pi) = 309(1)$ Hz, where the uncertainties are smaller as the multi-dimensional fitting takes into account more data points for a single fitting operation, rather than a linear fit to twelve data points as in Fig. 6.10. Both values are within the error margins of the values obtained via Fig. 6.10. The method also estimates the absolute optomechanical detuning for the experiment.

INITIAL THERMAL OCCUPATION AND SIDEBAND COOLING. Due to the finite temperature of the resonator, there is a thermal occupation of phonons in the mode. The experiment is performed at $T = 300$ K, giving a thermal occupation of [Eq. (6.1)]

$$\bar{n}_{\text{th}} = \left[\exp\left(\frac{\hbar\omega_{\text{m}}}{k_{\text{b}}T}\right) - 1\right]^{-1} \approx \frac{k_{\text{b}}T}{\hbar\omega_{\text{m}}} = 766(2) \,, \tag{6.56}$$

where k_{b} is the Boltzmann constant, and the approximation to the limit of high temperature ($k_{\text{b}}T \gg \hbar\omega_{\text{m}}$) is made. However, as the optomechanical interaction is driven, the mechanical state is sideband cooled to a lower occupation. In the limit of weak optomechanical coupling, the effective mechanical occupancy in the steady-state is given by [450]

$$\bar{n} = \frac{\bar{n}_{\text{th}}}{2\pi} \int_{-\infty}^{\infty} d\omega \, |\chi_{\text{bb}}(\omega)|^2 = \frac{\bar{n}_{\text{th}}}{1 + C} \,, \tag{6.57}$$

where the optomechanical cooperativity is as given in Eq. (6.49). This results in a steady-state mean occupancy of the unconditioned mechanical state of $\bar{n}_{\text{eff}} = 4.5(1) \cdot 10^2$, corresponding to a sideband-cooling factor of $\simeq 1.7$.

6.4.4 *Phonon subtraction heralding and fidelity*

Each time a phonon is subtracted via the optomechanical interaction, an anti-Stokes photon is created, and detection of this photon heralds the subtraction operation. Detecting a two-photon coincidence heralds a simultaneous two-phonon subtraction. The following explains how the heralding is performed in the experiment.

The created anti-Stokes photons couple out of the cavity and into the taper with an efficiency given by the resonator linewidth and taper coupling. The backscattered light from the resonator is separated out using a circulator and a portion of the light used for heralding to condition the heterodyne measurement, see Fig. 6.12. Because the single-photon avalanche photodetectors[xv] (SPAD)s used are not photon-number resolving, another beam splitter is used so that coincident photons are directed to separate detectors for coincidence detection. With this setup, a click on one SPAD heralds a single-phonon subtraction and simultaneous clicks on both detectors heralds a two-phonon subtraction, as illustrated in Fig. 6.12.

To ensure the fidelity of the heralding measurement, the number of spurious detector clicks must be low to avoid false heralding. There are three main sources of spurious clicks that will decrease the fidelity of the heralding: (i) dark counts from the detectors, (ii) masked multi-photon events on one detector as the detectors are not photon-resolving and thus gives only one click for such events, and (iii) pump photons hitting the detectors. All three sources are minimised as described below. Optical losses in the heralding process in practice affects only the heralding probability, meaning the time between heralding events is longer, but the fidelity is unchanged.

DARK COUNTS. Spurious clicks when no photon is incident on a detector are referred to as dark counts, and in the context of this experiment these dark clicks reduce the fidelity of the heralding operation. The rate of dark counts on detector is typically an increasing function of the detector's quantum efficiency, where the quantum efficiency is the ratio of time-averaged clicks to incident photons [177, 502]. For the SPADs used here, the combination of a gated operation[xvi] with a long deadtime after a detection event, and a 12.5 % quantum efficiency, gives a rate of spurious dark counts of ~1 Hz, which is much smaller than the ~0.3 kHz rate of single-photon clicks on each detector. With these rates, one in about 300 single-clicks is a spurious click, ensuring a high heralding fidelity ($300/(1+300) \simeq 0.996$). Also, note that the anti-Stokes photons not resulting in a detector click due to the low quantum efficiency do not reduce the fidelity of the heralding – they do not influence validity of the measured clicks.

[xv] ID Quantique id210
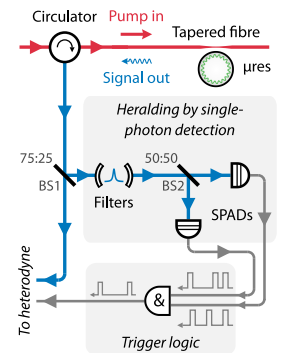
Figure 6.12. Subtraction operation heralding arm.

[xvi] The detector works by biasing an InGaAs/InP junction so that when a photon is absorbed in the InGaAs layer, the resulting electron hole is multiplied due to the high voltage, creating an avalanche of carriers before the avalanche is quenched. The gating can be performed by biasing the junction only for a set gate time at some rate. This reduces dark counts due to thermal excitations or afterpulsing. See for instance Refs. 503 or 504 for more about SPADs.

SUPPRESSING MULTI-PHOTON EVENTS. The rate of photons hitting the detectors must small enough to avoid multi-photon events on one detector resulting in a single click from that detector. The detectors are operated in gated mode, where the detector is sensitive to incoming photons for only a short amount of time at a fixed rate, sending a click detection signal if at least one photon has been detected in this time window. With a known gate time duration and known rate of anti-Stokes photons impinging on a detector, an estimate of the probability of multi-photon events at a detector can be calculated.

To calculate the probabilities, firstly, calculate the time-averaged photon rate emerging from the cavity

$$\langle R_{\text{cav}} \rangle = \langle \hat{a}_{\text{out}}^{\dagger}(t)\hat{a}_{\text{out}}(t) \rangle = \eta_{\text{opt}}\bar{n}_{\text{th}}\frac{G^2}{\kappa_{\text{aS}} + \gamma} \sim 10^8 \, \text{Hz} \,, \tag{6.58}$$

for the system parameters of this experiment. Accounting for various optical losses due to component imperfection and beam splitters, the time-averaged rate of photons impinging on a detector is

$$\langle R_{\text{det}} \rangle = \eta_{\text{path}}\eta_{\text{BS1}}\eta_{\text{filters}}\eta_{\text{BS2}} \langle R_{\text{cav}} \rangle \sim 10^6 \, \text{Hz} \,, \tag{6.59}$$

where the losses from the cavity up to the first beam splitter (see Fig. 6.12) due to the tapered fibre and insertion losses can be expressed by a transmission efficiency $\eta_{\text{path}} \simeq 0.67$, the filters have a transmission of $\eta_{\text{filters}} \simeq 0.15$, and the beam splitters have transmissions according to their ratios, $\eta_{\text{BS1}} = 0.25$ and $\eta_{\text{BS2}} = 0.50$.

After determining the anti-Stokes photon flux at the detector, consider the number of photons impinging on the detector over the gate time window which is when a click can be measured. Using an effective gate length of $t_{\text{gate}} = 3.5 \, \text{ns}$ (at a 50 kHz gate rate, dead time after detection event 18 µs), the time-averaged photon number over a gate window is

$$\bar{N}_{\text{det}} = \eta_{\text{SPAD}} \langle R_{\text{det}} \rangle \, t_{\text{gate}} \sim 10^{-3} \,, \tag{6.60}$$

where $\eta_{\text{SPAD}} = 0.125$ is the quantum efficiency of the detectors. Note also that a 3.5 ns gate at a 50 kHz rate means the detector is active 175 µs s^{-1} or about 0.2 % of the time. The rate of impinging photons multiplied by the quantum efficiency and the active time gives $\langle R_{\text{det}} \rangle \, \eta_{\text{SPAD}} \cdot 2 \cdot 10^{-4} = {\sim}25 \, \text{Hz}$, compared to the observed 0.3 kHz count rate.

As the light from the cavity originates from a thermal state, the anti-Stokes photon statistics follows the Bose–Einstein distribution [Eq. (6.3)], and the probability for N_{det} photons to impinge on a detector can be calculated given the time-averaged number $\bar{N}_{\text{det}}$,

$$\Pr(N|\bar{N}) = \frac{\bar{N}^n}{(\bar{N}+1)^{N+1}} \sim \begin{cases} 0.997 & \text{for } N = 0 \\ 10^{-3} & \text{for } N = 1 \\ 10^{-6} & \text{for } N = 2 \end{cases} \,, \tag{6.61}$$

showing a three orders of magnitude smaller probability for two photons rather than one photon impinging on a detector over the gate time. This means that one in thousand clicks

is due to a multi-photon event at one detector, which will have a small impact on the heralding fidelity.

SUPPRESSING PUMP PHOTONS VIA FILTERING. Optical filters are used to make sure only anti-Stokes photons reach the SPADs to ensure high fidelity heralding. The detection band of the SPADs covers a broad wavelength range and any photon reaching the SPADs in the heralding arm that is not an anti-Stokes photon results in a spurious heralding event, which incorrectly triggers the heterodyne measurement.

In particular, photons at the pump wavelength are likely to cause spurious clicks as the pump is very strong, meaning that very small imperfections in the setup, for instance a small back-reflection from a fibre connection, can cause a significant number of pump photons in the heralding arm.[xvii] Furthermore, it is not only the anti-Stokes signal field that is backscattered in the resonator, but also pump light is backscattering due to imperfections in the resonator – as discussed in Chapter 4 on backscattering suppression.

To filter out pump photons SPADs, Fabry–Pérot optical filters[xviii] with FWHM bandwidth 120 MHz and tuneable centre frequencies are used. The filters are used in series to doubly suppress the pump, and a circulator is used between the two to avoid a cavity being formed between the two filters because of backreflections. The free spectral range of the filters is 25 GHz, ensuring that when the centre frequency is tuned to the anti-Stokes signal, the suppression of the pump ≃8 GHz away from the anti-Stokes is high, as is the suppression for any higher harmonics anti-Stokes light.

To estimate the suppression of the pump provided by the two filters, the relative transmission[xix] of one filter can be calculated from its free spectral range and linewidth [505]

$$
T(v) = \left[1 + \left(\frac{2F^{\text{filt}}}{\pi} \right)^2 \sin^2 \left(\pi \frac{v}{v_{\text{FSR}}^{\text{filt}}} \right) \right]^{-1} , \tag{6.62}
$$

where the finesse is the ratio of the FSR to the linewidth, $F^{\text{filt}} = v_{\text{FSR}}^{\text{filt}}/\Delta v^{\text{filt}} = 208$ [Eq. (2.13)]. A plot of the relative transmission for one filter is shown in Fig. 6.13. At the pump frequency $T(8\,\text{GHz}) = -41\,\text{dB}$ for one filter, doubling to $-82\,\text{dB}$ for two filters in series. If only one filter is used, the count rate roughly doubles compared to using two filters, suggesting the second filter removes roughly 300 pump photons per second (and implying that the first filter removes $\sim 10^6$ pump photons per second). Based on the coarse estimate that $-41\,\text{dB}$ suppression removes 300 photons per second at the last filter, the number of pump photons making it through to the detector is $\sim 2 \cdot 10^{-2}$ Hz compared to the eight orders of magnitude higher $\sim 10^6$ Hz anti-Stokes photos [Eq. (6.59)], ensuring good heralding fidelity.

The filters' centre frequencies are temperature tuned ($\sim 1.6\,\text{GHz}\,\text{K}^{-1}$) by thermoelectric cooler elements, and thermistors provide temperature sensing for feedback control. To control the filter temperature, thermoelectric-cooler controller[xx] (TECCs) are used. Each TECC has an internal PID loop, stabilising the temperature by reading the resistance of the thermistor in the connected filter and applying a current to the thermoelectric element

[xvii] A 9 mW input power corresponds to a rate of $9\,\text{mW}/(\hbar\omega_{\text{p}}) \sim 10^{17}$ photons/s flowing in the setup. A reflection of only 1 ppm gives $\sim 10^{11}$ photons/s of reflected photons, which is comparable to the $\sim 10^8$ photons/s rate of anti-Stokes photons emerging from the cavity [Eq. (6.58)]. By suppressing the pump by for instance 80 dB the rate reduces to $\sim 10^3$ photons/s.

[xviii] Micron Optics FFPI

[xix] The insertion losses of an optimally tuned filter is at the 1 dB level.
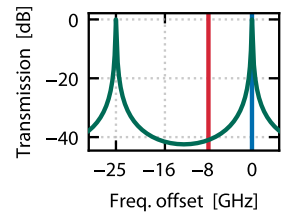
Figure 6.13. The calculated transmission of a single Fabry–Pérot filter with 25 GHz FSR and 120 MHz FWHM bandwidth. The pump frequency (red) and anti-Stokes frequency are annotated for a perfectly tuned filter.

[xx] Thorlabs TED200C

to keep the thermistor resistance at the desired setpoint. However, due to fluctuations in the laboratory environment at minute and hour timescales, the setpoints of the TECCs must be continuously tuned to keep the filters' centre frequencies stable with respect to the frequency of the anti-Stokes signal. This procedure is described in Section 6.4.7.

To initially tune the filters, the local oscillator laser is brought to the anti-Stokes frequency and connected to the filters one by one optimising their transmission on a photodiode and/or using an optical spectrum analyser.

6.4.5   *Heterodyne detection for state characterisation*

A heterodyne detection setup is used to obtain information about the click-conditioned mechanical state. The schematic in Fig. 6.14 shows how the click signals from the heralding arm triggers an oscilloscope[xxi] to measure the heterodyne signal from the balanced photodetector.[xxii]

Ideally, the light from the cavity-locked pump laser would be used as the local oscillator in the heterodyne setup for frequency stability; however, because the bandwidth of the balanced detector is only 400 MHz, the local oscillator must be separated by less than 400 MHz from the anti-Stokes signal in frequency. Therefore a separate laser to the pump laser is used as the local oscillator for the heterodyne setup, and this LO laser is locked to the pump laser frequency as described in Section 6.4.7. In the experiment, a high heterodyne frequency is desirable so that the state evolves little per rotation of the measurement basis, but the frequency must be low enough to keep the heterodyne signal within the bandwidth of the detector. A heterodyne frequency of $\omega_\mathrm{het}/(2\pi) = 214\,\mathrm{MHz}$ is chosen.

SAMPLING RATE.   To perform the state tomography at the time of subtraction and observe the time-domain change in the mean phonon occupancy, the sampling rate of the measurement must be sufficiently high to resolve the time-domain feature. The decay time of the subtraction feature is approximately given by the inverse of the effective mechanical linewidth, $[(\gamma + G^2/\kappa_\mathrm{aS})]^{-1} \simeq 29\,\mathrm{ns}$, giving approximately 90 sampling points over the feature when the oscilloscope is operated at a sampling rate of 3.125 GSs^{-1}. In order to digitally bandpass filter the time-domain data as described in the data analysis section 6.5.1, the frequency resolution must be finer than the bandwidth of the heterodyne signal. At the high sampling rate used, a large number of points per trace is needed to ensure a sufficient frequency resolution. Therefore, each time trace captured is 4.00 µs long, giving $12.5 \cdot 10^3$ points per trace, which corresponds to a frequency resolution of 250 kHz – a meaningful resolution for bandpass-filtering the heterodyne signal with a bandwidth comparable to the effective mechanical linewidth, ~11 MHz.

xxi Tektronix MSO64
(4 GHz bandwidth)

xxii Insight BPD-1
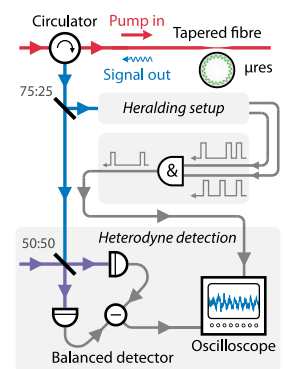
Figure 6.14. Heterodyne detection arm. Illustrating the triggering setup for two-phonon subtraction measurements.

TRIGGERING OF THE HETERODYNE MEASUREMENT. In addition to a sufficiently high heterodyne sampling rate, the click conditioning must be accurately timed to resolve the subtraction feature. A fixed offset between the heralding event and triggering of the heterodyne can be calculated and corrected for in the analysis, but any jitter in the conditioning timing will smear out the subtraction feature in time and cause mis-conditioned values to contribute to the tomogram.

Considering one-phonon subtraction events first, the single-photon click signals from one SPAD can be used directly as a trigger for the oscilloscope. The jitter of the click signal compared to the arrival time of the photon is ~0.2 ns, which is in fact smaller than the 0.320 ns separation between samples as set by the oscilloscope sampling rate. As the oscilloscope's trigger jitter is <40 ps, it is currently the sampling rate that limits the timing resolution of the single-photon heralding, but the resolution is much finer than the subtraction-feature decay time of ≃29 ns and the effect should be small.

For characterising two-phonon subtraction events, the heterodyne measurement should trigger off two-photon coincidence events. To implement the coincidence triggering, the detectors are synchronisedly gated, meaning that the time window over which the detectors are active is the same. With the gated operation, simple AND logic on the click signals from the two detectors can be used for heralding the two-photon coincidences with good approximation, with timings as described below. Using this implementation, the rate of two-photon coincidences is ~2 Hz.

Due to the synchronised operation, the 3.5 ns gate time sets the maximum time separation between click signals from the two detectors within the same gate, and the 100 ns width of the click signal (Fig. 6.15) guarantees that if both detectors click for a gate, their click signals overlap in time. As the system is gated at 50 kHz, there is a minimum time of 20 µs between clicks from different gates, guaranteeing that click signals from separate gates will not overlap. Ensuring equal-length cabling from the gating signal source[xxiii] to the SPADs, and equal lengths from the SPADs to the oscilloscope where the AND logic is performed, the time window over which clicks are considered simultaneous is the same as the effective gate length, 3.5 ns which is short compared to the subtraction-feature decay time. If a greater timing resolution is required, post-selection of smaller click-separation can be performed.

NOTE ON THE NUMBER OF ANTI-STOKES PHOTONS AND SIDEBAND COOLING. The number of anti-Stokes photons impinging on the heterodyne beam splitter can be calculated by a similar analysis to the one showing the time-averaged number of photons at the SPADs [Eqs. (6.58) to (6.60)]. Accounting for the optical circuit losses and detector efficiency, less than one anti-Stokes photon is on average being used for state tomography in the heterodyne measurement within the timescale that the mechanical oscillator is taken out of equilibrium ($\simeq 2 \cdot 29$ ns).

It is important to note that the heterodyne detection does not condition or change the mechanical state. The heterodyne measurement is a linear measurement, giving information about the field quadratures, not the number of photons or the optical power – i.e.,
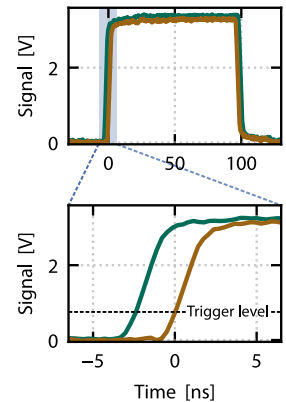
Figure 6.15. Click signals from SPADs. The oscilloscope triggers when both channels are above the trigger level of 750 mV.

the heterodyne measurement is linear in operators ($\hat{a}$) versus the nonlinear click detection ($\hat{a}^\dagger\hat{a}$) performed in the other arm of the setup. An ensemble of heterodyne signal measurements can be used to describe the prepared mechanical states through statistical methods given high-fidelity heralding of the prepared states.

The heralding of subtraction events is used to trigger the heterodyne measurements, aligning data from thousands of measurements where the time of subtraction is known. However, the rate of scattering events taking place in the resonator is high compared to the length of the time traces, which means that over the duration of a single time-trace measurement, many photons scatter off phonons, not only the heralded one. The many scattering events reduce the ensemble's mean occupation below the initial thermal occupation everywhere else than where the heralded subtractions are aligned in time. This effect is the sideband cooling of the state,

$$\bar{n}_{\text{th}} \rightarrow \bar{n} = \frac{\bar{n}_{\text{th}}}{1 + C} \ . \tag{6.63}$$

6.4.6   *Interleaved measurement protocol*

To obtain sufficient statistics for a good signal-to-noise ratio in both the time-domain analysis and the state tomography, $2.4 \cdot 10^5$ events are measured for each of the one- and two-phonon-subtracted states. In addition, the same number of randomly triggered events are obtained to measure the initial, laser-cooled thermal state, and another $2.4 \cdot 10^5$ randomly triggered events are captured with the heterodyne port that is normally connected to the cavity disconnected to measure the shot noise level.

Because of the relatively small probability of detecting a click [Eq. (6.61)], and the much smaller square of the former probability for a double click, acquiring tens of thousands of measurements takes time. At a rate of roughly 300 single clicks per second, obtaining $2.4 \cdot 10^5$ measurements for single-phonon subtraction events takes about 13 minutes. However, the double click rate is much lower at about two coincidences per second, meaning it takes about 30 hours to obtain.

Over the course of 30 hours the experimental conditions can change affecting losses and other parameters to such an extent that the measurements obtained at the beginning are different from those obtained at the end – effectively sampling a set of experimental conditions, which the analysis will subsequently average over. To make sure the measurements are sampling the same conditions, a protocol considering the substantial event rate difference is used.

The one- and two-click measurements are interleaved in smaller batches to make sure they both sample the same experimental conditions. The measurements are split up in alternating batches of 5000 measurements. Obtaining 5000 coincidences takes roughly 35 minutes. To make sure the following 5000 single-photon events are obtained over a similar timescale to sample the experimental conditions, the measurement is artificially slowed down by dividing the batch into even smaller batches of 100 traces, each batch obtained in less than a second, but with delays between them to space them out. The delays are random,

sampled from a Poissonian distribution with a mean corresponding to the average delay time needed for the 5000 single-click measurements to take the same amount of time as the coincidences.

The whole measurement procedure for obtaining $2.4 \cdot 10^5$ measurements of each one- and two-click data takes about 60 hours.

6.4.7 *Feedback loops for experimental stability*

A lab environment is seldom as static as the experimentalist wants it to be. For precision measurements there are typically three ways to circumvent the problems related to drifts or fluctuations in the experiment: measure faster than the timescale of the disturbance, averaging many measurements over a long time to sample the range of the drifts and converge to an average value, or to try to counteract the disturbances by stabilising the experiment. In this work, a combination of the latter two is used.

As described in the previous subsection, the measurement runs over hours to obtain the necessary statistics to get a good signal-to-noise ratio, and over this long averaging time, drifts can change important experimental parameters like the optomechanical coupling or the heterodyne frequency. Even though these parameters can be averaged over, it is preferable to reduce disturbances to the experiment.

The laboratory ambient temperature is a very challenging parameter to control within a narrow and stable range. In this laboratory, the temperature is controlled by the inlet air temperature and an additional control by a circulation unit in the lab providing local cooling and, in principle, fine control. However, accurate temperature control is challenging, and the PID settings and sensor-position of the local cooling unit causes fairly regular oscillations in the lab temperature with an average period of 15 minutes, in addition to slow drifts over the day, Fig. 6.16. In particular, these temperature fluctuations are a challenge for the narrow bandwidth Fabry–Pérot optical filters, as their centre frequency is temperature tuned, and moves more than one FWHM bandwidth per 0.1 K change in temperature.

To mitigate the impact of the temperature and other environmental fluctuations, the optical fibre-based setup is built using polarisation maintaining fibre when possible, and a number of stabilisation loops are used. The pump laser frequency is locked to the pump cavity resonance using a PDH lock scheme as described in Section 3.6.2. The other loops are described in the following, and includes the centre frequency of the optical filters in the heralding arm, the pump optical power, and the local oscillator frequency.
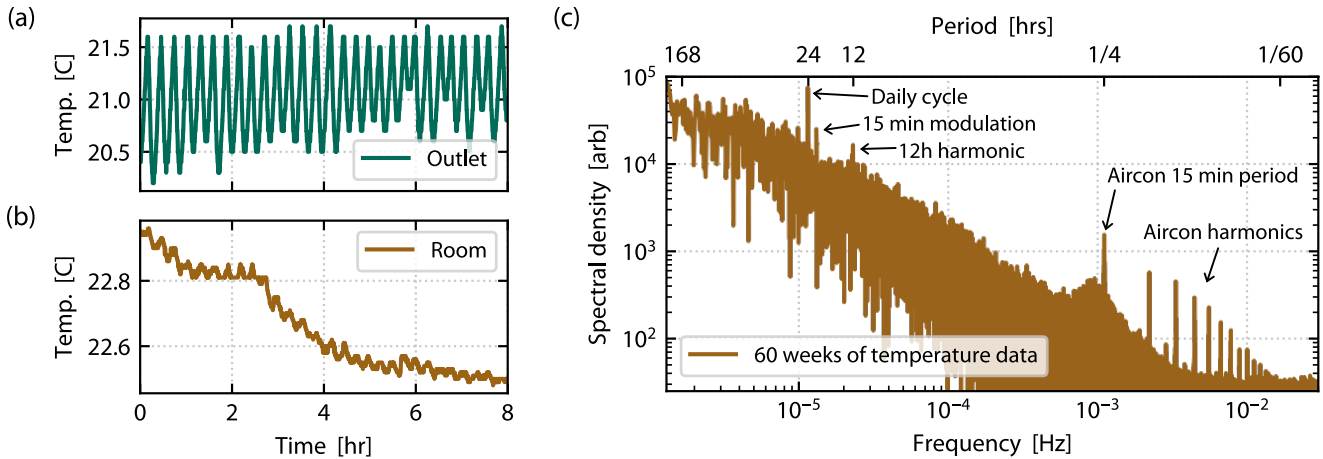
Figure 6.16. Lab temperature stability. (a) The air temperature as measured at the outlet of the air-conditioning unit oscillates with a peak-to-peak amplitude of up to 1 K with a period of 15 minutes. (b) A sensor close to the experiment measures the air temperature over the same time period, and the strong oscillations from the air-conditioning unit can be seen as a ~0.05 K oscillation on top of a larger drift over the eight hour period. (c) From 60 weeks of time-domain data for the sensor close to the experiment, the spectral density of the fluctuations over the time period is calculated. The spectrum shows a tall peak at 15 minutes, with a lobe of drift, as well as higher harmonics of the 15 minute peak. In the lower-frequency end of the spectrum, the daily 24 hour peak is strong and with small modulation sidebands due to the strong 15 minute cycle. Also the harmonics of the daily cycle can be seen, with the 12 hour half-daily peak easily visible. Finally the 15 minute modulation by the air conditioning can be seen as sidepeaks about the 24 hour peak. The data was obtained at a 0.1 Hz rate between January 2021 and March 2022.

STABILISING THE OPTICAL FILTERS FOR ANTI-STOKES HERALDING. The Fabry–Pérot optical filters used for ensuring heralding fidelity are temperature tuned, and thus sensitive to the environment. The TEC controllers used for temperature tuning stabilise the thermistor resistance, which in principle stabilises the temperature and thus the filter's centre frequency. However, when running the experiment, it is clear that despite the TECCs' PID loops, the centre frequencies of the filters change with respect to the anti-Stokes light.

In order to keep the filters tuned to the anti-Stokes light to ensure a high count rate and keep the suppression of the pump high, the setpoints of the TECCs must be tuned at a faster rate than the fluctuations. Each TECC has an analogue input that changes the setpoint of the TECC but only accepts sub-Hz modulation, setting a limit on how fast any feedback can be implemented.

A slow feedback loop is implemented by feeding the count rate back to the TECC, as shown in Fig. 6.7. The count rate is read off one of the SPADs by a computer that controls two outputs of a mV-level DC source[xxiv] connected to the respective TECCs. The TECCs have a $2\,\Omega\,\text{mV}^{-1}$ setpoint tuning for the $10\,\text{k}\Omega$ thermistor used in this experiment. The loop has a simple implementation, addressing one TECC at the time doing these steps: (1) reads the current count rate from the SPAD, (2) changes the voltage by $2\,\text{mV}$, (3) waits for $3\,\text{s}$, (4) reads the count rate again and keeps the new voltage if the count rate has increased or reverts to the previous voltage if not. After completing this procedure for both filters in sequence, the procedure is repeated but with a voltage change of $-2\,\text{mV}$.

[xxiv] Tektronix AFG3022C

The long wait time of $3\,\text{s}$ between changes in the setpoint is due to the limit on the speed of the modulation set by the TECC. The full cycle takes 12 seconds, meaning only small changes over slow timescales can be compensated for by this sub-Hz, gentle lock.
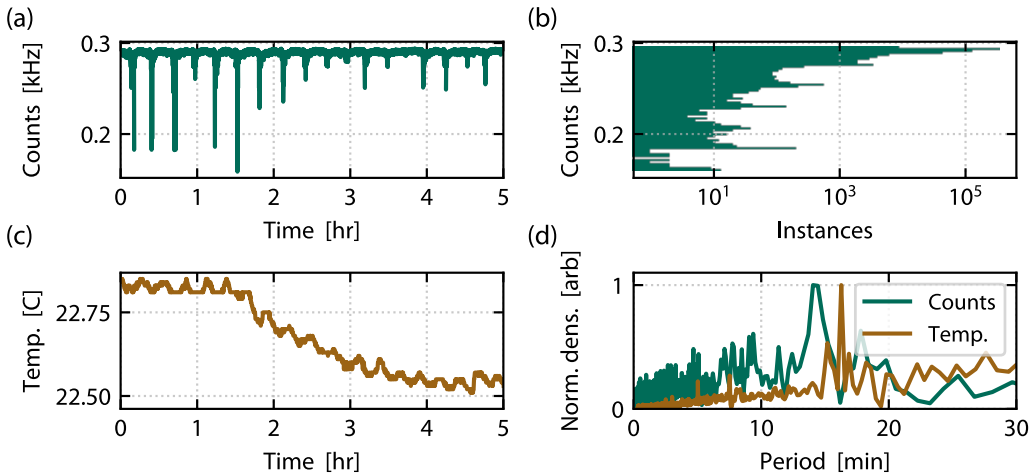
Figure 6.17. Count rate stability and ambient temperature. (a) The single-click count rate of one SPAD when both filters are in place in the heterodyne arm, controlled by TECCs and their setpoints dynamically tuned. The dips in the count rate happens over timescale that is short comparable to the feedback loop bandwidth. (b) A histogram of the measured count rate, showing that even though the count rate has deep dips as shown in (a), the distribution is skewed towards high count rates. In fact, 98 % of the time is spent measuring the 10 % highest count rates. (c) The ambient temperature in the room over the same time period as panel (a). (d) The normalised spectral density of the count rate and temperature over the same 15 hour period, showing features around a 15 minute period.

Figure 6.17 shows the count rate whilst the feedback loop is running, where the impact of the ambient temperature fluctuations is evident. The deep dips in the count rate coincide in time with when the fan in the air-conditioning ramps up, giving a rush of cold air. This effect happens at a fast timescale that the lock does not work well to counteract. However, these events typically have a width of <30 s, and thus over time have little impact. As the histogram in Fig. 6.17(b) shows, the count rate is in the top 10 % for more than 98 % of the time.

PUMP INPUT POWER STABILISATION. The power of the pump field can fluctuate due to for instance temperature changes. This is unwanted as the intracavity photon number is linearly dependent on the pump power, and the optomechanical coupling rate $G \propto \sqrt{N_{\text{cav}}}$, meaning that the heterodyne signal will be affected [the sideband cooling and variance baseline changes, see Eq. (6.40)]. As the experiment runs for approximately 60 hours to obtain the measurement data, the drift in the power can be significant over this time, and therefore stabilising the power is beneficial.

To stabilise the pump power a computer controlled PID feedback loop is set up, as shown in Fig. 6.18. The pump laser is amplified by an EDFA due to the many taps and multiple decibels of insertion losses before the pump reaches the cavity, so by controlling the amplification, the pump power can be stabilised. In order to measure the pump power, a weakly reflecting beamsplitter is inserted just before the pump reaches the cavity to make sure power fluctuations are suppressed (only the circulator for separating out the backscattered anti-Stokes and a polarisation controller comes after the power stabilisation loop). Feeding back the measured optical power to the EDFA current completes the loop.
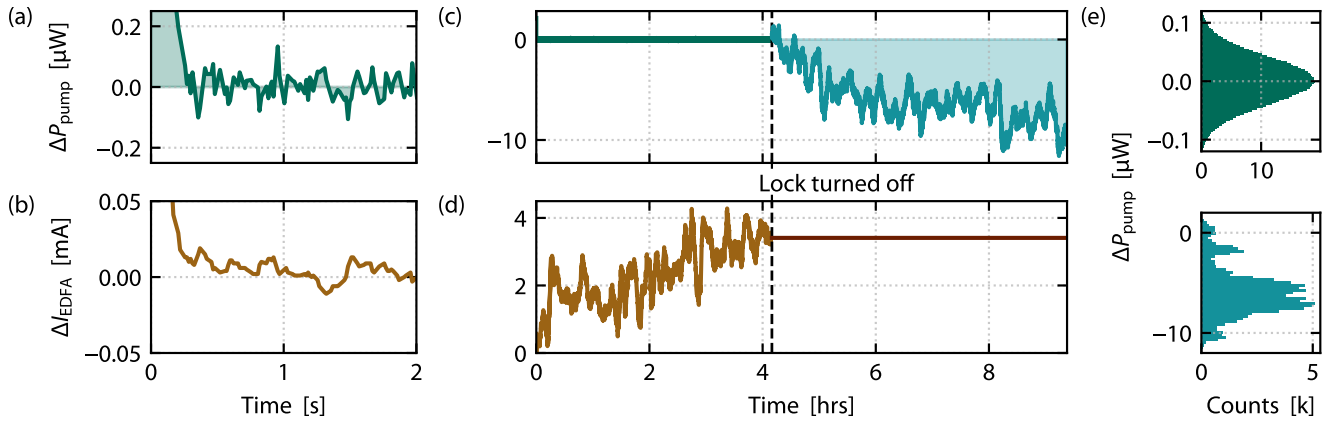
Figure 6.19. Measurement of optical pump power stability. (a) The deviation in the measured power from the PID setpoint of 500 μW power shown for the first seconds as the PID is turned on. The PID loop operates every 21 ms on average, corresponding to a 47 Hz rate. (b) The EDFA current as set by the PID for over the same time window as panel (a). (c,d) Long term optical power deviation from setpoint and EDFA current for the locked and free running system. The dashed line indicates the time at which the PID is turned off, letting the power run free, and thus the EDFA current kept constant as there is no feedback. (e) Histograms of the optical power deviation from the setpoint for the stabilised (top) and free running (bottom). The standard deviation of the locked power is 41 nW or $8 \cdot 10^{-5}$ relative to the setpoint.

The PID controller is implemented in Python, reading optical power from a power meter[xxv] and tuning the current on the EDFA[xxvi] accordingly. As there is no friction or hysteresis in the system, only a proportional control is needed, and the values of the integrative and derivative coefficients are set to zero. The speed of the Python loop is limited to approximately 21 ms by the readout time of the optical power meter. If a faster loop is needed, the power meter could be swapped for an analogue photodiode connected to a PID controller and a voltage-controlled variable optical attenuator. The feedback speed will then be limited by the bandwidths of the PD and VOA.

[xxv] Thorlabs PM100D with a S155C probe

[xxvi] Thorlabs EDFA100P

To test the performance of this power locking setup, the optical power readings are logged with the lock engaged and free running to compare. Figure 6.19 shows the result from just under 10 hours of logging. The histogram of the deviation from the setpoint whilst locking [Fig. 6.19(e)] shows a distribution around the setpoint with a standard deviation of 41 nW, which means the lock keeps the power within a relative deviation of approximately $1.6 \cdot 10^{-4}$ to the setpoint for 68 % of the time.

LOCAL OSCILLATOR LASER FREQUENCY STABILISATION. When performing the heterodyne detection, the frequency separation between the anti-Stokes signal and the heterodyne local oscillator (LO) should be constant between each captured trace to ensure a uniform heterodyne frequency over the course of the measurement. This is beneficial so that the time-traces can be effectively bandpass filtered to suppress shot noise, as well as to mix down the signal correctly for the tomography of the mechanical state, as explained in the next section, Section 6.5.

At the time these experiments were performed, a second laser was used as the heterodyne LO, so ensuring a constant frequency between the pump and LO lasers is desirable. As the pump laser is locked to the pump mode of the cavity, the absolute wavelength of the pump laser can drift over time due to for instance temperature changes in the resonator,

Figure 6.18. Schematic of the optical pump power stabilisation. The variable optical attenuator is used to ensure the EDFA does not operate close to its low threshold or maximum amplification.

causing the pump resonance to move in absolute frequency. When the absolute frequency of the pump light changes, the anti-Stokes photons change their frequency correspondingly, and thus the LO laser must change its frequency to keep the heterodyne frequency stable.

A slow frequency lock of the LO laser to the pump laser is implemented by measuring the beat note between the two lasers and feeding any deviation from the desired beat note the back to the LO laser frequency, see Fig. 6.20. The beat note is measured on fast photodiode[xxvii] using an electronic spectrum analyser.[xxviii] The LO laser is tuned so that the beat note with the pump is at the desired frequency separation $v_{\mathrm{beat}} = (\omega_{\mathrm{m}} + \omega_{\mathrm{het}})/(2\pi) = 8.16\,\mathrm{GHz}+214\,\mathrm{MHz}$, then the beat note is remeasured every second a PID uses the difference between the measured and the desired v_{beat} to control a DC voltage[xxix] fed to the piezo on the laser. The PID is computer-implemented with only the proportional coefficient enabled.

Since the data for this work was obtained, an alternative approach for generating the LO with better frequency stability was based on using an optical modulator on the pump laser local oscillator, see Fig. 6.7. The modulated LO has been used in subsequent work, including an extension to the work here, described briefly in the outlook section of this chapter.
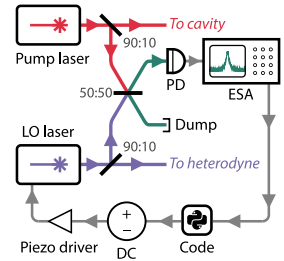
Figure 6.20. Locking of the heterodyne local oscillator frequency.

[xxvii] Thorlabs DET08CFC

[xxviii] HP 8562E

[xxix] Tektronix AFG1062

6.5   DATA ANALYSIS, RESULTS AND DISCUSSION

After having described the experimental setup, how the system is characterised, and how the data is captured in the previous section, the focus now turns to how the data is processed and interpreted. The goal is to obtain the evolving quadratures of the mechanical state for each measurement in the ensemble, for each of the event types. From the quadratures, the dynamics of each of the generated states can be inferred by averaging over the corresponding ensemble of measurements, and the generated states can be characterised in phase space by building a two-dimensional histogram of the quadrature values at the time of the event.

This section first describes how the captured heterodyne signal is filtered and demodulated to extract the mechanical quadratures. With knowledge of the time domain quadratures, the dynamics of the mean occupation of the mechanical state is inferred, and via tomography, the Gaussian initial thermal and non-Gaussian phonon-subtracted mechanical states are characterised in phase space by their *s*-parametrised Wigner functions.
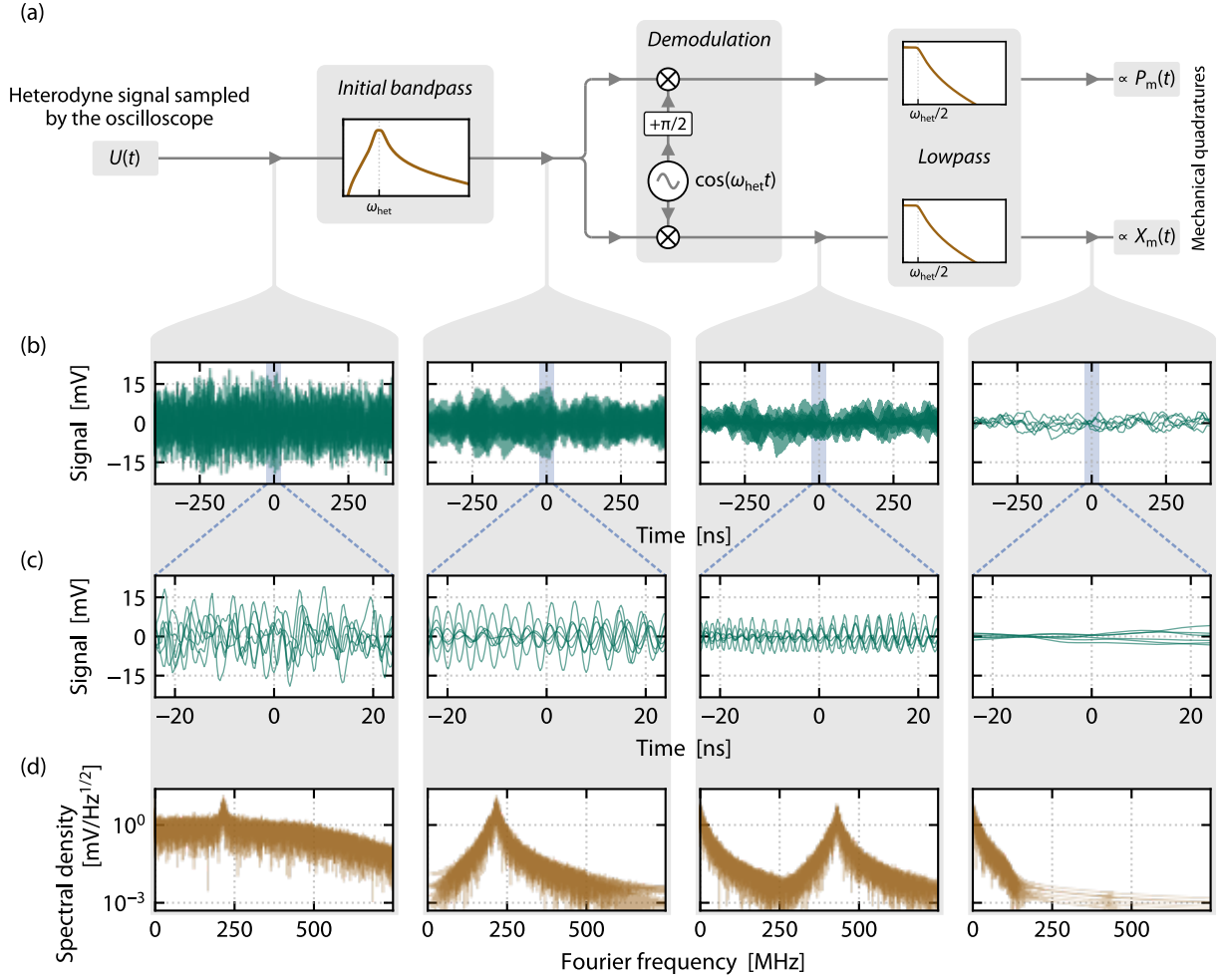
Figure 6.21. Filtering and demodulation of the heterodyne signal. (a) Schematic of the analysis procedure, all performed digitally in post-processing. (b,c) Six example time domain traces overlaid for each step of the procedure. (d) Frequency domain by Fourier transformation of the time domain data.

6.5.1 *Calculating the mechanical quadratures by demodulation*

The heterodyne signal gives information about the quadrature of the anti-Stokes light emerging from the resonator, and because the mechanical state is mapped onto the scattered anti-Stokes light, the signal is correlated to the mechanical state. The details of how the measured quadratures on the heterodyne relate to the mechanical quadratures, see Appendix B. This section considers technically how the signal from the balanced detector can be demodulated to give its quadratures components via a demodulation technique. The demodulation mixes down the heterodyne signal with quadrature signals at the heterodyne frequency. To improve the signal-to-noise ratio of the anti-Stokes signal and thus achieve a greater overall measurement efficiency, the heterodyne signal is first digitally filtered in post-processing to remove broadband vacuum noise.

The procedure for the filtering and demodulation is shown in Fig. 6.21 and is described in the following.

PRE-DEMODULATION DIGITAL BANDPASS FILTERING. The measured heterodyne signal contains frequency components over a wide range set by the GHz-bandwidth of the measurement, but only a small portion of the spectrum contains the anti-Stokes signal of interest. Therefore, by filtering the heterodyne signal in a narrow band around the anti-Stokes carrier frequency reduces the frequency components that are adding noise. This improves the signal-to-noise ratio of the heterodyne measurement, allowing to extract more precise quadratures. This step is essential to resolve the non-Gaussianity of the phonon-subtracted thermal states – a comparison between filtered and unfiltered results is shown later in Fig. 6.31.

The spectral part of interest in the heterodyne signal is the anti-Stokes signal, which is primarily within a band given by the effective mechanical linewidth of ~10 MHz at the heterodyne frequency $\omega_{\text{het}}/(2\pi)$ = 214 MHz. The bandwidth of the time domain measurement is set by the oscilloscope sampling rate and the heterodyne detector. Using a sampling rate of 3.125 GSs^{-1}, the heterodyne measurement contains frequency components up to half this frequency, as shown in Fig. 6.23(a). The bandwidth of heterodyne detector is an effective 400-MHz lowpass filter on the heterodyne data resulting in a roll-off in the spectrum from 400 MHz. Because the anti-Stokes signal is below the cutoff frequency of the detector and also much narrower than the detector bandwidth, the effective filtering of the detector does not influence the anti-Stokes signal (Enzian [165] discusses this in more detail).

Knowing the bandwidth and centre frequency of the anti-Stokes signal, a suitable bandpass filter is chosen to keep the anti-Stokes signal and remove broadband noise. A Butterworth filter[xxx] in a bandpass configuration with a centre frequency equal to the heterodyne frequency, 3-dB-bandwidth of 50 MHz and of order two is used, see Fig. 6.22 for the filter's transmission spectrum. Figure 6.23 shows the effect of the filter, displaying spectra before and after the bandpass filtering. The filter bandwidth is chosen to be broader than the effective mechanical linewidth, $2\gamma_{\text{eff}} = 11$ MHz, to ensure the signal itself if not filtered out [406].

DEMODULATION TO OBTAIN THE QUADRATURES. The term quadrature is borrowed from signal processing and electrical engineering where a signal at some frequency can be decomposed into its orthogonal components, the so-called in-phase and (out-of-phase) quadrature signals. To extract the optical quadrature of the anti-Stokes light that is emerging from the cavity, the quadratures at the heterodyne carrier frequency can be computed via a technique often referred to as in-phase–quadrature (IQ) demodulation [506].[xxxi] The procedure is shown in Fig. 6.21(a).

To explain the demodulation technique and how it enables tomography of the mechanical state it is important to understand the characteristics of the generated states and the technical details of the heterodyne measurement – the latter is illustrated in Fig. 6.24. Technically, there are three subtleties that must be examined, the rotating measurement basis of the heterodyne measurement, the (lack of a) phase reference for the local oscillator light field, and the fixed phase offset between the heterodyne signal carrier and the
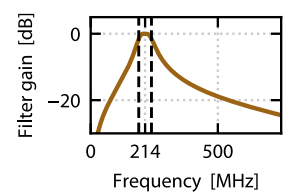
Figure 6.22. Butterworth bandpass filter for initial filtering of heterodyne signal: centre 214 MHz, 3-dB-bandwidth 50 MHz, order 2.

[xxx] The digital filters and the discrete Fourier transformation used in this work are performed in Python using the Scipy package (which relies mostly on Fortran implementations for its routines).

[xxxi] IQ modulation is a widely used technique, for example underpinning many digital communication systems, such as the Wi-Fi standard.
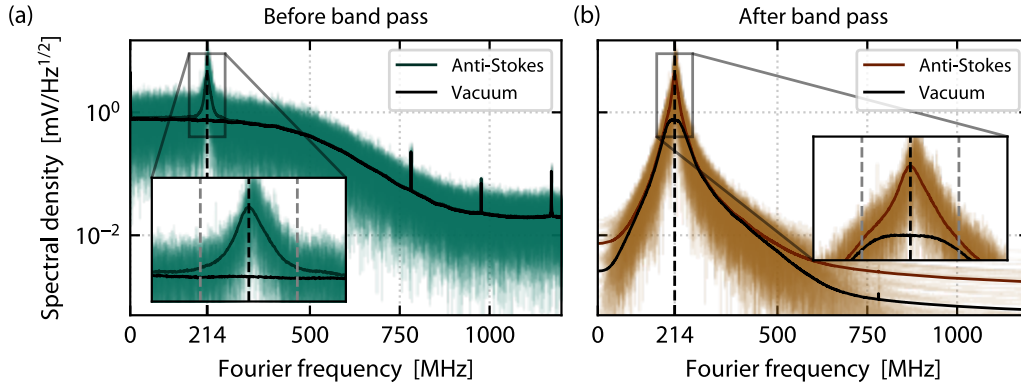
Figure 6.23. Spectral content of the heterodyne signal before and after bandpass filtering. (a) Pre filtering, showing 25 individual anti-Stokes spectra and the mean of 2000 spectra in a darker shade. The mean of $2 \cdot 10^4$ spectra for vacuum input to the heterodyne is shown in black. The dashed line indicates the heterodyne frequency and the grey dashed lines in the inset indicates the bandwidth of the bandpass filter. (b) The same data as in panel (a) after passing the data through the bandpass filter shown in Fig. 6.22.

demodulation local oscillator used in post-processing. After describing the demodulation in words, a calculation follows.

Considering the rotating measurement basis first: because of the difference in frequency between the anti-Stokes carrier and local oscillator fields, the heterodyne measurement can be thought of as a homodyne measurement with a rotating measurement basis. The output of the heterodyne measurement corresponds to a quadrature of the anti-Stokes light field in a basis given by the the phase $\theta = \omega_{\mathrm{het}} t$ between the two light fields incident at the heterodyne beam splitter, which is changing with time at a speed equal to the heterodyne frequency. In the notation of the cartoon picture in Fig. 6.24, the measurement basis X'', P'' is rotating with respect to the anti-Stokes light quadratures X', P'.

When the heterodyne frequency is faster than the evolution of the mechanical state, this measurement can resolve how both of the quadratures are moving in phase space, as the rotation of the measurement basis is faster than the state, hence enabling the measurement to sample the state across a range of different basis rotations before the state moves. The timescale of the mechanical state evolution in the experiment can be inferred from the Langevin equations [Eq. (5.23)] to be at a rate of order γ, which is small in comparison to the heterodyne frequency: $\gamma/\omega_{\mathrm{het}} \simeq 1.5 \cdot 10^{-2}$, and therefore the experiment is within the regime where the heterodyne signal describes the state evolution for a rotating basis.

The stability of measurement basis rotation speed is important for the demodulation procedure, as a change in the speed will result in attributing a datapoint to the wrong position in phase space. The variability of the rotation speed is given by the frequency stability of the LO field over the time scale of each time trace. The linewidth of the LO laser is <0.1 kHz, corresponding to a coherence time of ~10 ms, which is several orders of magnitude longer than the measurement time of 4 μs. Thus, the measurement basis rotation speed can be considered constant over a single time trace.

The second subtlety, the lack of a phase reference for the local oscillator field in the heterodyne measurement, does not pose an issue for the current experiment because
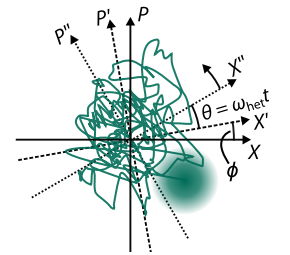
Figure 6.24. Pictorial illustration of the heterodyne measurement bases for a single time trace. The measurement basis X'', P'' is rotating with the heterodyne frequency ω_{het} compared to the anti-Stokes light field quadrature X', P'. When mixing-down, the unknown phase between the carrier and down-mixing LO causes a fixed phase ϕ between basis of the mixed down quadratures and the measured, rotating quadrature.

the generated states are symmetric around the origin in phase space. To perform phase-sensitive tomography in order to characterise states with angular dependence in phase space, the phase of the LO field must be known so that for each measurement, not only is the measurement basis rotation is constant in speed over the measurement, but the starting point is known. Consider a single time-trace measurement: when the oscilloscope is triggered, if the phase of the LO field is unknown, the start rotation θ_0 of the rotating measurement basis in relation to some choice of an optical quadrature is unknown. If an ensemble of measurements is used to populate a two-dimensional histogram, but the basis of the measurements are uncorrelated and unknown, any angular dependence in phase space is washed out. However, for a symmetric state like in this work, there is no angular dependence and thus random θ_0s have no effect on the tomogram.

Lastly and similarly, because of the lack of a phase reference for the LO optical field, the phase offset between the laser LO and demodulation LO is unknown. This adds another random offset in the starting phase for each measurement in the ensemble, called ϕ in Fig. 6.24. As the states characterised in this work have no angular dependence in phase space, this offset is not of importance.

DEMODULATION CALCULATION. The following calculation shows that the demodulation procedure indeed yields the mechanical quadratures and illustrates mathematically the points above.

The heterodyne voltage signal can be expressed in terms of the field operators of the light emerging from the cavity $\hat{a}_{\text{out}}$ [Eq. (6.36)]

$$U(t) \propto \hat{a}_{\text{out}}(t)e^{-i\omega_{\text{het}}t} + \hat{a}^{\dagger}_{\text{out}}(t)e^{i\omega_{\text{het}}t} . \tag{6.64}$$

As shown in Fig. 6.21, the demodulation procedure mixes down (multiplies) the heterodyne signal with the quadrature signals $\cos(\omega_{\text{het}}t + \phi)$ and $\sin(\omega_{\text{het}}t + \phi)$, where the ϕ accounts for the unknown phase between the heterodyne carrier and the quadrature signals to be multiplied with the heterodyne signal. Performing the multiplication for the case of the cosine, defining the shorthand $\theta \equiv \omega_{\text{het}}t$, the demodulated signal can be expressed

$$s_{\cos}(t) \equiv U(t)\cos(\theta + \phi) \propto A(\theta, \phi)\,\hat{a}_{\text{out}}(t) + A^*(\theta, \phi)\,\hat{a}^{\dagger}_{\text{out}}(t) , \tag{6.65}$$

where, using the identity $\cos(x) = [e^{ix} + e^{-ix}]/2$,

$$A(\theta, \phi) = \frac{e^{i(\theta+\phi)} + e^{-i(\theta+\phi)}}{2}\, e^{-i\theta} = \frac{e^{i\phi}}{2}\left[1 + e^{-i2(\theta+\phi)}\right] . \tag{6.66}$$

Using a lowpass filter with cutoff frequency $\omega_{\text{het}}/2$ (Fig. 6.25) after the down-mixing removes terms oscillating at $2\omega_{\text{het}}$. Hence, the second term can be discarded, resulting in

$$A_{\text{LP}} = \cos(\phi) + i\sin(\phi) , \tag{6.67}$$
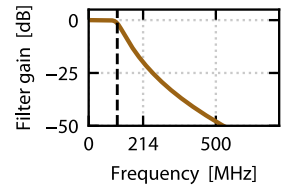
Figure 6.25. Butterworth lowpass filter for for removing the harmonic from the demodulated signal: cutoff frequency 112.5 MHz, order 7.

by Euler's formula. Inserting this result back into the expression for the demodulated signal (6.65),

$$s_{\cos}(t) \propto \left[\hat{a}_{\text{out}}(t) + \hat{a}_{\text{out}}^\dagger(t)\right]\cos(\phi) + \left[\hat{a}_{\text{out}}(t) - \hat{a}_{\text{out}}^\dagger(t)\right]\text{i}\sin(\phi) . \tag{6.68}$$

By the definition, the quadratures of the anti-Stokes field from the cavity in terms of its creation and annihilation operators are

$$X_{\text{out}} = 2^{-1/2}(\hat{a}_{\text{out}}^\dagger + \hat{a}_{\text{out}}) \tag{6.69}$$

$$P_{\text{out}} = 2^{-1/2}\text{i}(\hat{a}_{\text{out}}^\dagger - \hat{a}_{\text{out}}) , \tag{6.70}$$

and thus the demodulated signal Eq. (6.68) can be expressed in terms of the output field quadratures

$$s_{\cos}(t) \propto X_{\text{out}}(t)\cos(\phi) - P_{\text{out}}(t)\sin(\phi) , \tag{6.71}$$

which means the demodulated signal is proportional to a quadrature in a basis rotated by ϕ with respect to the optical quadrature. As long as ϕ does not vary over the timescale of a single trace (which is guaranteed by the milli-second coherence time of the LO laser in this experiment), the demodulated signal represents the evolution of the rotated quadrature.

A similar analysis for demodulating with the sinusoid local oscillator $\sin(\omega_{\text{het}}t + \phi)$ can be done, resulting in

$$s_{\sin}(t) \propto X_{\text{out}}(t)\sin(\phi) + P_{\text{out}}(t)\cos(\phi) , \tag{6.72}$$

i.e., the sinusoidally demodulated signal gives the orthogonal, similarly rotated quadrature. Thus, the demodulated, low-passed quadrature signals are proportional to the rotated optical quadratures of the incoming light. Because of the milli-second coherence time of the LO laser and the practically infinite coherence time of the demodulation signal, ϕ will be constant over the duration of a single time trace. That means that for each time trace i captured on the oscilloscope, the demodulated quadratures represent the mechanical quadratures up to some phase ϕ_i.

The rotations ϕ_i of the demodulated versus mechanical quadratures would be important if the generated states to be characterised where non-symmetric about the origin in phase space. If that were the case, the demodulation phases ϕ_i would have needed to be known for each individual time trace in order to rotate each measurement to a common basis before using the measurement ensemble to build a phase space histogram. But because the states characterised in this work are symmetric in phase space they have no angular dependence in phase space and thus the phase ϕ is not of importance as long as it is constant over a single trace: for an ensemble with a large number of measurements, randomly assigned ϕ_is will ensure the measurements are distributed over all rotations.

Figure 6.26 shows the evolution in phase space for a vacuum trace and a one-phonon-subtraction event trace as determined by this demodulation technique.
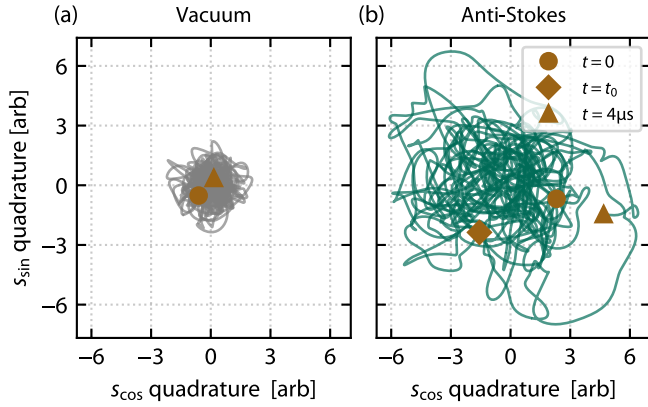
Figure 6.26. Phase space evolution for a single time trace of duration $4\,\mu s$, $1.25 \cdot 10^4$ points. (a) Evolution for a trace where the vacuum is measured on the heterodyne beamsplitter, start and end points annotated. (b) Evolution for a trace where the anti-Stokes signal is measured for a one-phonon-subtraction event occurring at $t = t_0$.

NOTE ON COMPUTER RAM USE. Due to the large dataset considered in this work, the analysis requires a computer with generous memory. Considering only one event type, the full dataset is $2.4 \cdot 10^5$ time traces with $1.25 \cdot 10^4$ data points each, giving a total of $3 \cdot 10^9$ data points. A typical floating number representation uses 64 bits per float, giving a total of 25 GB for storing a single copy of the time-domain data for one event type. Considering the filtering operations require Fourier transforming the data, then mixing down to two quadratures, et cetera, it is clear that the memory requirements are significant. Using a computer with 64 GB memory and with some compression of data and memory management, the analysis can be performed for one event type at the time.

6.5.2   *Dynamics of the mechanical occupation and the overall measurement efficiency*

From the demodulated quadratures, the dynamics of the mean occupation about the different heralding event types can be calculated from the ensemble variance at each time step. Furthermore, the ensemble variance also gives the overall measurement efficiency η, a measure of how effectively the mechanical state is transduced onto the anti-Stokes light and then detected by the heterodyne measurement.

The computed ensemble variance in the heterodyne signal for each time step, $\sigma^2(t)$, is shown in Fig. 6.27 for a small ensemble of 10^4 time traces for one-phonon subtraction events, as well for a vacuum input to the heterodyne setup. The ensemble variance is plotted as function in time about the heralding time t_0 for the subtraction events, whereas the vacuum measurements are semi-randomly conditioned simply by triggering the measurement at a fixed rate. The vacuum measurement is used to normalise the obtained quadratures to units of vacuum noise.

The parameter t_0 is the offset between the time when the oscilloscope is triggered and the time when the heterodyne detector measures the one-phonon subtraction events. It is a global offset for all traces of the one-subtraction event type, depending primarily on the oscilloscope trigger level used, cable lengths from the SPAD to the oscilloscope and SPAD processing delays. The parameter is determined by the ensemble variance, set to the time when the ensemble variance reaches its maximum. For the one-subtraction measurement $t_0 \simeq -33\,\text{ns}$.
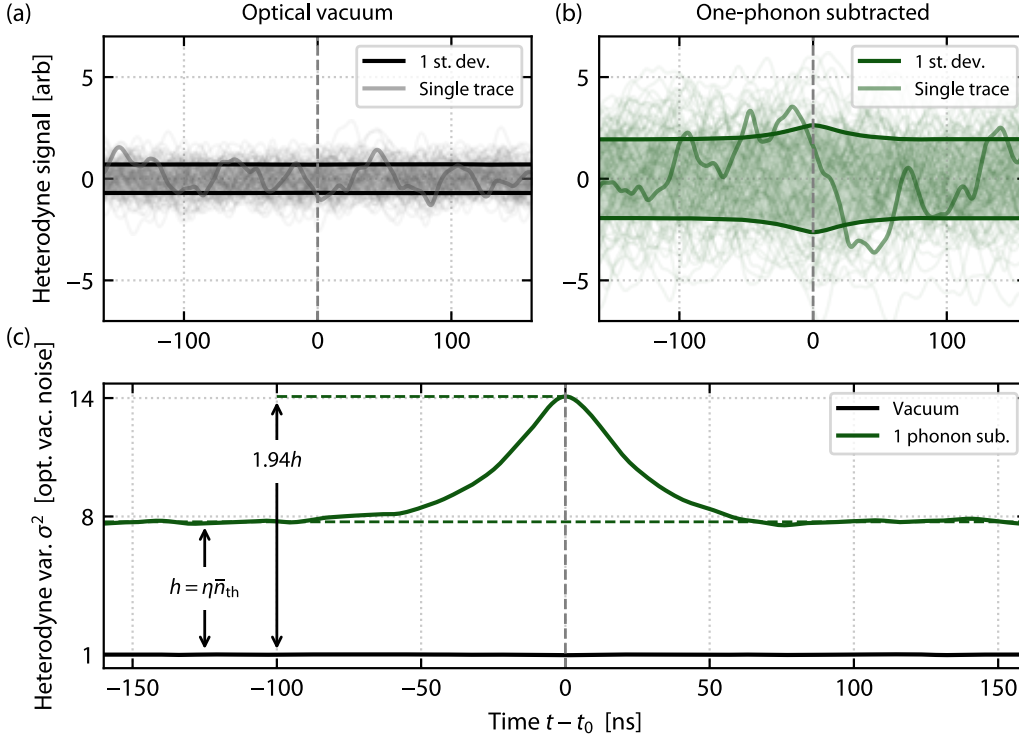
Figure 6.27. The dynamics of the heterodyne signal variance and its relation to the measurement efficiency. (a) 100 individual time traces measuring the optical vacuum noise on the heterodyne. The ensemble standard deviation for each time for 10^4 traces is shown. (b) Similar plot as (a) but for single-phonon subtraction, i.e., with anti-Stokes light impinging on the heterodyne detector and triggering off single-photon events. (c) The ensemble variance of the vacuum and anti-Stokes signals, normalised so that the vacuum noise has a value of 1. The height of the signal above the vacuum far away from the click event is the product of the initial thermal occupation and the measurement efficiency, $h = \eta \bar{n}_{\text{th}}$. Comparing the height far away from the subtraction event to the height of the peak at the heralding time $t = t_0$, the variance nearly doubles. The deviation from the expected doubling is attributed to spurious clicks lowering the fidelity of the heralding as well as the digital filtering of the heterodyne signal. Using only 10^4 traces for this calculation, some noise can be seen on the variance curve. The symmetry of the ensemble variance with respect to the heralding time is captured by the theoretical model (6.40), essentially due to the coherence time of the anti-Stokes photons.

In Fig. 6.27, it can be seen that the variance above the vacuum noise at maximum variance roughly doubles compared to the variance far from the heralding time. At times far from the heralding time, the variance of the heterodyne signal above vacuum reflects the mean occupation of the randomly conditioned state, thus the initial sideband cooled state's occupation. Similarly, at the heralding time, the height above the vacuum noise reflects the subtracted state's mean occupation. Defining the value of the variance far away from the heralding time $\sigma_{\text{init}}^2 \equiv \sigma^2(t \to \pm\infty)$, the expected factor of increase for n subtracted phonons can be expressed via Eq. (6.40),

$$V_{n-} = \frac{\sigma_{n-}^2(t = t_0) - 1}{\sigma_{n-}^2(t \to \pm\infty) - 1} = n + 1 \, , \tag{6.73}$$

for $n \in \{1, 2\}$. For the one-phonon subtraction event the experimentally observed ensemble variance increase factor is $V_{1-} = 1.94$, close to the predicted doubling of the mean

thermal occupation. The difference between the experimentally determined variance and the theoretical prediction is attributed primarily to the pre-filtering before the quadrature demodulation (see Section 6.5.4 for the impact of filtering), as well as the small infidelity of the heralding operations due to the spurious SPAD clicks from dark counts and pump photons incident on the detectors.

Figure 6.27 also shows that the ensemble variance is essentially symmetric around the heralding time, as expected from the theoretical model (6.40). A qualitative picture for understanding the shape of the ensemble variance is similar to that of a correlation measurement: the coherence time of the anti-Stokes photons used for click measurements is related to the optical and mechanical decay rates of the system, and the temporal envelope of the photons leaving the cavity is symmetric around the heralding time.

DETERMINING THE OVERALL MEASUREMENT EFFICIENCY. The height of the anti-Stokes ensemble variance above the vacuum noise gives information about how efficiently the heterodyne detector measures the mechanical state. As a simple picture, for a heterodyne measurement in the steady state and normalised to the vacuum noise, a perfect measurement efficiency $\eta = 1$ would mean an average occupation of $\bar{n}_{th}$ phonons in the mechanical mode gives an ensemble variance of $\bar{n}_{th}$ above the vacuum on the heterodyne. Conversely, if no difference is observed in the ensemble variance between vacuum and the signal inputs to the heterodyne, there is no measurement efficiency, $\eta = 0$.

Therefore the measurement of the initial thermal state far from the heralding event and the vacuum measurement can be used to determine the overall efficiency [Eq. (6.39)]

$$\sigma_{init}^2 = \eta \bar{n}_{th} + 1, \quad \implies \quad \eta = \frac{\sigma_{init}^2 - 1}{\bar{n}_{th}} = 0.908(2)\,\% \,, \tag{6.74}$$

for the data presented in this work.

The overall efficiency can be used to calculate the smoothening parameter s of the experiment, which indicates how much the phase-space distribution smoothed compared the Wigner and Husimi Q functions. A perfectly efficient measurement $\eta = 1$ would result in the Husimi Q function of the mechanics being measured by the heterodyne. The s parameter for a heterodyne setup is given by

$$s = \frac{\eta - 2}{\eta} = -219.3(5) \,, \tag{6.75}$$

for this experiment [Eq. (6.44)]. The value corresponds to a total added noise corresponding to $|s|/2 \simeq 110$ mechanical quanta by the measurement. At the time when this experiment was carried out, the achieved s parameter constituted a 15 times improvement to the forefront of optics-based mechanical tomography set by Muhonen et al. [421],[xxxii] where fast, pulsed measurements outside the resolved sideband regime were used. A recent publication by Patel et al. [422] demonstrated phonon-subtraction to a thermal state in optomechanical crystals in an experiment similar to the work presented here but only for

[xxxii] Muhonen et al. [421] demonstrate a single-pulse imprecision for the mechanical state of nine times the mechanical zero-point motion. However, due to coupling to other mechanical modes, the conditioned state width is limited to 58 times the mechanical zero-point motion, which corresponds to an s-parameter of $-(58^2) = -3364$ [418].
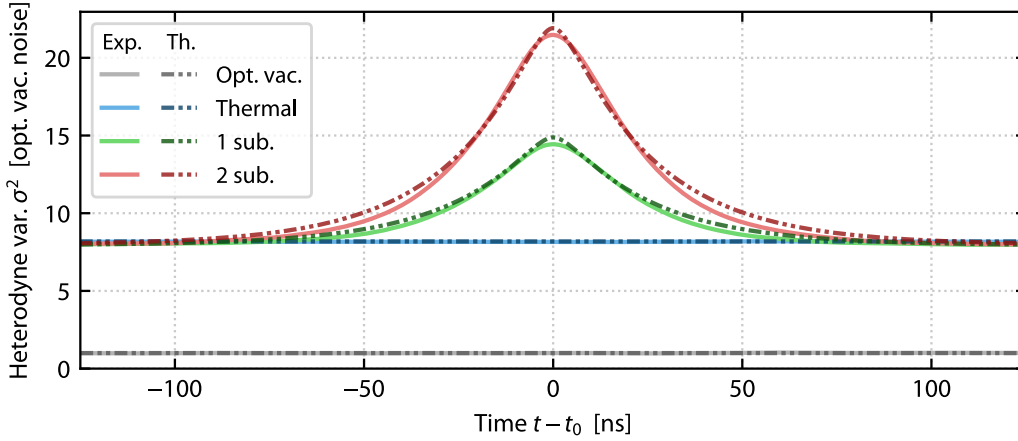
Figure 6.28. Dynamics of the mechanical occupation about the heralding time. For the single- and two-phonon subtraction cases the variance increases by factors of 1.94 and 2.94, respectively, at the time of the herald event compared to the initial variance of 7.96. The Poissonian error bars of relative size $(2.4 \cdot 10^5)^{-1/2} \sim 10^{-3}$ are not shown.

single-quanta operations, showing $s \simeq -1340$, or about six times higher added noise than the work described here.

SCALING TO UNITS OF THE MECHANICAL ZERO-POINT. With a known overall measurement efficiency η and a known initial mean occupation due to sideband cooling, the units of the obtained quadratures can be scaled from vacuum units to the mechanical zero-point fluctuations, x_{zp}. The cooling factor $\bar{n}_{th}/\bar{n} \simeq 1.69$ must be taken into account because the experiment does not provide an independent readout of the mechanical state, but instead the mechanical state is sideband-cooled during readout, scaling the mean variance on the heterodyne signal. The mechanical zero-point fluctuations are given by

$$\sigma_{init}^2 - 1 = \bar{n}_{th}\eta = \bar{n}x_{zp}^2 \,, \tag{6.76}$$

where Eq. (6.74) has been used. Thus, the factor to be applied to the quadratures to cast them from units of vacuum noise to mechanical zero point is

$$\mathcal{N} = \left[\eta \frac{\bar{n}_{th}}{\bar{n}} \right]^{-1/2} . \tag{6.77}$$

MULTI-SUBTRACTION ENSEMBLE VARIANCE. Figure 6.28 shows the full ensemble variances for both the one- and two-phonon-subtracted mechanical states, as well as for an ensemble of randomly conditioned initial thermal state measurements and for the vacuum measurement. The measurement of the initial thermal state is useful to characterise the initial Gaussian state, and confirm that it agrees with the data for the one- and two-phonon-subtracted states far away from the heralding time t_0. Because the number of time traces per event type used to compute each time step is $n_{samp} = 2.4 \cdot 10^5$, the statistical Poissonian error bars are very small – of relative size $n_{samp}^{-1/2} \sim 10^{-3}$ – and thus not shown.

For the single- and two-phonon subtraction cases, it is observed that at the time of the herald event, the variance increases by factors of 1.94 and 2.94, respectively, compared to the

initial variance of 7.96. These numbers are close to the doubling and tripling of the variance above the vacuum as expected from Eq. (6.40). The initial bandpass filtering is the main source of discrepancy due to the smoothening it represents (see Section 6.5.4). Curves of the expected dynamic response of the ensemble variance of an obtained quadrature as the mechanical state is taken out of equilibrium [Eq. (6.40)] are overlaid for each event type. The theoretical curves use the heralding time t_0 as the only free fitting parameter, other parameters are inferred from separate measurements.

6.5.3   *Tomography of the mechanical state at the time of subtraction*

Having calculated the mechanical quadratures of an ensemble of measurements, a two-dimensional histogram of the values of the quadratures at a given time can be produced. Such a histogram corresponds to the *s*-parameterised Wigner function of the heralded state at the chosen time. This is a tomographic technique because the histograms are produced by varying the state of the detector (here the phase between the heterodyne LO and the anti-Stokes light) such that the state is projected onto a range of bases, sampling the state at a range of angles in phase space [507]. The statistical error in the histograms is Poissonian as there is an integer number of measurements distributed over an integer number of bins [179, Ch. 5].

For a thermal state, the phase space is a Gaussian feature centred at the origin, whereas for the subtracted states the distribution becomes non-Gaussian displaying a ring-like shape centred around the origin. The experimentally determined phase-space distributions W_s are plotted in Fig. 6.29 for the initial thermal state, the single-phonon subtracted state, and the two-phonon subtracted state. The single- and two-phonon subtracted cases show the highly non-Gaussian nature of the states.

RADII OF THE RING-STRUCTURES IN PHASE SPACE. As the states are phase invariant and thus symmetric around the origin, the non-Gaussianity can be quantified in terms of the radius of the ring shape, which increases with the number of subtracted quanta. Theoretical predictions for the radii of the phase-space rings are calculated in Appendix B.2.4. For one-phonon subtracted state the radius is

$$X_{1-} = \sqrt{\frac{1 + \eta\bar{n}}{\eta\bar{n}} \left(\eta\bar{n} - 2 \right)} \, , \tag{6.78}$$

when $\eta\bar{n} > 2$ and for the two-subtracted state

$$X_{2-} = \sqrt{\frac{1 + \eta\bar{n}}{\eta\bar{n}} \left[-4 + \eta\bar{n} + \sqrt{2\left(4 + (\eta\bar{n})^2\right)} \right]} \, . \tag{6.79}$$

for $\eta\bar{n} > 2\sqrt{6} - 4$. The respective radii are indicated by the dash-dotted lines in Fig. 6.29(c,d), which agree with the phase-space distributions W_s experimentally obtained. The bounds
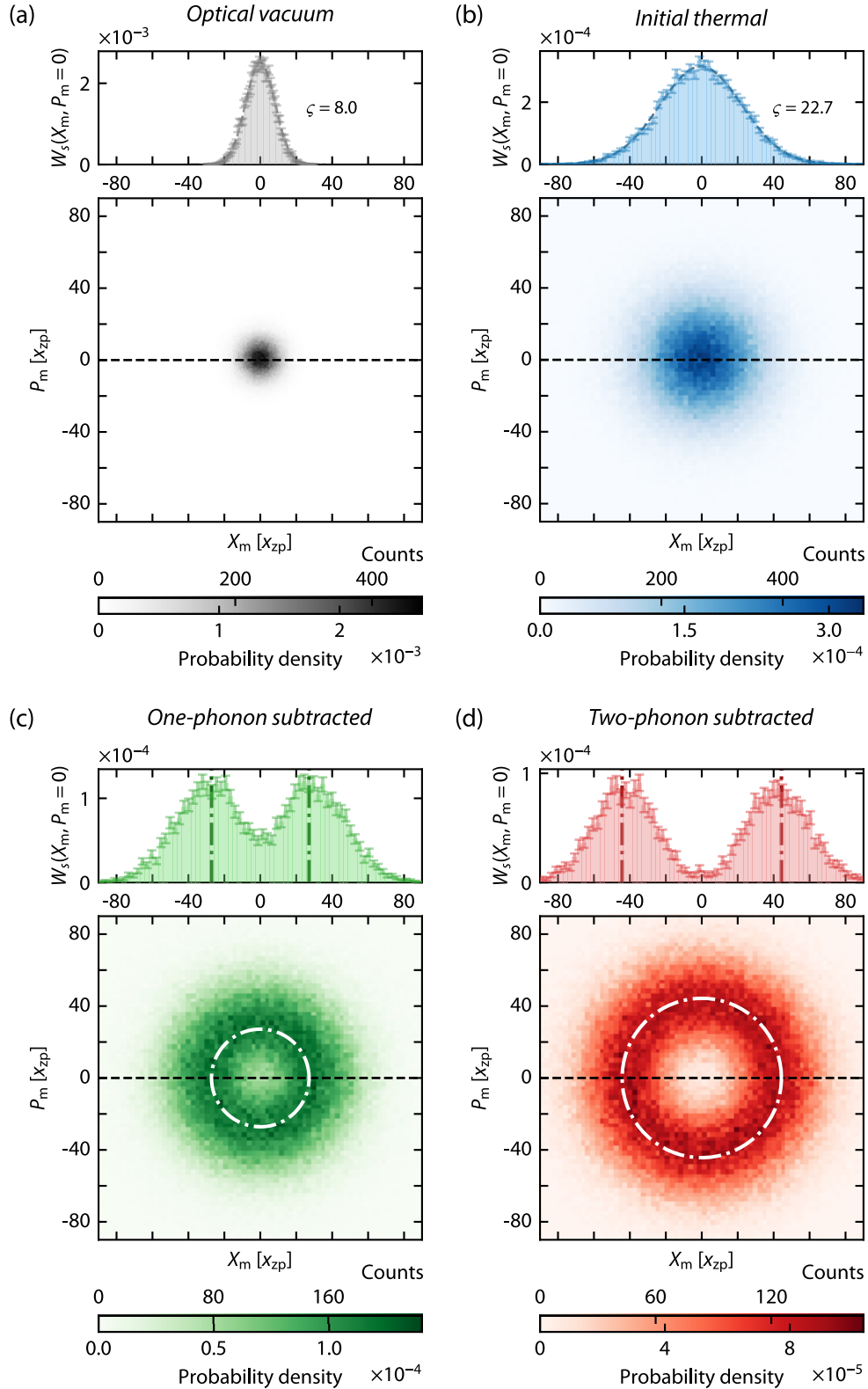
Figure 6.29. Phase-space tomograms for the four differently conditioned states. (a) As a reference, the phase-space distribution (Husimi Q function) of the optical vacuum, measured when no optomechanical signal is impinging on the heterodyne detector. (b-d) Reconstructed s-parameterised Wigner functions W_s for the (b) initial, (c) single-phonon subtracted and (d) two-phonon subtracted mechanical thermal states. The axes are plotted in units of the mechanical zero-point fluctuations x_{zp} [Eq. (6.77)]. For single- and two-phonon subtraction, the increasingly non-Gaussian shape of the phase space is observed, with the dash-dotted lines indicating the theoretically predicted maxima for the W_s functions. All panels show slices of the phase space at $P_m = 0$ on the top, and the standard deviation of the fitted Gaussians to the vacuum and initial thermal state, ς, are annotated. The error bars in the histograms are Poissonian error bars.
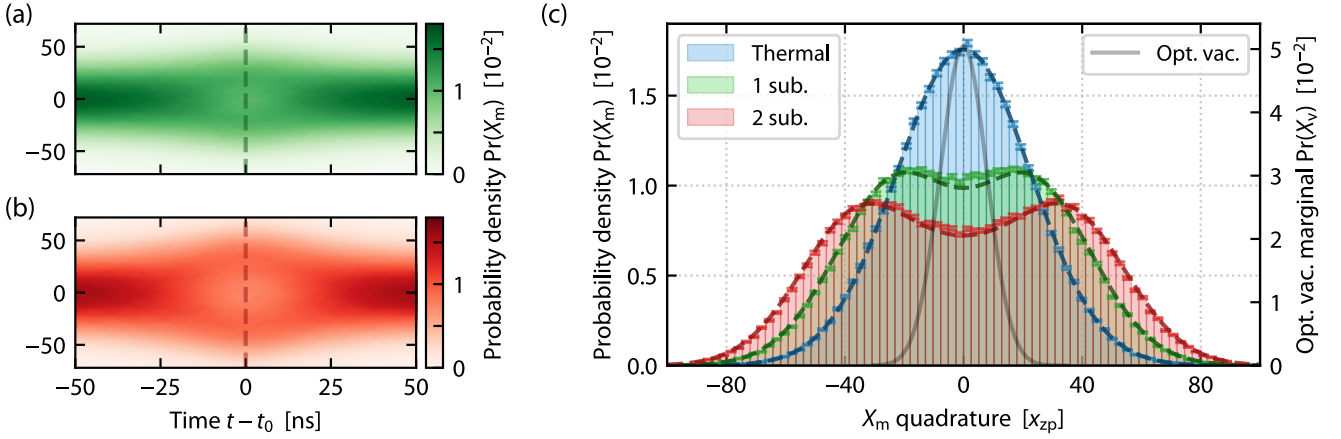
Figure 6.30. Dynamics and non-Gaussian marginals at the heralding time. (a,b) Marginal distributions for the X-quadrature of the mechanical oscillator as a function of time for (a) one- and (b) two-photon subtraction. (c) The marginal distributions at heralding event, $t = t_0$, for the differently conditioned mechanical states. The histograms are constructed from the observed values of the heterodyne signal at t_0, whereas the dashed lines represent the theoretical prediction of the marginals given the measurement efficiency and initial mechanical occupation. The indicated errors in the histograms are Poissonian.

determine the overall efficiencies needed to resolve the phase-space rings, namely

$$\eta_{1-} > \frac{2}{\bar{n}} \simeq 0.62\,\%\,, \quad \eta_{2-} > \frac{2\sqrt{6}-4}{\bar{n}} \simeq 0.28\,\% \tag{6.80}$$

for the one- and two-phonon subtracted states.

PROBABILITY DENSITY MARGINALS. Like the density operator of a quantum state, the Wigner quasiprobability distribution fully characterises a quantum state, and the expectation value of any observable can be computed from it [179]. Here, due to inefficiencies in the measurement, it is the s-parameterised Wigner function that is obtained, which is a smoothened Wigner function where the degree of smoothening is captured by the s parameter. Due to the imperfect reconstruction of the Wigner function, the probability distributions calculated from W_s are also smoothened in comparison to the true probability marginals.

From the W_s tomograms, the smoothened probability distributions of the mechanical quadratures can be computed. Figure 6.30(a,b) show the experimentally obtained and predicted marginals of the X_m-quadrature distribution,

$$\Pr(X_m) \propto \int_{-\infty}^{\infty} \mathrm{d}P_m \, W_s(X_m, P_m)\,, \tag{6.81}$$

as a function of time about the herald event. The plots illustrate how the mechanical state transforms by the single- and two-phonon subtraction operations from an initial Gaussian state to a non-Gaussian state with a bimodal quadrature probability distribution, and then returns back to equilibrium, similarly the dynamics of the mean occupation.

The non-Gaussianity generated by the subtractions is most pronounced at the heralding time, and the marginals at this time are compared in Fig. 6.30(c). The bimodal nature of the distribution is more distinct for the two-phonon subtracted state in comparison
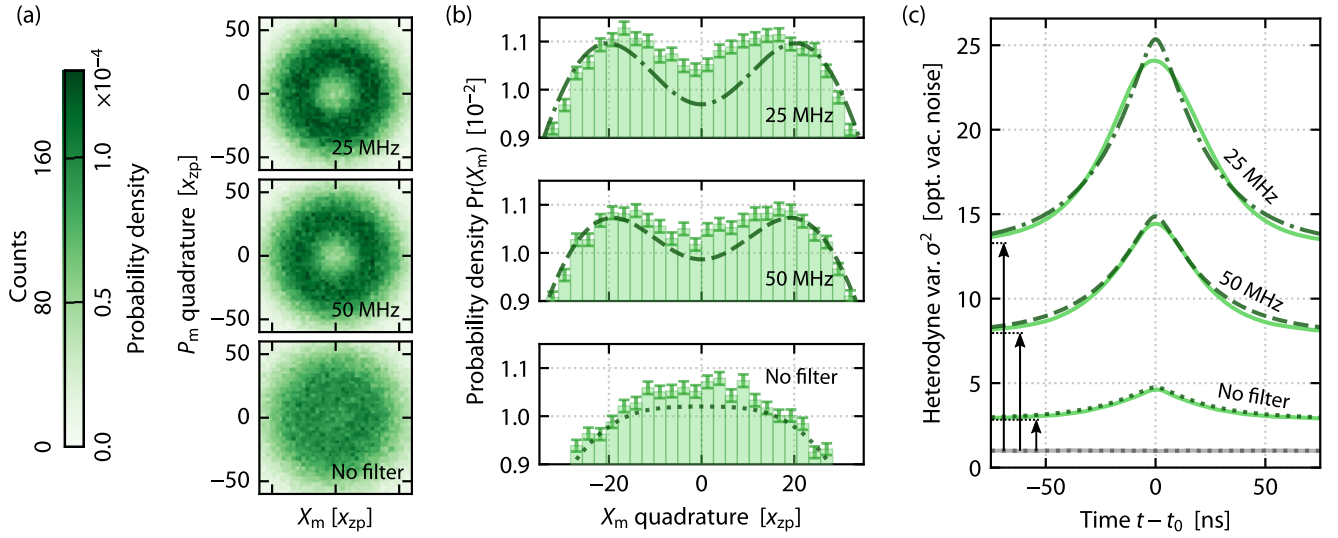
Figure 6.31. Comparison of initial filtering passband widths. The bandpass filtering of the heterodyne signal before demodulation reduces the contribution of the vacuum noise. No filtering is compared to 50 MHz and 25 MHz filter widths. (a) Tomograms of the resulting parametrised Wigner functions W_s given the three different filtering conditions. When no filter is applied, the ring shape of the state cannot be distinguished. (b) Computed marginal distributions for the corresponding tomograms in (a). The dark lines show the expected distribution given the computed measurement efficiency. (c) The time domain ensemble variance normalised to the the optical vacuum noise for the three filtering bandwidths (measurement data as solid lines and theoretical curves in dashed lines). With decreasing bandpass width, the vacuum noise is reduced in absolute terms, giving a comparatively larger variance in the signal. The measurement efficiency is increasing as the separation between the vacuum noise and signal baseline is increasing. However, narrow-bandwidth filtering smoothens the ensemble variance, increasingly distorting the measurement ensembles compared to the theoretical curves.

to the single-phonon subtracted case, in line with the overlaid theoretical predictions as derived in Appendix B.

6.5.4 *Impact of the bandpass pre-filtering*

The initial bandpass filtering of the heterodyne signal reduces the broadband vacuum noise relative to the signal, increasing the measurement efficiency. Figure 6.31 compares the results when no filter is applied to two different filter bandwidths.

If the initial bandpass filtering is not applied, the overall measurement efficiency is reduced to about one quarter, $\eta_{\text{unfilt}} \simeq 0.25\,\%$. This results in an s parameter of larger magnitude, $s_{\text{unfilt}} \simeq -814$, corresponding to about 407 added noise quanta compared to 110 when the filtering for the results presented earlier is applied. With the higher number of added noise quanta for the unfiltered case, the W_s distribution is smoothened to an extent where ring-like structure in phase space cannot be resolved for one-phonon subtraction events, as in shown in Fig. 6.31(a). That η_{unfilt} is insufficient to resolve the ring in the phase space is as expected from Eq. (6.80), where the minimum efficiency for resolving the circle was calculated to be 0.62 %. The position marginal of the W_s distribution shows no bimodality, see Fig. 6.31(b).

Conversely, filtering more aggressively than what was done for the results presented earlier, using a passband of only 25 MHz instead of 50 MHz, the overall efficiency $\eta_{\text{narrow}} \simeq$

1.59 %, giving approximately 62 added quanta of noise. The contrast of the ring to the surroundings is improved as shown in Fig. 6.31(a).

The question becomes how aggressively can one filter, will the efficiency keep increasing? In the limit of narrowing the filter, as long as there is any signal in the band, there will also be some residual vacuum noise left in the same band, which means the efficiency must converge to a finite value. However, before reaching this limit, the impact of narrower filtering will decrease the anti-Stokes signal itself, and the signal-to-noise will not improve as both the signal and vacuum is filtered equally in relative terms. But even before that, the filtering starts to affect the ability to resolve the quadrature dynamics, resulting in a reduced height of the peak in the heterodyne variance.

Figure 6.31(c) shows that narrower filter increases the contrast in signal variance to vacuum variance, but comes at the expense of smoothening the ensemble variance. As the bandpass width decreases, the vacuum noise is reduced, resulting in a smaller ensemble variance in the vacuum measurement. The ensemble variance in the signal is also reduced as the filter pass band is narrowing, but relatively less than for the vacuum because most of the signal peak is unchanged by the filtering, and thus the relative signal-to-noise is improving. When the filter bandwidth becomes narrower than the bandwidth of the signal, the filtering will not improve the signal to noise any further.

6.6   CONCLUSION AND OUTLOOK

This chapter demonstrates preparation and characterisation of non-Gaussian states of mechanical motion via optomechanics. The experiment utilises photon counting for conditioning optical heterodyne measurements to perform tomography on the generated states. Together with the simultaneous work by Patel *et al.* [422], it is the first experiment to show generation of non-Gaussian mechanical states via single- and two-phonon subtraction from a thermal state. This work advances the state of the art in optics-based mechanical phase-space tomography by setting a new record for minimising the measurement noise, achieving an added noise corresponding to only 110 mechanical quanta, which is more than an order of magnitude compared to the previous record [421]. As measurement noise masks non-classicality of states, the reduction in added noise represents a step closer to the currently outstanding goal of tomography of non-classical mechanical states within optomechanics.

Furthermore, the techniques developed here can be utilised for a range of mechanical quantum state engineering applications taking advantage of single- and multiple-phonon addition and subtraction operations. In particular, these operations can be applied to a mechanical squeezed state for superposition state preparation [416], using for instance reservoir engineering promising route to generate the squeezing in such protocols [413, 508]. A high-efficiency anti-Stokes interaction provides a means to implement a quantum memory device that can efficiently write and read quantum states to and from the acoustic mode [450].

There are several routes to be pursued in parallel to improve the experiment towards non-classical state generation and characterisation. To generate non-classical mechanical states, it is an advantage to be close to the mechanical ground state. Operation at cryogenic temperatures reduces the initial thermal occupation, but more importantly, it improves the mechanical linewidth as material contributions to the mechanical decay rate are reduced at low temperatures [160–163]. With a smaller mechanical linewidth, the optomechanical cooperativity improves, yielding better control over the mechanical motion.

In order to make the experiment able to characterise non-classical states, the measurement efficiency must be improved in order for the *s*-parameter for the tomography to improve to avoid the non-classical features to be smoothened out. The next section outlines some possible improvements.

6.6.1 *Avenues for increasing the measurement efficiency*

A non-unity overall measurement efficiency limits the ability to measure non-classical features in phase space. For an optomechanical tomography experiment the efficiency is fundamentally set by two parameters: the strength of the optomechanical interaction as it sets how efficiently the mechanical state transfers onto the optical state, and the optical losses before detection of the optical state.

There are six main routes for increasing the important overall measurement efficiency parameter in this experiment.

The efficiency of the mechanical state transfer can be improved by increasing the optical drive strength, utilising the optomechanical strong coupling available for Brillouin optomechanical systems [64].

The state transfer efficiency is also enhanced by a lower mechanical decay rate. For the crystalline barium fluoride resonator, this decay rate will be significantly reduced by operation at cryogenic temperatures.

Better optical coupling of the microresonator to the optical taper with respect to the intrinsic cavity losses improves the readout of the optical state. To achieve this, better phase matching between the resonator and taper is necessary, which is currently limited by the propagation constant mismatch between the barium fluoride resonator and the silica taper. Optimised tapered fibres or prism coupling can improve the phase matching. Furthermore, using an anti-Stokes mode with a spatial distribution that enables particularly good taper coupling can also yield efficiency gains.

Using highly efficient superconducting-nanowire single-photon detectors (SNSPDs) instead of the avalanche detectors currently used will allow the reflectivity of the beam splitter dividing the anti-Stokes light into the heralding and heterodyne arms to be reduced, thus representing lower optical losses for the heterodyne detection setup. The group now has this ability as the author set up a commercial, sorption-fridge-cooled SNSPD system after this work was carried out.[xxxiii]

Alternatively, an independent readout scheme, utilising a Stokes interaction for mechanical state preparation, followed by an anti-Stokes interaction for the readout, provides

[xxxiii] The SNSPDs were used for click detection in related experimental work: An optical interferometer with phase control in one arm was inserted before the heralding detectors, erasing information about the time of phonon-subtraction. Interference between the subtraction events can then be observed in the heterodyne quadrature measurement. A manuscript on this project is currently in preparation.

a route to remove the beam-splitter for state heralding completely, reducing the optical losses further.

Lastly, implementing homodyne detection instead of heterodyne detection improves the tomography by avoiding the added noise due to simultaneous measurement of both quadratures. This effectively relaxes the measurement efficiency requirement, and makes it possible to achieve an s-parameter of $s > -1$ for resolving non-classical features in phase space.

Implementing these improvements provides a promising path to achieving an overall anti-Stokes readout measurement efficiency of >50 %, which is required to observe negativity of a quantum phase-space distribution – a key signature of non-classicality and a powerful resource for quantum-enhanced technologies.

6.6.2   *Measurement cooling: The mechanical state conditioned on no subtraction*

In this work, the mechanical state is measured at phonon-subtraction events, which leads to a substantial increase in the mean occupation at the heralding time given by the number of subtracted phonons. What if, instead, measurements were made when no phonon is subtracted?

By the same Bayesian argument as for the one- and multi-subtraction events – where the obtained knowledge of a subtraction event updates the probability estimation of the state to have a larger occupation – a high-fidelity no-subtraction event gives a *lower* occupation. That no subtraction occurred increases the probability of the state having a lower occupation. The absence of an anti-Stokes-photon click effectively heralds a cooled state.

In the current experiment, the rate of subtractions is high because of the high optical pump power that sideband-cools the thermal state. Therefore, the measured mean occupation far away from the heralding events represents the sideband-cooled state. Considering a single heterodyne measurement, it is conditioned on a subtraction event that happened at a specific time with high fidelity, but that does not mean there were no other subtraction events over the duration of the time trace. In fact, at a mean rate of ~10^8 subtractions per second [Eq. (6.58)], a subtraction occurs on average every ~10 ns. These subtractions average out across the ensemble, and the calculated ensemble variance at time steps away from the time of the conditioning click-event can be interpreted as the occupation resulting from a probability-weighted average of zero-subtraction and any multi-subtraction event. Thus, if the experiment could condition on zero-subtraction events, the ensemble variance should be reduced at the heralding time.

Preliminary theory work led by colleagues J. Clarke and E. Cryer-Jenkins shows that in the absence of open-system dynamics and dissipation, the relative mean phonon-number varies with time as

$$\frac{\bar{n}_{\mathrm{n=0}}}{\bar{n}}(t) = \frac{T(t)^2}{1 + \bar{n}[1 - T(t)^2]} \, , \tag{6.82}$$

where $T(t) = \cos\zeta = \cos(Gt)$ is the transmission of the optomechanical beamsplitter and G the optomechanical coupling. This function is plotted in Fig. 6.32, showing that the state swap between light and mechanics is different than the typical sinusoid evolution.
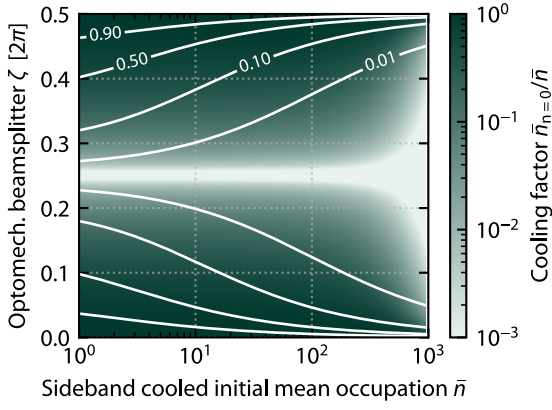
Figure 6.32. Cooling ratio $\bar{n}_{n=0}/\bar{n}$ for zero subtractions in a closed system with no dissipation for varying values of the sideband-cooled mean occupation $\bar{n}$ and $\zeta = Gt$.

By performing a similar intracavity variance analysis as for the phonon-subtraction case, at the time of no subtraction $\tau = t - t_0$, the variance of the intracavity quadrature for an initial occupation $\bar{n}$ is

$$\langle X_{\mathrm{cav}}^2(\tau) \rangle = \frac{1}{2} + \eta_{\mathrm{OM}}\bar{n}\left\{1 - \frac{\xi(1-\xi)}{1+\xi(-1+\xi/2+r^2/4)}\left[\frac{\gamma e^{-\kappa_{\mathrm{aS}}|\tau|} - \kappa_{\mathrm{aS}}e^{-\gamma|\tau|}}{\gamma - \kappa_{\mathrm{aS}}}\right]^2\right\}, \quad (6.83)$$

where $\xi = r^2\eta_{\mathrm{OM}}\bar{n}$, in which r is the reflectivity of the heralding beam splitter (the real transmission coefficient to the heralding arm), and the optomechanical efficiency is

$$\eta_{\mathrm{OM}} = \frac{G^2}{\kappa_{\mathrm{aS}}(\gamma + \kappa_{\mathrm{aS}})}. \quad (6.84)$$

Equation (6.83) is valid when $\xi \ll 1$, i.e., for the weak optomechanical coupling regime and low beamsplitter reflectivity. Plots of this expression as a function of time for various beam splitter reflectivities and the system parameters in this work (Table 6.1) shows reduction in the occupation, Fig. 6.33.

EXPERIMENTAL CONSIDERATIONS. Despite the dip feature in Fig. 6.33, the experimental implementation is challenging, and some initial considerations are presented in the following.

The section on subtraction operation fidelity, Section 6.4.4, shows that in the present measurement, the rate of subtraction events is much higher than the rate of clicks at the heralding detectors. In the work presented in this chapter, the heralding fidelity is largely unaffected by these high losses, and the effective discarding of heralding events only makes a measurement take more time. This changes when seeking to condition the state on times of no-subtraction: the heralding setup must guarantee with high certainty that there was no scattering event at a certain time to avoid measuring the heterodyne signal at times where no click was detected but a scattering event occurred. Currently, the setup does the opposite, as it guarantees a high fidelity for the click events ($\approx$0.996), but the fidelity of a no-scattering event when there is no click is very low.

The main limitation in the heralding setup for increasing the heralding probability of subtraction events and thus improving the fidelity of zero-subtraction events is the
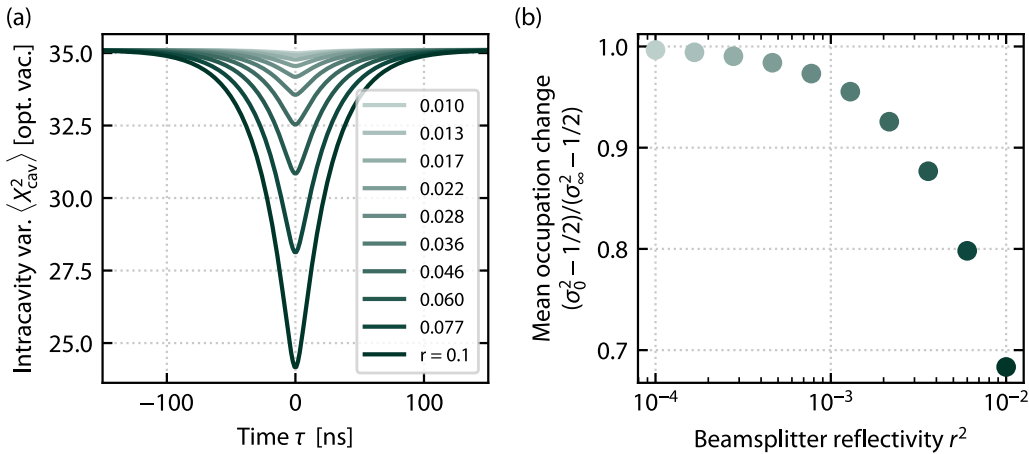
Figure 6.33. Intracavity quadrature variance for a zero-subtraction event. (a) Time dynamic of the variance, showing the decrease in the occupation at the time of the time of zero-subtraction for various values of the heralding beam splitter reflection coefficient r. (b) The change in the mean occupation at the no-subtraction heralding time compared to times far away.

single-photon detectors. Firstly, due to the gating of the detectors, they are measuring only 0.02 % of the time, meaning that by configuration there is no click 99.98 % of the time regardless of the number of incident photons. By synchronising the oscilloscope triggering to the gating of the SPADs, making sure measurements are obtained only at times where there is a gate and the detectors do not click, the fidelity of heralding zero-click states is greatly improved. Furthermore, in the context of increasing the fidelity of no clicks, the quantum efficiency of the detectors can be increased as the number of dark counts now do not reduce the fidelity, but takes the role of losses in the subtraction experiment; they reduce the probability of heralding an event as zero click, but do not reduce the validity of a heralded zero-click event. However, the maximum quantum efficiency of the SPADs is only 20 %, meaning only every 5th photon gives a click.

Superconducting-nanowire single-photon detectors can reach quantum efficiencies upwards of 90 %. They are also beneficial because they have a down time of only approximately 100 ns between detection events, making them able to operate at a rate orders of magnitude higher than SPADs. These detectors will greatly improve the quantum efficiency by several multiples and be helpful for increasing the zero-subtraction fidelity.

The zero-subtraction heralding fidelity can be increased further by increasing the out-coupling rate of anti-Stokes photons from the cavity and by reducing the losses of these photons from the cavity to the single-photon detectors. More efficient out-coupling of anti-Stokes light can be achieved by the steps outlined earlier for increasing the taper coupling efficiency. Also a pair of optical resonances with more favourable properties for out-coupling can be selected.

Implementing the changes described above to improve the heralding fidelity of zero-click operations, the additional cooling beyond initial laser cooling might be possible to observe as a dip in the variance of the heterodyne signal at the zero-click time.

Conclusions, appendices & references
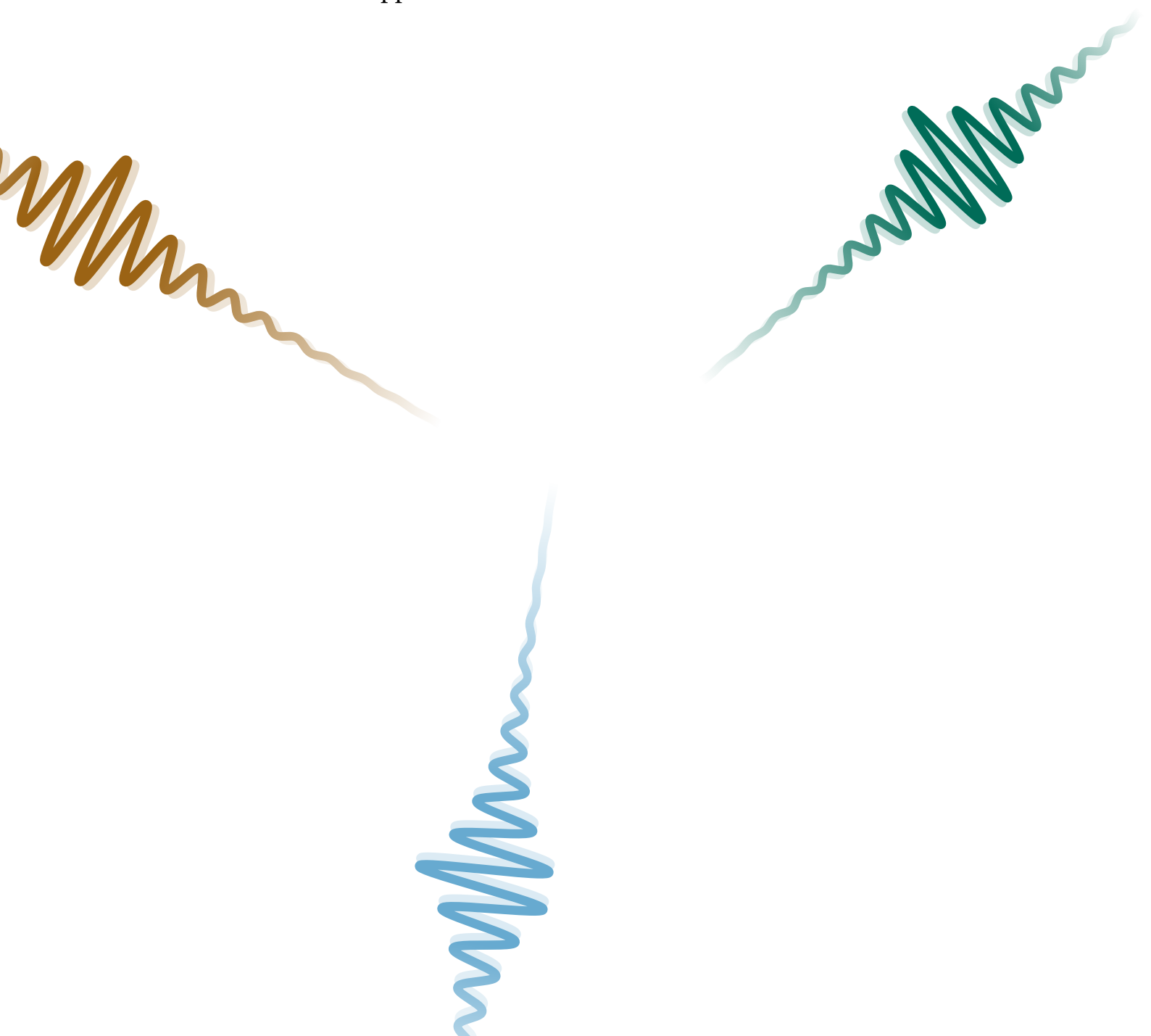
CHAPTER 7

Concluding remarks

Optical microresonators are extensively utilised in optics, providing resonant enhancement that enables research into and application of nonlinear optical effects. Scientific and technological advances over the past decades have resulted in the development of several different types of microresonators that are employed in a range of areas including sensing, metrology, communications, optomechanics, and quantum optics to name a few prominent examples. A widely used type of microresonator is the whispering-gallery-mode resonator, where optical fields propagate along the perimeter of a circular structure. These resonators can support counterpropagating optical modes, central to both parts of the work presented in this thesis.

7.1   COHERENT CONTROL OF BACKSCATTERING IN OPTICAL MICRORESONATORS

Light propagating in a WGM resonator can couple from one propagation direction to the other via reflecting off scatterers that can be intrinsic or extrinsic to the resonator. These backreflections are often unwanted as they can compromise the performance of microresonator experiments and applications, for instance symmetry-breaking-based sensing, optomechanics applications, laser gyroscopes and dual frequency combs. Therefore the backscattering problem has attracted more attention over the last years, with publications showing suppression techniques for backscattering in waveguide ring resonators and WGM resonators.

This thesis presents a method for coherently suppressing the intrinsic backscattering in optical WGM microresonators. The work described in this thesis demonstrates a record suppression exceeding 34 dB (noise limited) from an already low backscattering level where frequency splitting of the optical resonance is not resolved. The backscattering is coherently controlled by introducing a sub-wavelength-size scatterer within the near-field of the resonator. The scatterer's position determines the phase and amplitude of the induced backscattering, and by tuning its position, destructive interference between the induced and intrinsic backscattering can reduce unwanted optical backreflections.

Multiple measurements across three different resonators demonstrate the experimental viability of the presented technique, and the results align with the theoretical framework and model. The measured impact on the optical quality factor due to the presence of the tip is orders of magnitude smaller than the achieved suppression, and optimisation of the scatterer size and material can help to improve this ratio even further.

Longer term stability of the suppression and reproducibility for a given scatterer position has not been investigated as a part of this work. An integrated approach will give

improved stability by reducing any thermal-expansion effects affecting the present work to a minimum and because the miniaturised system allows better vibrational and environmental isolation. An integrated MEMS-based scatterer for tuneable backscattering suppression and control can also be envisaged, where active feedback on the scatterer position in order to keep the suppression at a desirable level can be implemented.

This work expands the microresonator control toolbox by adding a method that shows unprecedented backscattering reduction and over a broad bandwidth compared to alternative, optomechanical methods. The technique demonstrated here can both improve existing systems and enable the development of new high-accuracy, portable optical spectroscopy systems, gyroscopes, and other sensors. The technique is of particular interest for on-chip WGM and waveguide ring resonators, where a scatterer may be permanently integrated on the chip during fabrication or in post, reducing the complexity of the suppression method. The work might be useful for improving and optimising systems for research as well as out-of-lab uses of microresonators beyond the proof-of-concept stage.

7.2   GENERATION AND CHARACTERISATION OF NON-GAUSSIAN STATES OF MECHANICAL MOTION VIA BRILLOUIN OPTOMECHANICS

The coupling of coherent light fields and mechanical degrees of freedom allows one to generate and probe quantum states of motion, mapping the mechanical motion onto the light field; or conversely, providing coherent control over the mechanical motion. Coherent coupling between photons and phonons has proven useful in the context of the current rapid advance in quantum technologies for sensing, metrology, and information transfer and processing. One use-case, where promising results have already been demonstrated in optomechanical experiments, is the transduction of quantum information from optical frequencies to microwave frequencies compatible with electronics. This type of frequency conversion for quantum information might prove essential for future quantum networks. The fidelity of the transduction, i.e., the likeness of the input state to the output state, must be high for a quantum network to work efficiently and reliably, and there is still a long way to go to boost the fidelity and operation rates. An important step toward better quantum control and measurement of mechanical states within optomechanics is to generate and characterise non-classical mechanical states.

The second part of this thesis contributes toward the goal of non-classical mechanical state generation and characterisation via optomechanics by demonstrating multi-phonon subtraction and advancing the state-of-the-art overall measurement efficiency of a mechanical state via optics-based tomography. Building on techniques from quantum optics, the phase-space distributions of non-Gaussian, phonon-subtracted mechanical thermal states are measured via Brillouin optomechanics using photon counting for state preparation and simultaneous optical heterodyne detection for state characterisation.

The room-temperature measurements show that the laser-cooled, initial thermal state is transformed by the phonon subtraction events from an initial Gaussian in phase space into a ring shape with a diameter that increases with the number of phonons subtracted.

The experiment is the first observation of the effect that when two phonons are subtracted from a thermal mechanical state, the mean phonon occupation triples.

The work advances the state of the art for optics-based tomography of mechanical states by showing more than one order of magnitude improvement in the *s*-parameter, which captures the effects of measurement inefficiencies and added noise in tomography and state reconstruction experiments. Further improving the overall measurement efficiency provides a path towards tomography of non-classical mechanical states via optomechanics, an important outstanding goal in the optomechanics community.

The protocols used in this work can be applied to future room-temperature or cryogenic experiments to exploit and characterise the non-Gaussian and non-classical properties these operations generate. The advance in the measurement efficiency for optics-based tomography of mechanical states will be useful not only for Brillouin-based cavity optomechanics but for a broad range of both applied and fundamental studies of mechanical quantum-state engineering and tomography. Pursuing this line of research will facilitate the development of mechanical-oscillator-based quantum technology such as quantum memories exploiting the long coherence times available, and help explore fundamental physics including the quantum-to-classical transition.

APPENDIX A

The n-quanta-subtracted thermal state

The density matrix of the resulting state when n quanta are subtracted from or added to a thermal state is calculated, and the change to the mean occupation is computed. The result is valid for any bosonic system, but it is presented here as subtraction or addition of phonons to mechanical thermal state. The calculation follows that of the supplementary material of G. Enzian,* L. Freisem,* J. J. Price,* A. Ø. Svela* *et al.* [75].

A thermal state $\rho_{\bar{n}}$ of a mechanical oscillator with mean occupation number $\bar{n}$ can be expressed in the number basis as

$$\rho_{\bar{n}} = \sum_{m=0}^{\infty} \frac{\bar{n}^m}{(\bar{n}+1)^{m+1}} |m\rangle \langle m| \tag{A.1}$$

$$= (1-q) \sum_{m=0}^{\infty} q^m |m\rangle \langle m| \,, \tag{A.2}$$

where the shorthand $q \equiv \bar{n}/(\bar{n}+1) < 1$.

An n-phonon *subtraction* operation to the thermal state $\rho_{\bar{n}}$ generates the state

$$\rho_{n-} = \frac{b^n \rho_{\bar{n}} b^{\dagger n}}{\mathrm{Tr}(b^n \rho_{\bar{n}} b^{\dagger n})} \,, \tag{A.3}$$

whereas for an n-phonon *addition* operation to $\rho_{\bar{n}}$, the resulting state is

$$\rho_{n+} = \frac{b^{\dagger n} \rho_{\bar{n}} b^n}{\mathrm{Tr}(b^{\dagger n} \rho_{\bar{n}} b^n)} \,. \tag{A.4}$$

A.1 MULTI-PHONON SUBTRACTION DENSITY MATRIX AND MEAN OCCUPATION

The mean phonon number of the n-phonon-subtracted state ρ_{n-} is given by

$$\langle b^\dagger b \rangle_{n-} = \mathrm{Tr}\left(\rho_{n-} b^\dagger b\right) = \frac{\mathrm{Tr}\left(b^n \rho_{\bar{n}} b^{\dagger n} b^\dagger b\right)}{\mathrm{Tr}\left(b^n \rho_{\bar{n}} b^{\dagger n}\right)}. \tag{A.5}$$

First calculate the trace terms $\mathrm{Tr}\left(b^k \rho_{\bar{n}} b^{\dagger k}\right)$. Inserting the density matrix in the number basis (A.2) in Eq. (A.5) and using

$$b^k |m\rangle = \begin{cases} \sqrt{m!/(m-k)!}\,|m-k\rangle & \text{for } m \geq k \\ 0 & \text{otherwise} \end{cases} \tag{A.6}$$

(valid for $k \in \mathbb{N}$), gives

$$\mathrm{Tr}\left(b^k \rho_{\bar{n}} b^{\dagger k}\right) = (1-q) \sum_{m=0}^{\infty} q^m \langle m | b^{\dagger n} b^n | m \rangle \tag{A.7}$$

$$= (1-q)q^k \sum_{m=0}^{\infty} \frac{m!}{(m-k)!} q^{m-k}. \tag{A.8}$$

Noting that the factorial fraction can be rewritten

$$\frac{m!}{(m-k)!} = \frac{m(m-1)\cdots 1}{(m-k)(m-k-1)\cdots 1} = m(m-1)\cdots(m-k+1), \tag{A.9}$$

for $m \geq k$, the contents of the sum in Eq. (A.8) can be written

$$m(m-1)\cdots(m-k+1)q^{m-k} = m(m-1)\cdots(m-k+2)\frac{\mathrm{d}}{\mathrm{d}q}q^{m-k+1} \tag{A.10}$$

$$\vdots$$

$$= \frac{\mathrm{d}^k}{\mathrm{d}q^k}q^m, \tag{A.11}$$

Inserting this result into Eq. (A.8) gives

$$\mathrm{Tr}\left(b^k \rho_{\bar{n}} b^{\dagger k}\right) = (1-q)q^k \sum_{m=0}^{\infty} \frac{\mathrm{d}^k}{\mathrm{d}q^k}q^m \tag{A.12}$$

$$= (1-q)q^k \frac{\mathrm{d}^k}{\mathrm{d}q^k} \sum_{m=0}^{\infty} q^m \tag{A.13}$$

$$= (1-q)q^k \frac{\mathrm{d}^k}{\mathrm{d}q^k}\left(\frac{1}{1-q}\right), \tag{A.14}$$

where the sum of the geometric series when $|q| < 1$ was used. Performing the subsequent derivatives,

$$\frac{\mathrm{d}^k}{\mathrm{d}q^k}\left(\frac{1}{1-q}\right) = \frac{\mathrm{d}^{k-1}}{\mathrm{d}q^{k-1}}\left(\frac{1}{(1-q)^2}\right) \tag{A.15}$$

$$= \frac{\mathrm{d}^{k-2}}{\mathrm{d}q^{k-2}}\left(\frac{1\cdot 2}{(1-q)^3}\right) \tag{A.16}$$

$$\vdots$$

$$= \frac{k!}{(1-q)^{k+1}}, \tag{A.17}$$

the trace terms can finally be expressed

$$\mathrm{Tr}\left(b^k \rho_{\bar{n}} b^{\dagger k}\right) = \frac{k!}{(1-q)^k}q^k. \tag{A.18}$$
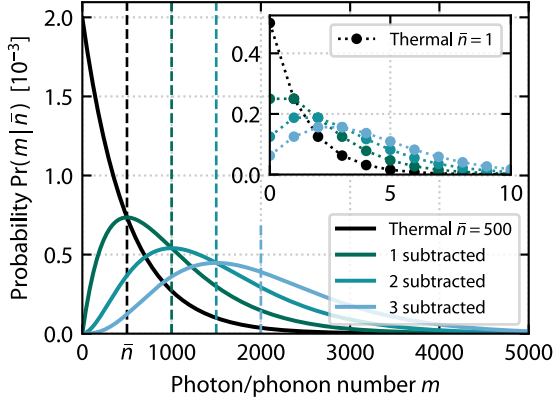
Figure A.1. Occupation probability distributions for thermal and subtracted thermal states for an initial thermal state with mean occupation $\bar{n} = 500$. The mean occupation increases by $(n + 1)$-fold for n subtractions as shown by the dashed lines. The inset shows the distributions for a smaller initial thermal state with $\bar{n} = 1$. Note that the ordinate axis in the inset is in units of unity, not scaled like the main axis.

NUMBER-BASIS DENSITY OPERATOR FOR THE SUBTRACTED STATE. This expression for the trace, Eq. (A.18), may be inserted into Eq. (A.3) to give the explicit form of the density operator for the subtracted state

$$\rho_{n-} = \frac{(1-q)^n}{n!\,q^n}\,(1-q)\sum_{m=0}^{\infty}q^m b^n\,|m\rangle\langle m|\,b^{\dagger n} \tag{A.19}$$

$$= \frac{(1-q)^{n+1}}{n!\,q^n}\sum_{m=0}^{\infty}q^m\frac{m!}{(m-n+1)!}\,|m\rangle\langle m| \tag{A.20}$$

$$= \frac{(1-q)^{n+1}}{n!\,q^n}\sum_{m=n}^{\infty}q^m\frac{m!}{(m-n)!}\,|m-n\rangle\langle m-n| \tag{A.21}$$

$$= \frac{(1-q)^{n+1}}{n!\,q^n}\sum_{m=0}^{\infty}q^{m+n}\frac{(m+n)!}{m!}\,|m\rangle\langle m| \tag{A.22}$$

$$= \sum_{m=0}^{\infty}(1-q)^{n+1}q^m\frac{(m+n)!}{n!m!}\,|m\rangle\langle m| \tag{A.23}$$

$$= \sum_{m=0}^{\infty}p_{n-}(m)\,|m\rangle\langle m|\,, \tag{A.24}$$

where

$$p_{n-}(m) = (1-q)^{n+1}q^m\binom{m+n}{n}, \tag{A.25}$$

when using the definition of the binomial coefficient.[i] Plots of the number distributions for the thermal and first three subtracted states is shown in Fig. A.1.

[i] $\binom{x}{y} = x!/[y!(x-y)!]$

MEAN OCCUPATION NUMBER. To finally calculate the mean phonon occupation of the subtracted state, the result of the general trace term Eq. (A.18) can be inserted into Eq. (A.5) (where the trace in the numerator has been cyclically permutated)

$$\langle b^{\dagger}b\rangle_{n-} = \frac{\mathrm{Tr}\left(b^{n+1}\rho_{\bar{n}}b^{\dagger n+1}\right)}{\mathrm{Tr}\left(b^n\rho_{\bar{n}}b^{\dagger n}\right)} \tag{A.26}$$

$$= \frac{(n+1)!\,q^{n+1}/(1-q)^{n+2}}{n!\,q^n/(1-q)^{n+1}} \tag{A.27}$$

$$= (n+1)\frac{q}{1-q} = (n+1)\bar{n}. \tag{A.28}$$

Thus, for n-phonon subtraction the mean occupation increases by a factor of $n + 1$

$$\bar{n} \rightarrow (n + 1)\,\bar{n}\,. \tag{A.29}$$

A.2   THE CASE OF MULTI-PHONON ADDITION

A similar calculation allows one to calculate the density operator and the mean phonon number of the n-phonon-added state ρ_{n+}, which are given by

$$\rho_{n+} = \sum_{m=0}^{\infty} p_{n+}(m)\,|m\rangle\langle m|\,, \tag{A.30}$$

$$p_{n+}(m) = (1 - q)^{n+1} q^{m-n} \binom{m}{n}\,, \tag{A.31}$$

$$\langle b^{\dagger} b \rangle_{n+} = (n + 1)\bar{n} + n\,. \tag{A.32}$$

Here, the binomial coefficient $\binom{m}{n} = 0$ for $m < n$, such that phonon-number states $|m\rangle$ with $m < n$ of ρ_{n+} are unoccupied. This property also leads to the observation that the phonon-number distribution of ρ_{n+} and ρ_{n-} are equal up to a shift $p_{n+}(m) = p_{n-}(m - n)$.

APPENDIX B

Phase-space distribution of a phonon-subtracted thermal state

The phase-space distribution of the phonon-subtracted thermal state is presented taking into account experimental inefficiencies. Colleagues J. Clarke and L. Freisem took a lead on performing these calculations.

A perfect heterodyne detection scheme measures the Husimi Q function of the mechanical state, but considering the inefficiencies and losses in the measurement, the Q function is smoothened to an s-parametrised Wigner function W_s with $s < -1$. The calculations obtain the marginal distributions for the W_s function for the subtracted states.

B.1   MARGINAL QUADRATURE DISTRIBUTIONS OF THE MECHANICAL STATE

This section calculates an expression for the n-subtracted state's position quadrature marginal of given an efficiency η up to the heterodyne detection: $\mathrm{pr}_{n-}(X_{\mathrm{m}}; \eta)$.

B.1.1   *The Glauber–Sudarshan* P *function of the subtracted state*

The Glauber–Sudarshan P representation of phase space is useful when working with coherent states[i] as the density operator $\hat{\rho}$ of a quantum state can be diagonalised in the coherent state basis using the P function [179]

$$\hat{\rho} = \int \mathrm{d}^2\beta \, P(\beta) \, |\beta\rangle \langle\beta| \, . \tag{B.1}$$

where $\beta = 2^{-1/2}(X_{\mathrm{m}} + iP_{\mathrm{m}})$ for the mechanical quadratures $X_{\mathrm{m}}, P_{\mathrm{m}}$. The P function of the thermal state $\hat{\rho}_{\mathrm{th}}$ with mean occupation $\bar{n}$ is given by

$$P_{\mathrm{th}}(\beta) = \frac{1}{\pi\bar{n}} \exp\left(-\frac{|\beta|^2}{\bar{n}}\right) \, . \tag{B.2}$$

By using the density operator of the subtracted state as expressed in terms of the thermal state as given in Eq. (A.3), the P function of $\hat{\rho}_{n-}$ can be obtained

$$P_{n-}(\beta) = \frac{1}{n!\bar{n}^n} |\beta|^{2n} P_{\mathrm{th}}(\beta). \tag{B.3}$$

Note that $P_{n-}(\beta)$ only depends on the magnitude of β, which demonstrates the rotational symmetry of the subtracted thermal state in phase space.

[i] The coherent state is the eigenstate of the annihilation operator, $\hat{b}|\beta\rangle = \beta|\beta\rangle$, where $\beta \in \mathbb{C}$ and can be expressed by the phase-space quadratures x, p as $\beta = 2^{-1/2}(x + ip)$.

B.1.2 *The position quadrature marginal*

The marginal of the position quadrature X_m for the subtracted state $\hat{\rho}_{n-}$ can be calculated from $\langle X_\mathrm{m}|\hat{\rho}_{n-}|X_\mathrm{m}\rangle$, which gives

$$\mathrm{pr}_{n-}(X_\mathrm{m}) = \int \mathrm{d}^2\beta \, P_{n-}(\beta) \, |\langle X_\mathrm{m}|\beta\rangle|^2 \tag{B.4}$$

$$= \frac{\exp\left(-\frac{X_\mathrm{m}^2}{1+2\bar{n}}\right)}{n!\pi^{\frac{3}{2}}\sqrt{1+2\bar{n}}} \sum_{k=0}^{n}\sum_{l=0}^{k}\binom{n}{k}\binom{2k}{2l}\Gamma\left[n-k+\frac{1}{2}\right]\Gamma\left[l+\frac{1}{2}\right]X_\mathrm{m}^{2(k-l)}\frac{(2\bar{n})^{k-l}}{(1+2\bar{n})^{2k-l}}, \tag{B.5}$$

where

$$\Gamma\left[m+\frac{1}{2}\right] = \frac{(2m)!}{4^m m!}\sqrt{\pi} \tag{B.6}$$

for $m \in \mathbb{N}$. The marginal $\mathrm{pr}_{n-}(X_\mathrm{m})$ is corresponds to the position marginal of the Wigner function $\int \mathrm{d}P_\mathrm{m} W(X_\mathrm{m}, P_\mathrm{m})$.

Note that due to the rotational symmetry of the state, also the probability marginals are invariant under the transformation

$$X_\mathrm{m} \to X_\mathrm{m}(\theta) = X_\mathrm{m}\cos\theta + P_\mathrm{m}\sin\theta, \tag{B.7}$$

which allows the heterodyne detection in Chapter 6 to have no phase reference.

B.1.3 *The influence of inefficiencies in measurement*

The experiment does not give access to the mechanical state directly, but the anti-Stokes light is used as a proxy for the mechanical state. The proxy is not a perfect representation of the mechanical state because of inefficiencies such as the non-perfect mechanics-light transduction efficiency and optical losses.

Describing the overall measurement efficiency η, the quadrature marginal given losses, $\mathrm{pr}(X_\mathrm{m}; \eta)$, can be described by a beamsplitter model for loss [179, Ch. 4]

$$\mathrm{pr}(X_\mathrm{m}; \eta) = \frac{1}{\sqrt{\pi(1-\eta)}} \int_{-\infty}^{+\infty} \mathrm{d}X' \, \mathrm{pr}(X') \exp\left[-\frac{\eta}{1-\eta}\left(X' - \frac{X_\mathrm{m}}{\sqrt{\eta}}\right)^2\right], \tag{B.8}$$

which is essentially the convolution of the lossless marginal $\mathrm{pr}(X_\mathrm{m})$ with a Gaussian due to the vacuum entering at the port of the virtual beam splitter, and a rescaling of the amplitude due to the lost photons. Inserting $\mathrm{pr}_{n-}(X_\mathrm{m})$ from Eq. (B.5) into Eq. (B.8) yields

$$\mathrm{pr}_{n-}(X_\mathrm{m}; \eta) = \frac{\exp\left[-X_\mathrm{m}^2\left(\frac{1}{1-\eta} - \frac{B^2}{A}\right)\right]}{n!\pi^2\sqrt{(1+2\bar{n})(1-\eta)A}} \sum_{k=0}^{n}\sum_{l=0}^{k}\sum_{p=0}^{k-l}\binom{n}{k}\binom{2k}{2l}\binom{2(k-l)}{2r}\Gamma\left[n-k+\frac{1}{2}\right]$$
$$\Gamma\left[l+\frac{1}{2}\right]\Gamma\left[r+\frac{1}{2}\right]\left(\frac{BX_\mathrm{m}}{A}\right)^{2(k-l-r)}\frac{(2\bar{n})^{k-l}}{(1+2\bar{n})^{2k-l}}A^{-r}, \tag{B.9}$$

where $A = 1/(1+2\bar{n}) + \eta/(1-\eta)$ and $B = \sqrt{\eta}(1-\eta)$.

The description so far takes into account the optical losses and optomechanical efficiency in how well the optical state of the anti-Stokes light at the input port of the heterodyne detector represents the mechanical state. This section also takes into account how that optical state impinging on the heterodyne detector is measured, thus a full picture of how the mechanical state is measured by the heterodyne detection.

B.2.1   *The Husimi* Q *function and smoothening*

Heterodyne detection projects an optical state $\hat{\rho}$ entering the detector onto a coherent state $|\alpha\rangle$. An outcome $\alpha = 2^{-1/2}(X_{\text{opt}} + iP_{\text{opt}})$ occurs with probability proportional to $\text{Tr}(|\alpha\rangle\langle\alpha|\hat{\rho}) = \langle\alpha|\hat{\rho}|\alpha\rangle$. The outcome is proportional to the definition of the Husimi Q function [179, Ch. 3]

$$Q(\alpha) = \frac{1}{2\pi}\langle\alpha|\hat{\rho}|\alpha\rangle\;, \tag{B.10}$$

which means that heterodyne detection measures the real-valued and non-negative Q function of the optical state $\hat{\rho}$ up to a proportionality factor. The Q function can be understood as a smoothened Wigner function, referred to as an s-parameterised Wigner function W_s where $s = 0$ is the Wigner function and $s = -1$ is the Q function.

The marginals of the Q function are smoothened compared to the quadrature marginals of the optical state that is to be measured, which can be understood as added noise due to the simultaneous measurement of two orthogonal quadratures [500]. The marginal of the Q function

$$\text{pr}(X_{\text{opt}}; s = -1) = \int dP_{\text{opt}}\; Q(X_{\text{opt}}, P_{\text{opt}}) \tag{B.11}$$

can be expressed as the true marginal for the state that is measured convolved with a Gaussian of width equal to the vacuum noise entering at the heterodyne frequency:

$$\text{pr}(X_{\text{opt}}; s = -1) = \frac{1}{\sqrt{\pi}}\int dX'\; \text{pr}(X')\exp\left[-(X_{\text{opt}} - X')^2\right]\;. \tag{B.12}$$

Note that the smoothened marginal is phase-invariant.

Thus, for the experiment considered here, in the case of a lossless transduction of the mechanical state onto the optical state impinging on the detector, $\eta = 1$, the optical heterodyne detection measures the Q function of the mechanical state, $Q(X_{\text{m}}, P_{\text{m}})$ perfectly, which is the smoothened Wigner function $W_{s=-1}$, whose marginals are smoothened in comparison to the mechanical state's true marginals.

In the case of measurement inefficiencies, $\eta < 1$, the s parameter is not -1, and thus it is not the Q function of the mechanical state that is obtained by the heterodyne detector, but an s-parameterised Wigner function W_s with the s parameter given by [179, Ch. 4]

$$s = \frac{1}{\eta}(\eta - 2)\begin{cases} = -1 & \text{for } \eta = 1 \\ < -1 & \text{for } \eta < 1 \end{cases}. \tag{B.13}$$

Note that the s parameter accounts only for the smoothening of the measured phase space due to the inefficiencies, but losses also means the quadratures are rescaled accordingly due to the reduced field amplitude, which will be accounted for in Eq. (B.20).

B.2.2   *The s-parameterised Wigner function for the subtracted state*

So far, it is clear that when performing heterodyne detection with inefficiencies, the obtained phase space representation is smoothened more than the Q function of the mechanical state $Q(X_\mathrm{m}, P_\mathrm{m})$. The additional smoothening is accounted for by the s-parameterised Wigner function. To compute the smoothened marginals as measured for the phonon-subtracted state given arbitrary efficiency η, W_s in terms of the derived P_{n-} function is computed.

For a general (non-symmetric) quantum state with quadratures x, p, the s-parametrised Wigner function can be computed by convolving the P function with a two-dimensional Gaussian

$$W_s(x, p) = (P * \mathcal{G}_s)(x, p),\tag{B.14}$$

where $*$ represents the two-dimensional convolution and the Gaussian is

$$\mathcal{G}_s(x, p) = \frac{1}{\pi(1-s)}\exp\left(-\frac{x^2 + p^2}{1-s}\right).\tag{B.15}$$

Written out, the s-parametrised Wigner function is

$$W_s(x, p) = \frac{1}{\pi(1-s)}\iint_{-\infty}^{\infty}\mathrm{d}x'\mathrm{d}p'\, P(x', p')$$
$$\times \exp\left(-\frac{(x-x')^2 + (p-p')^2}{1-s}\right).\tag{B.16}$$

In the case of n-phonon subtraction, the s-parametrised Wigner function is given by convolution of P_{n-} and a Gaussian

$$W_s(X_\mathrm{m}, P_\mathrm{m}) = (P_{n-} * \mathcal{G}_s)(X_\mathrm{m}, P_\mathrm{m}).\tag{B.17}$$

By substituting in Eq. (B.3) for the P function in Eq. (B.16) and using $\beta = 2^{-1/2}(X_\mathrm{m} + iP_\mathrm{m})$, the full form for the n-phonon subtracted state is then

$$W_{s,n-}(X_\mathrm{m}, P_\mathrm{m}) = \frac{2^{-n}\bar{n}^{-1-n}}{\pi^2(1-s)n!}\iint_{-\infty}^{\infty}\mathrm{d}X'_\mathrm{m}\mathrm{d}P'_\mathrm{m}\left[\left(X'^2_\mathrm{m} + P'^2_\mathrm{m}\right)^n\right.$$
$$\left.\times \exp\left(-\frac{X'^2_\mathrm{m} + P'^2_\mathrm{m}}{2\bar{n}} - \frac{(X'_\mathrm{m} - X_\mathrm{m})^2 + (P'_\mathrm{m} - P_\mathrm{m})^2}{1-s}\right)\right],$$
$$\tag{B.18}$$

which describes the phase space as measured by the heterodyne detection for arbitrary efficiency η via the s parameter as defined in Eq. (B.13).

B.2.3 *The measured marginal distributions*

Finally, the position marginal of the inefficiently captured mechanical state as measured via heterodyne detection, $\Pr(X_\mathrm{m})$, is calculated. This corresponds to the marginals that are obtained from the experimental data by taking the sum across one axis of the W_s tomograms for the states generated in the experiment:

$$\Pr(X_\mathrm{m}) \approx \frac{1}{\mathcal{N}} \sum_{P_\mathrm{m}} W_s(X_\mathrm{m}, P_\mathrm{m}) , \tag{B.19}$$

normalised by $\mathcal{N} = \sum_{X_\mathrm{m}} \Pr(X_\mathrm{m})$.

To calculate the expected marginal probability distribution $\Pr(X_\mathrm{m})$ as measured by the heterodyne, the loss-rescaled W_s [500] can be integrated

$$\Pr(X_\mathrm{m}) = \frac{1}{\eta} \int \mathrm{d}P_\mathrm{m} \ W_s(X_\mathrm{m}\eta^{-1/2}, P_\mathrm{m}\eta^{-1/2}) , \tag{B.20}$$

which can be recast

$$\Pr(X_\mathrm{m}) = \frac{1}{\sqrt{\eta}} \int \mathrm{d}p \ W_s(X_\mathrm{m}\eta^{-1/2}, p) \tag{B.21}$$

$$= \frac{1}{\sqrt{\pi|s|\eta}} \int \mathrm{d}X' \ \mathrm{pr}(X') \exp\left[-\frac{(X' - X_\mathrm{m}/\sqrt{\eta})^2}{|s|} \right] , \tag{B.22}$$

by using the relation between the true marginal distribution $\mathrm{pr}(X_\mathrm{m})$ and the marginal of the s-parameterised Wigner function $\mathrm{pr}(X_\mathrm{m}; s)$ for $s < 0$,

$$\mathrm{pr}(X_\mathrm{m}; s) = \frac{1}{\sqrt{\pi|s|}} \int \mathrm{d}X' \ \mathrm{pr}(X') \exp\left[-\frac{(X_\mathrm{m} - X')^2}{|s|} \right] . \tag{B.23}$$

Alternatively, $\Pr(X_\mathrm{m})$ can be computed by inserting the mechanical quadrature marginal considering losses Eq. (B.9) into the expression for the heterodyne marginal Eq. (B.12).

Both methods give the following expression for the measured marginal of the n-phonon subtracted state:

$$\Pr_{n-}(X_\mathrm{m}) = \frac{1}{\sqrt{\pi}} \int \mathrm{d}X' \ \mathrm{pr}_{n-}(X'; \eta) \exp\left[-(X_\mathrm{m} - X')^2 \right] \tag{B.24}$$

$$= \frac{\exp\left(-\frac{X_\mathrm{m}^2}{2(1+\eta\bar{n})}\right)}{n!\pi^2\sqrt{2(1+\eta\bar{n})}} \sum_{k=0}^{n} \sum_{l=0}^{k} \sum_{r=0}^{k-l} \binom{n}{k}\binom{2k}{2l}\binom{2(k-l)}{2r} \Gamma\left[n-k+\frac{1}{2}\right]\Gamma\left[l+\frac{1}{2}\right]\Gamma\left[r+\frac{1}{2}\right]$$

$$X_\mathrm{m}^{2(k-l-r)} \ \frac{(2\eta\bar{n})^{k-l}}{(1+2\eta\bar{n})^{l+r}[2(1+\eta\bar{n})]^{2(k-l)-r}} . \tag{B.25}$$
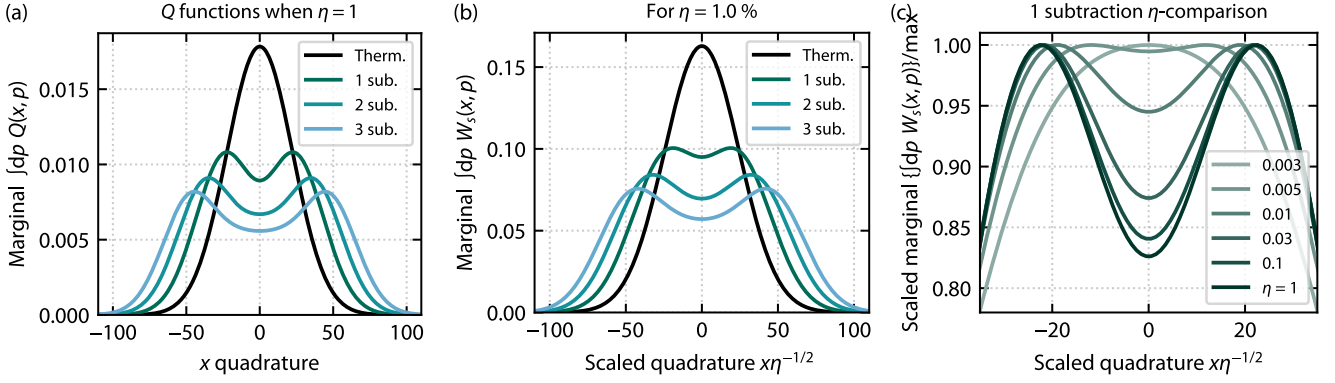
Figure B.1. Phase-space marginals for varied measurement efficiency. The plots show marginals of the obtained phase space via heterodyne detection for the thermal and first three subtracted states. (a) When $\eta = 1$ the obtained phase space corresponds to the Q function of the respective states. Note the increasingly non-Gaussian shape of the subtracted states. (b) For $\eta < 1$ the obtained phase space corresponds to the s-parameterised Wigner function W_s with $s < -1$, here shown for $\eta = 0.01$ ($s = -199$), which is approximately the efficiency achieved in this experiment. Note the lower contrast in the non-Gaussian features compared to (a) due to the smoothening from the added noise. The quadrature is also scaled due to the associated amplitude losses. (c) A comparison of marginals computed from W_s for varying η where the each marginal is scaled to its maximum for comparable scales. For the lowest efficiencies the bimodality cannot be resolved.

The measured marginal distributions of the thermal state $\hat{\rho}_{\bar{n}}$, single-phonon subtracted state $\hat{\rho}_{1-}$, and two-phonon subtracted state $\hat{\rho}_{2-}$ are then

$$\mathrm{Pr}_{\mathrm{th}}(X_{\mathrm{m}}) = \frac{1}{\sqrt{2\pi(1+\bar{n}')}} \exp\left[-\frac{X_{\mathrm{m}}^2}{2(1+\bar{n}')}\right] \tag{B.26a}$$

$$\mathrm{Pr}_{1-}(X_{\mathrm{m}}) = \frac{1}{2}\mathrm{Pr}_{\mathrm{th}}(X_{\mathrm{m}})\left\{\frac{2+\bar{n}'}{1+\bar{n}'} + \frac{4\bar{n}'}{[2(1+\bar{n}')]^2}X_{\mathrm{m}}^2\right\} \tag{B.26b}$$

$$\mathrm{Pr}_{2-}(X_{\mathrm{m}}) = \frac{1}{2}\mathrm{Pr}_{\mathrm{th}}(X_{\mathrm{m}})\left\{\frac{8+8\bar{n}'+3(\bar{n}')^2}{4(1+\bar{n}')^2} + \frac{4\bar{n}'+(\bar{n}')^2}{2(1+\bar{n}')^3}X_{\mathrm{m}}^2 + \frac{(2\bar{n}')^2}{[2(1+\bar{n}')]^4}X_{\mathrm{m}}^4\right\} \tag{B.26c}$$

where $\bar{n}' = \eta\bar{n}$. These expressions simplify to the marginals of the mechanical Q function when $\eta = 1$, as expected when the mechanical state is perfectly transduced onto the optical state reaching the heterodyne detector.

Figure B.1 shows plots of the marginals Eq. (B.26) for varying efficiencies.

B.2.4   *Location of maxima of the marginals and phase-space*

If the detection efficiency is sufficiently high, a non-Gaussian state with a dip at the origin can be observed in phase space.

For the single-phonon subtracted state, if the detection efficiency such that $\eta\bar{n} > 2$, the maxima for the measured distribution $\mathrm{Pr}_{1-}(X_{\mathrm{m}})$ occur at $X_{\mathrm{m}} = \pm X_1$, where

$$X_1 = \sqrt{\frac{(1+\eta\bar{n})(\eta\bar{n}-2)}{\eta\bar{n}}} . \tag{B.27}$$

The location of the maxima of $\mathrm{Pr}_{1-}(X_{\mathrm{m}})$ can be related to the radius at which the maxima occur in W_s. First, consider the expression for the P function of the single-phonon

subtracted state by choosing $n = 1$ in Eq. (B.3). The maxima of $P_{1-}(\beta)$ occur at a radius $\sqrt{2\bar{n}}$ from the origin. Integrating $P_{1-}(\beta)$ over one quadrature gives an expression for marginal of this P function: $\mathrm{pr}_{1-}(X_m; s = +1)$. The maxima of $\mathrm{pr}_{1-}(X_m; s = +1)$ occur at $X_m = \pm\sqrt{\bar{n}}$. Hence, there is a factor of $\sqrt{2}$ difference between the distance of the maxima from the origin of $\mathrm{pr}_{1-}(X_m; s = +1)$ and $P_{1-}(\beta)$. Second, using Eq. (B.23) and a two-dimensional convolution to get from the P function to W_s, the factor of $\sqrt{2}$ difference persists at the level of $\mathrm{Pr}_{1-}(X_m)$ and W_s. Hence, for $\hat{\rho}_{1-}$ the maxima of $W_s(X_m, P_m)$ occur at a radius of $r_1 = \sqrt{2}X_1$.

For the two-phonon subtracted state and $\eta\bar{n} > -4+2\sqrt{6}$, the maxima for the measured distribution of two-phonon subtracted state $\mathrm{Pr}_{2-}(X_m)$ occur at $X_m = \pm X_2$, where

$$X_2 = \sqrt{\frac{1 + \eta\bar{n}}{\eta\bar{n}}\left[-4 + \eta\bar{n} + \sqrt{2(4 + (\eta\bar{n})^2)}\right]}. \qquad \text{(B.28)}$$

A similar calculation to the one sketched above gives that for $\hat{\rho}_{2-}$ the maxima of $W_s(X_m, P_m)$ occur at a radius $r_2 = \sqrt{2}X_2$.

References

[1] V. B. Braginsky, M. L. Gorodetsky, and V. S. Ilchenko, *Quality-factor and nonlinear properties of optical whispering-gallery modes,* Phys. Lett. A 137, 393 (1989).

[2] G. C. Righini, Y. Dumeige, P. Féron, M. Ferrari, G. N. Conti, D. Ristic, and S. Soria, *Whispering gallery mode microresonators: Fundamentals and applications,* Riv. del Nuovo Cim. 34, 435 (2011).

[3] A. B. Matsko, A. A. Savchenkov, D. Strekalov, V. S. Ilchenko, and L. Maleki, *Review of applications of whispering-gallery mode resonators in photonics and nonlinear optics,* IPN Prog. Rep. 42-162 (2005).

[4] A. Chiasera, Y. Dumeige, P. Féron, M. Ferrari, Y. Jestin, G. Nunzi Conti, S. Pelli, S. Soria, and G. Righini, *Spherical whispering-gallery-mode microresonators,* Laser Photonics Rev. 4, 457 (2010).

[5] K. J. Vahala, *Optical microcavities,* Nature 424, 839 (2003).

[6] A. N. Oraevsky, *Whispering-gallery waves,* Quantum Elec. 32, 377 (2002).

[7] D. Yu, M. Humar, K. Meserve, R. C. Bailey, S. N. Chormaic, and F. Vollmer, *Whispering-gallery-mode sensors for biological and physical sensing,* Nat. Rev. Methods Primers 1, 83 (2021).

[8] F. Vollmer and D. Yu, *Optical Whispering Gallery Modes for Biosensing*, Biological and Medical Physics, Biomedical Engineering (Springer Nature, Cham, 2020).

[9] A. B. Matsko, ed., *Practical Applications of Microresonators in Optics and Photonics*, 1st ed. (CRC Press, Boca Raton, FL, 2009).

[10] J. Heebner, R. Grover, and T. Ibrahim, *Optical Microresonators*, Optical Sciences, Vol. 138 (Springer, New York, 2008).

[11] R. K. Chang and A. J. Campillo, eds., *Optical Processes in Microcavities*, Advanced Series in Applied Physics, Vol. 3 (World Scientific, Singapore, 1996).

[12] R. W. Boyd, *Nonlinear Optics*, 3rd ed. (Academic Press, London, 2008).

[13] G. S. He, *Nonlinear Optics and Photonics* (Oxford University Press, Oxford, 2014).

[14] P. D. Drummond and M. Hillery, *The Quantum Theory of Nonlinear Optics* (Cambridge University Press, Cambridge, 2014).

[15] M. Aspelmeyer, T. J. Kippenberg, and F. Marquardt, *Cavity optomechanics,* Rev. Mod. Phys. 86, 1391 (2014).

[16] L. Del Bino, J. M. Silver, S. L. Stebbings, and P. Del'Haye, *Symmetry breaking of counter-propagating light in a nonlinear resonator,* Sci. Rep. 7, 43142 (2017).

[17] Q.-T. Cao, H. Wang, C.-H. Dong, H. Jing, R.-S. Liu, X. Chen, L. Ge, Q. Gong, and Y.-F. Xiao, *Experimental demonstration of spontaneous chirality in a nonlinear microresonator,* Phys. Rev. Lett. 118, 033901 (2017).

[18] A. A. Savchenkov, A. B. Matsko, M. Mohageg, D. V. Strekalov, and L. Maleki, *Parametric oscillations in a whispering gallery resonator,* Opt. Lett. 32, 157 (2007).

[19] I. S. Grudinin and L. Maleki, *Ultralow-threshold Raman lasing with CaF$_2$ resonators,* Opt. Lett. 32, 166 (2007).

[20] S. M. Spillane, T. J. Kippenberg, and K. J. Vahala, *Ultralow-threshold Raman laser using a spherical dielectric microcavity,* Nature 415, 621 (2002).

[21] V. S. Ilchenko, A. A. Savchenkov, A. B. Matsko, and L. Maleki, *Nonlinear optics and crystalline whispering gallery mode cavities,* Phys. Rev. Lett. 92, 043903 (2004).

[22] T. Carmon and K. J. Vahala, *Visible continuous emission from a silica microphotonic device by third-harmonic generation,* Nat. Phys. 3, 430 (2007).

[23] E. Verhagen, S. Deléglise, S. Weis, A. Schliesser, and T. J. Kippenberg, *Quantum-coherent coupling of a mechanical oscillator to an optical cavity mode,* Nature 482, 63 (2012).

[24] A. Schliesser and T. J. Kippenberg, Cavity optomechanics with whispering-gallery mode optical micro-resonators, in *Advances In Atomic, Molecular, and Optical Physics*, Vol. 58, edited by P. Berman, E. Arimondo, and C. Lin (Academic Press, Sausalito, CA, 2010) pp. 207–323.

[25] T. J. Kippenberg and K. J. Vahala, *Cavity opto-mechanics,* Opt. Express 15, 17172 (2007).

[26] T. J. Kippenberg, H. Rokhsari, T. Carmon, A. Scherer, and K. J. Vahala, *Radiation-pressure induced mechanical oscillation of an optical microcavity,* Phys. Rev. Lett. 95, 033901 (2005).

[27] G. S. Wiederhecker, P. Dainese, and T. P. Mayer Alegre, *Brillouin optomechanics in nanophotonic structures,* APL Photonics 4, 071101 (2019).

[28] R. Van Laer, R. Baets, and D. Van Thourhout, *Unifying Brillouin scattering and cavity optomechanics,* Phys. Rev. A 93, 053828 (2016).

[29] G. Bahl and T. Carmon, Brillouin optomechanics, in *Cavity Optomechanics: Nano- and Micromechanical Resonators Interacting with Light*, Quantum Science and Technology, edited by M. Aspelmeyer, T. J. Kippenberg, and F. Marquardt (Springer, Berlin; Heidelberg, 2014) Chap. 8, pp. 157–168.

[30] G. Bahl, J. Zehnpfennig, M. Tomes, and T. Carmon, *Stimulated optomechanical excitation of surface acoustic waves in a microdevice,* Nat. Commun. 2, 403 (2011).

[31] B. J. Eggleton, C. G. Poulton, and R. Pant, *Inducing and harnessing stimulated Brillouin scattering in photonic integrated circuits,* Adv. Opt. Photonics 5, 536 (2013).

[32] I. S. Grudinin, A. B. Matsko, and L. Maleki, *Brillouin lasing with a caf$_2$ whispering gallery mode resonator,* Phys. Rev. Lett. 102, 043902 (2009).

[33] M. Tomes and T. Carmon, *Photonic micro-electromechanical systems vibrating at X-band (11-GHz) rates,* Phys. Rev. Lett. 102, 113601 (2009).

[34] N. Toropov, G. Cabello, M. P. Serrano, R. R. Gutha, M. Rafti, and F. Vollmer, *Review of biosensing with whispering-gallery mode lasers,* Light Sci. Appl. 10, 42 (2021).

[35] X. Jiang, A. J. Qavi, S. H. Huang, and L. Yang, *Whispering-gallery sensors,* Matter 3, 371 (2020).

[36] W. Liu, Y.-L. Chen, S.-J. Tang, F. Vollmer, and Y.-F. Xiao, *Nonlinear sensing with whispering-gallery mode microcavities: From label-free detection to spectral fingerprinting,* Nano Lett. 21, 1566 (2021).

[37] K. D. Heylman, K. A. Knapper, E. H. Horak, M. T. Rea, S. K. Vanga, and R. H. Goldsmith, *Optical microresonators for sensing and transduction: A materials perspective,* Adv. Mater. 29, 1700037 (2017).

[38] M. R. Foreman, J. D. Swaim, and F. Vollmer, *Whispering gallery mode sensors,* Adv. Opt. Photonics 7, 168 (2015).

[39] V. S. Ilchenko and A. B. Matsko, *Optical resonators with whispering-gallery modes — Part II: Applications,* IEEE J. Sel. Top. Quantum Electron. 12, 15 (2006).

[40] F. Vollmer, S. Arnold, and D. Keng, *Single virus detection from the reactive shift of a whispering-gallery mode,* Proc. Natl. Acad. Sci. 105, 20701 (2008).

[41] G. Anetsberger, E. Gavartin, O. Arcizet, Q. P. Unterreithmeier, E. M. Weig, M. L. Gorodetsky, J. P. Kotthaus, and T. J. Kippenberg, *Measuring nanomechanical motion with an imprecision below the standard quantum limit,* Phys. Rev. A 82, 061804 (2010).

[42] T. J. Kippenberg, R. Holzwarth, and S. A. Diddams, *Microresonator-based optical frequency combs,* Science 332, 555 (2011).

[43] A. B. Matsko, A. A. Savchenkov, N. Yu, and L. Maleki, *Whispering-gallery-mode resonators as frequency references. I. Fundamental limitations,* J. Opt. Soc. Am. B 24, 1324 (2007).

[44] P. Del'Haye, A. Schliesser, O. Arcizet, T. Wilken, R. Holzwarth, and T. J. Kippenberg, *Optical frequency comb generation from a monolithic microresonator,* Nature 450, 1214 (2007).

[45] D. V. Strekalov, C. Marquardt, A. B. Matsko, H. G. L. Schwefel, and G. Leuchs, *Nonlinear and quantum optics with whispering gallery resonators,* J. Opt. 18, 123002 (2016).

[46] J. U. Fürst, D. V. Strekalov, D. Elser, A. Aiello, U. L. Andersen, C. Marquardt, and G. Leuchs, *Quantum light from a whispering-gallery-mode disk resonator,* Phys. Rev. Lett. 106, 113901 (2011).

[47] P. Marin-Palomo, J. N. Kemal, M. Karpov, A. Kordts, J. Pfeifle, M. H. P. Pfeiffer, P. Trocha, S. Wolf, *et al.*, *Microresonator-based solitons for massively parallel coherent optical communications,* Nature 546, 274 (2017).

[48] C. Reimer, M. Kues, P. Roztocki, B. Wetzel, F. Grazioso, B. E. Little, S. T. Chu, *et al.*, *Generation of multiphoton entangled quantum states by means of integrated frequency combs,* Science 351, 1176 (2016).

[49] M. Metcalfe, *Applications of cavity optomechanics,* Appl. Phys. Rev. 1, 031105 (2014).

[50] J. Pfeifle, V. Brasch, M. Lauermann, Y. Yu, D. Wegner, T. Herr, K. Hartinger, *et al.*, *Coherent terabit communications with microresonator Kerr frequency combs,* Nat. Photonics 8, 375 (2014).

[51] J. Kerr, *A new relation between electricity and light: Dielectrified media birefringent,* Philos. Mag. 50, 337 (1875).

[52] D. K. Armani, T. J. Kippenberg, S. M. Spillane, and K. J. Vahala, *Ultra-high-Q toroid microcavity on a chip,* Nature 421, 925 (2003).

[53] B. Gayral, J. M. Gérard, A. Lemaître, C. Dupuis, L. Manin, and J. L. Pelouard, *High-Q wet-etched GaAs microdisks containing InAs quantum boxes,* Appl. Phys. Lett. 75, 1908 (1999).

[54] I. S. Grudinin, V. S. Ilchenko, and L. Maleki, *Ultrahigh optical Q factors of crystalline resonators in the linear regime,* Phys. Rev. A 74, 063806 (2006).

[55] P. Del'Haye, S. A. Diddams, and S. B. Papp, *Laser-machined ultra-high-Q microrod resonators for nonlinear optics,* Appl. Phys. Lett. 102, 221119 (2013).

[56] D. S. Weiss, V. Sandoghdar, J. Hare, V. Lefèvre-Seguin, J.-M. Raimond, and S. Haroche, *Splitting of high-Q Mie modes induced by light backscattering in silica microspheres,* Opt. Lett. 20, 1835 (1995).

[57] S. Kim, J. M. Taylor, and G. Bahl, *Dynamic suppression of Rayleigh backscattering in dielectric resonators,* Optica 6, 1016 (2019).

[58] A. Ø. Svela, J. M. Silver, L. Del Bino, S. Zhang, M. T. M. Woodley, M. R. Vanner, and P. Del'Haye, *Coherent suppression of backscattering in optical microresonators,* Light Sci. Appl. 9, 204 (2020).

[59] A. Ashkin, *Acceleration and trapping of particles by radiation pressure,* Phys. Rev. Lett. 24, 156 (1970).

[60] A. Ashkin and J. M. Dziedzic, *Optical trapping and manipulation of viruses and bacteria,* Science 235, 1517 (1987).

[61] B. P. Abbott *et al.* (LIGO Scientific Collaboration and Virgo Collaboration), *Observation of gravitational waves from a binary black hole merger,* Phys. Rev. Lett. 116, 061102 (2016).

[62] J. W. S. Rayleigh, *The problem of the whispering gallery,* Philos. Mag. 20, 1001 (1910).

[63] R. D. Richtmyer, *Dielectric Resonators,* J. Appl. Phys. 10, 391 (1939).

[64] G. Enzian, M. Szczykulska, J. Silver, L. Del Bino, S. Zhang, I. A. Walmsley, P. Del'Haye, and M. R. Vanner, *Observation of Brillouin optomechanical strong coupling with an 11 GHz mechanical mode,* Optica 6, 7 (2019).

[65] S. Barzanjeh, A. Xuereb, S. Gröblacher, M. Paternostro, C. A. Regal, and E. M. Weig, *Optomechanics for quantum technologies,* Nat. Phys. 18, 15 (2022).

[66] N. Lauk, N. Sinclair, S. Barzanjeh, J. P. Covey, M. Saffman, M. Spiropulu, and C. Simon, *Perspectives on quantum transduction,* Quantum Sci. Techn. 5, 020501 (2020).

[67] J. T. Hill, A. H. Safavi-Naeini, J. Chan, and O. Painter, *Coherent optical wavelength conversion via cavity optomechanics,* Nat. Commun. 3, 1196 (2012).

[68] H. J. Kimble, *The quantum internet,* Nature 453, 1023 (2008).

[69] I. Siddiqi, *Engineering high-coherence superconducting qubits,* Nat. Rev. Mater. 6, 875 (2021).

[70] K. Fang, M. H. Matheny, X. Luan, and O. Painter, *Optical transduction and routing of microwave phonons in cavity-optomechanical circuits,* Nat. Photonics 10, 489 (2016).

[71] R. N. Patel, Z. Wang, W. Jiang, C. J. Sarabalis, J. T. Hill, and A. H. Safavi-Naeini, *Single-mode phononic wire,* Phys. Rev. Lett. 121, 040501 (2018).

[72] A. Zivari, R. Stockill, N. Fiaschi, and S. Gröblacher, *Non-classical mechanical states guided in a phononic waveguide,* Nat. Phys. in print, online (2022).

[73] A. Zivari, N. Fiaschi, R. Burgwal, E. Verhagen, R. Stockill, and S. Gröblacher, *On-chip distribution of quantum information using traveling phonons,* arxiv, 2204.05066 (2022).

[74] G. Enzian, J. J. Price, L. Freisem, J. Nunn, J. Janousek, B. C. Buchler, P. K. Lam, and M. R. Vanner, *Single-phonon addition and subtraction to a mechanical thermal state,* Phys. Rev. Lett. 126, 033601 (2021).

[75] G. Enzian,* L. Freisem,* J. J. Price,* A. Ø. Svela*, J. Clarke, B. Shajilal, J. Janousek, B. C. Buchler, P. K. Lam, and M. R. Vanner, *Non-Gaussian mechanical motion via single and multi-phonon subtraction from a thermal state,* Phys. Rev. Lett. 127, 243601 (2021).

[76] J. W. S. Rayleigh, *The Theory of Sound,* 2nd ed., Vol. II (MacMillian and Co., New York, 1896).

[77] H. Barrell, *The Rayleighs and the National Physical Laboratory,* Appl. Opt. 3, 1125 (1964).

[78] J. W. S. Rayleigh, *Further applications of Bessel's functions of high order to the whispering gallery and allied problems,* Philos. Mag. 27, 100 (1914).

[79] C. V. Raman and G. A. Sutherland, *Whispering-gallery phenomena at St. Paul's cathedral,* Nature 108, 42 (1921).

[80] C. V. Raman and G. A. Sutherland, *On the whispering-gallery phenomenon,* Proc. R. Soc. Lond. A 100, 424 (1922).

[81] K. G. Budden, H. G. Martin, and N. F. Mott, *The ionosphere as a whispering gallery,* Proc. R. Soc. Lond. A 265, 554 (1962).

[82] K. Aki and P. Richards, *Quantitative Seismology*, Geology Seismology (University Science Books, Sausalito, CA, 2002).

[83] O. Wright, *Gallery of whispers,* Phys. World 25, 31 (2012).

[84] T. H. Maiman, *Stimulated optical radiation in ruby,* Nature 187, 493 (1960).

[85] C. G. B. Garrett, W. Kaiser, and W. L. Bond, *Stimulated emission into optical whispering modes of spheres,* Phys. Rev. 124, 1807 (1961).

[86] M. Gao, Q.-F. Yang, Q.-X. Ji, H. Wang, L. Wu, B. Shen, J. Liu, G. Huang, L. Chang, *et al.*, *Probing material absorption and optical nonlinearity of integrated photonic materials,* arxiv, 2111.00105 (2021).

[87] M. L. Gorodetsky, A. A. Savchenkov, and V. S. Ilchenko, *Ultimate Q of optical microsphere resonators,* Opt. Lett. 21, 453 (1996).

[88] A. A. Savchenkov, A. B. Matsko, D. Strekalov, M. Mohageg, V. S. Ilchenko, and L. Maleki, *Low threshold optical oscillations in a whispering gallery mode caf₂ resonator,* Phys. Rev. Lett. 93, 243905 (2004).

[89] G. Lin, S. Diallo, R. Henriet, M. Jacquot, and Y. K. Chembo, *Barium fluoride whispering-gallery-mode disk-resonator with one billion quality-factor,* Opt. Lett. 39, 6009 (2014).

[90] V. Lefèvre-Seguin, *Whispering-gallery mode lasers with doped silica microspheres,* Opt. Mater. 11, 153 (1999).

[91] J. P. Reithmaier, G. Sęk, A. Löffler, C. Hofmann, S. Kuhn, S. Reitzenstein, L. V. Keldysh, V. D. Kulakovskii, T. L. Reinecke, and A. Forchel, *Strong coupling in a single quantum dot-semiconductor microcavity system,* Nature 432, 197 (2004).

[92] A. Gondarenko, J. S. Levy, and M. Lipson, *High confinement micron-scale silicon nitride high Q ring resonator,* Opt. Express 17, 11366 (2009).

[93] V. N. Astratov, S. Yang, S. Lam, B. D. Jones, D. Sanvitto, D. M. Whittaker, A. M. Fox, M. S. Skolnick, A. Tahraoui, P. W. Fry, and M. Hopkinson, *Whispering gallery resonances in semiconductor micropillars,* Appl. Phys. Lett. 91, 071115 (2007).

[94] I. H. Malitson, *Interspecimen comparison of the refractive index of fused silica,* J. Opt. Soc. Am. 55, 1205 (1965).

[95] G. P. Agrawal, *Nonlinear Fiber Optics*, 4th ed. (Academic Press, Burlington, MA; London, 2007).

[96] P. Del'Haye, *Optical frequency comb generation in monolithic microresonators,* PhD thesis, LMU München (2011).

[97] G. Mie, *Beiträge zur Optik trüber Medien, speziell kolloidaler Metallösungen,* Ann. Phys. 330, 377 (1908).

[98] P. Debye, *Der Lichtdruck auf Kugeln von beliebigem Material,* Ann. Phys. 335, 57 (1909).

[99] M. Oxborrow, *Traceable 2-D finite-element simulation of the whispering-gallery modes of axisymmetric electromagnetic resonators,* IEEE Trans. Microw. Theory Tech. 55, 1209 (2007).

[100] S. Schiller, *Asymptotic expansion of morphological resonance frequencies in Mie scattering,* Appl. Opt. 32, 2181 (1993).

[101] B. E. Little, J. P. Laine, and H. A. Haus, *Analytic theory of coupling from tapered fibers and half-blocks into microsphere resonators,* J. Light. Technol. 17, 704 (1999).

[102] C. C. Lam, P. T. Leung, and K. Young, *Explicit asymptotic formulas for the positions, widths, and strengths of resonances in Mie scattering,* J. Opt. Soc. Am. B 9, 1585 (1992).

[103] M. Gorodetsky and A. Fomin, *Geometrical theory of whispering-gallery modes,* IEEE J. Sel. Top. Quantum Electron. 12, 33 (2006).

[104] I. Breunig, B. Sturman, F. Sedlmeir, H. G. L. Schwefel, and K. Buse, *Whispering gallery modes at the rim of an axisymmetric optical resonator: Analytical versus numerical description and comparison with experiment,* Opt. Express 21, 30683 (2013).

[105] Y. A. Demchenko and M. L. Gorodetsky, *Analytical estimates of eigenfrequencies, dispersion, and field distribution in whispering gallery resonators,* J. Opt. Soc. Am. B 30, 3056 (2013).

[106] H. A. Antosiewicz, Bessel functions of fractional order, in *Handbook of Mathematical Functions*, Applied Mathematics No. 55, edited by M. Abramowitz and I. A. Segun (National Bureau of Standards, Washington D.C., 1964) Chap. 10.

[107]   B. E. Little, J.-P. Laine, and S. T. Chu, *Surface-roughness-induced contradirectional coupling in ring and disk resonators,* Opt. Lett. 22, 4 (1997).

[108]   M. L. Gorodetsky, A. D. Pryamikov, and V. S. Ilchenko, *Rayleigh scattering in high-Q microspheres,* J. Opt. Soc. Am. B 17, 1051 (2000).

[109]   T. J. Kippenberg, S. M. Spillane, and K. J. Vahala, *Modal coupling in traveling-wave resonators,* Opt. Lett. 27, 1669 (2002).

[110]   L. N. Menegozzi and W. E. Lamb, *Theory of a ring laser,* Phys. Rev. A 8, 2103 (1973).

[111]   A. Venugopalan, D. Kumar, and R. Ghosh, *Optical mode-coupling in a ring due to a back-scatterer,* Pramana 40, 107 (1993).

[112]   A. Mazzei, S. Götzinger, L. de S. Menezes, G. Zumofen, O. Benson, and V. Sandoghdar, *Controlled coupling of counterpropagating whispering-gallery modes by a single Rayleigh scatterer: A classical problem in a quantum optical light,* Phys. Rev. Lett. 99, 173603 (2007).

[113]   J. Zhu, S. K. Özdemir, L. He, and L. Yang, *Controlled manipulation of mode splitting in an optical microcavity by two Rayleigh scatterers,* Opt. Express 18, 23535 (2010).

[114]   S. Arnold, M. Khoshsima, and I. Teraoka, *Shift of whispering-gallery modes in microspheres by protein adsorption,* Opt. Lett. 28, 272 (2003).

[115]   J. Zhu, S. K. Özdemir, Y. F. Xiao, L. Li, L. He, D. R. Chen, and L. Yang, *On-chip single nanoparticle detection and sizing by mode splitting in an ultrahigh-Q microresonator,* Nat. Photonics 4, 46 (2010).

[116]   B. Peng, S. K. Özdemir, M. Liertzer, W. Chen, J. Kramer, H. Yılmaz, J. Wiersig, S. Rotter, and L. Yang, *Chiral modes and directional lasing at exceptional points,* Proc. Natl. Acad. Sci. 113, 6845 (2016).

[117]   C. Wang, X. Jiang, G. Zhao, M. Zhang, C. W. Hsu, B. Peng, A. D. Stone, L. Jiang, and L. Yang, *Electromagnetically induced transparency at a chiral exceptional point,* Nat. Phys. 16, 334 (2020).

[118]   J. Knittel, J. D. Swaim, D. L. McAuslan, G. A. Brawley, and W. P. Bowen, *Back-scatter based whispering gallery mode sensing,* Sci. Rep. 3, 2974 (2013).

[119]   M. Mohageg, A. Savchenkov, and L. Maleki, *Coherent backscattering in lithium niobate whispering-gallery-mode resonators,* Opt. Lett. 32, 2574 (2007).

[120]   F. de Fornel, *Evanescent Waves*, Optical Sciences, Vol. 73 (Springer, Berlin; London, 2001).

[121]   F. Sedlmeir, *Crystalline Whispering Gallery Mode Resonators*, PhD thesis, Friedrich–Alexander–Universität Erlangen–Nürnberg (2016).

[122]   H. H. Li, *Refractive index of alkaline earth halides and its wavelength and temperature derivatives,* J. Phys. Chem. Ref. Data 9, 161 (1980).

[123]   E. Hecht, *Optics*, 5th ed. (Pearson, Boston, MA, 2017).

[124]   V. S. Ilchenko, X. S. Yao, and L. Maleki, *Pigtailing the high-Q microsphere cavity: A simple fiber coupler for optical whispering-gallery modes.* Opt. Lett. 24, 723 (1999).

[125]   J. C. Knight, G. Cheung, F. Jacques, and T. A. Birks, *Phase-matched excitation of whispering-gallery-mode resonances by a fiber taper,* Opt. Lett. 22, 1129 (1997).

[126]   M. Cai, O. Painter, and K. J. Vahala, *Observation of critical coupling in a fiber taper to a silica-microsphere whispering-gallery mode system,* Phys. Rev. Lett. 85, 74 (2000).

[127]   X. Zhang and A. M. Armani, *Silica microtoroid resonator sensor with monolithically integrated waveguides,* Opt. Express 21, 23592 (2013).

[128]   M. H. Pfeiffer, J. Liu, M. Geiselmann, and T. J. Kippenberg, *Coupling ideality of integrated planar high-Q microresonators,* Phys. Rev. Appl. 7, 024026 (2017).

[129]   B. E. Little, S. T. Chu, H. A. Haus, J. Foresi, and J. Laine, *Microring resonator channel dropping filters,* J. Light. Technol. 15, 998 (1997).

[130]   O. González-Cortez, R. A. Carrillo-Betancourt, J. Hernández-Cordero, and A. M. Velázquez-Benítez, Functional tapered fiber devices using polymeric coatings, in *Fiber Optics*, edited by G. Huerta-Cuellar (IntechOpen, Rijeka, 2021) Chap. 2.

[131]   S. M. Spillane, T. J. Kippenberg, O. J. Painter, and K. J. Vahala, *Ideality in a fiber-taper-coupled microresonator system for application to cavity quantum electrodynamics,* Phys. Rev. Lett. 91, 043902 (2003).

[132]   A. Yariv, *Universal relations for coupling of optical power between microresonators and dielectric waveguides,* Electron. Lett. 36, 321 (2000).

[133]   D. G. Rabus, *Integrated Ring Resonators*, Optical Sciences, Vol. 127 (Springer, Berlin; Heidelberg, 2007).

[134] H. A. Haus, *Waves and fields in optoelectronics*, Solid State Physical Electronics (Prentice-Hall, London, 1984).

[135] J. Zhu, M. Zohrabi, K. Bae, T. M. Horning, M. B. Grayson, W. Park, and J. T. Gopinath, *Nonlinear characterization of silica and chalcogenide microresonators,* Optica 6, 716 (2019).

[136] M. Borselli, T. J. Johnson, and O. Painter, *Beyond the Rayleigh scattering limit in high-Q silicon microdisks: theory and experiment,* Opt. Express 13, 1515 (2005).

[137] T. J. A. Kippenberg, *Nonlinear Optics in Ultra-high-Q Whispering-Gallery Optical Microcavities,* PhD thesis, California Institute of Technology (2004).

[138] T. Carmon, Lan Yang, and K. Vahala, *Dynamical thermal behavior and thermal self-stability of microcavities,* Opt. Express 12, 4742 (2004).

[139] X. Jiang and L. Yang, *Optothermal dynamics in whispering-gallery microresonators,* Light Sci. Appl. 9, 24 (2020).

[140] L. He, *Whispering Gallery Mode Microresonators for Lasing and Single Nanoparticle Detection,* PhD thesis, Washington University in St. Louis (2012).

[141] H. Gao, Y. Jiang, Y. Cui, L. Zhang, J. Jia, and L. Jiang, *Investigation on the thermo-optic coefficient of silica fiber within a wide temperature range,* J. Light. Technol. 36, 5881 (2018).

[142] I. H. Malitson, *Refractive properties of barium fluoride,* J. Opt. Soc. Am. 54, 628 (1964).

[143] T. Zhou, J. feng Zhang, B. qing Hu, and H. guang Yang, *Measurements of the thermo-optic coefficient of a barium fluoride single crystal,* Appl. Opt. 33, 2620 (1994).

[144] T. S. Aurora, S. M. Day, T. E. Duerr, and D. O. Pederson, *Thermal expansion and index of refraction variation in barium fluoride,* Solid State Ion. 5, 625 (1981).

[145] D. B. Leviton and B. J. Frey, *Temperature-dependent absolute refractive index measurements of synthetic fused silica,* in *Optomechanical Technologies for Astronomy*, Vol. 6273, edited by E. Atad-Ettedgui, J. Antebi, and D. Lemke (SPIE, 2006) p. 62732K.

[146] M. Okaji, N. Yamada, K. Nara, and H. Kato, *Laser interferometric dilatometer at low temperatures: application to fused silica SRM 739,* Cryogenics 35, 887 (1995).

[147] G. New, *Introduction to Nonlinear Optics* (Cambridge University Press, Cambridge, 2011).

[148] D. Milam, *Review and assessment of measured values of the nonlinear refractive-index coefficient of fused silica,* Appl. Opt. 37, 546 (1998).

[149] D. Milam, M. J. Weber, and A. J. Glass, *Nonlinear refractive index of fluoride crystals,* Appl. Phys. Lett. 31, 822 (1977).

[150] A. E. Kaplan, *Light-induced nonreciprocity, field invariants, and nonlinear eigenpolarizations,* Opt. Lett. 8, 560 (1983).

[151] R. W. Ziolkowski and J. B. Judkins, *Full-wave vector Maxwell equation modeling of the self-focusing of ultrashort optical pulses in a nonlinear Kerr medium exhibiting a finite response time,* J. Opt. Soc. Am. B 10, 186 (1993).

[152] G. N. Ghalanos, J. M. Silver, L. Del Bino, N. Moroney, S. Zhang, M. T. M. Woodley, A. Ø. Svela, and P. Del'Haye, *Kerr-nonlinearity-induced mode-splitting in optical microresonators,* Phys. Rev. Lett. 124, 223901 (2020).

[153] L. Hill, G.-L. Oppo, M. T. M. Woodley, and P. Del'Haye, *Effects of self- and cross-phase modulation on the spontaneous symmetry breaking of light in ring resonators,* Phys. Rev. A 101, 013823 (2020).

[154] M. T. M. Woodley, J. M. Silver, L. Hill, F. Copie, L. Del Bino, S. Zhang, G.-L. Oppo, and P. Del'Haye, *Universal symmetry breaking dynamics for the Kerr interaction of counter-propagating light in dielectric ring resonators,* Phys. Rev. A 98, 053863 (2018).

[155] M. T. M. Woodley, L. Hill, L. Del Bino, G.-L. Oppo, and P. Del'Haye, *Self-switching Kerr oscillations of counterpropagating light in microresonators,* Phys. Rev. Lett. 126, 043901 (2021).

[156] A. Ø. Svela, J. M. Silver, L. D. Bino, G. Ghalanos, N. Moroney, M. T. M. Woodley, S. Zhang, M. R. Vanner, and P. Del'Haye, *Spontaneous symmetry breaking based near-field sensing with a microresonator,* in *Conference on Lasers and Electro-Optics* (Optical Society of America, 2019) p. JM3B.3.

[157] E. Iannone, *Telecommunication Networks*, 1st ed., Devices, Circuits, and Systems (CRC Press, Boca Raton, FL, 2017).

[158] M. F. Thorpe, Phonons in amorphous solids, in *Physics of Structurally Disordered Solids*, edited by S. S. Mitra (Springer US, Boston, MA, 1976) pp. 623–663.

[159] S. Hunklinger, *Phonons in amprophous materials,* J. Phys. Colloques 43, 461 (1982).

[160] S. Ohno, T. Sonehara, E. Tatsu, A. Koreeda, and S. Saikan, *kHz stimulated Brillouin spectroscopy,* Rev. Sci. Instrum. 77, 123104 (2006).

[161] G. S. MacCabe, H. Ren, J. Luo, J. D. Cohen, H. Zhou, A. Sipahigil, M. Mirhosseini, and O. Painter, *Nano-acoustic resonator with ultralong phonon lifetime,* Science 370, 840 (2020).

[162] S. Galliou, M. Goryachev, R. Bourquin, P. Abbé, J. P. Aubry, and M. E. Tobar, *Extremely low loss phonon-trapping cryogenic acoustic cavities for future physical experiments,* Sci. Rep. 3, 2132 (2013).

[163] W. H. Renninger, P. Kharel, R. O. Behunin, and P. T. Rakich, *Bulk crystalline optomechanics,* Nat. Phys. 14, 1 (2018).

[164] C. M. Kube, *Elastic anisotropy of crystals,* AIP Adv. 6, 095209 (2016).

[165] G. Enzian, *Brillouin cavity optomechanics with whispering-gallery microresonators*, PhD thesis, Univeristy of Oxford (2020).

[166] A. E. Fomin, M. L. Gorodetsky, I. S. Grudinin, and V. S. Ilchenko, *Nonstationary nonlinear effects in optical microspheres,* J. Opt. Soc. Am. B 22, 459 (2005).

[167] E. D. Marquardt, J. P. Le, and R. Radebaugh, Cryogenic material properties database, in *Cryocoolers 11*, edited by R. G. Ross (Springer US, Boston, MA, 2002) pp. 681–687.

[168] J. P. Ibe, P. P. Bey, S. L. Brandow, R. A. Brizzolara, N. A. Burnham, D. P. DiLella, K. P. Lee, C. R. K. Marrian, and R. J. Colton, *On the electrochemical etching of tips for scanning tunneling microscopy,* J. Vac. Sci. Technol. A 8, 3570 (1990).

[169] A.-S. Lucier, *Preparation and Characterization of Tungsten Tips Suitable for Molecular Electronics Studies*, Master's thesis, McGill University (2004).

[170] T. Hagedorn, E. Ouali, W. Paul, and D. Oliver, *Refined tip preparation by electrochemical etching and ultrahigh vacuum treatment to obtain atomically sharp tips for scanning tunneling microscope and atomic force microscope,* Rev. Sci. Instrum. 82, 113903 (2011).

[171] I. Ekvall, E. Wahlström, D. Claesson, H. Olin, and E. Olsson, *Preparation and characterization of electrochemically etched W tips for STM,* Meas. Sci. Technol. 10, 11 (1999).

[172] M. Rezeq, J. Pitters, and R. Wolkow, *Tungsten nanotip fabrication by spatially controlled field-assisted reaction with nitrogen,* J. Chem. Phys. 124, 204716 (2006).

[173] R. Zhang and D. G. Ivey, *Preparation of sharp polycrystalline tungsten tips for scanning tunneling microscopy imaging,* J. Vac. Sci. Technol. B 14, 1 (1996).

[174] G. Nunzi Conti, S. Berneschi, F. Cosi, S. Pelli, S. Soria, G. C. Righini, M. Dispenza, and A. Secchi, *Planar coupling to high-Q lithium niobate disk resonators,* Opt. Express 19, 3651 (2011).

[175] R. W. P. Drever, J. L. Hall, F. V. Kowalski, J. Hough, G. M. Ford, A. J. Munley, and H. Ward, *Laser phase and frequency stabilization using an optical resonator,* Appl. Phys. B 31, 97 (1983).

[176] E. Black, LIGO Technical Note: Notes on the Pound-Drever-Hall technique, (1998).

[177] M. Fox, *Quantum Optics: An Introduction*, Oxford Masters Series in Physics (Oxford University Press, Oxford, 2006).

[178] H. A. Haus, Detection, in *Electromagnetic Noise and Quantum Optical Measurements*, Advanced Texts in Physics (Springer, Berlin; Heidelberg, 2000) Chap. 9, pp. 281–304.

[179] U. Leonhardt, P. L. Knight, and A. Miller, *Measuring the Quantum State of Light*, Cambridge Studies in Modern Optics (Cambridge University Press, Cambridge, 1997).

[180] A. T. Young, *Rayleigh scattering,* Phys. Today 35, 42 (1982).

[181] J. W. Strutt (Rayleigh), *On the scattering of light by small particles,* Philos. Mag. 41, 447 (1871).

[182] J. W. S. Rayleigh, *On the electromagnetic theory of light,* Philos. Mag. 12, 81 (1881).

[183] V. Twersky, *Rayleigh scattering,* Appl. Opt. 3, 1150 (1964).

[184] M. I. Stockman, *Nanoplasmonics: The physics behind the applications,* Phys. Today 64, 39 (2011).

[185] A. Ø. Svela, J. M. Silver, L. Del Bino, S. Zhang, M. T. M. Woodley, M. R. Vanner, and P. Del'Haye, *Suppressing intrinsic backscattering in ultra-high-Q optical microresonators,* in *Conference on Lasers and Electro-Optics Pacific Rim (CLEO-PR)* (Optical Society of America, 2020) pp. C5B–4.

[186] A. Ø. Svela, J. M. Silver, L. Del Bino, S. Zhang, M. T. M. Woodley, M. R. Vanner, and P. Del'Haye, *>30 dB suppression of intrinsic backscattering in whispering-gallery-mode microresonators,* in *Conference on Lasers and Electro-Optics* (Optical Society of America, 2021) p. STu1F.2.

[187] A. Ø. Svela, J. M. Silver, L. Del Bino, S. Zhang, M. T. M. Woodley, M. R. Vanner, and P. Del'Haye, *More than 34 dB backscattering suppression in microresonators,* in *CLEO/Europe-EQEC* (IEEE, 2021) pp. ED–4.3.

[188] A. Ø. Svela, keyoscacquire: Keysight oscilloscope acquire, (2021), avaliable on Github and PyPi, github.com/asvela/keyoscacquire .

[189] J. Matres and W. V. Sorin, *Simple model for ring resonators backscatter,* Opt. Express 25, 3242 (2017).

[190] F. C. MacKintosh and S. John, *Coherent backscattering of light in the presence of time-reversal-noninvariant and parity-nonconserving media,* Phys. Rev. B 37, 1884 (1988).

[191] A. A. Golubentsev, *Suppression of interference effects in multiple scattering of light,* Sov. Phys. JETP Engl. Transl. 59, 26 (1984).

[192] J. Wiersig, *Structure of whispering-gallery modes in optical microdisks perturbed by nanoparticles,* Phys. Rev. A 84, 063828 (2011).

[193] J. Wiersig, A. Eberspächer, J.-B. Shim, J.-W. Ryu, S. Shinohara, M. Hentschel, and H. Schomerus, *Nonorthogonal pairs of copropagating optical modes in deformed microdisk cavities,* Phys. Rev. A 84, 023845 (2011).

[194] X. Kuai, L. Wei, F. Yang, W. Yan, Z. Li, and X. Wang, *Suppression method of optical noises in resonator-integrated optic gyroscopes,* Sensors 22, 2889 (2022).

[195] W. W. Chow, J. Gea-Banacloche, L. M. Pedrotti, V. E. Sanders, W. Schleich, and M. O. Scully, *The ring laser gyro,* Rev. Mod. Phys. 57, 61 (1985).

[196] C. Etrich, P. Mandel, R. Centeno Neelen, R. J. C. Spreeuw, and J. P. Woerdman, *Dynamics of a ring-laser gyroscope with backscattering,* Phys. Rev. A 46, 525 (1992).

[197] F. Dell'Olio, T. Tatoli, C. Ciminelli, and M. Armenise, *Recent advances in miniaturized optical gyroscopes,* J. Eur. Opt. Soc. Rapid 9, 14013 (2014).

[198] W. Liang, V. S. Ilchenko, A. A. Savchenkov, E. Dale, D. Eliyahu, A. B. Matsko, and L. Maleki, *Resonant microphotonic gyroscope,* Optica 4, 114 (2017).

[199] Q.-F. Yang, X. Yi, K. Y. Yang, and K. Vahala, *Counter-propagating solitons in microresonators,* Nat. Photonics 11, 560 (2017).

[200] E. Lucas, G. Lihachev, R. Bouchand, N. G. Pavlov, A. S. Raja, M. Karpov, M. L. Gorodetsky, and T. J. Kippenberg, *Spatial multiplexing of soliton microcombs,* Nat. Photonics 12, 699 (2018).

[201] N. M. Kondratiev and V. E. Lobanov, *Modulational instability and frequency combs in whispering-gallery-mode microresonators with backscattering,* Phys. Rev. A 101, 013816 (2020).

[202] A. E. Kaplan and P. Meystre, *Enhancement of the Sagnac effect due to nonlinearly induced nonreciprocity.* Opt. Lett. 6, 590 (1981).

[203] Y.-Y. Li, Q.-T. Cao, J.-h. Chen, X.-C. Yu, and Y.-F. Xiao, *Microcavity sensor enhanced by spontaneous chiral symmetry breaking,* Phys. Rev. Appl. 16, 044016 (2021).

[204] J. M. Silver, L. Del Bino, M. T. M. Woodley, G. N. Ghalanos, A. Ø. Svela, N. Moroney, S. Zhang, K. T. V. Grattan, and P. Del'Haye, *Nonlinear enhanced microresonator gyroscope,* Optica 8, 1219 (2021).

[205] N. Moroney, L. Del Bino, M. Woodley, G. Ghalanos, J. Silver, A. Svela, S. Zhang, and P. Del'Haye, *Logic gates based on interaction of counterpropagating light in microresonators,* J. Light. Technol. 38, 1414 (2020).

[206] L. Del Bino, N. Moroney, and P. Del'Haye, *Optical memories and switching dynamics of counterpropagating light states in microresonators,* Opt. Express 29, 2193 (2021).

[207] L. Del Bino, J. M. Silver, M. T. M. Woodley, S. L. Stebbings, X. Zhao, and P. Del'Haye, *Microresonator isolators and circulators based on the intrinsic nonreciprocity of the Kerr effect,* Optica 5, 279 (2018).

[208] D. J. Wilson, V. Sudhir, N. Piro, R. Schilling, A. Ghadimi, and T. J. Kippenberg, *Measurement-based control of a mechanical oscillator at its thermal decoherence rate,* Nature 524, 325 (2015).

[209] E. Kim, M. D. Baaske, and F. Vollmer, *Towards next-generation label-free biosensors: recent advances in whispering gallery mode sensors,* Lab Chip 17, 1190 (2017).

[210] B. E. Little, S. T. Chu, W. Pan, and Y. Kokubun, *Microring resonator arrays for VLSI photonics,* IEEE Photonics Technol. Lett. 12, 323 (2000).

[211] W. McCutcheon, *Backscattering in nonlinear microring resonators via a Gaussian treatment of coupled cavity modes,* APL Photonics 6, 066103 (2021).

[212] X. Yi, Y.-F. Xiao, Y.-C. Liu, B.-B. Li, Y.-L. Chen, Y. Li, and Q. Gong, *Multiple-Rayleigh-scatterer-induced mode splitting in a high-Q whispering-gallery-mode microresonator,* Phys. Rev. A 83, 023803 (2011).

[213] M. Jaffe, L. Palm, C. Baum, L. Taneja, A. Kumar, and J. Simon, *Understanding and suppressing backscatter in optical resonators,* arxiv, 2205.05203 (2022).

[214] M.-A. Miri, F. Ruesink, E. Verhagen, and A. Alù, *Optical nonreciprocity based on optomechanical coupling,* Phys. Rev. Appl. 7, 064014 (2017).

[215] F. Ruesink, J. P. Mathew, M.-A. Miri, A. Alù, and E. Verhagen, *Optical circulation in a multimode optomechanical resonator,* Nat. Commun. 9, 1798 (2018).

[216] F. Ruesink, M.-A. Miri, A. Alù, and E. Verhagen, *Nonreciprocity and magnetic-free isolation based on optomechanical interactions,* Nat. Commun. 7, 13662 (2016).

[217] S. Götzinger, O. Benson, and V. Sandoghdar, *Influence of a sharp fiber tip on high-Q modes of a microsphere resonator,* Opt. Lett. 27, 80 (2002).

[218] M.-A. Miri and A. Alù, *Exceptional points in optics and photonics,* Science 363, eaar7709 (2019).

[219] J. Wiersig, *Enhancing the sensitivity of frequency and energy splitting detection by using exceptional points: Application to microcavity sensors for single-particle detection,* Phys. Rev. Lett. 112, 203901 (2014).

[220] S. E. Harris, *Electromagnetically induced transparency,* Phys. Today 50, 36 (1997).

[221] L. V. Hau, S. E. Harris, Z. Dutton, and C. H. Behroozi, *Light speed reduction to 17 metres per second in an ultracold atomic gas,* Nature 397, 594 (1999).

[222] S. Weis, R. Rivière, S. Deléglise, E. Gavartin, O. Arcizet, A. Schliesser, and T. J. Kippenberg, *Optomechanically induced transparency,* Science 330, 1520 (2010).

[223] A. H. Safavi-Naeini, T. P. M. Alegre, J. Chan, M. Eichenfield, M. Winger, Q. Lin, J. T. Hill, D. E. Chang, and O. Painter, *Electromagnetically induced transparency and slow light with optomechanics,* Nature 472, 69 (2011).

[224] S. Biasi, F. Ramiro-Manzano, F. Turri, P.-É. Larré, M. Ghulinyan, I. Carusotto, and L. Pavesi, *Hermitian and non-Hermitian mode coupling in a microdisk resonator due to stochastic surface roughness scattering,* IEEE Photon. J. 11, 1 (2019).

[225] M. W. Puckett, K. Liu, N. Chauhan, Q. Zhao, N. Jin, H. Cheng, J. Wu, R. O. Behunin, P. T. Rakich, K. D. Nelson, and D. J. Blumenthal, *422 million intrinsic quality factor planar integrated all-waveguide resonator with sub-MHz linewidth,* Nat. Commun. 12, 934 (2021).

[226] A. Li, T. Van Vaerenbergh, P. De Heyn, P. Bienstman, and W. Bogaerts, *Backscattering in silicon microring resonators: a quantitative analysis,* Laser Photonics Rev. 10, 420 (2016).

[227] F. Morichetti, A. Canciamilla, M. Martinelli, A. Samarelli, R. M. De La Rue, M. Sorel, and A. Melloni, *Coherent backscattering in optical microring resonators,* Appl. Phys. Lett. 96, 081112 (2010).

[228] F. Morichetti, A. Canciamilla, C. Ferrari, M. Torregiani, A. Melloni, and M. Martinelli, *Roughness induced backscattering in optical silicon waveguides,* Phys. Rev. Lett. 104, 033902 (2010).

[229] S. Werquin, S. Verstuyft, and P. Bienstman, *Integrated interferometric approach to solve microring resonance splitting in biosensor applications,* Opt. Express 21, 16955 (2013).

[230] A. Li and W. Bogaerts, *Fundamental suppression of backscattering in silicon microrings,* Opt. Express 25, 2092 (2017).

[231] Y. Hu, L. Shao, S. Arnold, Y.-C. Liu, C.-Y. Ma, and Y.-F. Xiao, *Mode broadening induced by nanoparticles in an optical whispering-gallery microcavity,* Phys. Rev. A 90, 043847 (2014).

[232] C. F. Bohren and D. R. Huffman, *Absorption and Scattering of Light by Small Particles* (John Wiley & Sons, Weinheim, 1998).

[233] R. Carminati and J. C. Schotland, *Principles of Scattering and Transport of Light* (Cambridge University Press, Cambridge, 2021).

[234] M. I. Mishchenko, L. D. Travis, and A. A. Lacis, *Scattering, absorption, and emission of light by small particles* (Cambridge University Press, Cambridge, 2002).

[235] M. Kerker, The scattering functions for spheres, in *The Scattering of Light and Other Electromagnetic Radiation*, Physical Chemistry: A Series of Monographs, Vol. 16, edited by E. M. Loebl (Academic Press, New York, 1969) Chap. 5.

[236] L. He, S. K. Özdemir, J. Zhu, W. Kim, and L. Yang, *Detecting single viruses and nanoparticles using whispering gallery microlasers,* Nat. Nanotechnol. 6, 428 (2011).

[237] D. Keng, X. Tan, and S. Arnold, *Whispering gallery micro-global positioning system for nanoparticle sizing in real time,* Appl. Phys. Lett. 105, 071105 (2014).

[238] Y. Zhi, X.-C. Yu, Q. Gong, L. Yang, and Y.-F. Xiao, *Single nanoparticle detection using optical microcavities,* Adv. Mater. 29, 1604920 (2017).

[239] S. Rosenblum, Y. Lovsky, L. Arazi, F. Vollmer, and B. Dayan, *Cavity ring-up spectroscopy for ultrafast sensing with optical microresonators,* Nat. Commun. 6, 6788 (2015).

[240] G. Anetsberger, O. Arcizet, Q. P. Unterreithmeier, R. Rivière, A. Schliesser, E. M. Weig, J. P. Kotthaus, and T. J. Kippenberg, *Near-field cavity optomechanics with nanomechanical oscillators,* Nat. Phys. 5, 909 (2009).

[241] E. Gavartin, P. Verlot, and T. J. Kippenberg, *A hybrid on-chip optomechanical transducer for ultrasensitive force measurements,* Nat. Nanotechnol. 7, 509 (2012).

[242] Y. Chen, Y. Yin, L. Ma, and O. G. Schmidt, *Recent progress on optoplasmonic whispering-gallery-mode microcavities,* Adv. Opt. Mater. 9, 2100143 (2021).

[243] K. G. Cognée, H. M. Doeleman, P. Lalanne, and A. F. Koenderink, *Cooperative interactions between nano-antennas in a high-Q cavity for unidirectional light sources,* Light Sci. Appl. 8, 115 (2019).

[244] F. Ruesink, H. M. Doeleman, R. Hendrikx, A. F. Koenderink, and E. Verhagen, *Perturbing open cavities: Anomalous resonance frequency shifts in a hybrid cavity-nanoantenna system,* Phys. Rev. Lett. 115, 203904 (2015).

[245] Y.-F. Xiao, Y.-C. Liu, B.-B. Li, Y.-L. Chen, Y. Li, and Q. Gong, *Strongly enhanced light-matter interaction in a hybrid photonic-plasmonic resonator,* Phys. Rev. A 85, 031805 (2012).

[246] H. M. Doeleman, C. D. Dieleman, C. Mennes, B. Ehrler, and A. F. Koenderink, *Observation of cooperative purcell enhancements in antenna–cavity hybrids,* ACS Nano 14, 12027 (2020).

[247] X. Fan, W. Zheng, and D. J. Singh, *Light scattering and surface plasmons on small spherical particles,* Light Sci. Appl. 3, e179 (2014).

[248] D. Tzarouchis and A. Sihvola, *Light scattering by a dielectric sphere: Perspectives on the Mie resonances,* Appl. Sci. 8, 184 (2018).

[249] K. Kolwas, A. Derkachova, and M. Shopa, *Size characteristics of surface plasmons and their manifestation in scattering properties of metal particles,* J. Quant. Spectrosc. Radiat. Transf. 110, 1490 (2009).

[250] H. M. Doeleman, *Hybrid resonators for light trapping and emission control*, PhD thesis, University of Amsterdam (2019).

[251] Y. Hong and B. M. Reinhard, *Optoplasmonics: basic principles and applications,* J. Opt. 21, 113001 (2019).

[252] M. R. Foreman and F. Vollmer, *Theory of resonance shifts of whispering gallery modes by arbitrary plasmonic nanoparticles,* New J. Phys. 15, 083006 (2013).

[253] S. I. Shopova, R. Rajmangal, S. Holler, and S. Arnold, *Plasmonic enhancement of a whispering-gallery-mode biosensor for single nanoparticle detection,* Appl. Phys. Lett. 98, 243104 (2011).

[254] F. Vollmer, D. Braun, A. Libchaber, M. Khoshsima, I. Teraoka, and S. Arnold, *Protein detection by optical shift of a resonant microcavity,* Appl. Phys. Lett. 80, 4057 (2002).

[255] H.-C. Ren, F. Vollmer, S. Arnold, and A. Libchaber, *High-Q microsphere biosensor – analysis for adsorption of rodlike bacteria,* Opt. Express 15, 17410 (2007).

[256] I. Teraoka and S. Arnold, *Theory of resonance shifts in TE and TM whispering gallery modes by nonradial perturbations for sensing applications,* J. Opt. Soc. Am. B 23, 1381 (2006).

[257] P. Zijlstra, M. Orrit, and A. F. Koenderink, Metal nanoparticles for microscopy and spectroscopy, in *Nanoparticles: Workhorses of Nanoscience*, edited by C. de Mello Donegá (Springer, Berlin, Heidelberg, 2014) Chap. 3, pp. 53–98.

[258] K. Manthiram and A. P. Alivisatos, *Tunable localized surface plasmon resonances in tungsten oxide nanocrystals,* J. Am. Chem. Soc. 134, 3995 (2012).

[259] D. P. Rai and R. K. Thapa, *A theoretical study of bulk tungsten (W) based on momentum transfer,* Adv. Opt. 2014, 814909 (2014).

[260] O. Klein, S. Donovan, M. Dressel, and G. Grüner, *Microwave cavity perturbation technique: Part I: Principles,* Int. J. Infrared Milli. Waves 14, 2423 (1993).

[261] R. A. Waldron, *Perturbation theory of resonant cavities,* Proc. IEE C 107, 272 (1960).

[262] L. Deych and J. Rubin, *Rayleigh scattering of whispering gallery modes of microspheres due to a single dipole scatterer,* Phys. Rev. A 80, 061805 (2009).

[263] J. T. Rubin and L. Deych, *Ab initio theory of defect scattering in spherical whispering-gallery-mode resonators,* Phys. Rev. A 81, 053827 (2010).

[264] L. Deych and V. Shuvayev, *Spectral modification of whispering-gallery-mode resonances in spheroidal resonators due to interaction with ultra-small particles,* Opt. Lett. 40, 4536 (2015).

[265] M. D. Baaske, M. R. Foreman, and F. Vollmer, *Single-molecule nucleic acid interactions monitored on a label-free microcavity biosensor platform,* Nat. Nanotechnol. 9, 933 (2014).

[266] K. Srinivasan and O. Painter, *Mode coupling and cavity–quantum-dot interactions in a fiber-coupled microdisk cavity,* Phys. Rev. A 75, 023814 (2007).

[267] A. Kaplan, M. Tomes, T. Carmon, M. Kozlov, O. Cohen, G. Bartal, and H. G. L. Schwefel, *Finite element simulation of a perturbed axial-symmetric whispering-gallery mode and its use for intensity enhancement with a nanoparticle coupled to a microtoroid,* Opt. Express 21, 14169 (2013).

[268] J. D. Jackson, *Classical Electrodynamics*, 2nd ed. (John Wiley & Sons, New York, 1975).

[269] D. E. Aspnes, *Local-field effects and effective-medium theory: A microscopic perspective,* Am. J. Phys. 50, 704 (1982).

[270] A. Aubret, M. Orrit, and F. Kulzer, *Understanding local-field correction factors in the framework of the Onsager–Böttcher model,* ChemPhysChem 20, 345 (2019).

[271] E. Zaremba and B. N. J. Persson, *Dynamic polarizability of small metal particles,* Phys. Rev. B 35, 596 (1987).

[272] Y. Xu, S.-J. Tang, X.-C. Yu, Y.-L. Chen, D. Yang, Q. Gong, and Y.-F. Xiao, *Mode splitting induced by an arbitrarily shaped Rayleigh scatterer in a whispering-gallery microcavity,* Phys. Rev. A 97, 063828 (2018).

[273] F. Ruesink, *Manipulating light with ring resonators coupled to antennas and mechanical motion,* PhD thesis, Technische Universiteit Eindhoven (2017).

[274] F. Ruesink, H. M. Doeleman, E. Verhagen, and A. F. Koenderink, *Controlling nanoantenna polarizability through backaction via a single cavity mode,* Phys. Rev. Lett. 120, 206101 (2018).

[275] W. S. M. Werner, K. Glantschnig, and C. Ambrosch-Draxl, *Optical constants and inelastic electron-scattering data for 17 elemental metals,* J. Phys. Chem. Ref. Data 38, 1013 (2009).

[276] Y. Qizheng, L. Jin, and Y. Haiyan, *A displaced dipole model for spheres in a non-uniform field,* J. Electrostat. 56, 1 (2002).

[277] A. Lakhtakia, *Macroscopic theory of the coupled dipole approximation method,* Opt. Commun. 79, 1 (1990).

[278] L. Novotny and B. Hecht, *Principles of Nano-Optics* (Cambridge University Press, Cambridge, 2006).

[279] G. Guendelman, Y. Lovsky, E. Yacoby, O. E. Mor, I. Kaplan-Ashiri, O. Goldbart, and B. Dayan, *Three-dimensional sensing of arbitrarily shaped nanoparticles by whispering gallery mode resonators,* Opt. Express 28, 31297 (2020).

[280] L. Deych and L. Yang, *Effects of the magnetodipole corrections on the spectra of spheroidal whispering gallery mode resonators interacting with a dielectric nanoparticle,* Opt. Lett. 45, 1435 (2020).

[281] V. Shuvayev and L. Deych, *Ab initio computational analysis of spectral properties of dielectric spheroidal resonators interacting with a subwavelength nanoparticle,* Phys. Rev. E 99, 013310 (2019).

[282] M. R. Foreman, F. Sedlmeir, H. G. L. Schwefel, and G. Leuchs, *Dielectric tuning and coupling of whispering gallery modes using an anisotropic prism,* J. Opt. Soc. Am. B 33, 2177 (2016).

[283] N. Le Thomas, U. Woggon, W. Langbein, and M. V. Artemyev, *Effect of a dielectric substrate on whispering-gallery-mode sensors,* J. Opt. Soc. Am. B 23, 2361 (2006).

[284] F. Azeem, L. S. Trainor, P. A. Devane, D. S. Norman, A. Rueda, N. J. Lambert, M. Kumari, M. R. Foreman, and H. G. L. Schwefel, *Dielectric perturbations: anomalous resonance frequency shifts in optical resonators,* Opt. Lett. 46, 2477 (2021).

[285] M. R. Foreman, D. Keng, E. Treasurer, J. R. Lopez, and S. Arnold, *Whispering gallery mode single nanoparticle detection and sizing: the validity of the dipole approximation,* Opt. Lett. 42, 963 (2017).

[286] L. Deych and V. Shuvayev, *Theory of nanoparticle-induced frequency shifts of whispering-gallery-mode resonances in spheroidal optical resonators,* Phys. Rev. A 92, 013842 (2015).

[287] C. F. Bohren and D. R. Huffman, Particles small compared with the wavelength, in *Absorption and Scattering of Light by Small Particles* (John Wiley & Sons, Weinheim, 1998) Chap. 5.

[288] A. Mazzei, *Cavity enhanced optical processes in microsphere resonators*, PhD thesis, Humboldt-Universität zu Berlin (2008).

[289] L. Novotny, The history of near-field optics, in *Progress in Optics*, Vol. 50, edited by E. Wolf (Elsevier, 2007) Chap. 5, pp. 137–184.

[290] C. Schmidt, M. Liebsch, A. Klein, N. Janunts, A. Chipouline, T. Käsebier, C. Etrich, F. Lederer, E.-B. Kley, A. Tünnermann, and T. Pertsch, *Near-field mapping of optical eigenstates in coupled disk microresonators*, Phys. Rev. A 85, 033827 (2012).

[291] S. Blaize, F. Gesuele, I. Stefanon, A. Bruyant, G. Lérondel, P. Royer, B. Martin, A. Morand, P. Benech, and J.-M. Fedeli, *Real-space observation of spectral degeneracy breaking in a waveguide-coupled disk microresonator*, Opt. Lett. 35, 3168 (2010).

[292] J. Stone, *Interactions of hydrogen and deuterium with silica optical fibers: A review*, J. Light. Technol. 5, 712 (1987).

[293] J. D. Downie, M.-J. Li, and S. Makovejs, Single-mode fibers for high speed and long-haul transmission, in *Handbook of Optical Fibers*, edited by G.-D. Peng (Springer, Singapore, 2019) pp. 3–39.

[294] I. Hughes and T. Hase, *Measurements and Their Uncertainties* (Oxford University Press, Oxford, 2010).

[295] Y. Dumeige, S. Trebaol, L. Ghisa, T. K. N. Nguyên, H. Tavernier, and P. Féron, *Determination of coupling regime of high-Q resonators and optical gain of highly selective amplifiers*, J. Opt. Soc. Am. B 25, 2073 (2008).

[296] A.-I. Botean, *Thermal expansion coefficient determination of polylactic acid using digital image correlation*, E3S Web Conf. 32, 01007 (2018).

[297] C. Hagart-Alexander, in *Instrumentation Reference Book*, edited by W. Boyes (Butterworth-Heinemann, Boston, 2010) 4th ed., pp. 269–326.

[298] J. Kepler, *De cometis Libelli tres* (Augustæ Vindelicorum, Augsburg, 1619).

[299] S. Gröblacher, *Quantum Opto-Mechanics with Micromirrors*, 1st ed., Springer Theses (Springer, Berlin, Heidelberg, 2012).

[300] B. Fu, E. Sperber, and F. Eke, *Solar sail technology — A state of the art review*, Prog. Aerosp. Sci. 86, 1 (2016).

[301] J. C. Maxwell, *A Treatise on Electricity and Magnetism*, Cambridge Library Collection - Physical Sciences, Vol. 2 (Cambridge University Press, Cambridge, 2010).

[302] P. Lebedew, *Untersuchungen über die Druckkräfte des Lichtes*, Ann. Phys. 311, 433 (1901).

[303] E. F. Nichols and G. F. Hull, *The pressure due to radiation*, Proc. Am. Acad. Arts Sci. 38, 559 (1903).

[304] B. G. Levi, *Work on atom trapping and cooling gets a warm reception in Stockholm*, Phys. Today 50, 17 (1997).

[305] C. N. Cohen-Tannoudji and W. D. Phillips, *New mechanisms for laser cooling*, Phys. Today 43, 33 (1990).

[306] D. J. Wineland and W. M. Itano, *Laser cooling*, Phys. Today 40, 34 (1987).

[307] V. B. Braginsky and A. B. Manukin, *Ponderomotive effects of electromagnetic radiation*, Sov. Phys. JETP Engl. Transl. 25, 653 (1967).

[308] J. Aasi, J. Abadie, B. P. Abbott, R. Abbott, T. D. Abbott, M. R. Abernathy, C. Adams, T. Adams, P. Addesso, *et al.* (LIGO Scientific Collaboration and Virgo Collaboration), *Enhanced sensitivity of the ligo gravitational wave detector by using squeezed states of light*, Nat. Photonics 7, 613 (2013).

[309] A. Buikema, C. Cahillane, G. L. Mansell, C. D. Blair, R. Abbott, C. Adams, R. X. Adhikari, A. Ananyeva, S. Appert, *et al.*, *Sensitivity and performance of the Advanced LIGO detectors in the third observing run*, Phys. Rev. D 102, 062003 (2020).

[310] M. Aspelmeyer, P. Meystre, and K. Schwab, *Quantum optomechanics*, Phys. Today 65, 29 (2012).

[311] L. Brillouin, *Diffusion de la lumière et des rayons X par un corps transparent homogène – Influence de l'agitation thermique*, Ann. Phys. 9, 88 (1922).

[312] J. Zehnpfennig, G. Bahl, M. Tomes, and T. Carmon, *Surface optomechanics: calculating optically excited acoustical whispering gallery modes in microspheres*, Opt. Express 19, 14240 (2011).

[313] S. Diallo, J.-P. Aubry, and Y. K. Chembo, *Effect of crystalline family and orientation on stimulated Brillouin scattering in whispering-gallery mode resonators*, Opt. Express 25, 29934 (2017).

[314] G. Lin, S. Diallo, K. Saleh, R. Martinenghi, J.-C. Beugnot, T. Sylvestre, and Y. K. Chembo, *Cascaded brillouin lasing in monolithic barium fluoride whispering gallery mode resonators*, Appl. Phys. Lett. 105, 231103 (2014).

[315] G. Bahl, M. Tomes, F. Marquardt, and T. Carmon, *Observation of spontaneous Brillouin cooling*, Nat. Phys. 8, 203 (2012).

[316] J. Yin *et al.*, *Satellite-based entanglement distribution over 1200 kilometers,* Science 356, 1140 (2017).

[317] A. Lele, *Quantum Technologies and Military Strategy*, Advanced Sciences and Technologies for Security Applications (Springer, Cham, 2021).

[318] P. Knight and I. Walmsley, *UK national quantum technology programme,* Quantum Sci. Techn. 4, 040502 (2019).

[319] J. P. Dowling and G. J. Milburn, *Quantum technology: the second quantum revolution,* Phil. Trans. R. Soc. A 361, 1655 (2003).

[320] E. Polino, M. Valeri, N. Spagnolo, and F. Sciarrino, *Photonic quantum metrology,* AVS Quantum Sci. 2, 024703 (2020).

[321] V. Giovannetti, S. Lloyd, and L. Maccone, *Advances in quantum metrology,* Nat. Photonics 5, 222 (2011).

[322] C. L. Degen, F. Reinhard, and P. Cappellaro, *Quantum sensing,* Rev. Mod. Phys. 89, 035002 (2017).

[323] G. Vittorio, L. Seth, and M. Lorenzo, *Quantum-enhanced measurements: Beating the standard quantum limit,* Science 306, 1330 (2004).

[324] N. Gisin and R. Thew, *Quantum communication,* Nat. Photonics 1, 165 (2007).

[325] I. M. Georgescu, S. Ashhab, and F. Nori, *Quantum simulation,* Rev. Mod. Phys. 86, 153 (2014).

[326] T. H. Johnson, S. R. Clark, and D. Jaksch, *What is a quantum simulator?* EPJ Quantum Technol. 1, 10 (2014).

[327] M. A. Nielsen and I. L. Chuang, *Quantum Computation and Quantum Information*, 2nd ed. (Cambridge University Press, Cambridge, 2010).

[328] R. P. Feynman, *Simulating physics with computers,* Int. J. Theor. Phys. 21, 467 (1982).

[329] Editorial Team, *40 years of quantum computing,* Nat. Rev. Phys. 4, 1 (2022).

[330] M. Mohseni, P. Read, H. Neven, S. Boixo, V. Denchev, R. Babbush, A. Fowler, V. Smelyanskiy, and J. Martinis, *Commercialize quantum technologies in five years,* Nature 543, 171 (2017).

[331] E. T. Campbell, B. M. Terhal, and C. Vuillot, *Roads towards fault-tolerant universal quantum computation,* Nature 549, 172 (2017).

[332] D. P. DiVincenzo, *The physical implementation of quantum computation,* Fortschr. Phys. 48, 771 (2000).

[333] D. Gottesman and I. L. Chuang, *Demonstrating the viability of universal quantum computation using teleportation and single-qubit operations,* Nature 402, 390 (1999).

[334] P. Shor, *Algorithms for quantum computation: discrete logarithms and factoring,* in *Proceedings 35th Annual Symposium on Foundations of Computer Science*, edited by S. Goldwasser (1994) pp. 124–134.

[335] L. K. Grover, *A fast quantum mechanical algorithm for database search,* in *Proceedings of the Twenty-Eighth Annual ACM Symposium on Theory of Computing* (Association for Computing Machinery, New York, 1996) pp. 212–219.

[336] B. Rogers, N. L. Gullo, G. D. Chiara, G. M. Palma, and M. Paternostro, *Hybrid optomechanics for quantum technologies,* Quantum Measur. Quantum Meteorol. 2, 11 (2014).

[337] A. A. Clerk, K. W. Lehnert, P. Bertet, J. R. Petta, and Y. Nakamura, *Hybrid quantum systems with circuit quantum electrodynamics,* Nat. Phys. 16, 257 (2020).

[338] A. Laucht, F. Hohls, N. Ubbelohde, M. F. Gonzalez-Zalba, D. J. Reilly, S. Stobbe, T. Schröder, *et al.*, *Roadmap on quantum nanotechnologies,* Nanotechnology 32, 162003 (2021).

[339] L. M. Duan, M. D. Lukin, J. I. Cirac, and P. Zoller, *Long-distance quantum communication with atomic ensembles and linear optics,* Nature 414, 413 (2001).

[340] D. E. Chang, V. Vuletić, and M. D. Lukin, *Quantum nonlinear optics – photon by photon,* Nat. Photonics 8, 685 (2014).

[341] M. Mirhosseini, A. Sipahigil, M. Kalaee, and O. Painter, *Superconducting qubit to optical photon transduction,* Nature 588, 599 (2020).

[342] N. Fiaschi, B. Hensen, A. Wallucks, R. Benevides, J. Li, T. P. M. Alegre, and S. Gröblacher, *Optomechanical quantum teleportation,* Nat. Photonics 15, 817 (2021).

[343] B. M. Brubaker, J. M. Kindem, M. D. Urmey, S. Mittal, R. D. Delaney, P. S. Burns, M. R. Vissers, K. W. Lehnert, and C. A. Regal, *Optomechanical ground-state cooling in a continuous and efficient electro-optic transducer,* arxiv, 2112.13429 (2021).

[344] M. Forsch, R. Stockill, A. Wallucks, I. Marinković, C. Gärtner, R. A. Norte, F. van Otten, A. Fiore, K. Srinivasan, and S. Gröblacher, *Microwave-to-optics conversion using a mechanical oscillator in its quantum ground state,* Nat. Phys. 16, 69 (2020).

[345] N. J. Lambert, A. Rueda, F. Sedlmeir, and H. G. L. Schwefel, *Coherent conversion between microwave and optical photons — an overview of physical implementations,* Adv. Quantum Technol. 3, 1900077 (2020).

[346] A. P. Higginbotham, P. S. Burns, M. D. Urmey, R. W. Peterson, N. S. Kampel, B. M. Brubaker, G. Smith, K. W. Lehnert, and C. A. Regal, *Harnessing electro-optic correlations in an efficient mechanical converter,* Nat. Phys. 14, 1038 (2018).

[347] R. W. Andrews, R. W. Peterson, T. P. Purdy, K. Cicak, R. W. Simmonds, C. A. Regal, and K. W. Lehnert, *Bidirectional and efficient conversion between microwave and optical light,* Nat. Phys. 10, 321 (2014).

[348] S. A. McGee, D. Meiser, C. A. Regal, K. W. Lehnert, and M. J. Holland, *Mechanical resonators for storage and transfer of electrical and optical quantum states,* Phys. Rev. A 87, 053818 (2013).

[349] A. H. Safavi-Naeini and O. Painter, *Proposal for an optomechanical traveling wave phonon–photon translator,* New J. Phys. 13, 013017 (2011).

[350] K. Stannigel, P. Rabl, A. S. Sørensen, P. Zoller, and M. D. Lukin, *Optomechanical transducers for long-distance quantum communication,* Phys. Rev. Lett. 105, 220501 (2010).

[351] A. P. Reed, K. H. Mayer, J. D. Teufel, L. D. Burkhart, W. Pfaff, M. Reagor, L. Sletten, X. Ma, *et al.*, *Faithful conversion of propagating quantum information to mechanical motion,* Nat. Phys. 13, 1163 (2017).

[352] K. Stannigel, P. Komar, S. J. M. Habraken, S. D. Bennett, M. D. Lukin, P. Zoller, and P. Rabl, *Optomechanical quantum information processing with photons and phonons,* Phys. Rev. Lett. 109, 013603 (2012).

[353] W. K. Wootters and W. H. Zurek, *A single quantum cannot be cloned,* Nature 299, 802 (1982).

[354] P. K. Shandilya, D. P. Lake, M. J. Mitchell, D. D. Sukachev, and P. E. Barclay, *Optomechanical interface between telecom photons and spin quantum memory,* Nat. Phys. 17, 1420 (2021).

[355] A. Wallucks, I. Marinković, B. Hensen, R. Stockill, and S. Gröblacher, *A quantum memory at telecom wavelengths,* Nat. Phys. 16, 772 (2020).

[356] C. Galland, N. Sangouard, N. Piro, N. Gisin, and T. J. Kippenberg, *Heralded single-phonon preparation, storage, and readout in cavity optomechanics,* Phys. Rev. Lett. 112, 143602 (2014).

[357] R. Horodecki, P. Horodecki, M. Horodecki, and K. Horodecki, *Quantum entanglement,* Rev. Mod. Phys. 81, 865 (2009).

[358] K. Heshami, D. G. England, P. C. Humphreys, P. J. Bustard, V. M. Acosta, J. Nunn, and B. J. Sussman, *Quantum memories: emerging applications and recent advances,* J. Mod. Opt. 63, 2005 (2016).

[359] N. Sangouard, C. Simon, H. de Riedmatten, and N. Gisin, *Quantum repeaters based on atomic ensembles and linear optics,* Rev. Mod. Phys. 83, 33 (2011).

[360] A. Schliesser, G. Anetsberger, R. Rivière, O. Arcizet, and T. J. Kippenberg, *High-sensitivity monitoring of micromechanical vibration using optical whispering gallery mode resonators,* New J. Phys. 10, 095015 (2008).

[361] Y. Michimura and K. Komori, *Quantum sensing with milligram scale optomechanical systems,* Eur. Phys. J. D 74, 126 (2020).

[362] D. Mason, J. Chen, M. Rossi, Y. Tsaturyan, and A. Schliesser, *Continuous force and displacement measurement below the standard quantum limit,* Nat. Phys. 15, 745 (2019).

[363] P. H. Kim, B. D. Hauer, C. Doolin, F. Souris, and J. P. Davis, *Approaching the standard quantum limit of mechanical torque sensing,* Nat. Commun. 7, 13165 (2016).

[364] F. Monteiro, S. Ghosh, A. G. Fine, and D. C. Moore, *Optical levitation of 10-ng spheres with nano-g acceleration sensitivity,* Phys. Rev. A 96, 63841 (2017).

[365] W. Yu, W. C. Jiang, Q. Lin, and T. Lu, *Cavity optomechanical spring sensing of single molecules,* Nat. Commun. 7, 12311 (2016).

[366] D. Navarro-Urrios, E. Kang, P. Xiao, M. F. Colombano, G. Arregui, B. Graczykowski, N. E. Capuj, M. Sledzinska, C. M. Sotomayor-Torres, and G. Fytas, *Optomechanical crystals for spatial sensing of submicron sized particles,* Sci. Rep. 11, 7829 (2021).

[367] A. H. Safavi-Naeini, S. Gröblacher, J. T. Hill, J. Chan, M. Aspelmeyer, and O. Painter, *Squeezed light from a silicon micromechanical resonator,* Nature 500, 185 (2013).

[368] T. P. Purdy, P.-L. Yu, R. W. Peterson, N. S. Kampel, and C. A. Regal, *Strong optomechanical squeezing of light,* Phys. Rev. X 3, 031012 (2013).

[369] J. Zhang, B. Peng, S. Kim, F. Monifi, X. Jiang, Y. Li, P. Yu, L. Liu, Y.-x. Liu, A. Alù, and L. Yang, *Optomechanical dissipative solitons,* Nature 600, 75 (2021).

[370] J. J. Viennot, X. Ma, and K. W. Lehnert, *Phonon-number-sensitive electromechanics,* Phys. Rev. Lett. 121, 183601 (2018).

[371] I. Galinskiy, Y. Tsaturyan, M. Parniak, and E. S. Polzik, *Phonon counting thermometry of an ultracoherent membrane resonator near its motional ground state,* Optica 7, 718 (2020).

[372] J. D. Cohen, S. M. Meenehan, G. S. MacCabe, S. Gröblacher, A. H. Safavi-Naeini, F. Marsili, M. D. Shaw, and O. Painter, *Phonon counting and intensity interferometry of a nanomechanical resonator,* Nature 520, 522 (2015).

[373] V. B. Braginsky and F. Ya Khalili, *Quantum measurements* (Cambridge University Press, Cambridge, 1992).

[374] S. Bose, K. Jacobs, and P. L. Knight, *Preparation of nonclassical states in cavities with a moving mirror,* Phys. Rev. A 56, 4175 (1997).

[375] S. Mancini, V. I. Man'ko, and P. Tombesi, *Ponderomotive control of quantum macroscopic coherence,* Phys. Rev. A 55, 3042 (1997).

[376] W. Marshall, C. Simon, R. Penrose, and D. Bouwmeester, *Towards quantum superpositions of a mirror,* Phys. Rev. Lett. 91, 130401 (2003).

[377] S. Mancini, V. Giovannetti, D. Vitali, and P. Tombesi, *Entangling macroscopic oscillators exploiting radiation pressure,* Phys. Rev. Lett. 88, 120401 (2002).

[378] A. S. Parkins and H. J. Kimble, *Quantum state transfer between motion and light,* J. Opt. B: Quantum Semiclass. Opt. 1, 496 (1999).

[379] J. Zhang, K. Peng, and S. L. Braunstein, *Quantum-state transfer from light to macroscopic oscillators,* Phys. Rev. A 68, 013808 (2003).

[380] S. Mancini, D. Vitali, and P. Tombesi, *Scheme for teleportation of quantum states onto a mechanical resonator,* Phys. Rev. Lett. 90, 137901 (2003).

[381] C. Genes, A. Mari, D. Vitali, and P. Tombesi, in *Advances in Atomic Molecular and Optical Physics*, Advances In Atomic, Molecular, and Optical Physics, Vol. 57, edited by P. R. B. E. Arimondo and C. C. Lin (Academic Press, 2009) Chap. 2, pp. 33–86.

[382] S. Gröblacher, K. Hammerer, M. R. Vanner, and M. Aspelmeyer, *Observation of strong coupling between a micromechanical resonator and an optical cavity field,* Nature 460, 724 (2009).

[383] J. D. Teufel, D. Li, M. S. Allman, K. Cicak, A. J. Sirois, J. D. Whittaker, and R. W. Simmonds, *Circuit cavity electromechanics in the strong-coupling regime,* Nature 471, 204 (2011).

[384] A. D. O'Connell, M. Hofheinz, M. Ansmann, R. C. Bialczak, M. Lenander, E. Lucero, M. Neeley, D. Sank, H. Wang, M. Weides, J. Wenner, J. M. Martinis, and A. N. Cleland, *Quantum ground state and single-phonon control of a mechanical resonator,* Nature 464, 697 (2010).

[385] J. Chan, T. P. M. Alegre, A. H. Safavi-Naeini, J. T. Hill, A. Krause, S. Gröblacher, M. Aspelmeyer, and O. Painter, *Laser cooling of a nanomechanical oscillator into its quantum ground state,* Nature 478, 89 (2011).

[386] L. Qiu, I. Shomroni, P. Seidler, and T. J. Kippenberg, *Laser cooling of a nanomechanical oscillator to its zero-point energy,* Phys. Rev. Lett. 124, 173601 (2020).

[387] J. D. Teufel, T. Donner, D. Li, J. W. Harlow, M. S. Allman, K. Cicak, A. J. Sirois, J. D. Whittaker, K. W. Lehnert, and R. W. Simmonds, *Sideband cooling of micromechanical motion to the quantum ground state,* Nature 475, 359 (2011).

[388] T. A. Palomaki, J. D. Teufel, R. W. Simmonds, and K. W. Lehnert, *Entangling mechanical motion with microwave fields,* Science 342, 710 (2013).

[389] R. Riedinger, S. Hong, R. A. Norte, J. A. Slater, J. Shang, A. G. Krause, V. Anant, M. Aspelmeyer, and S. Gröblacher, *Non-classical correlations between single photons and phonons from a mechanical oscillator,* Nature 530, 313 (2016).

[390] R. Riedinger, A. Wallucks, I. Marinković, C. Löschnauer, M. Aspelmeyer, S. Hong, and S. Gröblacher, *Remote quantum entanglement between two micromechanical oscillators,* Nature 556, 473 (2018).

[391] C. F. Ockeloen-Korppi, E. Damskägg, J. M. Pirrkalainen, M. Asjad, A. A. Clerk, F. Massel, M. J. Woolley, and M. A. Sillanpää, *Stabilized entanglement of massive mechanical oscillators,* Nature 556, 478 (2018).

[392] J. Chen, M. Rossi, D. Mason, and A. Schliesser, *Entanglement of propagating optical modes via a mechanical interface,* Nat. Commun. 11, 943 (2020).

[393] S. Barzanjeh, E. S. Redchenko, M. Peruzzo, M. Wulf, D. P. Lewis, G. Arnold, and J. M. Fink, *Stationary entangled radiation from micromechanical motion,* Nature 570, 480 (2019).

[394] E. E. Wollman, C. U. Lei, A. J. Weinstein, J. Suh, A. Kronwald, F. Marquardt, A. A. Clerk, and K. C. Schwab, *Quantum squeezing of motion in a mechanical resonator,* Science 349, 952 (2015).

[395] S. Hong, R. Riedinger, I. Marinković, A. Wallucks, S. G. Hofer, R. A. Norte, M. Aspelmeyer, and S. Gröblacher, *Hanbury Brown and Twiss interferometry of single phonons from an optomechanical resonator,* Science 358, 203 (2017).

[396] Y. Chu, P. Kharel, T. Yoon, L. Frunzio, P. T. Rakich, and R. J. Schoelkopf, *Creation and control of multi-phonon Fock states in a bulk acoustic-wave resonator,* Nature 563, 666 (2018).

[397] C. Whittle, E. D. Hall, S. Dwyer, N. Mavalvala, V. Sudhir, R. Abbott, A. Ananyeva, C. Austin, L. Barsotti, *et al.,* *Approaching the motional ground state of a 10-kg object,* Science 372, 1333 (2021).

[398] O. Romero-Isart, A. C. Pflanzer, F. Blaser, R. Kaltenbaek, N. Kiesel, M. Aspelmeyer, and J. I. Cirac, *Large quantum superpositions and interference of massive nanometer-sized objects,* Phys. Rev. Lett. 107, 020405 (2011).

[399] E. Barausse, E. Berti, T. Hertog, S. A. Hughes, P. Jetzer, P. Pani, T. P. Sotiriou, N. Tamanini, H. Witek, K. Yagi, N. Yunes, *et al.,* *Prospects for fundamental physics with LISA,* Gen. Relativ. Gravit. 52, 81 (2020).

[400] M. Bonaldi, A. Borrielli, A. Chowdhury, G. Di Giuseppe, W. Li, N. Malossi, F. Marino, B. Morana, *et al.,* *Probing quantum gravity effects with quantum mechanical oscillators,* Eur. Phys. J. D 74, 178 (2020).

[401] I. Pikovski, M. R. Vanner, M. Aspelmeyer, M. S. Kim, and Č. Brukner, *Probing Planck-scale physics with quantum optics,* Nat. Phys. 8, 393 (2012).

[402] A. Bassi, K. Lochan, S. Satin, T. P. Singh, and H. Ulbricht, *Models of wave-function collapse, underlying theories, and experimental tests,* Rev. Mod. Phys. 85, 471 (2013).

[403] L. Diósi, *Testing spontaneous wave-function collapse models on classical mechanical oscillators,* Phys. Rev. Lett. 114, 050403 (2015).

[404] D. Carney, A. Hook, Z. Liu, J. M. Taylor, and Y. Zhao, *Ultralight dark matter detection with mechanical quantum sensors,* New J. Phys. 23, 023041 (2021).

[405] M. Rossi, D. Mason, J. Chen, Y. Tsaturyan, and A. Schliesser, *Measurement-based quantum control of mechanical motion,* Nature 563, 53 (2018).

[406] M. Rossi, D. Mason, J. Chen, and A. Schliesser, *Observing and verifying the quantum trajectory of a mechanical resonator,* Phys. Rev. Lett. 123, 163601 (2019).

[407] M. Brunelli, D. Malz, A. Schliesser, and A. Nunnenkamp, *Stroboscopic quantum optomechanics,* Phys. Rev. Research 2, 023241 (2020).

[408] V. Sudhir, D. J. Wilson, R. Schilling, H. Schütz, S. A. Fedorov, A. H. Ghadimi, A. Nunnenkamp, and T. J. Kippenberg, *Appearance and disappearance of quantum correlations in measurement-based feedback control of a mechanical oscillator,* Phys. Rev. X 7, 011001 (2017).

[409] M. R. Vanner, I. Pikovski, G. D. Cole, M. S. Kim, Č. Brukner, K. Hammerer, G. J. Milburn, and M. Aspelmeyer, *Pulsed quantum optomechanics,* Proc. Natl. Acad. Sci. 108, 16182 (2011).

[410] K. Børkje, A. Nunnenkamp, and S. M. Girvin, *Proposal for entangling remote micromechanical oscillators via optical measurements,* Phys. Rev. Lett. 107, 123601 (2011).

[411] V. Bergholm, W. Wieczorek, T. Schulte-Herbrüggen, and M. Keyl, *Optimal control of hybrid optomechanical systems for generating non-classical states of mechanical motion,* Quantum Sci. Techn. 4, 034001 (2019).

[412] P. Neveu, J. Clarke, M. R. Vanner, and E. Verhagen, *Preparation and verification of two-mode mechanical entanglement through pulsed optomechanical measurements,* New J. Phys. 23, 023026 (2021).

[413] I. Shomroni, L. Qiu, and T. J. Kippenberg, *Optomechanical generation of a mechanical catlike state by phonon subtraction,* Phys. Rev. A 101, 33812 (2020).

[414] J. Clarke, P. Sahium, K. E. Khosla, I. Pikovski, M. S. Kim, and M. R. Vanner, *Generating mechanical and optomechanical entanglement via pulsed interaction and measurement,* New J. Phys. 22, 063001 (2020).

[415] J. Clarke and M. R. Vanner, *Growing macroscopic superposition states via cavity quantum optomechanics,* Quantum Sci. Techn. 4, 014003 (2019).

[416] T. J. Milburn, M. S. Kim, and M. R. Vanner, *Nonclassical-state generation in macroscopic systems via hybrid discrete-continuous quantum measurements,* Phys. Rev. A 93, 053818 (2016).

[417] L. A. Kanari-Naish, J. Clarke, S. Qvarfort, and M. Vanner, *Two-mode Schrödinger-cat states with non-linear optomechanics: generation and verification of non-gaussian mechanical entanglement,* Quantum Sci. Techn. 7, 035012 (2022).

[418] M. R. Vanner, I. Pikovski, and M. S. Kim, *Towards optomechanical quantum state reconstruction of mechanical motion,* Ann. Phys. 527, 15 (2015).

[419] D. Leibfried, D. M. Meekhof, B. E. King, C. Monroe, W. M. Itano, and D. J. Wineland, *Experimental determination of the motional quantum state of a trapped atom,* Phys. Rev. Lett. 77, 4281 (1996).

[420] J. F. Goodwin, G. Stutter, R. C. Thompson, and D. M. Segal, *Resolved-sideband laser cooling in a Penning trap,* Phys. Rev. Lett. 116, 143002 (2016).

[421] J. T. Muhonen, G. R. La Gala, R. Leijssen, and E. Verhagen, *State preparation and tomography of a nanomechanical resonator with fast light pulses,* Phys. Rev. Lett. 123, 113601 (2019).

[422] R. N. Patel, T. P. McKenna, Z. Wang, J. D. Witmer, W. Jiang, R. Van Laer, C. J. Sarabalis, and A. H. Safavi-Naeini, *Room-temperature mechanical resonator with a single added or subtracted phonon,* Phys. Rev. Lett. 127, 133602 (2021).

[423] T. Corbitt, C. Wipf, T. Bodiya, D. Ottaway, D. Sigg, N. Smith, S. Whitcomb, and N. Mavalvala, *Optical dilution and feedback cooling of a gram-scale oscillator to 6.9 mK,* Phys. Rev. Lett. 99, 160801 (2007).

[424] C. H. Metzger and K. Karrai, *Cavity cooling of a microlever,* Nature 432, 1002 (2004).

[425] A. H. Safavi-Naeini and O. Painter, Optomechanical crystal devices, in *Cavity Optomechanics: Nano- and Micromechanical Resonators Interacting with Light*, Quantum Science and Technology, edited by M. Aspelmeyer, T. J. Kippenberg, and F. Marquardt (Springer, Berlin; Heidelberg, 2014) Chap. 10, pp. 195–231.

[426] M. Eichenfield, J. Chan, R. M. Camacho, K. J. Vahala, and O. Painter, *Optomechanical crystals,* Nature 462, 78 (2009).

[427] M. Eichenfield, R. Camacho, J. Chan, K. J. Vahala, and O. Painter, *A picogram- and nanometre-scale photonic-crystal optomechanical cavity,* Nature 459, 550 (2009).

[428] R. Leijssen and E. Verhagen, *Strong optomechanical interactions in a sliced photonic crystal nanobeam,* Sci. Rep. 5, 15974 (2015).

[429] R. Burgwal and E. Verhagen, *Coupled nano-optomechanical cavities for enhancing nonlinear optomechanics,* in *Frontiers in Optics / Laser Science* (Optica, 2021) p. FTh4E.1.

[430] I. Favero, J. Sankey, and E. M. Weig, Mechanical resonators in the middle of an optical cavity, in *Cavity Optomechanics: Nano- and Micromechanical Resonators Interacting with Light*, Quantum Science and Technology, edited by M. Aspelmeyer, T. J. Kippenberg, and F. Marquardt (Springer, Berlin; Heidelberg, 2014) Chap. 5, pp. 83–119.

[431] J. D. Thompson, B. M. Zwickl, A. M. Jayich, F. Marquardt, S. M. Girvin, and J. G. Harris, *Strong dispersive coupling of a high-finesse cavity to a micromechanical membrane,* Nature 452, 72 (2008).

[432] N. P. Bullier, A. Pontin, and P. F. Barker, *Quadratic optomechanical cooling of a cavity-levitated nanosphere,* Phys. Rev. Res. 3, L032022 (2021).

[433] J. Millen, T. S. Monteiro, R. Pettit, and A. N. Vamivakas, *Optomechanics with levitated particles,* Rep. Prog. Phys. 83, 026401 (2020).

[434] D. W. C. Brooks, T. Botter, S. Schreppler, T. P. Purdy, N. Brahms, and D. M. Stamper-Kurn, *Non-classical light generated by quantum-noise-driven cavity optomechanics,* Nature 488, 476 (2012).

[435] G. Bahl, X. Fan, and T. Carmon, *Acoustic whispering-gallery modes in optomechanical shells,* New J. Phys. 14, 115026 (2012).

[436] A. D. Kashkanova, A. B. Shkarin, C. D. Brown, N. E. Flowers-Jacobs, L. Childress, S. W. Hoch, L. Hohmann, K. Ott, J. Reichel, and J. G. E. Harris, *Superfluid Brillouin optomechanics,* Nat. Phys. 13, 74 (2017).

[437] X. He, G. I. Harris, C. G. Baker, A. Sawadsky, Y. L. Sfendla, Y. P. Sachkou, S. Forstner, and W. P. Bowen, *Strong optical coupling through superfluid Brillouin lasing,* Nat. Phys. 16, 417 (2020).

[438] S. Gröblacher, J. B. Hertzberg, M. R. Vanner, G. D. Cole, S. Gigan, K. C. Schwab, and M. Aspelmeyer, *Demonstration of an ultracold micro-optomechanical oscillator in a cryogenic cavity,* Nat. Phys. 5, 485 (2009).

[439] N. Kiesel, F. Blaser, U. Delić, D. Grass, R. Kaltenbaek, and M. Aspelmeyer, *Cavity cooling of an optically levitated submicron particle,* Proc. Natl. Acad. Sci. 110, 14180 (2013).

[440] R. Burgwal, J. del Pino, and E. Verhagen, *Comparing nonlinear optomechanical coupling in membrane-in-the-middle and single-cavity systems,* New J. Phys. 22, 113006 (2020).

[441] H. Kaviani, C. Healey, M. Wu, R. Ghobadi, A. Hryciw, and P. E. Barclay, *Nonlinear optomechanical paddle nanocavities,* Optica 2, 271 (2015).

[442] T. K. Paraïso, M. Kalaee, L. Zang, H. Pfeifer, F. Marquardt, and O. Painter, *Position-squared coupling in a tunable photonic crystal optomechanical cavity,* Phys. Rev. X 5, 041024 (2015).

[443] A. Beccari, D. A. Visani, S. A. Fedorov, M. J. Bereyhi, V. Boureau, N. J. Engelsen, and T. J. Kippenberg, *Strained crystalline nanomechanical resonators with quality factors above 10 billion,* Nat. Phys. 18, 436 (2022).

[444] M. J. Bereyhi, A. Arabmogheghi, A. Beccari, S. A. Fedorov, G. Huang, T. J. Kippenberg, and N. J. Engelsen, *Perimeter modes of nanomechanical resonators exhibit quality factors exceeding* 10^9 *at room temperature,* Phys. Rev. X 12, 021036 (2022).

[445] M. Schlosshauer, *Decoherence, the measurement problem, and interpretations of quantum mechanics,* Rev. Mod. Phys. 76, 1267 (2005).

[446] D. Cattiaux, I. Golokolenov, S. Kumar, M. Sillanpää, L. Mercier de Lépinay, R. R. Gazizulin, X. Zhou, A. D. Armour, O. Bourgeois, A. Fefferman, and E. Collin, *A macroscopic object passively cooled into its quantum ground state of motion beyond single-mode cooling,* Nat. Commun. 12, 6182 (2021).

[447] P. Kharel, Y. Chu, M. Power, W. H. Renninger, R. J. Schoelkopf, and P. T. Rakich, *Ultra-high-Q phononic resonators on-chip at cryogenic temperatures,* APL Photonics 3, 066101 (2018).

[448] R. Y. Chiao, C. H. Townes, and B. P. Stoicheff, *Stimulated Brillouin scattering and coherent generation of intense hypersonic waves,* Phys. Rev. Lett. 12, 592 (1964).

[449] M. Tomes, F. Marquardt, G. Bahl, and T. Carmon, *Quantum-mechanical theory of optomechanical Brillouin cooling,* Phys. Rev. A 84, 063806 (2011).

[450] J. J. Price, *Brillouin cavity optomechanics: Single-quantum-level operations towards quantum memory applications*, PhD thesis, Imperial College London (2022).

[451] B. Sturman and I. Breunig, *Acoustic whispering gallery modes within the theory of elasticity,* J. Appl. Phys. 118, 013102 (2015).

[452] J. W. Jaeken and S. Cottenier, *Solving the Christoffel equation: Phase and group velocities,* Comput. Phys. Commun. 207, 445 (2016).

[453] Y. P. Varshni, *Temperature dependence of the elastic constants,* Phys. Rev. B 2, 3952 (1970).

[454] A. Jain, S. P. Ong, G. Hautier, W. Chen, W. D. Richards, S. Dacek, S. Cholia, D. Gunter, *et al.*, *The Materials Project: A materials genome approach to accelerating materials innovation,* APL Mater. 1, 011002 (2013).

[455] M. de Jong, W. Chen, T. Angsten, A. Jain, R. Notestine, A. Gamst, M. Sluiter, *et al.*, *Charting the complete elastic properties of inorganic crystalline compounds,* Sci. Data 2, 150009 (2015).

[456] D. Gerlich, *Elastic constants of barium fluoride between 4.2 and 300K,* Phys. Rev. 135, A1331 (1964).

[457] C. W. Gardiner and P. Zoller, *Quantum Noise*, 2nd ed., Springer Series in Synergetics (Springer, Berlin; Heidelberg, 2000).

[458] A. Barchielli and B. Vacchini, *Quantum Langevin equations for optomechanical systems,* New J. Phys. 17, 083004 (2015).

[459] W. P. Bowen and G. J. Milburn, *Quantum Optomechanics*, 1st ed. (CRC Press, Boca Raton, FL, 2016).

[460] B. Yurke and D. Stoler, *Generating quantum mechanical superpositions of macroscopically distinguishable states via amplitude dispersion,* Phys. Rev. Lett. 57, 13 (1986).

[461] M. Dakna, T. Anhut, T. Opatrný, L. Knöll, and D.-G. Welsch, *Generating Schrödinger-cat-like states by means of conditional measurements on a beam splitter,* Phys. Rev. A 55, 3184 (1997).

[462] A. Ourjoumtsev, H. Jeong, R. Tualle-Brouri, and P. Grangier, *Generation of optical 'schrödinger cats' from photon number states,* Nature 448, 784 (2007).

[463] D. V. Sychev, A. E. Ulanov, A. A. Pushkina, M. W. Richards, I. A. Fedorov, and A. I. Lvovsky, *Enlargement of optical Schrödinger's cat states,* Nat. Photonics 11, 379 (2017).

[464] A. Ourjoumtsev, R. Tualle-Brouri, J. Laurat, and P. Grangier, *Generating optical Schrödinger kittens for quantum information processing,* Science 312, 83 (2006).

[465] J. S. Neergaard-Nielsen, B. M. Nielsen, C. Hettich, K. Mølmer, and E. S. Polzik, *Generation of a superposition of odd photon number states for quantum information networks,* Phys. Rev. Lett. 97, 83604 (2006).

[466] M. S. Kim, *Recent developments in photon-level operations on travelling light fields,* J. Phys. B: At. Mol. Opt. Phys. 41, 133001 (2008).

[467] D. M. Meekhof, C. Monroe, B. E. King, W. M. Itano, and D. J. Wineland, *Generation of nonclassical motional states of a trapped atom,* Phys. Rev. Lett. 76, 1796 (1996).

[468] C. Monroe, D. M. Meekhof, B. E. King, and D. J. Wineland, *A "Schrödinger cat" superposition state of an atom,* Science 272, 1131 (1996).

[469] D. Leibfried, E. Knill, S. Seidelin, J. Britton, R. B. Blakestad, J. Chiaverini, D. B. Hume, W. M. Itano, J. D. Jost, C. Langer, R. Ozeri, R. Reichle, and D. J. Wineland, *Creation of a six-atom 'Schrödinger cat' state,* Nature 438, 639 (2005).

[470] D. T. Smithey, M. Beck, M. G. Raymer, and A. Faridani, *Measurement of the Wigner distribution and the density matrix of a light mode using optical homodyne tomography: Application to squeezed states and the vacuum,* Phys. Rev. Lett. 70, 1244 (1993).

[471] G. Enzian,[*] L. Freisem,[*] J. J. Price,[*] A. Ø. Svela[*], J. Clarke, B. Shajilal, J. Janousek, B. C. Buchler, P. K. Lam, and M. R. Vanner, *Single- and multi-phonon subtraction to a mechanical thermal state via brillouin optomechanics,* in *Frontiers in Optics / Laser Science* (Optica, 2021) p. LM6E.1.

[472] A. Ø. Svela, tektronix-func-gen: Tektronix arbitrary function generator control, (2021), avaliable on Github, github.com/asvela/tektronix-func-gen .

[473] C. Flühmann, T. L. Nguyen, M. Marinelli, V. Negnevitsky, K. Mehta, and J. P. Home, *Encoding a qubit in a trapped-ion mechanical oscillator,* Nature 566, 513 (2019).

[474] A. I. Lvovsky, H. Hansen, T. Aichele, O. Benson, J. Mlynek, and S. Schiller, *Quantum state reconstruction of the single-photon fock state,* Phys. Rev. Lett. 87, 050402 (2001).

[475] T. Gerrits, S. Glancy, T. S. Clement, B. Calkins, A. E. Lita, A. J. Miller, A. L. Migdall, S. W. Nam, R. P. Mirin, and E. Knill, *Generation of optical coherent-state superpositions by number-resolved photon subtraction from the squeezed vacuum,* Phys. Rev. A 82, 31802 (2010).

[476] A. Zavatta, V. Parigi, and M. Bellini, *Experimental nonclassicality of single-photon-added thermal light states,* Phys. Rev. A 75, 52106 (2007).

[477] V. Parigi, A. Zavatta, M. Kim, and M. Bellini, *Probing quantum commutation rules by addition and subtraction of single photons to/from a light field,* Science 317, 1890 (2007).

[478] Y. I. Bogdanov, K. G. Katamadze, G. V. Avosopiants, L. V. Belinsky, N. A. Bogdanova, A. A. Kalinkin, and S. P. Kulik, *Multiphoton subtracted thermal states: Description, preparation, and reconstruction,* Phys. Rev. A 96, 63803 (2017).

[479] S. Deléglise, I. Dotsenko, C. Sayrin, J. Bernu, M. Brune, J.-M. Raimond, and S. Haroche, *Reconstruction of non-classical cavity field states with snapshots of their decoherence,* Nature 455, 510 (2008).

[480] R. McConnell, H. Zhang, J. Hu, S. Ćuk, and V. Vuletić, *Entanglement with negative Wigner function of almost 3,000 atoms heralded by one photon,* Nature 519, 439 (2015).

[481] M. Hofheinz, H. Wang, M. Ansmann, R. C. Bialczak, E. Lucero, M. Neeley, A. D. O'Connell, D. Sank, J. Wenner, J. M. Martinis, and A. N. Cleland, *Synthesizing arbitrary quantum states in a superconducting resonator,* Nature 459, 546 (2009).

[482] K. J. Satzinger, Y. P. Zhong, H.-S. Chang, G. A. Peairs, A. Bienfait, M.-H. Chou, A. Y. Cleland, C. R. Conner, É. Dumur, J. Grebel, *et al.*, *Quantum control of surface acoustic-wave phonons,* Nature 563, 661 (2018).

[483] K. C. Lee, B. J. Sussman, M. R. Sprague, P. Michelberger, K. F. Reim, J. Nunn, N. K. Langford, P. J. Bustard, D. Jaksch, and I. A. Walmsley, *Macroscopic non-classical states and terahertz quantum processing in room-temperature diamond,* Nat. Photonics 6, 41 (2012).

[484] K. A. G. Fisher, D. G. England, J.-P. W. MacLean, P. J. Bustard, K. Heshami, K. J. Resch, and B. J. Sussman, *Storage of polarization-entangled THz-bandwidth photons in a diamond quantum memory,* Phys. Rev. A 96, 12324 (2017).

[485] S. T. Velez, K. Seibold, N. Kipfer, M. D. Anderson, V. Sudhir, and C. Galland, *Preparation and decay of a single quantum of vibration at ambient conditions,* Phys. Rev. X 9, 41007 (2019).

[486] M. Ringbauer, T. J. Weinhold, L. A. Howard, A. G. White, and M. R. Vanner, *Generation of mechanical interference fringes by multi-photon counting,* New J. Phys. 20, 53042 (2018).

[487] M. R. Vanner, M. Aspelmeyer, and M. S. Kim, *Quantum state orthogonalization and a toolset for quantum optomechanical phonon control,* Phys. Rev. Lett. 110, 010504 (2013).

[488] O. Suchoi, K. Shlomi, L. Ella, and E. Buks, *Time-resolved phase-space tomography of an optomechanical cavity,* Phys. Rev. A 91, 43829 (2015).

[489] M. Rashid, M. Toroš, and H. Ulbricht, *Wigner function reconstruction in levitated optomechanics,* Quantum Meas. Quantum Metrol. 4, 17 (2017).

[490] S. Bose, K. Jacobs, and P. L. Knight, *Scheme to probe the decoherence of a macroscopic object,* Phys. Rev. A 59, 3204 (1999).

[491] S. Bose, A. Mazumdar, G. W. Morley, H. Ulbricht, M. Toroš, M. Paternostro, A. A. Geraci, P. F. Barker, M. S. Kim, and G. Milburn, *Spin entanglement witness for quantum gravity,* Phys. Rev. Lett. 119, 240401 (2017).

[492] C. Marletto and V. Vedral, *Gravitationally induced entanglement between two massive particles is sufficient evidence of quantum effects in gravity,* Phys. Rev. Lett. 119, 240402 (2017).

[493] S. M. Barnett and P. M. Radmore, *Methods in Theoretical Quantum Optics*, Oxford Series in Optical and Imaging Sciences (Oxford University Press, Oxford, 1997).

[494] Y. Zhai, F. E. Becerra, B. L. Glebov, J. Wen, A. E. Lita, B. Calkins, T. Gerrits, J. Fan, S. W. Nam, and A. Migdall, *Photon-number-resolved detection of photon-subtracted thermal light,* Opt. Lett. 38, 2171 (2013).

[495] S. M. Barnett, G. Ferenczi, C. R. Gilson, and F. C. Speirits, *Statistics of photon-subtracted and photon-added states,* Phys. Rev. A 98, 013809 (2018).

[496] I. Ghiu, P. Marian, and T. A. Marian, *Loss of non-Gaussianity for damped photon-subtracted thermal states,* Phys. Scr. T160, 014014 (2014).

[497] K. Wakui, H. Takahashi, A. Furusawa, and M. Sasaki, *Photon subtracted squeezed states generated with periodically poled PKTiOPO$_4$,* Opt. Express 15, 3568 (2007).

[498] M. S. Kim, E. Park, P. L. Knight, and H. Jeong, *Nonclassicality of a photon-subtracted Gaussian field,* Phys. Rev. A 71, 043805 (2005).

[499] D. F. Walls and G. J. Milburn, Input–output formulation of optical cavities, in *Quantum Optics* (Springer, Berlin, Heidelberg, 2008) pp. 127–141.

[500] U. Leonhardt and H. Paul, *Realistic optical homodyne measurements and quasiprobability distributions,* Phys. Rev. A 48, 4598 (1993).

[501] T. Sonehara, Y. Konno, H. Kaminaga, S. Saikan, and S. Ohno, *Frequency-modulated stimulated Brillouin spectroscopy in crystals,* J. Opt. Soc. Am. B 24, 1193 (2007).

[502] Y. Kang, H. X. Lu, Y. H. Lo, D. S. Bethune, and W. P. Risk, *Dark count probability and quantum efficiency of avalanche photodiodes for single-photon detection,* Appl. Phys. Lett. 83, 2955 (2003).

[503] J. Zhang, M. A. Itzler, H. Zbinden, and J.-W. Pan, *Advances in InGaAs/InP single-photon detector systems for quantum communication,* Light Sci. Appl. 4, e286 (2015).

[504] A. Tosi, A. Della Frera, A. Bahgat Shehata, and C. Scarcella, *Fully programmable single-photon detection module for InGaAs/InP single-photon avalanche diodes with clean and sub-nanosecond gating transitions,* Rev. Sci. Instrum. 83, 013104 (2012).

[505] B. E. A. Saleh and M. C. Teich, *Fundamentals of Photonics*, 2nd ed. (John Wiley & Sons, New York; Chichester, 2007).

[506] Y. Li, The IQ imbalance model, in *In-Phase and Quadrature Imbalance: Modeling, Estimation, and Compensation* (Springer, New York, 2014) pp. 3–27.

[507] A. I. Lvovsky and M. G. Raymer, *Continuous-variable optical quantum-state tomography,* Rev. Mod. Phys. 81, 299 (2009).

[508] H. Zhan, G. Li, and H. Tan, *Preparing macroscopic mechanical quantum superpositions via photon detection,* Phys. Rev. A 101, 63834 (2020).

Copyright and permissions for reproduced material

Some figures and parts of figures in this thesis have been reproduced or adapted from the works of other authors. Copyright information and permissions to reproduce these works are listed below.

Figure 2.2:

(a) Reprinted from Del'Haye *et al.* [44] by permission from Springer Nature Copyright Nature Publishing Group, Licence number 5191490290866

Figure 2.9:

Adapted from Del Bino *et al.* [16] under a Creative Commons BY licence Copyright of the original figure: the Authors

Figure 5.2:

(a) Reprinted from Gröblacher *et al.* [438] by permission from Springer Nature Copyright Macmillan Publishers, Licence number 5184980425345

(b) Reprinted from Verhagen *et al.* [23] by permission from Springer Nature Copyright Macmillan Publishers, Licence number 5184341197630

(c) Reprinted from Anetsberger *et al.* [240] by permission from Springer Nature Copyright Macmillan Publishers, Licence number 5184320803095

(d) Reprinted from Chan *et al.* [385] by permission from Springer Nature Copyright Macmillan Publishers, Licence number 5184390137425

(e) Reprinted from Thompson *et al.* [431] by permission from Springer Nature Copyright Nature Publishing Group, Licence number 5184390701643

(f) Reprinted from Kiesel *et al.* [439] according to PNAS guidelines (non-commercial) Copyright the Authors

Figure 5.3:

(a) Adapted from Price [450] under a Creative Commons BY-NC licence Copyright of the original figure: John Price

Figure 6.7:

Adapted from Price [450] under a Creative Commons BY-NC licence Copyright of the original figure: John Price